UNIVERSITY OF SÃO PAULO
INSTITUTE OF CHEMISTRY
Graduate Program in Chemistry

CARLA SANTANA SANTOS

Development of an electrochemical microsensor for monitoring the respiration activity of single cells and animals by scanning electrochemical microscopy

Revised version of the thesis according to the Resolution CoPGr 5890. The original version is available in the Graduate Office at the Institute of Chemistry

São Paulo

Deposit date at the SPG:
November 11th 2019

CARLA SANTANA SANTOS

Desenvolvimento de microssensor eletroquímico para o monitoramento da atividade respiratória de células e animais por microscopia eletroquímica de varredura

Tese apresentada ao Instituto de Química da Universidade de São Paulo para obtenção do Título de Doutor em Ciências (Química)

Orientador: Prof. Dr. Mauro Bertotti

São Paulo
2019

Ficha Catalográfica elaborada eletronicamente pelo autor, utilizando o
programa desenvolvido pela Seção Técnica de Informática do ICMC/USP e
adaptado para a Divisão de Biblioteca e Documentação do Conjunto das Químicas da USP

Bibliotecária responsável pela orientação de catalogação da publicação:
Marlene Aparecida Vieira - CRB - 8/5562

Santos, Carla Santana
S237d Development of an electrochemical microsensor for monitoring the respiration activity of single cells and animals by scanning electrochemical microscopy / Carla Santana Santos. - São Paulo, 2019.
228 p.

Tese (doutorado) - Instituto de Química da Universidade de São Paulo. Departamento de Química Fundamental.
Orientador: Bertotti, Mauro

1. Eletroquímica. 2. Microeletrodo. 3. Microscopia eletroquímica de varredura. 4. Sensor de oxigênio. 5. Eletroquímica bipolar. I. T. II. Bertotti, Mauro, orientador.

I dedicate this thesis to my parents, Vera and Joaquim.
To my grandparents, Lúcia, Joaquim, Elias,
Paulina, Valdemar and Amelia.
To my siblings, Ivo, Paula and Henrique.
To Katty and Kelly.

Acknowledgements

Sorry for the no Portuguese speakers, but the acknowledgements was written in Portuguese to facilitate my feelings expression.

Primeiramente, eu agradeço aos meus pais, Vera e Joaquim, por tudo que eles me ensinaram e dividiram comigo durante todos esses anos de vida, especialmente por me mostrar a importância da educação e do trabalho. Obrigada também por me mostrar que a paciência e humildade são virtudes a serem trabalhadas diariamente. Ao meu pai, agradeço pelos momentos de descontração e conversas durante as corridas na USP e nas diversas caronas. Agradeço à minha mãe por ser um exemplo de mulher forte e independente. Aos meus irmãos Ivo, Paula e Henrique, obrigada pelos aprendizados de conviver e (sobre)viver em sociedade. Em especial à Paula, minha irmã-gêmea, agradeço imensamente por ter tanta paciência e cuidados comigo e também pela longa convivência (desde o útero). Obrigada por me ensinar a combater as diárias barreiras da vida, a trabalhar minha humildade e por me mostrar que as pessoas são diferentes, sendo o respeito a única união entre elas. Agradeço ao meu irmão caçula, Henrique, pela parceria sem igual, aos longos momentos de descontração e de estudo. Em memória dos meus avós Amélia, Elias, Joaquim, Lúcia e Valdemar, obrigada pelos ensinamentos, carinho e amor. Agradeço minha vó e madrinha Paulina por ser o exemplo de bondade e empatia em minha vida. Obrigada vó, por me ensinar a respeitar as diferenças desse mundo e reconhecer privilégios individuais. Agradeço aos meus familiares pelos momentos juntos: Chaves Santanas, Santos e Alfredos. Em especial agradeço aos meus tios Ana Cristina e Mauricio, por me mostrarem a encarar o mundo, descobrir novas culturas, sendo exemplos em dedicação e força de vontade. Amo vocês.

Ao Prof. Dr. Mauro Bertotti, agradeço por tudo que me proporcionou. Agradeço a cada ensinamento, que foram vários, desde os no campo da academia, quanto da política e do ensino. Agradeço por ter tanta paciência comigo, principalmente nos momentos de discussões em que muitas vezes nossas opiniões eram divergentes. Dessa forma, obrigada por respeitar as minhas opiniões. Obrigada por me incentivar e me fortalecer nos diversos momentos desafiadores que passei durante esse tempo. Agradeço por ser meu maior exemplo dentro do IQ por buscar a excelência no ensino e pesquisa, por valorizar a vivência e imersão no instituto e na USP, desde experiências de descontração até técnicoadministrativas. Obrigada por ter sido uma pessoa crítica e motivadora durante esses anos. Um *high five* pelas companhias nos bandejões. Agradeço imensamente por cada oportunidade que me fez chegar a esse dia.

Agradeço à minha co-orientadora Profa. Dra. Alicia Juliana Kowaltowski, por abrir a porta para essa oportunidade desafiadora de construirmos esse trabalho. Obrigada pelos ensinamentos, as críticas construtivas, por ser tão atenciosa, e por me dar oportunidade de conviver com as pessoas do LME, onde aprendi muito. Obrigada por me mostrar o mundo fantástico da bioenergética e a ser mais uma fã das mitocôndrias. Obrigada pela oportunidade de convivência, sendo um exemplo de mulher na ciência com muita dedicação, qualidade e objetividade. E também um exemplo dentro da instituição, buscando a melhoria do ensino e pesquisa.

I would like to express my gratefullness and appreciation to Herrn Prof. Dr. Wolfgang Schuhmann. Thanks for trusting on me and giving me the opportunity to work in your laboratory. Thanks for the several tips and discussions, for pressing and pushing me to keep in progress. Thanks for your friendship and for sharing your family with me (Jutta, Fabian, Jakob, Salo and Tim). Herzlichen Dank.

Obrigada aos atuais membros do LSEME pelas ajudas e momentos de discussões, distrações e bandejões: Ana Belarmino, Anand, Ananthi, Douglas, Fabiana, Gilberto, Jéssica, João, Matias, Matheus e Renato; e aos ex-LSEMEs, pelo aprendizado de trabalhar em equipe, colaborações e convivência: Abhishek, Alan Rogério, Alex, Aline Parlato, Aline Speranza, Ana Paula, Anna, Drochss, Eduardo, Gabriel, Lucas (Papete), Luiza Dantas, Nailson, Pollyana, Roselyn, Tony, Victor (Hurricane) e Vinicius. Agradeço aos convidados do período: Dario, Keely, Oliver, Saiful e Teena. Obrigada à Cristina e Lúcia, pelas conversas, ajuda e organização do laboratório.

Em especial, agradeço imensamente aos meus colegas Alex e Gabriel (novamente), peças essenciais e valiosas para minha vivência nesse período, pessoalmente e profissionalmente. Obrigada por cada ensinamento, discussões, críticas e incentivos. Amo vocês.

Aos ex-membros que passaram a barreira da sala 269 e hoje, mesmo longe, somos uma grande família de filhos científicos do sr. Bertotti (Joinha). *High-five-around-the-world* pelo tempo de descontração, ensinamentos e conselhos: Alex (novamente), Gabriel (novamente), Maiara, André, Bel, Helena, Tiago (Pé), Joca, Juliana, Thiago Paixão, Thiaguinho, Ana, Victor (Hurricane, novamente) e Lis.

Um agradecimento geral aos laboratórios e docentes que me deram suporte (infraestrutura ou discussões) e contribuíram direta e indiretamente nos trabalhos desenvolvidos, em especial aos docentes dos laboratórios de eletroquímica/eletroanalítica e analítica do instituto: Professores Claudimir Lago, Ivano Gutz, Lúcio Angnes, Roberto Torresi, Silvia Serrano, Susana Torresi e Thiago Paixão. Aos membros atuais e ex-membros do LME (bioquímica), em especial as divas: Camille (Cah), Fernanda (Nanda), Julia e a Pâmela. To the current, former and guest-ELAN members, specially to my collegues and friends Alex, Bettina, Corina, Dulce, Elena, Federica, Felipe, João, Michaela, Olga, Thomas E., Tsvetan and Vera. The period I spent in Bochum is filled with good memories because of them. Aos atuais e ex membros do LME (química), em especial, ao André (Conan), Aruã, Cintia, Fernando, Gabrielle, Jadielson, Jose Ribamar, Lucas (Furão), Marcos (Pinguim), Rafael Trivella (Erlen), Rafael Colombo (Dexter) e Vitor Martins. Aos atuais e ex-membros do LAIA, em especial, ao Eric Tavares (Pop), Fernando (Ferds), Iranaldo, Mauro (baiano) e ao Splinter. E ao pessoal do L_2ESQ: Haz, Iana, João (novamente), José (Zé Lindo), Leticia, Ligia, Luiza (Meg), Thalita, Thiago Selva, Vanessa, William e Wilson.

Grazie mille to the Professor Salvatore Daniele (Università Ca'Foscari) for the opportunity to work in his lab during my undergraduation.

Agradeço aos meus colaboradores das biológicas, que se tornaram grandes amigos no meio de tantos experimentos com enormes números de amostras e discussões de experimentos! Obrigada por fazer o tempo passar com diversão e bastante discussão científica: Ignacio Granja, Renata Bannitz, Katia Prieto e Felipe Macedo.

Obrigada aos meus colegas da graduação (turma 010), especialmente ao grupo Eixo, à Carol Guedes, à Carol Matos, ao Marcos (Blue) e à Stefhanie (Beibe) que me acompanharam de maneira mais próxima. Agradeço também as amizades que a USP me trouxe, essenciais para os momentos de descontração: Aninha Beltran, Daniel (Danidan), Daniel (Zozo), Gabriela Oliveira, Gilson Reis, Felipe (Panda), Larissa (Totó), Luiza

(Meg, novamente), João (novamente), Marcelo (Pai), Natalia Fritzen, Rafael (Erlen, novamente), Reinaldo Viana, Robson (Robgol), Rodrigo (Jake), Rodrigo (Ken), Thais Viggiani e Otavio (Vanderlei).

Aos meus professores da escola estadual Professor Luiz Gonzaga Pinto e Silva que me incentivaram mesmo sem grande estrutura, em especial aos professores Claudio, Juana, Luciana, Maria Celia, Marcos Vinicius e Patricia. Aos amigos da família pelo suporte e por me motivar, em especial aos Brandões, Brescianis, Bunzels, Ribeiros e Rugais.

Agradeço aos meus colegas de escola pela amizade e convivência, em especial a Amanda Moura pela atitude de valor imensurável de me doar a vaga para realizar a prova de bolsa integral do cursinho pré-vestibular Anglo, que foi essencial para meu ingresso na USP.

Um mol de agradecimentos aos meus amigos da vida que conheci no meu bairro, na escola, na USP, nos teatros, nas idas e vindas ao Rio e à Alemanha e que partilharam e partilham momentos de alegria e tristeza, me ajudando a construir o valor da amizade que respeito tanto. Obrigada pela amizade, pela paciência, pelas conversas e por estar ao meu lado quando preciso e precisei. Saibam que sem vocês não conseguiria alcançar nada, e mesmo se alcançasse, não teria o mesmo valor para mim por não ter companhias como vocês para comemorar. Amo vocês: Alessander Burger, Alex da Silva, Bruna Kaetano, Bruno Lima, Caroline Guedes, Daniel Imbiriba, Gabriel Negrão, Gabriella Felix, Giovanna Nastasi, Henrique Santos, João Junqueira, Julia Touriño, Letícia Mamede, Lucas Coimbra, Luciene Lima, Natache Abdalla, Paula Santos, Rafael Conceição, Regiany Pereira, Stefhanie Merino e Vanessa Sotero.

Ao Instituto de Química, pela estrutura: central analítica, aos diversos e qualificados docentes, aos prestativos funcionários e ao corpo discente. Aos funcionários da USP, que juntos ao corpo docente, são responsáveis pela excelência da melhor universidade do país. Agradeço também aos funcionários dos restaurantes universitários, input quase que diário nos meus 10 anos de USP. E por fim, ao suporte direto e indireto das agências de fomento CNPq, CAPES e FAPESP, em especial a FAPESP pela bolsa concedida para a realização desse doutorado (#2014/22396-6) e ao estágio no exterior (#2017/12629-1).

“If I have seen further
it is by standing on the shoulders of Giants”
Sir Isaac Newton

ABSTRACT

Santos, C. S. **Development of an electrochemical microsensor for monitoring the respiration activity of single cells and animals by scanning electrochemical microscopy.** 2019. 228 p. PhD Thesis - Graduate Program in Chemistry. Instituto de Química, Universidade de São Paulo, São Paulo.

This thesis shows results on the development of an O_2 micro/nanosensor for scanning electrochemical microscopy (SECM) application with the aim of monitoring changes in respiration activity over a single cell. The surface of platinum microelectrodes was modified by using a platinisation protocol in order to facilitate the eletron-transfer process regarding the O_2 reduction reaction, hence the sensitivity of the device was greatly enhanced. The stability of the microsensor and the nature of oxygen reduction reaction (ORR) products were also evaluated by SECM. The developed microsensor was employed in redox competition SECM operating mode to monitor local changes in the O_2 concentration of a single-cell (HS578T lineage) present in phosphate buffer medium during the addition of specific compounds to modulate the mitochondria activity. A similar protocol was used for examining the metabolism of a nematode (*Caenorhabditis elegans)* by scanning the O_2 microsensor over a single-animal, with particular attention being devoted to the reproductive system. Hence, SECM has been proven to be a powerful and reliable technique to investigate biochemical events related to cellular activity by means of oxygen consumption rate (OCR) with high spatial resolution. The last section of this thesis presents a novel scanning probe microscopy developed in the Prof. Schuhmann's group (Germany) employing bipolar electrochemistry concepts. The scanning bipolar electrochemical microscopy (SBECM) allows the independent acquisition of multi-microelectrodes responses localized close to a surface. In contrast of scanning a single probe as the conventional SECM, higher temporal resolution is obtained with SBECM. The results showed in this thesis confirmed the ability of the electrochemical probe techniques to acquire local O_2 concentration information and to provide deeper insight and comprehensive aspects in the biological area.

Keywords: Scanning Electrochemical Microscopy, SECM, Microelectrode, OCR, Oxygen sensor, bipolar electrochemistry.

RESUMO

Santos, C. S. **Desenvolvimento de microssensor eletroquímico para o monitoramento da atividade respiratória de células e animais por microscopia eletroquímica de varredura**. 2019. 228 p. Tese (Doutorado) - Programa de Pós-Graduação em Química. Instituto de Química, Universidade de São Paulo, São Paulo.

Nesta tese são apresentados resultados sobre o desenvolvimento de um micro/nanossensor de O_2 para aplicação em microscopia eletroquímica de varredura (SECM) com o objetivo de monitorar alterações na atividade respiratória em uma única célula. A superfície dos microeletrodos de platina foi modificada por meio de um protocolo de platinização, visando à facilitação do processo de transferência de elétrons da reação de redução do O_2. Como consequência, a sensibilidade do dispositivo no que diz respeito à detecção de O_2 foi bastante aumentada. A estabilidade do microssensor e a natureza dos produtos ORR também foram avaliadas por SECM. O microssensor desenvolvido foi empregado no modo de "competição redox" da SECM para monitorar alterações locais na concentração de O_2 em células (linhagem HS578T) em tampão fosfato durante a adição de substâncias específicas para modular a atividade das mitocôndrias. Um protocolo semelhante foi usado para examinar o metabolismo de um nemátodo (Caenorhabditis elegans) pela movimentação do microssensor de O_2 sobre um único animal, com atenção especial sendo dedicada ao sistema reprodutivo. Portanto, a SECM demonstrou ser uma técnica poderosa e confiável para investigar eventos bioquímicos relacionados à atividade celular com alta resolução espacial. A última seção desta tese apresenta uma nova modalidade de microscopia de varredura desenvolvida no grupo do Prof. Schuhmann (Alemanha), baseada em conceitos de eletroquímica bipolar. A microscopia eletroquímica bipolar de varredura (SBECM) permite a aquisição independente de respostas de multi-microeletrodos localizados próximos a uma superfície. Ao contrário do deslocamento de uma única sonda como na SECM convencional, no caso da SBECM dados são obtidos com maior resolução temporal. Os resultados apresentados nesta tese confirmaram a versatilidade das técnicas de sondas eletroquímicas para a obtenção de informações localizadas sobre a concentração de oxigênio e como ferramentas para a expansão de conhecimentos mais aprofundados e abrangentes na área biológica.

Palavras-chave: Microscopia Eletroquímica, SECM, Microeletrodo, OCR, sensor de oxigênio, eletroquímica bipolar.

CONTENTS

Aim of the thesis.

This thesis aims at showing results on the implementation of scanning electrochemical microscopy (SECM) as an analytical tool to get information on biological systems. The first bio-SECM equipment in Brazil was applied to study changes in the respiration activity of a single organism by measurements of O_2 concentration. The challenges involved the fabrication of a micro/nanosensor for high spatial resolution measurements, as well as the protocols to implement the bio-SECM technique to get reliable and reproducible information. A derived SECM workstation based on the bipolar concepts was developed to control a multi-probe, and such device was further applied to get high spatial and temporal resolution. Besides being used SECM tips, microelectrodes were used as sensors to determine the concentration of H_2O_2 in microscopic biological environments, such as plants and fungi. Micrometric pH sensors were also fabricated and employed to measure the pH at distinct sections of dissected midguts of insect larvae. The thesis is constituted by chapters, most of them corresponding to published articles.

Chapter 1.

State of the Art.

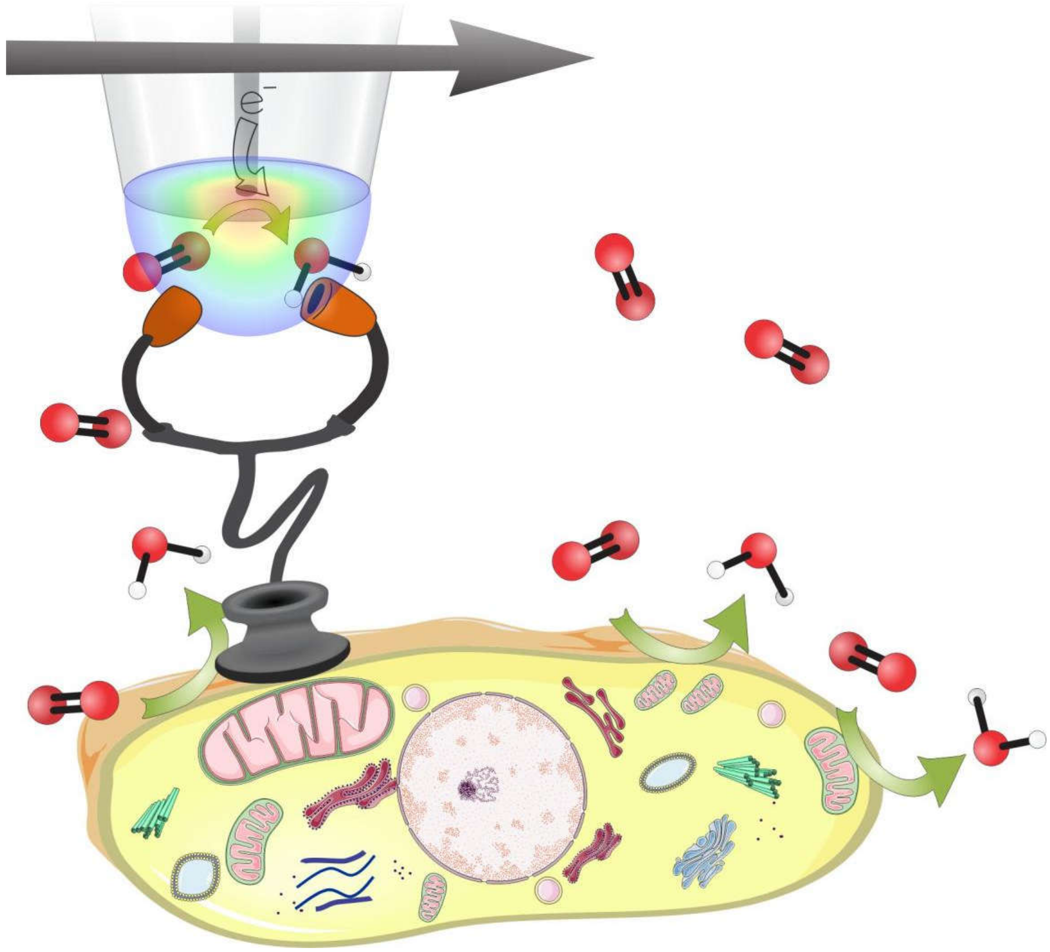

1.1. Scanning electrochemical microscopy.

Scanning electrochemical microscopy is considered to be an analytical tool for studies in microscopic and nanoscopic systems. Because many commercial SECM instruments have been recently commercialized, the range of applications of the technique has emerged in interdisciplinary areas. The advances in SECM have mainly focused on high-resolution measurements, such of nanoscopic scale and in the coupling of SECM to other techniques. However, the use of SECM as a routine analytical tool still requires caution, especially because the technique application depends on several complex parameters. Hence, it is not surprinsing that discussions on its reliability to get reproducible quantitative data have appeared in the literature, as thoroughly reported in a review paper from Kranz's group [1].

1.1.1. General concept.

Scanning probe microscopies (SPM) are techniques to investigate properties of a surface by means of a signal provided from a scanning probe. Then, the Scanning Electrochemical Microscopy (SECM) is a SPM technique where the probe is an electrode and, thus, the technique signal and resolution depend on features of this probe. The principle of the SECM is the fine control of the the movement of a microelectrode (tip) in *x, y, z* directions to investigate electrochemical properties of a sample (substrate). This is accomplished by positioning a biased microelectrode close to a substrate immersed in a solution. Such substrate can be polarized or unbiased, depending of its properties (insulating or conductive). The resulting current at the polarized tip depends on the faradaic process that occurs because of the presence of electroactive species in the solution or provided by the substrate, as well as and the distance between the end of the tip and the sample [2,3].

The simple SECM apparatus consists of 3 parts: a small electrochemical cell containing the substrate and and the electrodes, including the SECM tip; a bipotentiostat to control the electrochemical cell; and a positioning system to move accurately the tip over the substrate. A scheme of a SECM workstation is presented in Figure 1.1. The electrochemical cell may contain one or two working electrodes (tip or/and substrate), a reference electrode (RE) and a counter electrode (CE). The tip is held and moved by using a very accurate positioning system, which consists of a step motor (resolution of µm) and a piezoelectric ceramic (resolution of nm). The SECM tip is the main component of the system, once the microelectrode is responsible for the signal and the resolution of the technique.

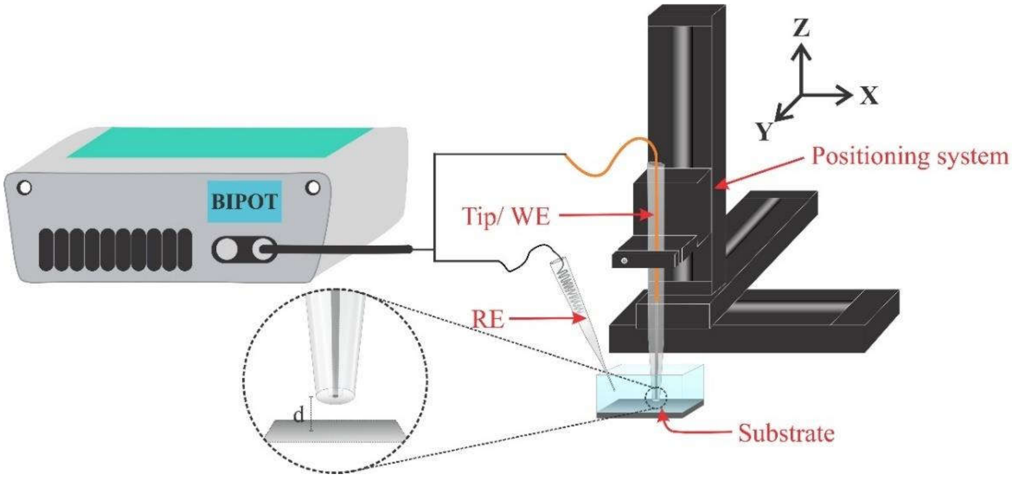

Figure 1.1. Scheme of the scanning electrochemical microscope workstation: Positioning system with the motors and the piezo cube; the tip; the electrochemical cell; the substrate; and the bipotentiostat.

1.1.2. Microelectrodes.

A microelectrode or ultramicroelectrode (UME) is a device known for having at least one of its dimension in the micrometric or sub-micrometric scale [4]. In a more restrict and technical way, the size is not the best parameter to define the concept of an UME, once the important aspect is the comparison of the thickness of the diffusion layer at a particular time with the size of the electrode. Thus, a microelectrode defined only by its size can have a non-micrometric response at certain experimental conditions [5,6]. In general aspects, microelectrodes are electrodes for whose the physical dimension is similar or smaller the one corresponding to the the diffusion layer at a defined condition [5]. At such conditions, the mass-transport towards the electrode surface is more effective.

Disc-shaped microelectrodes are typically used as SECM tips because of the easier mathematical treatment and available fabrication methods. At conditions where faradaic processes are important, mass-transport for microdisc-shaped electrodes occurs mainly by radial diffusion. If the overall electrode process is mass-transport controlled, current achieves a steady-state condition [7].

In the steady-state condition generated by a fast change of the applied potential, the microelectrode surface is involved by a hemispherical diffusion layer and the Equation 1.1 describes the current response:

$$j_L = \frac{nFD^{1/2}c}{\pi^{1/2}t^{1/2}} + \frac{4nFDc}{\pi r} \qquad \textit{Equation 1.1}$$

Where j_L is the current density at the steady-state (A.cm^{-2}), n is the number of electrons to the electrochemical reaction, F is the Faraday constant (s.A.mol^{-1}), D is the diffusion coefficient of the electroactive species (cm^2.s^{-1}), c is its concentration in the bulk (mol. cm^{-3}), t is the time elapsed after the potential change (s) and r is the microelectrode conductive radius (cm). The first term in the equation domains the current density at short times (Cottrell equation), whereas the second term is predominant in the steady-state condition at longer times. Considering the boundary condition for a disc-shaped microelectrode, Equation 1.1. can be rewritten to Equation 1.2. The X term is a geometric parameter and depends on the insulating part of the disc-shaped microelectrode. The relationship between the glass insulating sheath radius to the conductive fiber radius is a parameter known as RG (Figure 1.2)

$i_L = XnFDrc$ where $X = 4 + 0.55\,(RG - 0.67)^{-0.87}$ *Equation 1.2* [8]

UMEs fabricated for SECM experiments usually have small tip size to increase the resolution. However, for UMEs with very low RG values the electroactive species can also diffuse by the back of the electrode tip (see the scheme in Figure 1.3). This effect is named back diffusion and can influence the mass transport towards the electrode for SECM tips with RG < 10. For such microelectrodes the RG-dependent term X is higher to account for the extra-mass transport, then the measured current is higher than the one obtained for an UME with RG > 10, but with the same electroactive area [9].

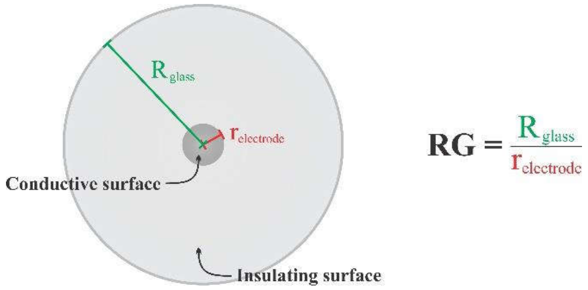

Figure 1.2. Schematic representation of a disc electrode surface, the insulating material and the factor RG.

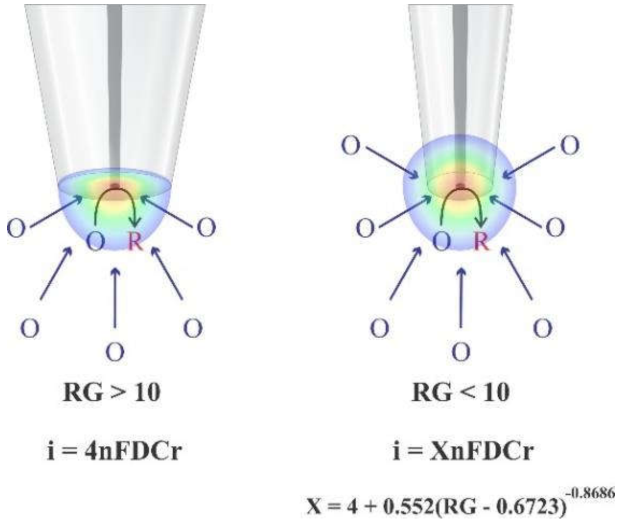

Figure 1.3. Influence of the back diffusion on the current measured at microelectrodes with different RG values [8].

Besides the steady-state condition, essential in SECM experiments as the idea is to get no time-dependent information, microelectrodes also present as benefits increased faradaic/capacitive current ratio and low ohmic drop because of the small size. Such features expand the use of UMEs to various applications such as in the control of industrial processes and to environmental measurements [10].

1.1.3. SECM operating modes.

The SECM can be used for electrochemical investigations in different operating modes: "*feedback mode*", "*generation/collection*" and "*redox competition*" [11–13].

In the feedback mode, the tip current depends on faradaic processes involving electroactive species, commonly reversible redox couples (redox mediators). The microelectrode is polarized to convert the redox mediator while it is positioned close to the substrate surface [14]. As mentioned before, the SECM steady-state current depends on the solution composition (concentration and diffusion coefficient of the electroactive species), but also on the nature of the substrate surface and the distance between the tip and the sample. Figure 1.4 shows a scheme of different processes taking place with a SECM tip close to both an insulating and a conductive surface in the presence of a redox mediator (O species).

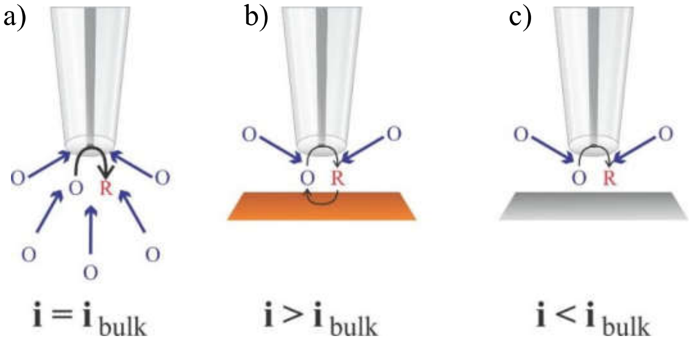

Figure 1.4. Electrochemical reduction of an oxidized species (O) at a microelectrode positioned far from a substrate (a) and close to a conductive (b) and an insulating (c) substrate.

In the bulk solution, current follows the Equation 1.2 once it depends only on the radial diffusion of O, hence surface characteristics are not important. However, when the tip is moved towards the sample surface, current changes as a function of both the distance and the substrate features. For a conductive material, the species generated in the electrochemical process at the tip (e.g: R) diffuses to the substrate surface. Because both species of the redox reversible couple are confined within a thin layer, a small potential is created, but great enough for allowing the reverse reaction to occur at the conductive sample surface (center image in Figure 1.4). Hence, even if the substrate is unbiased, an electron-transfer process takes place at its surface. The phenomenon is called positive feedback as countless redox cycles take place at the tip and the sample surface, leading to a higher SECM current in comparison to the value measured at the bulk condition [15]. The positive feedback effect is much more effective as the tip-substrate distance decreases and it depends on the conductive surface in promoting the electrochemical reaction. A different situation is noticed when the tip moves towards an insulating surface and because the diffusion of the electroactive is hindered by the glass walls of the SECM tip, a current decrease is observed during the experiment (right image in Figure 1.4). This effect is known as hindered diffusion or negative feedback [11] and is completely dependent on the RG of the microelectrode. A routine SECM experiment for investigating the reactivity of a surface consists in approaching the tip towards the sample surface while the tip is polarized at a potential to achieve a steady-state condition. Current values in such an experiment are measured as a function of the tip z position (i *vs.* d) and the resulting curve is known as approach curve [16]. The approach curves are usually plotted by normalization of both current (i / i *bulk*) and distance (d / r*, where* r *is the radius of the electroactive disc*), hence such normalized curve can be compared with others recorded in different experimental conditions, regardless the concentration and diffusion coefficient of the electroactive species. Hindered diffusion curves can also be used to determine the RG of the microelectrode, once the negative feedback effect is highly dependent on the geometry of the tip.

The generation/collection (G/C) mode is a variation of the feedback mode, but in this case the substrate must be polarized. The G/C mode is used to investigate the sample surface reactivity in respect to an electrochemical reaction [17] and this is accomplished by collecting the product generated at the substrate or at the tip. There are two possibilities in the G/C mode: the tip generation/substrate collection and the substrate generation/tip collection mode. When the tip generates an electroactive species for further collection at the substrate, information on the electrochemical reaction can be achieved, because of the high collection factor [18] due to the large area of the collector compared to the tip area. In the tip collection/substrate generation mode, the concentration profile of the generated species on the substrate can be obtained to investigate localized changes in surface reactivity. These modes are used for kinetics studies involving modified surfaces and to get information on diffusion coefficients, charge transfer coefficients and reaction mechanisms [19,20].

SECM can also be operated in redox competition (RC) configuration, where the tip and the substrate compete for the same electroactive species dissolved in solution. Accordingly, changes in tip current are noticed because of the simultaneous consumption of a specific compound by the substrate. This SECM mode was described by the Schuhmann's group and used to evaluate the catalytic activity of enzymes [13,21,22] and in cell analysis [23]. The SECM modes are used to evaluate local surface information and most of the theorical treatments consider the constant rate of the reaction occuring at the sample and the tip. Thus, the RC mode is complex to interprete as the consumption of an electroactive species at the tip/sample may influence the concentration gradient of the tip/sample.

1.1.4. Theorical description of approach curves in feedback mode.

The literature reports several mathematic expressions for describing the approach curves in the positive feedback and hindered diffusion modes. Those expressions are employed to describe the tip current as a function of the distance between tip and substrate [2]. The first mathematical description was reported by Kwak and Bard [14], followed by Ampheltt and Denuault [24], who proposed theoretical approach curves for some determined RG values. Lefrou and Cornut proposed mathematical expressions with the RG as a parameter and one can obtain theoretical approach curves for positive feedback and hindered diffusion modes [8,25]. The Equation 1.3 presents the final expression reported by Lefrou to positive feedback [26] and the Equation 1.4 is the resulting expression to the hindered diffusion/negative feedback described by Lefrou and Cornut [8].

$$I_T[L, RG] = \alpha[RG] + \frac{\pi}{4\beta[RG\}\arctan(L)} + (1 - \alpha[RG] - \frac{1}{2\beta[RG\}})\frac{2}{\pi}\arctan(L) \qquad \textit{Equation 1.3}$$

$$I_T[L, RG] = \frac{\frac{2,08}{RG^{0,358}}\left(L - \frac{0,145}{RG}\right) + 1,585}{\frac{2,08}{RG^{0,358}}(L - 0,0023RG) + 1,57 + \frac{\ln(RG)}{L} + \frac{2}{\pi RG}\ln(1 + \frac{\pi RG}{2L})} \qquad \textit{Equation 1.4}$$

, where α and β are constants that depend on the RG value and L is the normalization of the work distance (d) per the electrode radius (r).

The Figure 1.5 shows approach curves simulated using Equations 1.3 and 1.4. As one can see, hindered diffusion approach curves are highly dependent on the RG, and the higher the RG the lower the current for the same distance [2]. On the other hand, changes in the approach curves for positive feedback curves are much less dependent on RG values.

Approach curves are extremely important in SECM experiments to obtain local information about the sample surface, as topography, properties (insulating and conductive material) and reactivity [25,27,28]. Besides that, approach curves can be used to determine the RG of the electrode using theorical expressions.

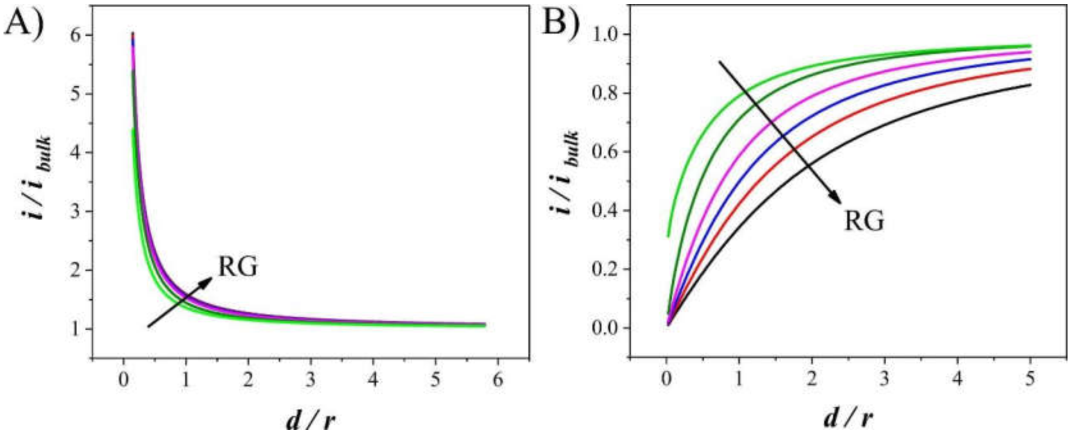

Figure 1.5. Theorical approach curves for (A) positive feedback and (B) hindered diffusion condition. RG values are: 1 (light green curves), 2 (dark green curves), 5 (pink curves), 10 (blue curves), 20 (red curves), 50 (black curves).

1.1.5. Application of SECM on biological samples.

The SECM has been largely applied in the investigation of biological samples, in the study of drugs effects in the metabolism, for evaluating enzymatic and cell activity and in topographic studies [29–33]. Because cells have microscopic dimensions and biological events often occur in short interval times, microelectrodes can be efficiently used as a tool to the investigation of biological samples/processes [34–36]. The local information is obtained with high spatial resolution by SECM. Hence, it is not surprising that bio-SECM has explored the challenge of working with complex samples in the last years to get information regarding cell permeability [37,38], cell topography [39,40], intra and extracelular reactions [41,42], oxidative stress in cells [43], and respiration activity in embryonic bovine cells [44,45]. However, the use of bio-SECM as an analytical tool to obtain local information of dynamics process with temporal and spatial resolution has still to be carefully evaluated [46–52].

1.2. Oxygen sensors.

The importance of oxygen is well-known as it is by far one of the molecules essential to life. Recently, the Nobel Prize was awarded to William G. Kaelin Jr, Sir Peter J. Ratcliffe and Gregg L. Semenza for their discoveries on how cells sense and adapt to oxygen availability (2019). A fundamental tool in this field are sensors able to determine the oxygen concentration. There are three basic methods for dissolved oxygen determination: chemical reaction based on the Winkler reaction; optical indicators using absorption changes or photoluminescence; electrochemical measurements using potentiometric, amperometric or conductometric principles. For on-time and continuous detection, the last two principles are widely used, however even with many advances in the optical sensors concerning sensitivity and miniaturization [53,54], the conventional method for room temperature conditions and biological samples is still the Clark electrode [55,56] (amperometric sensor). This is justified by the durability, easy handling, flexible application and reliable response of such electrochemical sensor. The Clark electrode consists of a bare platinum electrode with a Teflon membrane, which is employed as a barrier for increasing the selectivity. Hence, the sensing platform is only reached by O_2 diffusing through the membrane, and the response regarding any possible interfering compound is prevented [57].

Platinum surfaces are highly active for the oxygen reduction reaction (ORR) and the process takes place with the transfer of 4 electrons, resulting in water as the final product. Although platinum surfaces have high activity towards ORR, which means less negative applied potentials, such noble material is still expensive for wide application and, consequently, the search for low-cost and stable Pt-free alternative materials has attracted the attention of the scientific community [58]. Recently, many researches have focused in fuel cells to improve energy conversion and to prevent the use of fossil fuels. The ORR occurs at the cathode and many alternatives to platinum surfaces have been presented by changing the surface of electrodes with cobalt porphyrin [59,60], nickel with polymers [61], polyaniline incorporating iron and cobalt [62], or nanotubes materials [63]. The reduction of oxygen at such modified surfaces is a many-step mechanism, requires high negative potentials and so far platinum materials are still the best choice for ORR in general conditions [58,62,64]. The activity towards ORR depends on the solution pH and the nature of the platinum surface [58,65]. The detailed oxygen reduction mechanism on platinum surfaces is still under investigation and two paths are shown to be possible: the direct four-electron route, with no intermediate (Equation 1.5); and the two-sequential-steps with a stable intermediate (H_2O_2), Equation 1.6, which is partially reduced to H_2O (Equation 1.7), giving in the end a n_{eff} smaller than 4 [65].

$$O_2 + 4H^+ + 4e^- \rightleftharpoons 2H_2O \qquad \text{Equation 1.5}$$

$$O_2 + 2H^+ + 2e^- \rightleftharpoons H_2O_2 \qquad \text{Equation 1.6}$$

$$H_2O_2 + 2H^+ + 2e^- \rightleftharpoons 2H_2O \qquad \text{Equation 1.7}$$

1.3. Bioenergetics.

Bioenergetic studies the energy metabolism, the group of chemical reactions responsible to generate energy for the cell’s functionality. Recent studies show that it controls many other cellular processes, including inflammation and immunity, stem cell differentiation and cell death. Chemical energy conversion occurs mainly inside an important organelle, the mitochondria. Mitochondria are small organelles located within the cells and they execute the respiration process (Figure 1.6). The metabolism is linked to the energy generation in the respiration process which uses electrons originated from the glycose/substrates oxidation to convert oxygen to water in the electron transport chain

(ETC). The ETC process occurs through the four complexes in the mitochondrial intern membrane, and in this process a membrane potential is created by the protons pumped from the inner to the intermembrane space. This H^+ concentration gradient is responsible to provide energy to the ATP synthase (oxidative phosphorylation).

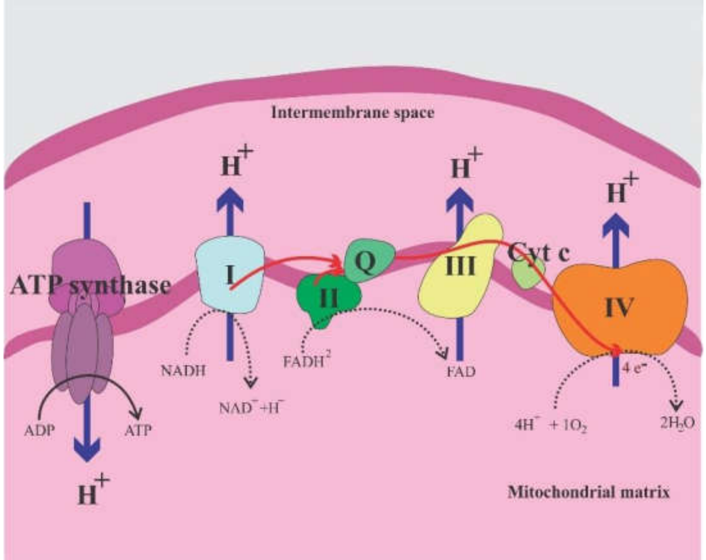

Figure 1.6. Schematic representation of mitochondria complexes.

Thus, the understanding of the mitochondrial respiration process is essential, once damages in the mitochondrial enzymes lead to the production of reactive oxygen species (ROS). ROS are linked to the development of diseases such as Parkinson and Alzheimer and to the aging process [66,67]. Recent studies showed that caloric restriction (diet) can promote a variation in the respiratory metabolism, reducing the ROS production and retarding the damages [68]. Therefore, tools to investigate the mitochondrial activity have been developed [69–71] and measurements of oxygen consumption are extremely important to obtain information on the ETC and the oxidative phosphorylation processes. Routinely, the respiration activity is monitored by means of the oxygen consumption rate (OCR) during experiments in which the individual mitochondrial complex function is modulated with specific inhibitors, reducing the OCR, or with uncoupling species, promoting the maximum OCR [72]. The majority of mitochondrial activity experiments are performed using a pool of isolated mitochondria because limitation in the sensitivity of oxygen sensors (Clark electrode). However, the cell/tissues handling can generate metabolic alteration. Methodologies have been recently developed to enhance the sensitivity of OCR measurements[69,73], among which the Seahorse commercial instrument presents the highest sensitivity to OCR determination. In this equipment, intact attached cells can be used as low concentration sample. However, as a disadvantage, the equipment is expensive and has no flexibility to the experimental arrangement [73]. The frontier of knowledge in bioenergetics is based on the differences in mitochondria (fusion and fission effects)[74] and the commercial equipment still does not have the capability to get mitochondria OCR. In this context, one of the main motivations of this work is to contribute in the development of new advances towards investigations in a single cell.

1.4. Bipolar Electrochemistry.

Bipolar electrochemistry has a typical experimental configuration consisting of two feeder electrodes and a bipolar electrode (BPE), which is placed between them. A potential is applied to the feeder electrodes and an electric field is provided across a diluted and inert electrolyte solution (Figure 1.7). The application of an electric field to an electrolyte solution via two feeder electrodes generates anodic and cathodic interfacial potential differences at the opposite extremities of a conductive object located in between (BPE). The electric field in the bipolar electrochemistry is typically applied by a pair (or more) of driving electrodes, which can be metallic (e.g., Au, Ag, Pt, or stainless steel), carbonaceous (e.g., glassy carbon or graphite), or nonpolarizable (e.g., Ag/AgCl reference electrode). The nature of the electric field formed between the driving electrodes depends on the cell geometry and the conductivity of the electrolyte[75].

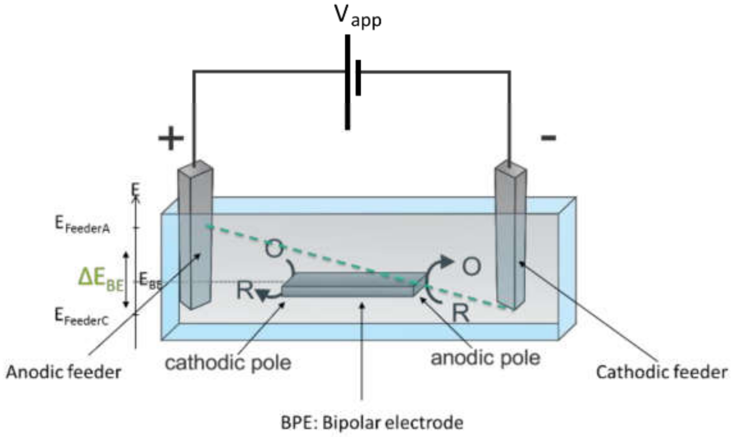

Figure 1.7. Schematic illustration of the principles of bipolar electrochemistry.

Reactions in bipolar electrode (BPE) surfaces take place because of the overpotential caused by the electric field (V_{app}) of the feeder electrodes, as seen in Figure 1.7. The potential depends on the position of the BPE in the field and the composition of the electrolyte solution (conductivity). As the BPE is a conductor, the potential E_{BE} is the same over its surface. However, the interfacial potential at the BPE surface and the solution changes from the equilibrium potential (E_{BE}) and varies along the length of the BPE due to the presence of an electric field in solution. The interfacial potential is higher at the ends of the BPE, so faradaic processes are always first observed at these regions (poles). The overpotential value depends on just two experimental conditions: the magnitude of V_{app} and the length of the BPE. As represented in Figure 1.7, overpotential varies from maximum to minimum value along the length of the BPE, in the anodic and cathodic poles[76]. This non-uniformity of the interfacial potential differences along the length of a BPE can be used to simultaneously drive reactions at different rates or to synthesize materials and thin films having a graded composition or density.

Consequently, oxidation and reduction reactions occur at the electrically unconnected, bipolar electrode (BPE)[75]. This characteristics of the bipolar electrochemistry has previously been exploited for site selective electrodeposition [77,78], electrochemically generated motion [79] or material characterisation [80.]. On the other hand, a closed bipolar electrochemical cell (Figure 1.8) can be used instead of the traditional open bipolar configuration (Figure 1.7.) [81–84]. The configuration of closed BPE consists of, basically, solutions physically separated from anodic and cathodic poles, and the only current path between the two half cells is through the bipolar electrode.

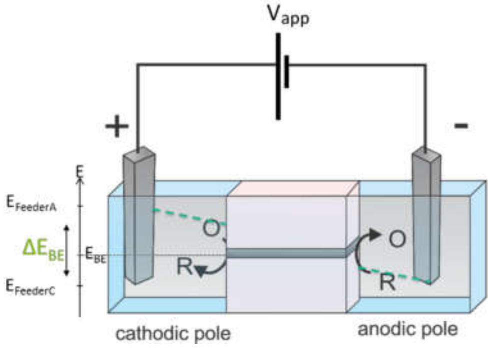

Figure 1.8. Schematic illustration of the bipolar electrode in the closed configuration.

As no contact to the BPE is required, the strategy commonly used to quantify a target analyte in bipolar electrochemistry experiments is based on chemiluminescence measurements: a reaction of interest occurs at one pole of the BPE and a different reaction produces a chemiluminescent species[85–88] at the other pole. Since anodic and cathodic currents at the BE have to be equal ($i_a = i_c$), the optical signal serves to derive the bipolar current. This strategy makes it possible for a large number of electrodes to be used in a simple setup, once it is a wireless-contact method. This advantage is essential in the sensing field because many different electrodes can be controlled simultaneously. During the past 30 years, many interesting bipolar electrochemical experiments have been reported in the literature for different applications, such as for improving the efficiency of electrosynthesis [89,90], photoelectrochemical cells [91,92], and even batteries [93,94]. As no ohmic contact is required for a reaction take place at the BPE, a specific reaction at one pole of the BPE is induced to move the electrode in the solution by bubbles production [95–97] (i.e., H_2 or O_2), generating sufficient propulsion to induce the movement of small

BPEs. Sensing devices developed based on the concept of bipolar electrochemistry[98,99] have demonstrated to be an excellent alternative for chemical and biological sensing [75,100].

1.5. References.

1. Izquierdo, J.; Knittel, P.; Kranz, C. *Anal. Bioanal. Chem.* **2018**, 410, 307–324.

2. *Scanning electrochemical microscopy,* Bard, A. J.; Mirkin, M. V. , Eds. Marcel Dekker: Eds New York; **2001**.

3. Barker, A. L.; Gonsalves, M.; MacPherson, J. V; Slevin, C. J.; Unwin, P. R. *Anal. Chim. Acta* **1999**, 385, 223-240.

4. Pons, S.; Fleischmann, M. *Anal. Chem.* **1987**, 50, 1391A-1399A.

5. Štulík, K.; Amatore, C.; Holub, K.; Mareček, V.; Kutner, W. *Pure Appl. Chem.* **2000**, 72 , 1483–1492.

6. Paixão, T. R. L. C.; Bertotti, M. *Quim. Nova* **2009**, 32 , 1306–1314.

7. *Electrochemical Methods: Fundamentals and applications*, Bard, A. J.; Faulkner, L. R., 2nd ed.; John Wiley & Sons, **2001**.

8. Cornut, R.; Lefrou, C. *J. Electroanal. Chem.* **2007**, 604, 91–100.

9. Zoski, C. G.; Mirkin, M. V. *Anal. Chem.* **2002**, 74 , 1986–1992.

10. Abreu, F. C.; Goulart, M. O. F.; Brett, A. M. O. *Biosens. Bioelectron.* **2002**, 17, 913–919.

11. Bard, A. J.; Fan, F. F.; Kwak, J.; Lev, O. *Anal. Chem.* **1989**, 61, 132–138.

12. Lu, X.; Wang, Q.; Liu, X. *Anal. Chim. Acta* **2007**, 601, 10–25.

13. Eckhard, K.; Chen, X.; Turcu, F.; Schuhmann, W. *Phys. Chem. Chem. Phys.* **2006**, 8, 5359–5365.

14. Kwak, J.; Bard, a J. *Anal. Chem.* **1989**, 61, 1221–1227.

15. Bard, A. J.; Fan, F. R. F.; Kwak, J.; Lev, O. *Anal. Chem.* **1989**, 61, 132–138.

16. Wipf, D. O.; Bard, A. J. *J. Electrochem. Soc.* **1991**, 138, 469–474.

17. Fernández, J. L.; Bard, A. J. *Anal. Chem.* **2003**, 75, 2967–2974.

18. Sánchez-Sánchez, C. M.; Rodríguez-López, J.; Bard, A. J. *Anal. Chem.* **2008**, 80, 3254–3260.

19. Tenent, R. C.; Wipf, D. O. *J. Solid State Electrochem.* **2009**, 13, 583–590.

20. Rodriguez-Lopez, J.; Alpuche-Aviles, M. A.; Bard, A. J. *Anal. Chem.* **2008**, 80, 1813–1818.

21. Karnicka, K.; Eckhard, K.; Guschin, D. A.; Stoica, L.; Kulesza, P. J.; Schuhmann,

W. *Electrochem. commun.* **2007**, 9, 1998–2002.

22. Eckhard, K.; Schuhmann, W. *Electrochim. Acta* **2007**, 53, 1164-1169.

23. Nebel, M.; Grützke, S.; Diab, N.; Schulte, A.; Schuhmann, W. *Angew. Chemie - Int. Ed.* **2013**, 52, 6335–6338.

24. Amphlett, J. L.; Denuault, G. *J. Phys. Chem. B* **1998**, 102, 9946–9951.

25. Lefrou, C.; Cornut, R. *Chemphyschem* **2010**, 11, 547–556.

26. Lefrou, C. *J. Electroanal. Chem.* **2006**, 592, 103–112.

27. Gamboa, J. C. M.; Peña, R. C.; Paixão, T. R. L. C.; Lima, A. S.; Bertotti, M. *Electroanalysis* **2010**, 22, 2627–2632.

28. *Scanning Electrochemical Microscopy,* Bard, A. J.; Mirkin, M. V., 2nd edition; CRC Press, **2012**.

29. In *Trends in Bioelectroanalysis,* Géza, N.; Lívia, N.; Matysik, F.-M., Ed.; **2017**, 281–339.

30. Yamada, H. *Electrochim. Acta* **2014**, 136, 233–239.

31. Actis, P.; Tokar, S.; Clausmeyer, J.; Babakinejad, B.; Mikhaleva, S.; Cornut, R.; Takahashi, Y.; López Córdoba, A.; Novak, P.; Shevchuck, A. I.; Dougan, J. A.; Kazarian, S. G.; Gorelkin, P. V.; Erofeev, A. S.; Yaminsky, I. V.; Unwin, P. R.; Schuhmann, W.; Klenerman, D.; Rusakov, D. A.; Sviderskaya, E. V.; Korchev, Y. E. *ACS Nano* **2014**, 8, 875–884.

32. Şen, M.; Takahashi, Y.; Matsumae, Y.; Horiguchi, Y.; Kumatani, A.; Ino, K.; Shiku, H.; Matsue, T. *Anal. Chem.* **2015**, 87, 3484–3489.

33. In *Electrochemical Strategies in Detection Science*, Holzinger, A.; Steinbach, C.; Kranz, C. RSC, **2016,** 125-169.

34. Amatore, C.; Arbault, S.; Koh, A. C. W. *Anal. Chem.* **2010**, 82, 1411-1419.

35. Zhang, B.; Adams, K. L.; Luber, S. J.; Eves, D. J.; Heien, M. L.; Ewing, A. G. *Anal. Chem.* **2008**, 80, 1394-1400.

36. Wightman, R. M. *Science.* **2006**, 311, 1570-1574.

37. Guo, J.; Amemiya, S. *Anal. Chem.* **2005**, 77, 2147-2156.

38. MacPherson, J. V.; Beeston, M. A.; Unwin, P. R.; Hughes, N. P.; Littlewood, D. *J. Chem. Soc. Faraday Trans.* **1995**, 91, 1407–1410.

39. Hirano, Y.; Nishimiya, Y.; Kowata, K.; Mizutani, F.; Tsuda, S.; Komatsu, Y. *Anal. Chem.* **2008**, 80, 9349–9354.

40. Hirano, Y.; Kowata, K.; Kodama, M.; Komatsu, Y. *Bioelectrochemistry* **2013**, 92, 1–5.

41. Cai, C.; Liu, B.; Mirkin, M. V.; Frank, H. A.; Rusling, J. F. *Anal. Chem.* **2002**, 74, 114–119.

42. Hengstenberg, A.; Blöchl, A.; Dietzel, I. D.; Schuhmann, W. *Angew. Chemie - Int. Ed.* **2001**, 40, 905–908.

43. Li, X.; Bard, A. J. *J. Electroanal. Chem.* **2009**, 628, 35–42.

44. Shiku, H.; Shiraishi, T.; Aoyagi, S.; Utsumi, Y.; Matsudaira, M.; Abe, H.; Hoshi, H.; Kasai, S.; Ohya, H.; Matsue, T. *Anal. Chim. Acta* **2004**, 522, 51–58.

45. Date, Y.; Takano, S.; Shiku, H.; Ino, K.; Ito-Sasaki, T.; Yokoo, M.; Abe, H.; Matsue, T. *Biosens. Bioelectron.* **2011**, 30, 100–106.

46. Polcari, D.; Dauphin-Ducharme, P.; Mauzeroll, J. *Chem. Rev.* **2016**, 116, 13234–13278.

47. Pitta Bauermann, L.; Schuhmann, W.; Schulte, A. *Phys. Chem. Chem. Phys.* **2004**, *6*, 4003–4008.

48. Beaulieu, I.; Kuss, S.; Mauzeroll, J.; Geissler, M. *Anal. Chem.* **2011**, 83, 1485–1492.

49. Edwards, M. A.; Martin, S.; Whitworth, A. L.; Macpherson, J. V.; Unwin, P. R. *Physiol. Meas.* **2006**, 27, 63-108.

50. Navratil, M.; Mabbott, G. A.; Arriaga, E. A. *Anal. Chem.* **2006**, 78, 4005–4009.

51. Roberts, W. S.; Lonsdale, D. J.; Griffiths, J.; Higson, S. P. J. *Biosens. Bioelectron.* **2007**, 23, 301–318.

52. Bergner, S.; Vatsyayan, P.; Matysik, F. M. *Anal. Chim. Acta* **2013**, 775, 1–13.

53. Quaranta, M.; Borisov, S. M.; Klimant, I. *Bioanal. Rev.* **2012**, 4, 115–157.

54. Wang, X. D.; Wolfbeis, O. S. *Chem. Soc. Rev.* **2014**, 43, 3666–3761.

55. Clark, L. C.; Wolf, R.; Granger, D.; Taylor, Z. *J. Appl. Physiol.* **1953**, 6, 189–193.

56. Kahn, J. S. *Anal. Biochem.* **1964**, 9, 389–391.

57. Stetter, J. R.; Li, J. *Chem. Rev.* **2008**, 108, 352–366.

58. Shao, M.; Chang, Q.; Dodelet, J. P.; Chenitz, R. *Chem. Rev.* **2016**, 116, 3594–3657.

59. Rahim, A.; Santos, L. S. S.; Barros, S. B. A.; Kubota, L. T.; Gushikem, Y. *Sensors Actuators, B Chem.* **2013**, 177, 231–238.

60. Winnischofer, H.; Otake, V. Y.; Dovidauskas, S.; Nakamura, M.; Toma, H. E.; Araki, K. In *Electrochimica Acta*; **2004**, 49, 3711–3718.

61. Martin, C. S.; Dadamos, T. R. L.; Teixeira, M. F. S. *Sensors Actuators, B Chem.* **2012**, 175, 111–117.

62. Wu, G.; More, K. L.; Johnston, C. M.; Zelenay, P. *Science*. **2011**, 332, 443–447.

63. Xiang, L.; Yu, P.; Zhang, M.; Hao, J.; Wang, Y.; Zhu, L.; Dai, L.; Mao, L. *Anal. Chem*. **2014**, 86, 5017–5023.

64. Sosna, M.; Denuault, G.; Pascal, R. W.; Prien, R. D.; Mowlem, M. *Sensors Actuators, B Chem*. **2007**, 123, 344–351.

65. Gómez-Marín, A.; Feliu, J.; Ticianelli, E. A. *ACS Catal*. **2018**, 8, 7931-7943.

66. *Bioenergetics*, Nicholls, D. G.; Ferguson, S. J.; Academic Press, 2013.

67. Figueira, T. R.; Barros, M. H.; Camargo, A. A.; Castilho, R. F.; Ferreira, J. C. B.; Kowaltowski, A. J.; Sluse, F. E.; Souza-Pinto, N. C.; Vercesi, A. E. *Antioxid. Redox Signal*. **2013**, 18, 2029–2074.

68. Balaban, R. S.; Nemoto, S.; Finkel, T. *Cell* **2005**, 120, 483–495.

69. Will, Y.; Hynes, J.; Ogurtsov, V. I.; Papkovsky, D. B. *Nat. Protoc*. **2006**, 1, 2563–2572.

70. Hütter, E.; Unterluggauer, H.; Garedew, A.; Jansen-Dürr, P.; Gnaiger, E. *Exp. Gerontol*. **2006**, 41, 103–109.

71. Rogers, G. W.; Brand, M. D.; Petrosyan, S.; Ashok, D.; Elorza, A. A.; Ferrick, D. A.; Murphy, A. N. *PLoS One* **2011**, 6, e21746.

72. *Drug-Induced Mitochondrial Dysfunction,* Dykens, J. A.; Will, Y.; John Wiley & Sons, **2008**, 1-616.

73. Zhang, J.; Nuebel, E.; Wisidagama, D. R. R.; Setoguchi, K.; Hong, J. S.; Horn, C. M. Van; Imam, S. S.; Vergnes, L.; Malone, C. S.; Koehler, C. M.; Teitell, M. a. *Nat. Protoc*. **2012**, 7, 1068–1085.

74. Westermann, B. *Nat. Rev. Mol. Cell Biol*. **2010**, 11, 872–884.

75. Fosdick, S. E.; Knust, K. N.; Scida, K.; Crooks, R. M. *Angewandte Chemie - International Edition*. **2013**, 52, 10438–10456.

76. Mavré, F.; Chow, K. F.; Sheridan, E.; Chang, B. Y.; Crooks, J. A.; Crooks, R. M. *Anal. Chem*. **2009**, 81, 6218–6225.

77. Braun, T. M.; Schwartz, D. T. *J. Electrochem. Soc*. **2015**, 162, D180-D185.

78. Loget, G.; Roche, J.; Kuhn, A. *Adv. Mater*. **2012**, 24, 5111-5116.

79. Eßmann, V.; Voci, S.; Loget, G.; Sojic, N.; Schuhmann, W.; Kuhn, A. *J. Phys. Chem. Lett*. **2017**, 8, 4930-4934.

80. Kayran, Y. U.; Eßmann, V.; Grützke, S.; Schuhmann, W. *ChemElectroChem* **2016**, 3, 399–403.

81. Goodwin, S.; Walsh, D. A. *ACS Appl. Mater. Interfaces* **2017**, 9, 23654–23661.

82. Poorghasem, R.; Saberi, R. S.; Shayan, M.; Mehrgardi, M. A.; Kiani, A. *Electrochim. Acta* **2016**, 222, 1483–1490.

83. Wu, M. S.; Liu, Z.; Shi, H. W.; Chen, H. Y.; Xu, J. J. *Anal. Chem.* **2015**, 87, 530–537.

84. Guerrette, J. P.; Oja, S. M.; Zhang, B. *Anal. Chem.* **2012**, 84, 1609–1616.

85. Lei, R.; Stratmann, L.; Schäfer, D.; Erichsen, T.; Neugebauer, S.; Li, N.; Schuhmann, W. *Anal. Chem.* **2009**, 81, 5070–5074.

86. Xiao, Y.; Xu, L.; Qi, L. W. *Talanta* **2017**, 165, 577–583.

87. Li, H.; Bouffier, L.; Arbault, S.; Kuhn, A.; Hogan, C. F.; Sojic, N. *Electrochem. commun.* **2017**, 77, 10–13.

88. Arora, A.; Eijkel, J. C. T.; Morf, W. E.; Manz, A. *Anal. Chem.* **2001**, 73, 3282–3288.

89. Ellis, K. G.; Jansson, R. E. W. *J. Appl. Electrochem.* **1981**, 11, 531–535.

90. Lee, J. K.; Shemilt, L. W.; Chun, H. S. *J. Appl. Electrochem.* **1989**, 19, 877–881.

91. Smotkin, E. S.; Cervera-March, S.; Bard, A. J.; Campion, A.; Fox, M. A.; Mallouk, T.; Webber, S. E.; White, J. M. *J. Phys. Chem.* **1987**, 91, 6–8.

92. Bouffier, L.; Arbault, S.; Kuhn, A.; Sojic, N. *Anal. Bioanal. Chem.* **2016**, 408, 7003–7011.

93. Wiesener, K.; Ohms, D.; Benczúr-Ürmössy, G.; Berthold, M.; Haschka, F. *J. Power Sources* **1999**, 84, 248–258.

94. Eßmann, V.; Barwe, S.; Masa, J.; Schuhmann, W. *Anal. Chem.* **2016**, 88, 8835–8840.

95. Loget, G.; Kuhn, A. *Lab Chip* **2012**, 12, 1967-1971.

96. Sentic, M.; Loget, G.; Manojlovic, D.; Kuhn, A.; Sojic, N. *Angew. Chemie - Int. Ed.* **2012**, 51, 11284–11288.

97. Loget, G.; Zigah, D.; Bouffier, L.; Sojic, N.; Kuhn, A. *Acc. Chem. Res.* **2013**, 46, 2513–2523.

98. Liu, R.; Liu, C.; Li, H.; Liu, M.; Wang, D.; Zhang, C. *Biosens. Bioelectron.* **2017**, 94, 335–343.

99. Chen, L.; Zhang, C.; Xing, D. *Sensors Actuators, B Chem.* **2016**, 237, 308–317.

100. Liu, H.; Xiang, Y.; Lu, Y.; Crooks, R. M. *Angew. Chemie - Int. Ed.* **2012**, 51, 6925–6928.

Chapter 2.

Fabrication and characterization of oxygen microsensors as a tip in Scanning Electrochemical Microscopy.

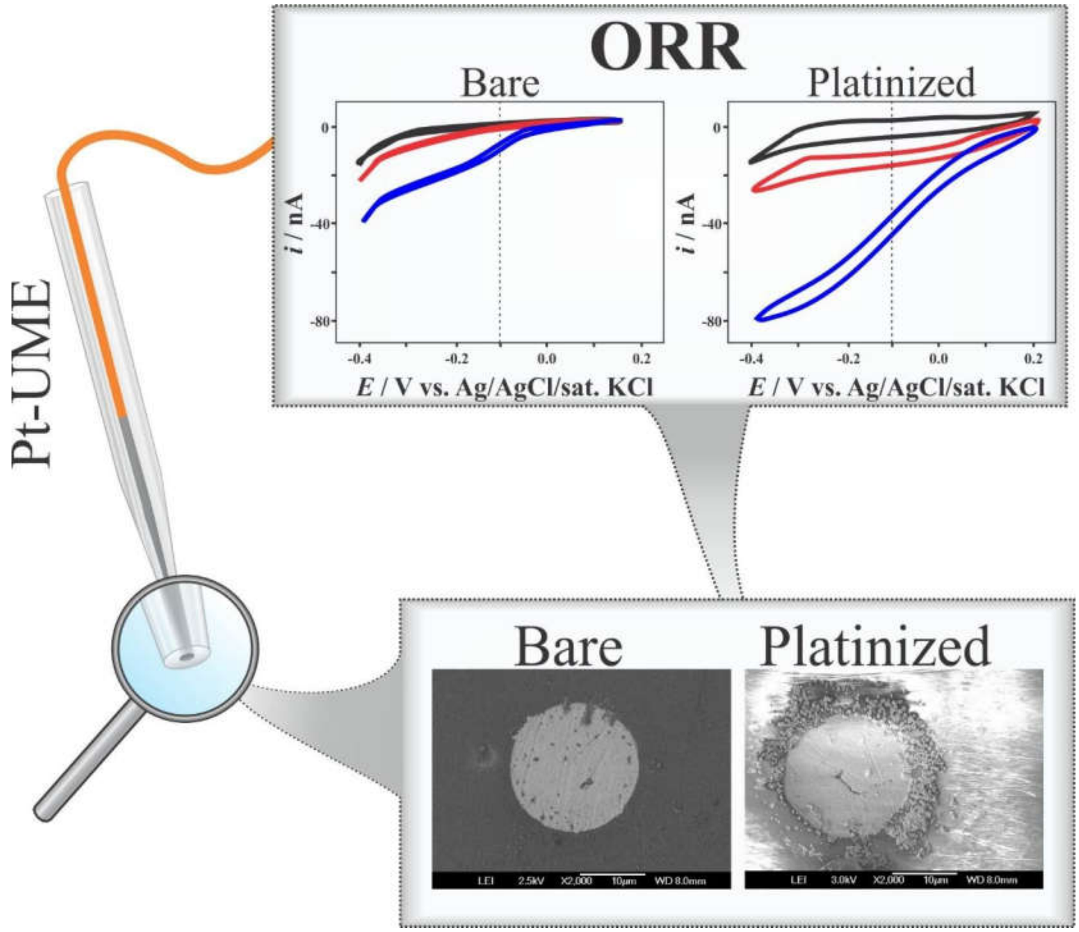

Herein, the development of the oxygen microsensor is shown, including the fabrication of the microelectrode, its characterization and the evaluation of the response towards the oxygen reduction reaction. The platinum microelectrode surface was platinised to enhance the current signal. This protocol allows a fresh platinum (black platinum) surface to be obtained, with concurrent ORR potential shift due to the high reactivity of the generated interface. Here the challenges of the small microelectrode fabrication to obtain high-spatial resolution information in a SECM image are discussed. Redox competition SECM (RC-SECM) experiments were performed using a polarized electrode as sample and these measurements were extremely essential to understand the RC-SECM behavior.

2.1. Experimental Section.

2.1.1. Chemicals.

All chemicals were used as received: hexaamineruthenium (III) chloride ($[Ru(NH_3)_6Cl_3]$, CAS 14282-91-8, Alfa Aesar), hexachloroplatinic acid hexahydrate ($H_2PtCl_6 \cdot 6H_2O$, CAS 18497-13-7, Sigma Aldrich), potassium ferricyanide(III) ($K_3Fe(CN)_6$, CAS 13746-66-2, Sigma Aldrich), phosphate buffer saline (Sigma Aldrich) and sulfuric acid (H_2SO_4, CAS 7664-93-9, Merck). The solutions were prepared using water purified via a Nanopure Infinity (Barnstead, USA). Measurements in absence and presence of oxygen were performed in solutions purged with argon and oxygen (Air Products SA, Brazil).

2.1.2. Potentiostats and SECM equipment.

The voltammetric and amperometric measurements were performed using a bipotentiostat/galvanostat Autolab PGSTAT30 (Ecochemie, Netherlands) in a 2 or 4 electrodes configuration: 1 reference electrode, 1 or 2 working electrodes and 1 counter electrode when 2 working electrodes were used. The scanning electrochemical microscopy SECM (Sensolytics GmbH, Germany) equipment is coupled to an inverted microscopy Axio Vert.A1 (Zeiss, Germany) and all the workstation is on a Cleanbench anti-vibration table inside a faraday cage (Hamilton Thorne, USA).

2.1.3. Reference and counter electrodes.

A homemade reference electrode was used in the electrochemical measurements. A silver wire (diameter 1 mm, Goodfellow, UK) was covered with AgCl by electrodeposition and then inserted in a pipette tip with saturated KCl (CAS 7447-40-7, Sigma Aldrich) solution. The ionic contact was a battery separator membrane [1]. The counter electrode was a cylindrical platinum bare (diameter 2 mm) and it was only used in 4-electrodes configuration experiments.

2.1.4. Scanning electron microscopy.

A scanning electron microscopy FESEM JSM-7401F (JEOL, Japan) was used to characterize the morphology of the platinised Pt microelectrodes surface.

2.1.5. Platinum micro/nanoelectrode fabrication.

To get localized information on a phenomenon that takes place at the vicinity of a surface, the size of the probe is a very important parameter. This means the dimension of the electrode limits its application for the understanding of a microenvironment by using SECM and to exploit the high spatial-resolution of the technique. Thereby, the fabrication of a microelectrode with desirable properties is very important. The common strategy for reducing the size of an electrode is to melt a visible piece of metal wire (here, platinum) inserted into a glass capillary while the system is pulled. Herein, this process was controlled by using a Flaming Brown Micropipette Puller P- 2000 (Sutter Instruments, USA) equipment where a glass capillary can be accurately positioned in a chamber where a CO_2 laser is aligned. For the platinum microelectrode fabrication, a piece of a platinum wire (hard, 99.99% purity, diameter 50 μm, Goodfellow, UK) is firstly inserted in the middle of a cleaned capillary (quartz, OD: 1.0 mm, ID 0.3 mm, Sutter Instruments, USA) and positioned in the middle of the chamber for heating. The success to obtain small tip microelectrodes depends on the heating and pulling parameters of the equipment. Then, the first step is to seal glass around the platinum wire and, for this, a locker must be positioned in the Puller to block the pulling (with a homemade locker made by using a wire). The sealing process occurs under pressure (450 mmHg) to reduce the formation of air bubbles and the pressure is applied by connecting a pump to tubes in the ends of the capillary. The optimized parameters used in this work were Heat 750, Fil 5, Vel 100, Del 120, Pull 1, one must consider any equipment variation and probably the values have to be adjusted. The sealing process is run by 8-10 cycles of 20 seconds using with the above-mentioned parameters and 40 seconds without heating (equipment is off). Following the sealing step, the pulling step is performed without the locker by using the following parameters: Heat 930, Fil 5, Vel 100, Del 150, Pull 200. The visual inspection is carefully performed using a microscope to check whether the platinum wire was completely pulled and diminished to the very end of the tip. The electric contact between the platinum wire and a Ni/Cr alloy or Cu wire (diameter 0.25 mm) is made using a molten indium wire (CAS 7440-74-6, diameter 0.25 mm, Alfa Aesar).

The platinum surface is exposed during the polishing process. The surface polishing is performed using a homemade machine (Figure 2.1) instead of the manual process. The microelectrode is attached to a micromanipulator and it drives the tip to an adapted computer hard disc (HD) with a rotating sand paper on its surface. The polishing process results in the cleaning of the disc-shaped platinum surface.

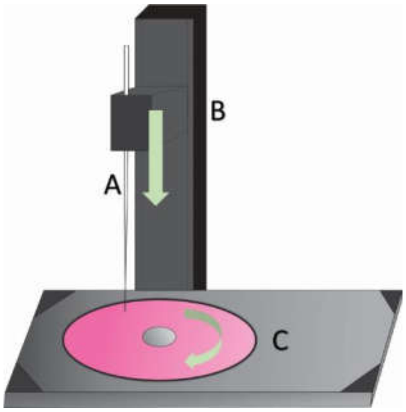

Figure 2.1. Scheme of the homemade polishing machine: the microelectrode holder (A), the micromanipulator in Z (B) and a HD with sand paper (C).

2.1.6. Characterization of the microelectrodes.

The electrochemical characterization of the disc platinum microelectrodes was performed by recording cyclic voltammograms in a 5 mmol L^{-1} $[Ru(NH_3)_6Cl_3]$ + 100 mmol L^{-1} KCl solution and approach curves towards an insulating surface in SECM experiments. The platinum radius and the RG values were calculated using theoretical parameters to fit the approach curves.

2.1.7. Oxygen microssensor.

Oxygen reduction reaction studies were performed by cyclic voltammetry in phosphate buffer or DMEM (Dulbecco's Modified Eagle Medium, cell medium, Thermo Fischer) solutions. The platinisation of the surface was performed in a 1 mmol L^{-1} $H_2PtCl_6 \cdot 6H_2O$ in 0.5 mol L^{-1} H_2SO_4 solution, scanning the potential from 0.3 V to -0.5 V vs. Ag/AgCl/sat. KCl.

2.1.8. Cell culture.

The cell lineage HS578T, a human epithelial cancer cell type from a mammary gland/breast tissue, was used in the experiments. The cells were grown in plastic flasks

(T75 ou T25, Sarstedt, Germany) in Dulbecco's Modified Eagle's Medium (DMEM, Thermo Fisher Scientific, USA) supplied with 10% fetal bovine serum and 1% penicillin and streptomycin. The cell culture was kept in an incubator at 37 ºC and 5% CO_2. The medium was changed at each 3 days and the cell culture was washed with phosphate buffer saline solution (PBS, pH 7.4) and plated in new flasks. A Petri dish (TC dish 35, Sarstedt, Germany) with 5.10^5 plated cells (high confluence level) in 2 mL of DMEM solution was used in SECM experiments.

2.2. Results and Discussion.

2.2.1. Characterization of the disc-shaped Pt microelectrodes.

Cyclic voltammograms were recorded in a 5 mmol L^{-1} [$Ru(NH_3)_6Cl_3$] in 100 mmol L^{-1} KCl solution for the electrochemical characterization of the disc-shaped platinum microelectrodes. A typical CV with sigmoidal profile with low hysteresis and a characteristic steady-state current is shown in Figure 2.2A. The radius of the microelectrode can be calculated using the Equation 1.2 and for a steady-state current of 11.2 nA the r value is found to be 6.4 µm.

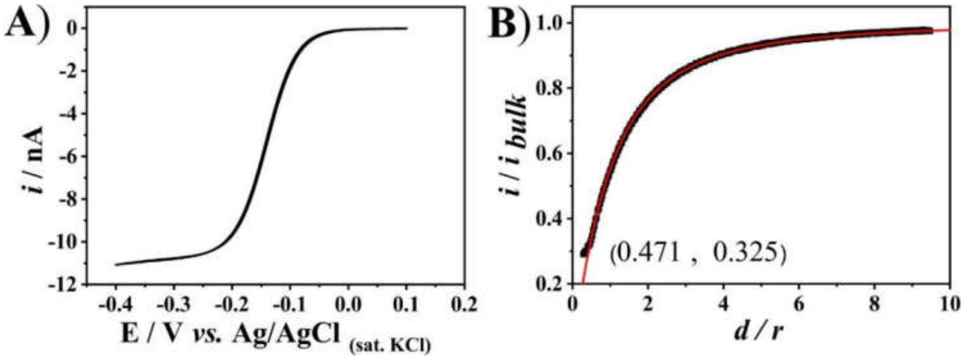

Figure 2.2. (A) Cyclic voltammogram recorded with a platinum microelectrode in a 5 mmol L^{-1} [$Ru(NH_3)_6Cl_3$] in 100 mmol L^{-1} KCl solution. Scan rate: 50 mV s^{-1} (B) Approach curve towards a silicon wafer surface. Theoretical curve (line) and experimental data (dots). Step rate: 10 µm s^{-1}. E_{tip}: - 0.4 V vs. Ag/AgCl(sat. KCl).

For SECM applications, the RG value is an important parameter and the geometry of the electrode cannot be assessed by cyclic voltammetry. The RG value can be determined by using an optical microscopy or by theoretical fitting of the approach curve obtained in an SECM experiment. As SECM can give information on the reactivity of the substrate surface because of its interaction with the microelectrode diffusion layer, the overall size of microelectrode (including the body glass) is very important. In the hypothetical case of a microelectrode with large RG, but relatively small platinum disc surface (Figure 2.3), the use of such probe will not provide information with high resolution.

Accordingly, the last step regarding the microelectrode characterization consisted in recording approach curves towards insulating surfaces, especially because the influence of the RG value on the shape of the approach curve is much more pronounced in comparison to conductive surfaces. Figure 2.2B shows an approach curve recorded during the movement of the tip towards a silicon wafer surface and the RG value determined by theoretical fitting of the data was 6.5.

The approach curve shown in Figure 2.2B is characteristic of a negative feedback profile, as current decreases during the approach of the microelectrode towards the insulating surface [2,3]. A change in the profile is noticed at short distances and this is usually caused because the electrode reaches the surface. Ideally at this condition, the normalized current should achieve 0 as the surface of the electrode would be completely blocked, however experimentally any tilt of the surface allows the material diffusion to the electrode surface. Hence, the tip touched the surface at $d / r = 0.471$ and $i / i_{bulk} = 0.325$. By taking into account the radius of the microelectrode, the tip reached the sample surface at a distance of 3.0 μm. This value shows how close this particular microelectrode can be positioned to a surface. Thus, the approach curve is a fundamental tool to characterize a fabricated microelectrode and to get information on RG and r values [4].

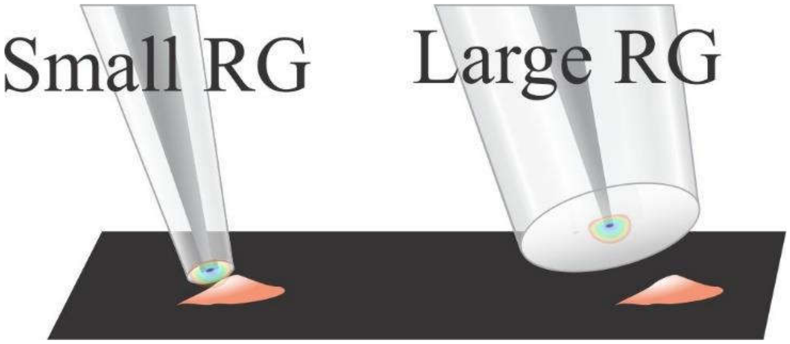

Figure 2.3. Scheme of microelectrodes with small and large RG (ratio between the glass body and the platinum disc diameters) close to an investigated sample.

As already pointed out, the size of the microelectrode (radius and RG) is the main issue regarding its use to map a cell surface with high resolution. The fabrication of nanoelectrode with radius comprising 300-500 nm (RG 10) is also possible with the described procedure (section 2.1.5). A cyclic voltammogram of a platinum nanoelectrode (r = 305 nm) is shown in the Figure 2.4. Advantages of using such nanoelectrode involve the possibility to place it close to the sample and to perform local measurements in a SECM set-up with high-spatial resolution. A disadvantage of using such small probes is associated with the loss in temporal resolution, once the tip must scan the whole area and this will take more time. Concerns with the time taken for the experiment are very important in biological studies to ensure the viability of the sample.

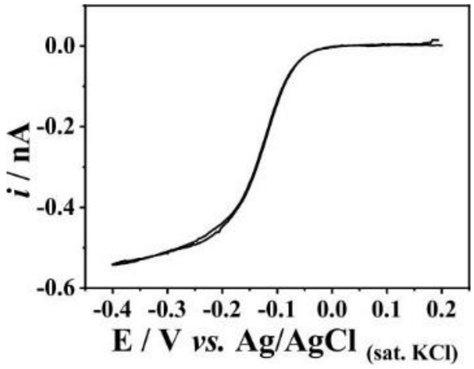

Figure 2.4. Cyclic voltammogram recorded with a platinum nanoelectrode (r = 305 nm) in a 5 mmol L^{-1} *[Ru(NH3)*$_6$*Cl*$_3$*] in 100 mmol* L^{-1} *KCl solution. Scan rate: 100 mV* s^{-1}.

2.2.2. Enhancing the signal of the oxygen sensor.

Investigations on the respiration of cells require the probe to have enough resolution to map changes in the oxygen concentration. As expected, current values for very small microelectrodes range in the nA or pA scale, hence strategies to reliably monitor small concentration changes are envisaged. The sensitivity of Pt microelectrodes towards oxygen detection can be enhanced by platinisation of bare platinum surfaces. This was accomplished by cycling the potential from 0.3 to – 0.5 V in a 1 mmol L^{-1} $H_2PtCl_6{\cdot}6H_2O$ and 0.5 mol L^{-1} H_2SO_4 solution. Typical voltammograms of such experiment are shown in Figure 2.5.

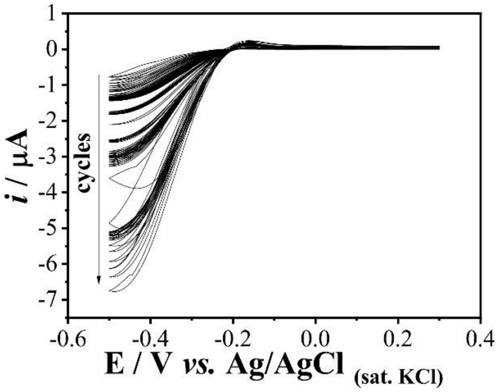

Figure 2.5. Consecutive cyclic voltammograms recorded with a platinum microelectrode in 1 mmol L^{-1} $H_2PtCl_6{\cdot}6H_2O$ and 0.5 mol L^{-1} H_2SO_4 solution. Scan rate: 100 mV s^{-1}.

The influence of the platinisation of the Pt surface on the oxygen reduction reaction was evaluated by recording voltammograms in air saturated, in absence of oxygen and in oxygen saturated phosphate buffer (pH 7.4) solutions. The voltammograms obtained with the bare platinum microelectrode in solutions containing oxygen (red and blue curves, Figure 2.6A) showed a cathodic current with onset potential at around – 0.3 V due to the oxygen reduction, with a slight steady-state condition at around – 0.8 V. Similar experiments were repeated with the platinised Pt microelectrode and the obtained voltammograms presented a shift in the ORR towards less negative values (onset potential at around 0 V vs Ag/AgCl/sat. KCl) (Figure 2.6B). Hence, efforts to modify the Pt surface were successful in terms of facilitating the ORR (probably because the generation of active catalytic Pt sites) and increasing the sensitivity (owing to the enlarged surface area).

Changes in the morphology of the platinum surface after the platinisation protocol were also evaluated by performing experiments in sulfuric acid solution. Cyclic voltammograms of a bare and a platinised platinum electrode in sulfuric acid solution are shown in Figure 2.7. The typical profile corresponding [5,6] to the adsorption/desorption hydrogen process takes place at around -0.1 V, platinum oxide reactions at more positive potentials and the oxygen evolution at around 1.3 V is clearly seen for the platinised microelectrode (black curve).

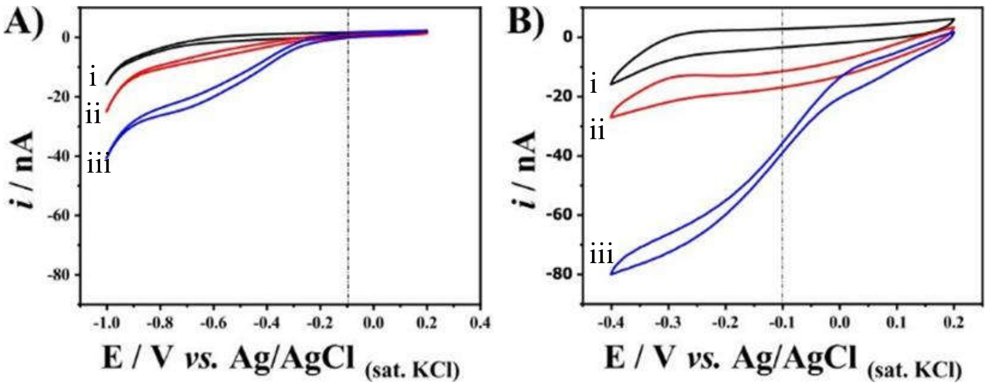

Figure 2.6. Cyclic voltammograms recorded with a bare (A) and a platinised (B) platinum microelectrode (r = 5 µm) in a phosphate buffer solution (pH 7.4). Black lines, i: absence of oxygen. Red lines, ii: air saturated solution. Blue lines, iii: oxygen saturated solution. Scan rate: 100 mV s^{-1}.

The number of potential cycles in the platinisation protocol was also investigated by recording voltammograms in phosphate buffer (pH 7.4) in the presence of oxygen. The voltammograms obtained using the bare platinum microelectrode and after the platinisation procedure from 5 to 100 cycles, shown in Figure 2.8A. The experiments were performed right after the platinisation process and each scan was recorded after the microelectrode surface polishing and evaluation of its response in a $[Ru(NH_3)_6]^{3+}$ solution for comparison. Figure 2.8B shows the relation in the steady state currents and the potentials to ORR (phosphate buffer pH 7.4) with the number of cycles in the platinisation process. As before, the platinisation process resulted in an enhancement in the current for ORR and the relation with the cycles indicated a saturation of this effect. With 100 cycles, the improvement was + 180 % of current registered with the bare electrode current. The saturation profile was also obtained in the potential relation with the cycles and the potential was - 0.2 V with 100 cycles.

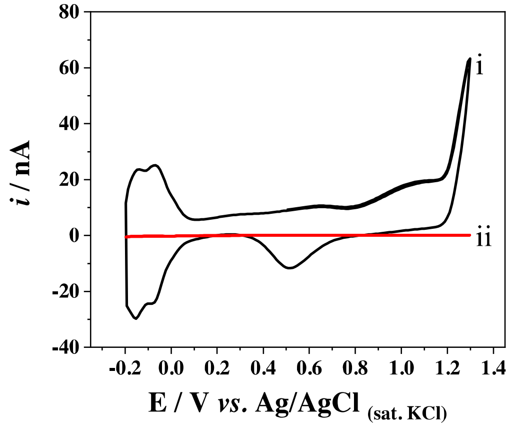

Figure 2.7. Cyclic voltammograms recorded with a platinised (black curve, i) and a bare (red curve, ii) platinum microelectrode (radius = 380 nm) in 0.5 mol L^{-1} H_2SO solution (argon purged for 5 minutes). Scan rate: 100 mV $s^{-1}{}_4$.

A simultaneous evaluation of the platinisation process was performed using the same microelectrodes by recording voltammograms in a 15 mmol L^{-1} $[Ru(NH_3)_6]^{3+}$ in 0.1 mol L^{-1} KCl solution, as shown in Figure 2.9. The current enhancement for microelectrodes prepared with more potential cycles is similar to the one observed for the ORR (Figure 2.8). However, no huge shift in the reduction potential was observed in this case and this is expected because the electron-transfer step associated to the reduction of $[Ru(NH_3)_6]^{3+}$ is very fast.

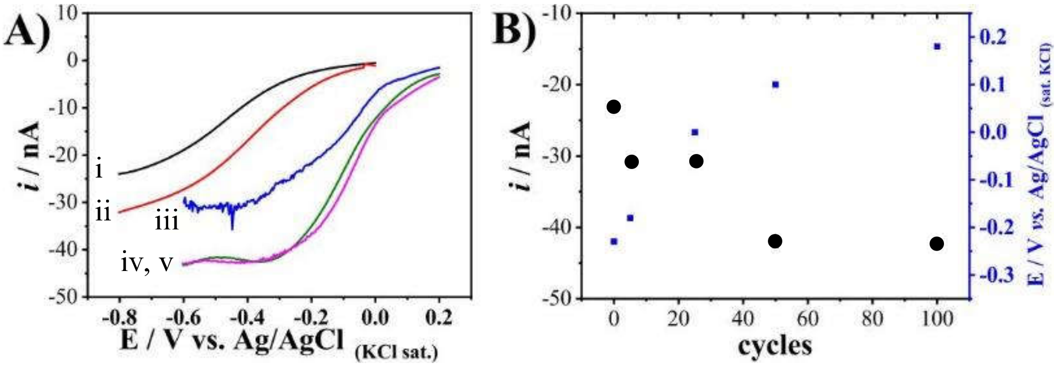

Figure 2.8. (A) Cyclic voltammograms recorded in phosphate buffer solution (oxygen saturated) using platinised platinum microelectrodes prepared with 5 (red curve, ii), 25 (blue curve, iii), 50 (green curve, iv) and 100 (pink curve, v) potential cycles and with the bare microelectrode (black curve, i). Scan rate: 20 mV s^{-1}. (B) Plot of steady-state current (●) and onset potential (■) for ORR values as a function of number of cycles in the platinisation step.

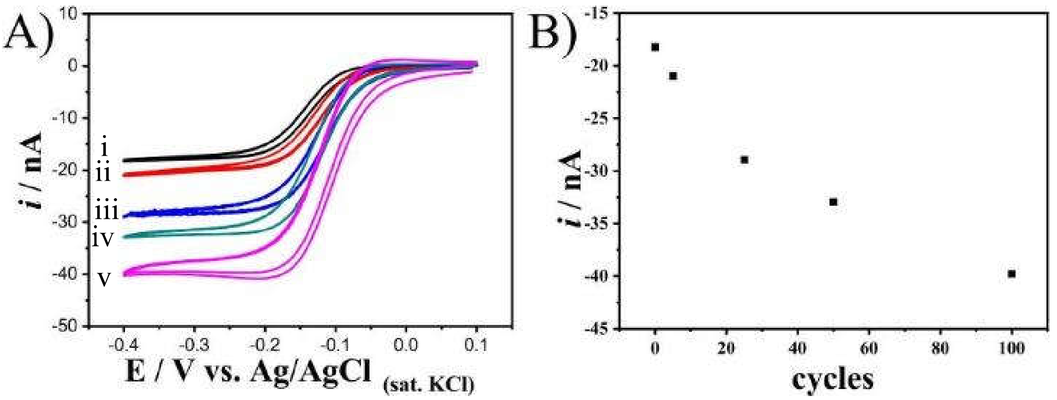

Figure 2.9. (A) Cyclic voltammograms recorded in 15 mmol L^{-1} [Ru(NH$_3$)$_6$]$^{3+}$ in 0.1 mol L^{-1} KCl solution (absence of oxygen) using a bare and platinised platinum microelectrodes prepared with different number of cycles in the platinisation (5, 25, 50 and 100, respectively i, ii,iii, iv and v). Scan rate: 20 mV s^{-1}. (B). Plot of steady-state current at – 0.4 V as a function of number of cycles in the platinisation step.

SEM images were obtained in order to demonstrate the changes in the morphology of the Pt microelectrode surface after the platinisation process (Figure 2.10). The presence of small grains on the disc platinum surface is clearly seen by comparing images A and B. The grains were spherical and most of them grew up in the extremities of the platinum disc, probably because the diffusion at the edges is more effective. Image B shows some grains over the glass surface and one does not have any plausible explanation for such observation. Nevertheless, such particles should not have any contribution to the current increase. In conclusion, the SEM images showed the platinisation process contribute to increase the area of the microelectrode and fresh spherical platinum grains with nanometric size are deposited, as shown in Figure 2.10 C and D.

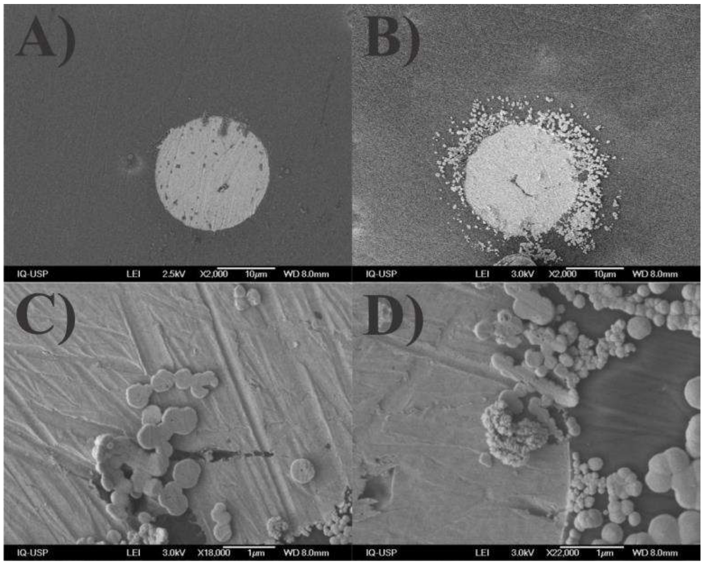

Figure 2.10. SEM images of the bare (A) and platinised (B) platinum microelectrode surface. (C) and (D) show details of the platinum deposits over the platinum surface.

2.2.3. Evaluation of the ORR by tip generator/substrate collector TG/SC experiment.

The platinisation of the platinum surface and consequent change in its morphology resulted in a potential shift regarding the ORR and a current enhancement. The generation of H_2O_2 during the oxygen reduction in a 2-electrons process, instead of the general 4-electrons process leading to H_2O as a product, should not be disregarded. Such possibility is not desired because the local formation of H_2O_2 during the oxygen monitoring could damage biological samples. Thus, an SECM experiment was performed to monitor the products generated by the proposed sensor during the ORR. For this, a platinised platinum microelectrode (r = 5 µm) was used in a tip generator/substrate collector (TG/SC) experiment. The TG/SC consisted in placing the tip close to a conducting substrate, then the tip is polarized to reduce dissolved oxygen and the generated products diffuse to the polarized substrate surface and are collected. Possible ORR products generated at the tip are H_2O (n = 4) and H_2O_2 (n = 2), and the latter can be oxidized at the substrate surface. The substrate was a platinum electrode (r = 0.5 mm) and the typical voltammogram corresponding to a fast reversible process was obtained for ($[Ru(NH_3)_6]^{3+}$) (Figure 2.11 A). The ability of such electrode to collect any H_2O_2 generated at the tip was demonstrated in Figure 2.11 B, as this compound is electroactive at 0.4 V at the platinum electrode (r = 0.5 mm).

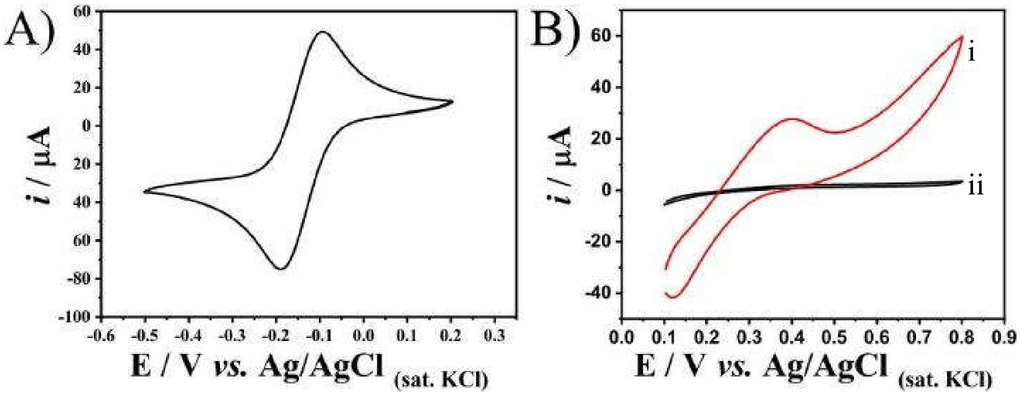

Figure 2.11. Cyclic voltammograms recorded with a platinum electrode (r = 0.5 mm) in 15 mmol L^{-1} $[Ru(NH_3)_6]^{3+}$ *in 0.1 mol* L^{-1} *KCl solution (A) and in phosphate buffer solution (ii, black curve in B) containing 10 mmol* L^{-1} H_2O_2 *(i,red curve in B). Scan rate: 100 mV* s^{-1}.

A preliminar TG/SC experiment was performed to determine the collection factor of the SECM setup using $[Ru(NH_3)_6]^{3+}$ as a probe. The platinised platinum microelectrode (r = 6.9 µm and RG = 5) was positioned at 5 µm from the substrate by recording an approach curve. Then, the substrate was polarized at 0.2 V to oxidize any $[Ru(NH_3)_6]^{2+}$ generated at the tip during the potential sweep. The resulting curves are presented in Figure 2.12. Current values for the tip and the substrate were close to 0 nA in the beginning of the experiment, when the tip potential changed from from 0.2 V to – 0.05 V. At more negative potentials applied to the tip, the cathodic reduction of $[Ru(NH_3)_6]^{3+}$ takes place at a rate controlled by the electron-transfer kinetics at the interface. At the substrate, a simultaneous anodic process is observed, which involves the regeneration of $[Ru(NH_3)_6]^{3+}$ from the $[Ru(NH_3)_6]^{2+}$diffusing from the tip. At – 0.25 V applied to the tip, the cathodic reduction of $[Ru(NH_3)_6]^{3+}$ is mass-transport controlled and a steady-state current is obtained. A similar situation is observed at the substrate, i.e., the steady-state situation is achieved, hence this is a clear confirmation that the substrate anodic current depends on the reduction process at the tip. The ratio between current at the substrate and current at the tip corresponds to the collection factor of this SECM set up and the values was found to be $i_{substrate}/i_{tip}$ = 0.9 (E_{tip} = - 0.4 V). Such high collection factor suggests the generated species at the tip was almost completely collected at the substrate at the tip-to-substrate distance (5 µm) employed in this study.

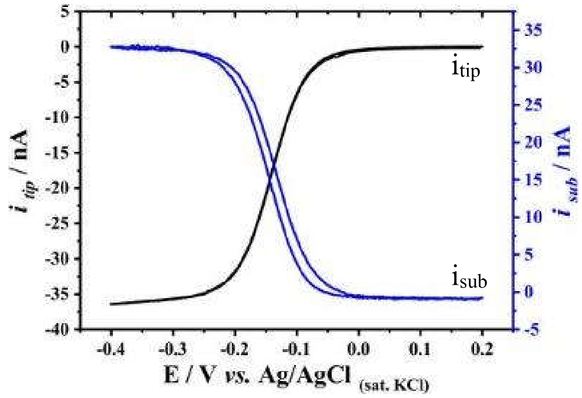

Figure 2.12. Tip generator/substrate collector curves. Black curve: cyclic voltammogram recorded at the tip (platinised platinum microelectrode) in 5 mmol L^{-1} $[Ru(NH_3)_6]^{3+}$ in 0.1 mol L^{-1} KCl solution. Scan rate: 100 mV s^{-1}. Blue curve: amperometric monitoring at the substrate (platinum electrode, r = 0.5 mm). $E_{substrate}$: +0.2 V. Tip-to-substrate distance: 5 µm.

The set up proposed for the TG/SC experiment showed a high collection factor, hence it would be useful for the investigation on the possible generation of H_2O_2 during the ORR at the platinised Pt microelectrode. Accordingly, a similar experiment was performed in phosphate buffer solution (pH 7.4) in absence and presence of oxygen (Figure 2.13). A cyclic voltammogram was recorded at the tip, while the substrate was polarized at + 0.4 V to oxidize any possible H_2O_2 generated at the tip during the ORR. The resulting curve in presence of O_2 showed no simultaneous increase of currents in the substrate and tip. The cathodic current due to the oxygen reduction reaction increased on scan at around – 0.1 V and reached a steady-state condition around – 0.6 V. While in the substrate, no anodic current increased and in absence and presence of O_2, the amperometric curves profile was the same. This result indicated a preference of ORR with 4 electron transfer at the platinised surface and no H_2O_2 was produced.

Then, the platinisation process contributed to the enhanciment of the sensitivity of the sensor and improved the electron transfer process to ORR due a reactive surface.

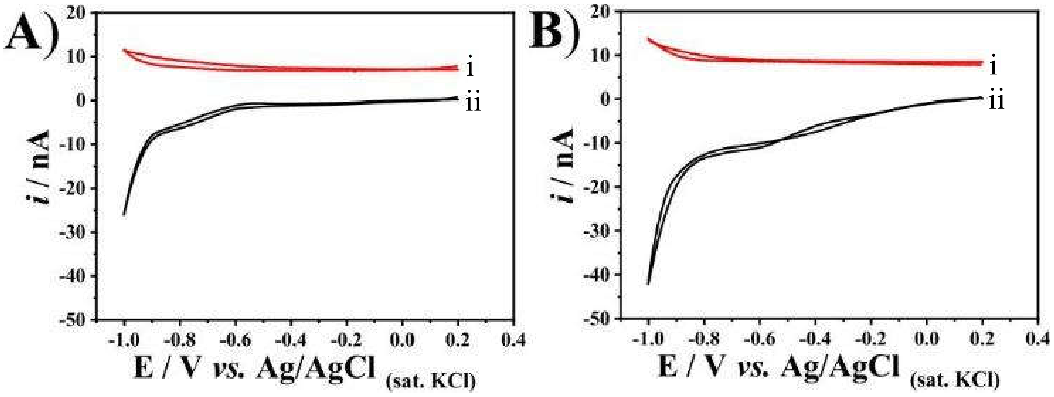

Figure 2.13. Tip generator/substrate collector curves. Black curves, ii: cyclic voltammogram recorded with a platinised platinum microelectrode in phosphate buffer solution in absence (A) and presence of oxygen (B). Scan rate: 100 mV s^{-1}. Red curves, i: amperometric monitoring at the substrate (platinum electrode (r = 0.5 mm). $E_{substrate}$: + 0.4 V. Tip-to-substrate distance: 5 µm.

2.2.4. Stability study of the platinised platinum microelectrode towards ORR.

The stability of the platinised Pt microelectrode towards the ORR was evaluated by applying a fixed potential to drive the desired reaction, for further current monitoring as a function of time. The experiment was performed using a platinised platinum microelectrode (100 cycles, r = 5 µm) in the SECM set up in order to control the working distance to different substrates. The tip was positioned at three distances from the sample surfaces: a silicon wafer or a Petri dish covered with cells (high confluence level). The results obtained in these experiments are presented in Figure 2.14. The working distance was determined by approach curves towards the sample surface and a cleaned area on the Petri dish was used for the experiment performed with the cells. The response of the platinised microelectrode presented high stability for all working distances and regardless the sample features. The current decrease at each tip-substrate distance followed the expected negative feedback effect. Despite the presence of the cells and cell extracts, no passivation of the microelectrode surface was noticed.

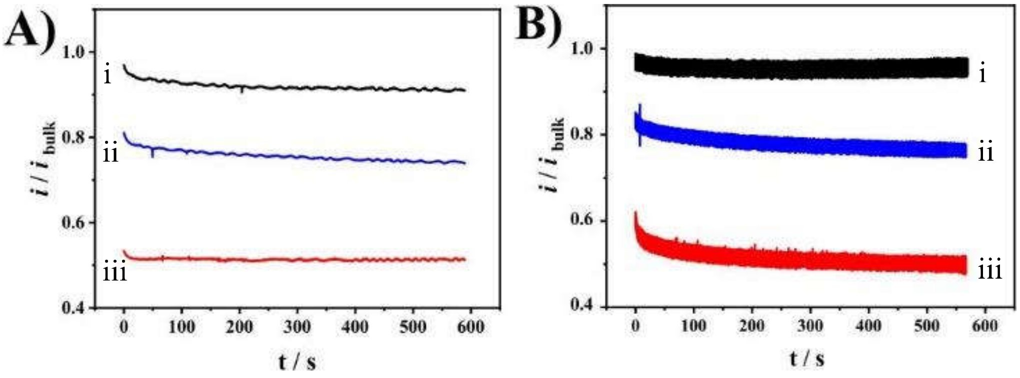

Figure 2.14. Current monitoring for a platinised platinum microelectrode at 60 µm (black lines, i), 15 µm (blue lines, ii) and 10 µm (red lines, iii) tip-substrate distance in DMEM solution. Substrate: (A) silicon wafer and (B) attached cells in high confluence. E_{tip}*: - 0.4 V.*

The same experiment in presence of the cells was repeated, but the microelectrode was repeatedly positioned at different working distances for the assessement of the reproducibility. The amperometric curves shown in Figure 2.15. *(A) Current monitoring recorded with a platinised platinum microelectrode at 60 µm (black and gray lines, i), 15 µm (red and pink lines, ii) and 10 µm (blue line, iii) tip-substrate distances in DMEM* *solution. Substrate: cells in high confluence.*A confirm high stable and reproducible responses were obtained at all distances. Before and after the amperometric experiments, cyclic voltammograms were recorded in 15 mmol L^{-1} $[Fe(CN)_6]^{3-}$ in 100 mmol L^{-1} KCl solution (Figure 2.15B). Reproducible sigmoidal voltammograms were obtained corresponding to the $[Fe(CN)_6]^{3-}$ reduction, confirming the absence of passivation of the electrode surface.

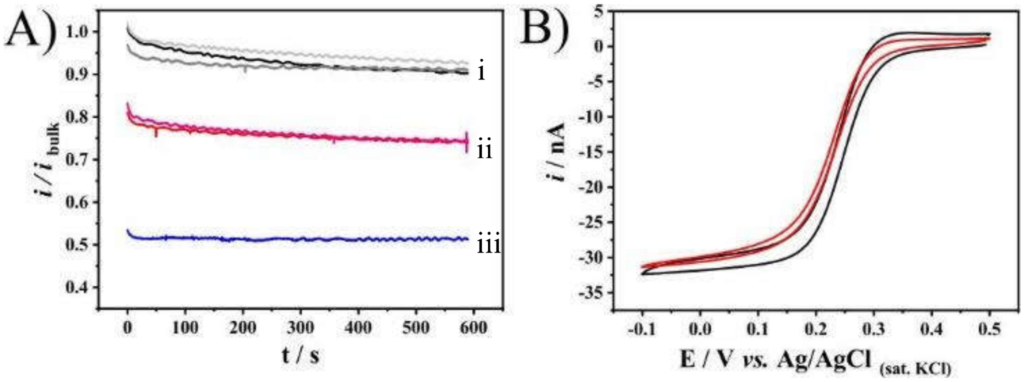

Figure 2.15. (A) Current monitoring recorded with a platinised platinum microelectrode at 60 µm (black and gray lines, i), 15 µm (red and pink lines, ii) and 10 µm (blue line, iii) tip-substrate distances in DMEM solution. Substrate: cells in high confluence. E_{tip}*: - 0.4 V. (B) Cyclic voltammograms recorded with the platinised platinum microelectrode in 15 mmol* L^{-1} $[Fe(CN)_6]^{3-}$ *in 100 mmol* L^{-1} *KCl before and after amperometric experiments. Scan rate: 100 mV* s^{-1}*.*

2.2.5. Redox competition mode condition.

The main aim of this work is to monitor changes in the oxygen concentration at the vicinity of a single cell using an amperometric sensor. Hence, oxygen is consumed by both, the cell and the sensor, and this mode in an SECM setup is named redox competition[7]. In order to simulate the consumption of oxygen by a single cell and to work at controlled conditions, preliminary experiments using this setup were performed with a biased platinum microelectrode (r = 25 µm). Such microelectrode was used as a sink for oxygen, resembling the respiration of a single cell. A platinised platinum microelectrode (r = 5 µm) was used as a tip and it was placed over the disc-Pt-25 µm in the SECM setup (Figure 2.16A).

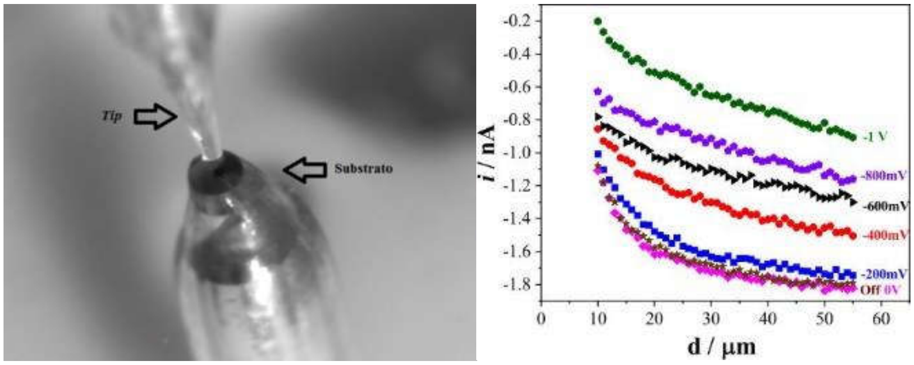

Figure. 2.16. (A) Photograph of the two microelectrodes in the SECM setup. (B)Approach curves recorded using a platinised platinum microelectrode (r = 5 µm, RG = 10) towards a platinum microelectrode surface (r = 25 µm) in DMEM solution. The substrate was unbiased and polarized at different potentials (0 V to – 1 V, as indicated in the figure), whereas the tip was polarized at – 0.6 V vs Ag/AgCl/sat. KCl.

The tip was polarized at a potential where the ORR takes place at mass-transport conditions (-0.6 V) and moved towards the sample, which was biased at different potentials. Figure. 2.16. *(A) Photograph of the two microelectrodes in the SECM setup. (B)Approach curves recorded using a platinised platinum microelectrode* shows the recorded approach curves with negative feedback profile, i.e., the cathodic current decreases as the tip is closer to the platinum surface. It should be pointed out that this substrate consumes oxygen and the reduction product is non electroactive (H_2O), hence the typical positive feedback effect expected for a platinum surface is not present in this case. Changes in the approach curves recorded at different potentials applied to the substrate are due to the redox competition effect, as the negative feedback due to hindered diffusion of O_2 is the same in all cases. The ORR current at the tip decreased as the substrate was biased at more negative potentials, and one can conclude the concentration gradient produced by the substrate influenced the current at the tip. On the other hand, as the tip is biased this can also can influence the current at the substrate because of the redox competition.

Hence, the sensor can also affect the oxygen concentration gradient of the sample. As a conclusion, the cell is a dynamic sample and its metabolism can be changed by the local disturbance of O_2 concentration. The influence of such problem can be minimized by using even smaller tips (nanometric dimensions) which will consume less oxygen or by performing experiments in different amperometric modes in which current measurements are done at different intervals and for a few milliseconds during the approach, such like in pulse methods.

2.3. References.

1. Pedrotti, J. J.; Angnes, L.; Gutz, I. G. R.; Quimica, I. De; Paulo, U. D. S.; Box, P. O.; Paulo, S. *Electroanalysis* **1996**, *8*, 673–674.

2. Kwak, J.; Bard, a J. *Anal. Chem.* **1989**, *61*, 1221–1227.

3. Bard, A. J.; Mirkin, M. V. *Scanning Electrochemical Microscopy*, 2nd editio.; CRC Press, 2012.

4. Cornut, R.; Bhasin, A.; Lhenry, S.; Etienne, M.; Lefrou, C. *Anal. Chem.* **2011**, *83* (24), 9669–9675.

5. Conway, B. E. *Prog. Surf. Sci.* **1995**, *49* (4), 331–452.

6. Will, F. G. *J. Electrochem. Soc.* **1965**, *112* (4), 451–455.

7. Eckhard, K.; Chen, X.; Turcu, F.; Schuhmann, W. *Phys. Chem. Chem. Phys.* **2006**, *8* (45), 5359.

Chapter 3.

Single-cell oxygen measurements by Scanning Electrochemical Microscopy to investigate the intracellular heterogeneous oxygen consumption

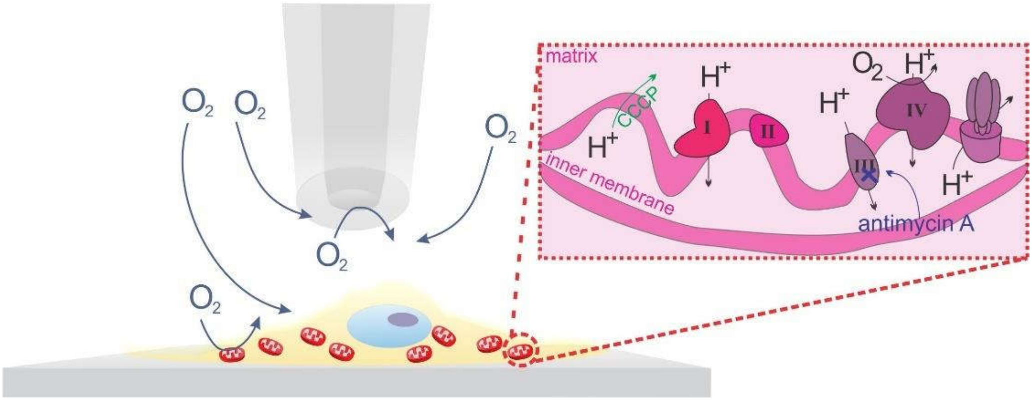

The developed oxygen microsensor discussed at the previous chapter was then applied to the single-cell measurement using SECM. The immortalized cells HS578T lineage was chosen due to its size and longtime resistance after removal from the culture condition. This work is considered to be the main contribution of the PhD thesis of Carla Santana Santos once many achievments were required to accomplish this work: the SECM knowledge and expertise, the experience in handling biological samples, to work with bio-SECM equipment, the fabrication of a sensor with resolution to map a cell and with stability to long-term measurements. Here, results on the use of SECM for studying biological samples for the first time in Brazil are presented. Many of the preliminary results concerning this work were presented in international and national conferences and, after a lot of discussions, we found a proper experimental design to confirm the heterogeneity of the respiration at the same cell. Besides that, we showed SECM can be used as a local respirometer, capable to measure the OCR of a single cell. The results obtained and presented in this chapter were published in a paper as follows:

Single Cell Oxygen Mapping (SCOM) by Scanning Electrochemical Microscopy Uncovers Heterogeneous Intracellular Oxygen Consumption. **Carla S. Santos**, Alicia J. Kowaltowski, Mauro Bertotti. *Scientific Reports*, 2017, Vol 7, article number 11428.

The mentioned paper is an open access article published in Scientific Reports (Publisher: Springer Nature) and the permission of use is allowed as soon as it is properly cited, as above.

Carla Santana Santos prepared the cell samples and performed the electrochemical measurements as the data analysis. C. S. S. planned the designed of experiments with the co-authors. All the authors analyzed the results, wrote the text and reviewed the final manuscript. C. S. S. made de figures and graphs and handled the submission to the journal

Cell culture was done by C. S. S. after a deep training with Maria Fermanda Forni. The OCR measurements in the commercial respirometer Seahorse XF Analyzers was done with the supervision of Camille C. Caldeira da Silva in the Prof. Alicia J. Kowaltowski's lab. During some SECM experiments, Carla had close support of Gabriel N. Meloni, due to her health condition and C. S. S. is completely grateful for his help and support.

3.1. Abstract.

We developed a highly sensitive oxygen consumption scanning microscopy system using platinised platinum disc microelectrodes. The system is capable of reliably detecting single-cell respiration, responding to classical regulators of mitochondrial oxygen consumption activity as expected. Comparisons with commercial multi-cell oxygen detection systems show that the system has comparable errors (if not smaller), with the advantage of being able to monitor inter and intra-cell heterogeneity in oxygen consumption characteristics. Our results uncover heterogeneous oxygen consumption characteristics between cells and within the same cell´s microenvironments. Single Cell Oxygen Mapping (SCOM) is thus capable of reliably studying mitochondrial oxygen consumption characteristics and heterogeneity at a single-cell level.

3.2. Introduction.

Because mitochondrial oxidative phosphorylation is the end-point of most metabolic processes, monitoring oxygen consumption is an effective manner to continuously and non-invasively evaluate energy metabolism in different cell types. Indeed, high-resolution commercial systems have been developed to monitor oxygen consumption in suspended biological samples, using Clark-type electrodes [1–3], and plated cultured cells [4], using fluorescent probes. These systems have been successfully used to uncover many different metabolic conditions, with applications as varied as in inherited mitochondrial diseases, inflammation, diabetes, neuroscience and aging [5–9]. Using specific inhibitors, oxygen consumption experiments can determine basal and maximal mitochondrial respiratory capacity, ATP-linked processes, non-ATP-producing respiration (thermogenesis and non-mitochondrial respiration) and estimate substrates used, among other parameters [4,10].

However, these techniques present the caveat of detecting only bulk oxygen consumption of the media in which the cells are suspended. They are therefore unable to detect heterogeneity of metabolic characteristics among different individual cells in the same culture, and cannot detect characteristics of this consumption within different areas of a single cell. To date, evaluations of mitochondrial metabolic heterogeneity within and among individual cells have mostly been conducted using fluorescent microscopy and probes for mitochondrial inner membrane potentials. Unfortunately, these evaluations are not quantitative and marred by many artifacts including phototoxicity, influence of plasma membrane potentials, artifacts due to aggregation and changes in mitochondrial mass and morphology [11,12].

We thus believe the area would greatly benefit from the development of single cell oxygen consumption techniques. Different techniques have been used to acquire topographical information with high spatial resolution, including atomic force microscopy (AFM), scanning electron microscopy (SEM) and scanning electrochemical microscopy (SECM), which is highly valuable in measurements of local electrochemical activity at interfaces [13–16]. Indeed, SECM has been used in the biological field to uncover enzymatic activities and cellular topography [14,17–30]. SECM has also been employed to investigate oocyte metabolism and oxygen consumption rates calculated as the difference of oxygen concentrations in the bulk of the solution and close to the cells [31], estimated according to spherical diffusion theory [31–34].

In this work, we present an effective and simple approach to evaluate oxygen consumption in the microenvironment of an individual cell, using a platinised platinum disc microelectrode as a tip in SECM configuration. Single Cell Oxygen Mapping (SCOM) experiments were carried out at a fixed tip-cell distance of 15 µm and high spatial resolution information on the oxygen consumption rates was obtained. The results were compared to those acquired with available commercial methods, and show that, while bulk measurements are compatible, our method adds significant spatial distribution information. The use of a platinised platinum microelectrode as a tip in a SECM configuration for mapping the oxygen concentration above a single-cell uncovers rich topographical heterogeneity in oxygen uptake characteristics within individual cells in culture, which may have important regulatory, physiological and pathological implications.

3.3. Experimental section.

3.3.1. Chemicals.

All reagents were of analytical grade and used as received (Sigma Aldrich, USA). Measurements in absence and presence of oxygen were performed in solutions purged with argon and oxygen (Air Products SA – Brazil).

3.3.2. Microelectrode fabrication and electrochemical characterization.

Platinum microelectrodes were fabricated by sealing a 50 µm diameter platinum wire (99.99% purity; hard, Goodfellow, UK) inside a quartz glass capillary (L, 150 mm; o.d., 1.0 mm; i.d., 0.3 mm, Sutter Instruments, USA). The capillary was then pulled using a P-

2000 Micropipette Puller (Sutter Instrument Company, USA). A Ag/AgCl (saturated KCl) electrode was used as reference. The microelectrodes were electrochemically characterized by recording cyclic voltammograms and approach curves over a silicon wafer in a 5 mmol L^{-1} $[Ru(NH_3)_6]Cl_3$ + 0.1 mol L^{-1} KCl solution. The electrochemically-active radius and the RG values (RG = rg/ r, where rg is the radius of the overall tip, including the active platinum disc and the surrounding insulator; r is the radius of the platinum microdisc) of two different microelectrodes were determined by fitting approach curves before the platinisation of the surface. Values were found to be 5 μm (RG = 8) and 500 nm (RG = 15). The smaller microelectrode was used in the SECM image experiment. The calibration plot for oxygen was prepared by using steady-state current values obtained from cyclic voltammograms recorded in a Gibco Dulbecco's phosphate buffered saline (Thermo Fisher Scientific, USA) solution containing oxygen at different concentrations.

3.3.3. HS578T cell culture conditions.

HS578T human breast cancer cells (ATCC) were grown in plastic flasks in Dulbecco's Modified Eagle's Medium, DMEM, (Thermo Fisher Scientific, USA) supplied with 10% fetal bovine serum, 1% penicillin and streptomycin. Temperature and pH were controlled in an incubator (5% CO_2 at 37º C).

3.3.4. Seahorse bioanalyzer oxygen consumption measurements.

HS578T cell oxygen consumption rates were investigated a using a SeaHorse XF 24 Analyzer (Seahorse Biosciences, USA). The experiment was performed in SeaHorse solution containing 5.10^4 attached cells per well of 24-well Seahorse plates (600 μL). Rates were measured for intact cells (basal respiration conditions) and in the presence of

0.6 μmol L^{-1} carbonyl cyanide m-chlorophenylhydrazoneine, CCCP (maximum respiration) and 2 μmol L^{-1} antimycin A (non-mitochondrial respiration).

3.3.5. Electrochemical experiments and SCOM.

Electrochemical experiments were carried out using an Autolab PGSTAT128 bipotentiostat/galvanostat (Ecochemie, Netherlands) and a Sensolytics (Sensolytics, Germany) SECM coupled to an inverted microscope (Zeiss, Germany). Platinum disc microelectrodes were platinised in a 1 mmol L^{-1} K_2 $PtCl_6$ + 0.5 mol L^{-1} H_2SO_4 solution by cycling the potential from 0.3 V to -0.5 V vs Ag/AgCl/saturated KCl (100 cycles) [35]. SECM experiments were performed over a Petri dish (TC dish 35, Sarstedt, Germany) filled with 2 mL of DMEM cell culture solution (37ºC, containing 5.10^4 HS578T plated cells). The tip-substrate distance was determined by performing approach curves at the Petri dish surface close to the cell. The tip was then positioned above the cell. Cell respiration activity was measured with a platinised platinum microelectrode (r = 5 μm) polarized at -0.4 V and positioned at a microelectrode-cell surface distance of about 15 μm (hindered diffusion region). Electrochemical images of a single cell were obtained with a platinised platinum microelectrode (r = 500 nm) by recording cyclic voltammograms (0.5 V to -0.6 V) after each movement of the tip in the x-y plane. In these experiments, since the SECM tip possessed submicrometer dimensions, it was positioned 15 μm above the cell surface, which is far from the hindered diffusion region. Hence, no topographical effects could be noted at this working distance.

3.4. Results.

3.4.1. Microelectrode development, characterization and calibration.

The development of a highly sensitive oxygen microscopy system using SECM included producing platinum disc microelectrodes which were platinised to increase the sensitivity and selectivity of the measurements. The platinisation step reduced overpotential for the electrochemical reduction of O_2 and enhanced the cathodic current, leading to higher sensitivity. Moreover, amperometric responses that were stable over large periods of time were obtained by using the platinised Pt microelectrode. Typical O_2 electrochemical detection responses of the constructed sensor can be seen in Figure 3.1, which shows cyclic voltammograms recorded in the absence of O_2 (Figure 5A, black line, i) air-saturated solution Figure 3.1A, red curve, ii) and O_2-saturated phosphate buffered saline solution (Figure 3.1A, blue curve, iii). A steady-state situation is achieved in curves ii and iii, which correspond to the electrochemical process involving O_2 reduction. Current values at -0.4 V were plotted as a function of O_2 concentration and the calibration plot is shown in Figure 3.1B. The linear plot ($R^2 = 0.99994$) shows the constructed platinised Pt microelectrode is a highly sensitive probe to monitor changes in O_2 concentrations, with a large dynamic concentration range.

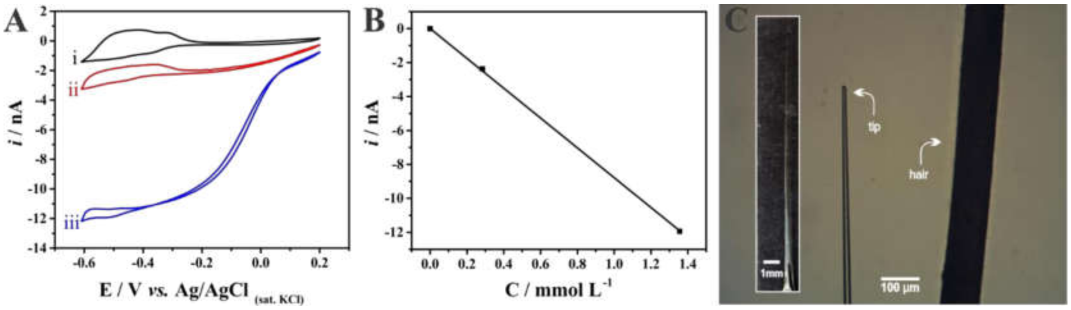

Figure 3.1. (A) Cyclic voltammograms recorded with a platinised Pt microelectrode in argon-saturated (black curve, i), air-saturated (red curve, ii) and O_2-saturated (blue curve, iii) phosphate buffered saline solution (pH 7.4). Scan rate: 100 mV s^{-1}. (B) Calibration plot from current values measured at -0.4 V. (C) Optical images of the tip compared to a single human hair.

3.4.2. Single Cell Oxygen Mapping (SCOM) by Scanning Electrochemical Microscopy: comparison with commercial systems.

To investigate cell respiration using the SECM system, the platinised Pt microelectrode was positioned over cultured HS578T cells (chosen for their large surface area) and biased at -0.4 V to monitor changes in local O_2 concentrations. After 10 minutes for current stabilization, the system displayed a stable current change over time, with good signal to noise relationships. To test for stability upon additions to the system, 2 μL of the culture media DMEM were added (Figure 3.2A, a). No alterations in current changes over time were seen, indicating a stable system in which additions could be made. Subsequently, we added known modifiers of cellular oxygen consumption: CCCP (Figure 3.2A, b), an uncoupler of oxidative phosphorylation which increases cellular oxygen consumption, and antimycin A (Figure 3.2A, c), a specific inhibitor of mitochondrial electron transport and, therefore, oxygen consumption. As expected for these regulators of cellular oxygen consumption, CCCP increased the change in current over time, while antimycin A eliminated it. Control experiments (results not shown) were performed in the absence of cells and no changes were observed upon addition of CCCP and antimycin A, demonstrating that the effects of these drugs were on the cells and not on electrode response. Thus, our SCOM strategy is applicable to cell cultures and presents an adequate response to known regulators of oxidative metabolism.

O_2 consumption rates were calculated from slope values measured along the recorded black curve shown in Figure 3.2A. This representation clearly shows that basal oxygen consumption rates are very significantly increased after the addition of CCCP, whereas these were close to 0 pA min^{-1} in the presence of antimycin A, demonstrating that the SCOM by SECM works well as a respirometer for cultured cells. Indeed, parallel experiments with a SeaHorse respirometer, the gold-standard commercial system available to measure plated cell oxygen consumption, showed similar profiles (Figure 3.2B), albeit with more dispersion.

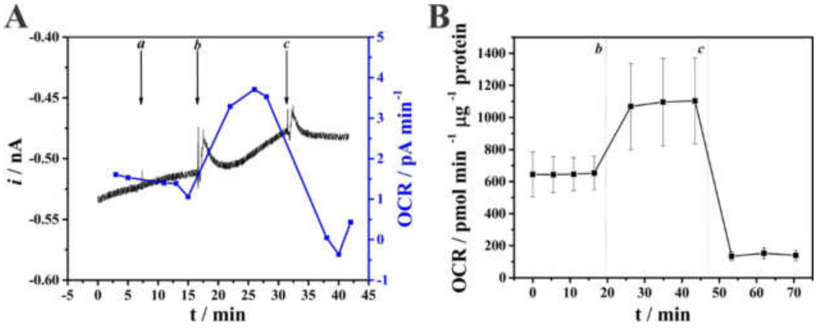

Figure 3.2. (A) Current monitoring using a platinised Pt microelectrode (-0.4 V) positioned at ~ 15 µm tip-substrate distance from an HS578T cell and O_2 consumption rate (OCR) values as a function of time. DMEM (2 µL, a), 2 µmol L^{-1} CCCP (b) and 2 µmol L^{-1} antimycin A (c) were added where indicated. (B) Oxygen consumption values obtained using a commercial SeaHorse Bioanalyzer under similar experimental conditions.

To confirm if the changes in measurements by SCOM were due to the modulation of respiratory activity and not chemical effects of the drugs, the same experiment was repeated, but the substances were added in the opposite order, i.e., antimycin A was added before CCCP. Once complex III is inhibited and the electron transport chain is blocked by antimycin A, the addition of CCCP should not cause any significant change in the respiratory activity. Indeed, the red curve *i* in Figure 3.3 shows current changes before and after addition of antimycin A and CCCP, respectively, and no net change in the oxygen consumption rates were observed, confirming the CCCP effect in Figure 3.2 was specific to mitochondrial respiration. The experiment was then repeated again under the same conditions in this cell, but CCCP was added before antimycin A; the trace obtained again resembles that in Figure 3.2A, with an increase in respiratory activity upon the addition of CCCP. Interestingly, we find that the increase in respiratory activity between individual cells presents some variability (196% and 230%, comparing Figure 3.2 and

Figure 3.3 curve *ii*). This shows that there are individual characteristics of cellular respiration, which can be uncovered with SCOM, but not commercial systems in which the values obtained are averages for a pool of cells. This is a noteworthy advantage of the proposed approach, since cellular oxygen consumption heterogeneity may be involved in many biological effects, but has not been studied to date.

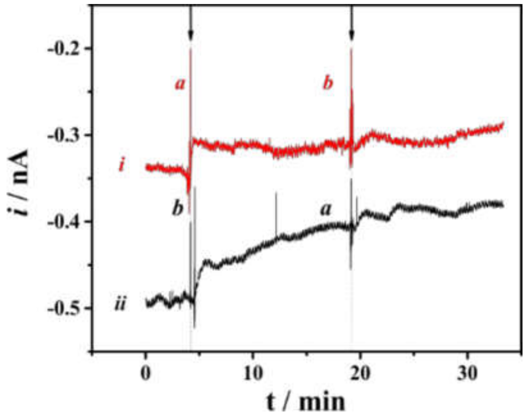

Figure 3.3. Current monitoring using a platinised Pt microelectrode positioned over HS578T cells. The arrows indicate the addition of antimycin A (a, 2 µmol L^{-1}) and CCCP (b, 2 µmol L^{-1}). The microelectrode was biased at -0.4 V.

Although the differences in respiratory stimulation seen for specific cells upon the addition of CCCP may be due to individual cell characteristics, current measurements in an SECM system depend on the concentration of the electroactive species as well as the distance between the tip (microelectrode) and the substrate (cell). At the working distance employed here (at around 15 µm using a microelectrode of r = 5 µm), the tip body inhibits lateral oxygen diffusion, acting as a physical barrier (hindered diffusion). Hence, the oxygen concentration in the layer between microelectrode and the cell is controlled by the hindered diffusion effect, the consumption by the tip and the consumption by the cell. Because the rate of electron transfer is the same throughout the experiment (the electrode potential is set at a fixed value) and the working distance is considered constant, these experimental parameters should not cause changes in measured current. Cell height was determined to be 3 μm by atomic force microscopy (AFM), and was thus much smaller than the working distance (15 μm), making any cellular shrinkage or expansion effect negligible. As a result of the hindered diffusion effect, the current decreases as the tip approaches the surface. Thus, the conversion of current into O_2 concentration is not straightforward, since the accurate distance between the cell and microelectrode surface is difficult to estimate, and could vary in separate measurements. In order to test the reliability of the system, we compared the SCOM/SECM respirometer to the commercial Seahorse respirometer in terms of reproducibility (Figure 3.4). Because SCOM measures oxygen consumption in single cells, while Seahorse respirometry measures a cell population, we normalized the readings as percentages of basal oxygen consumption. SeaHorse errors were calculated from measurements performed in four different wells, while the error bars for SCOM measurements correspond to different measurements of a single cell. Interestingly, we noted that variability in the SCOM by SECM was comparable or even lower than the multi-cell Seahorse system (Figure 3.4).

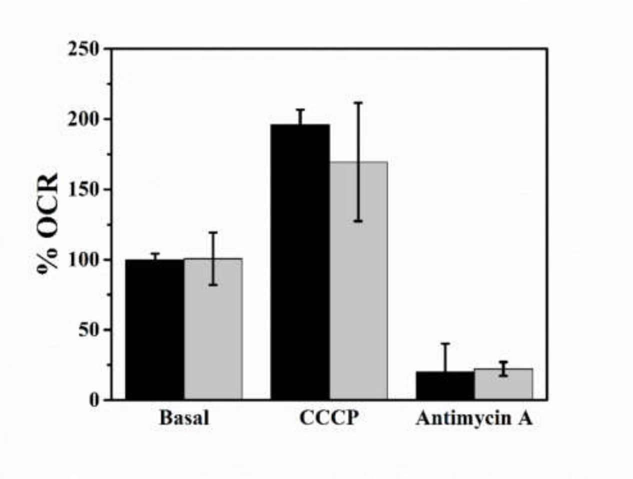

Figure 3.4. Percentage oxygen consumption rate (OCR) variation for HS578T cells using SCOM (black bars) and SeaHorse (gray bars) respirometers. Basal respiratory rates were used to normalize results, and the effects of CCCP and antimycin A were monitored under conditions described for Figure 3.2.

3.4.3. Single Cell Oxygen Mapping (SCOM).

Given the evidence that the SECM system was reliably measuring oxygen consumption, we scanned a submicrometric platinised Pt microelectrode (r = 500 nm) over cultured cells in order to get a map of respiratory activity. In this SCOM image experiment, the microelectrode-substrate distance was set at 15 μm (constant height) and the tip was scanned across the surface of two cells (*Figure 3.5*A), chosen because the lower one presented normal live cell morphology, while the top cell was rounded and seemed to be poorly attached, a characteristic of dead cells, which are not expected to respire. The tip was moved laterally in a horizontal (x-y) plane with 10 μm steps at 5 μm s^{-1}. Cyclic voltammograms were recorded only at the end of each step to minimize oxygen depletion [29,35]. Current values measured at -0.4 V were used to create the SCOM image (*Figure 3.5*). Experiments were performed before (*Figure 3.5*B) and after (*Figure 3.5*C) the addition of antimycin A (2 μmol L^{-1}). Current values were normalized (the highest current was defined as 1) and higher upon addition of the inhibitor compared to those values obtained under basal conditions, since oxygen consumption rates decreased.

The result is a map of oxygen consumption in the cell microenvironment, which shows that most of the area of the live cell coincides with areas of oxygen consumption (*Figure 3.5*B). An exception is the area of the nucleus (bulge on the center bottom), which has low consumption, as expected for a cellular area that lacks mitochondria. The dead cell, on the other hand, did not affect oxygen consumption currents. These differences disappear in the antimycin A-treated cell measurement (*Figure 3.5*C), indicating they are caused by oxygen consumption and not topography.

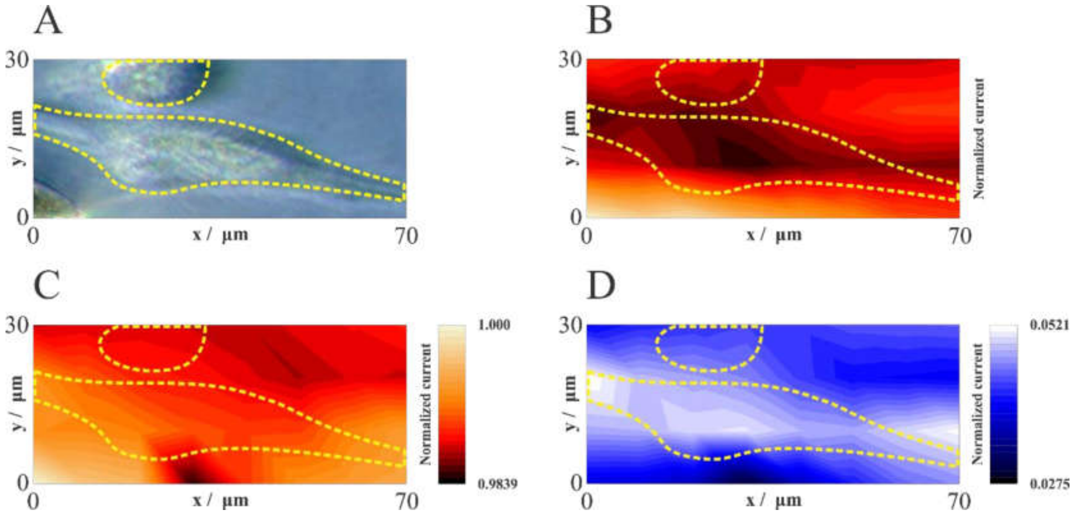

Figure 3.5. (A) Optical image of two cells. Normalized current map of the scanned area before (B) and after (C) addition of antimycin A (2 µmol L^{-1}). For B and C the highest oxygen reduction current was defined as 1. (D) Pixel subtraction map corresponding to normalized current values measured after (map C) and before (map B) the addition of antimycin A. E = -0.4 V, Pixel size = 10 x 10 µm. The dotted lines show the shape of the cells.

To further compare the inhibitor effect and generate a specific mitochondrial oxygen consumption map, normalized current values measured for intact cells (basal respiration condition) were subtracted from those corresponding to experiments performed in presence of antimycin A (non-mitochondrial respiration condition), generating the pixel subtraction map shown in Figure 3.5D. This map compensates for oxygen diffusion effects such as those caused by the mass of the dead cell and indicates areas of mitochondrial oxygen consumption within the live cell (white zones). Our cells are not morphologically similar to spheres and the oxygen consumption is not homogeneous throughout the cell, as shown in Figure 3.5B. Hence, spherical diffusion theory [31] is not appropriate to estimate oxygen consumption rate at our experimental conditions. In an attempt to give the reader information on the quantitative amount of O_2 molecules consumed in the respiration process as a function of time, we adopted a different approach: O_2 consumption rates values shown in Figure 3.2A were divided by the slope of the calibration plot (obtained at a microelectrode-silicon wafer surface distance of about 15 μm, i.e., a similar microelectrode-cell surface separation), uncovering quantitative changes in O_2 concentrations at the surface of the cell by unit of time. Taking into account the volume of the solution, the rate of O_2 consumption was found to be 342 (basal condition), 797 (in the presence of CCCP) and 114 pmol min^{-1} (in the presence of antimycin A). Interestingly, while the cell nucleus area was an expected area of low oxygen consumption, the map (Figure 3.5D) shows that cell extremities have very high oxygen consumption, and uncovers heterogeneous oxygen consumption characteristics within a single cell. It should be pointed out that the acquired images have a pixel size resolution of 10 μm, but the scanned area corresponding to the cells extremities is smaller than this value. Even considering this, the extremities of the cell demonstrate significant respiratory activity, leading to a higher oxygen consumption activity zone. In conclusion, the spatial resolution of the SCOM by SECM system thus allows for the visualization of different regions of mitochondrial respiration within a single cell.

3.5. Discussion.

Mitochondrial oxidative phosphorylation, as the end-point of energy metabolism, has been extensively studied as a means of understanding metabolic processes underlying physiological and pathological processes. The best way to study oxidative phosphorylation is the measurement of oxygen consumption rates associated with the use of mitochondrial respiratory regulators [1–4]. Oxygen consumption methods are advantageous since they are quantitative, specific and much less artifact-prone than fluorescence microscopy methods to evaluate mitochondrial function [11,12,36]. Currently available methodologies to evaluate mitochondrial respiration do so in bulk: tissue samples, isolated mitochondrial homogenates, intact and permeabilized cells [1–4].

However, recent findings studying mitochondrial parameters other than respiratory rates (such as morphology and inner membrane potentials) suggest there is significant heterogeneity both between different cells in a population and within different mitochondria within the same cell [37–42]. As a result, the development of methodologies capable of measuring oxygen consumption with single cell resolution has become of interest.

Here we developed and validated the use of a SCOM method using SECM and a platinised platinum disc microelectrode with a submicrometric tip (Figure 3.2). We have demonstrated the SCOM system is capable of reliably measuring single cell oxygen consumption, responding to mitochondrial respiratory modulators in the expected manner, and displaying stability during measurements and additions (Figure 3.2 and Figure 3.3). The system produces results that are comparable, if not better, than the gold-standard currently available commercial system to evaluate respiration in populations of plated cells (Figure 3.4), with the advantage of being able to uncover inter-cell variability (Figure 3.3). Moreover, the oxygen consumption rate can be assessed in a simpler way than those proposed in the literature [32,33], where this parameter was obtained by measuring oxygen concentrations at different distances from the cell surface: This approach has the disadvantage of being influenced by the effect of the working distance on current measurement, since currents also change because of the feedback effect. Finally, when used in a scanning configuration, the SCOM system developed here is able to create oxygen consumption maps, and uncovers heterogeneity in consumption patterns within the same cell (Figure 3.5), with enhanced mitochondrial oxygen consumption at the thinner ends of the cell.

We have thus successfully demonstrated the feasibility of non-invasive oxygen consumption microscopy experiments in biological samples, a development that will add to our knowledge of metabolic characteristics on a single-cell basis.

3.6. Acknowledgments.

The authors are grateful to CNPq and FAPESP for the financial support. Grants #2014/22396-6, 10/51906-1, 13/07937-8 and #2015-20776-9, São Paulo Research Foundation (FAPESP) to C.S.S., A.J.K., A.J.K. and M.B., respectively. The authors would like to thank Mr. Gabriel Meloni for the helpful discussions, Camille C. Caldeira da Silva for technical support and discussions on bioenergetics and Dr. Maria Fernanda Forni for help with cell cultures.

3.7. References.

1. Kahn, J. S. *Anal. Biochem.,* **1964** 9, 389–391.
2. Gnaiger, E., Steinlechner-Maran, R., Méndez, G., Eberl, T. & Margreiter, R. *J. Bioenerg. Biomembr.,* **1995**, 27, 583–596.
3. Simonnet, H., Vigneron, A. & Pouysségur, J. *Methods Enzymol.,***2014**, 542, 151–161.
4. Wu, M. *et al. AJP Cell Physiol.,* **2006**, 292, C125–C136.
5. Zharikov, S. & Shiva, S. *Biochem. Soc. Trans.,* **2013**, 41, 118–123.
6. Kramer, P. A., Ravi, S., Chacko, B., Johnson, M. S. & Darley-Usmar, V. M. *Redox Biol.,* **2014**, 2, 206–210.
7. Perry, C. G., Kane, D. A., Lanza, I. R. & Neufer, P. D. *Diabetes,***2013**, 62, 1041–1053.
8. Horan, M. P., Pichaud, N. & Ballard, J. W. O. *J. Gerontol. A Biol. Sci. med. Sci.,***2012**, 67 A, 1022–1035.
9. M.-L., H. *et al. Vascular Medicine (United Kingdom),* **2014**, 19, 67–74.
10. van der Windt, G. J. W., Chang, C. H. & Pearce, E. L. *Curr. Protoc. Immunol.,* **2016**, 113, 1–3.
11. Nicholls, D. G. *Methods Mol. Biol.,* **2012**, 810, 119–133.

12. Brand, M. D. & Nicholls, D. G. *Biochem. J.*, **2011**, 435, 297–312.

13. Wittstock, G., Burchardt, M., Pust, S. E., Shen, Y. & Zhao, C. *Angew. Chem. Int. Ed. Engl.,* **2007**, 46, 1584–1617.

14. Géza, N. & Lívia, N. Application of scanning electrochemical microscopy in bioanalytical chemistry. In *Trends in Bioelectroanalysis Bioanalytical Reviews* (ed. Matysik, F.-M.) 6, 281–339 (Springer, 2016).

15. Page, A., Kang, M., Armitstead, A., Perry, D. & Unwin, P. R. *Anal. Chem.*, **2017**, 89 (5), 3021- 3028.

16. Sun, T., Yu, Y., Zacher, B. J. & Mirkin, M. V. *Angew. Chemie - Int. Ed.,* **2014**, 53, 14120–14123.

17. Yamada, H. *Electrochim. Acta,* **2014**, 136, 233–239.

18. Actis, P. *et al. ACS Nano,* **2014**, 8, 875–884.

19. Şen, M. *et al. Anal. Chem.*, **2015**, 87, 3484–3489.

20. Beaulieu, I., Kuss, S., Mauzeroll, J., Geissler, M. *Anal. Chem.*, **2011**, 83, 1485–1492.

21. Schulte, A., Schuhmann, W. *Angew. Chemie - Int. Ed.*, **2007**, 46, 8760–8777.

22. Amemiya, S., Guo, J., Xiong, H. & Gross, D. A. *Anal. Bioanal. Chem.*, **2006**, 386, 458–471.

23. Bondarenko, A. *et al. Anal. Chem.,* **2016**, 88, 11436–11443.

24. Holt, K. B. & Bard, A. J. *Biochemistry,* **2005**, 44, 13214–13223.

25. Sridhar, A., De Boer, H. L., Van Den Berg, A. & Gac, S. Le. *PLoS One,* **2014**, 9, 4, e93618.

26. Takahashi, Y. *et al. Langmuir,* **2006**, 22, 10299–10306.

27. Yasukawa, T., Kondo, Y., Uchida, I. & Matsue, T. *Chem. Lett.,* **1998**, 8, 767–768.

28. Takahashi, Y. *et al. J. Am. Chem. Soc.,* **2010**, 132, 10118–10126.

29. Nebel, M., Grützke, S., Diab, N., Schulte, A. & Schuhmann, W. *Angew. Chemie - Int. Ed.,* **2013**, 52, 6335–6338.

30. Yasukawa, T., Kaya, T. & Matsue, T. *Anal. Chem.,* **1999**, 71, 4637–4641.

31. Sugimura, S. *et al. J. Reprod. Dev.,***2012**, 58, 636–641.

32. Shiku, H. *et al. Anal. Chem.,* **2001**, 73, 3751–3758.

33. Date, Y. *et al. Biosens. Bioelectron.,* **2011**, 30, 100–106.

34. Shiku, H. *et al. Sensors Actuators, B Chem.,* **2005**, 108, 597–602.

35. Nebel, M., Grützke, S., Diab, N., Schulte, A. & Schuhmann, W. *Faraday Discuss.*, **2013**, 164, 19-32.

36. Amigo, I. *et al. Biochem. J.,***2016**, 473, 3421–3449.

37. MacDonald, J. A., Fowle, W. H. & Woods PhD, D. C. *Micron.,* **2017**, 101, 25–31.

38. Boumelhem, B. B., Assinder, S. J., Bell-Anderson, K. S. & Fraser, S. T. *Adipocyte,* **2017**, 6, 112–123.

39. Sison, M. *et al. Sci. Rep*., **2017**, 7, 43275.

40. Fedorovich, S. V., Waseem, T. V. & Puchkova, L. V. *Rev. Neurosci.,* **2017**, 28(4), 363-373.

41. Stotland, A. & Gottlieb, R. A. *J. Mol. Cell. Cardiol.,* **2016**, 90, 53–58.

42. Wikstrom, J. D., Twig, G. & Shirihai, O. S. *Int. J. Biochem. Cell Biol.,* **2009**, 41, 1914–1927.

43. Lefrou, C. & Cornut, R. *Chemphyschem.,* **2010**, 11, 547–56 .

Chapter 4.

The investigation of the heterogeneous oxygen consumption on a single *Caenorhabditis elegans* animal

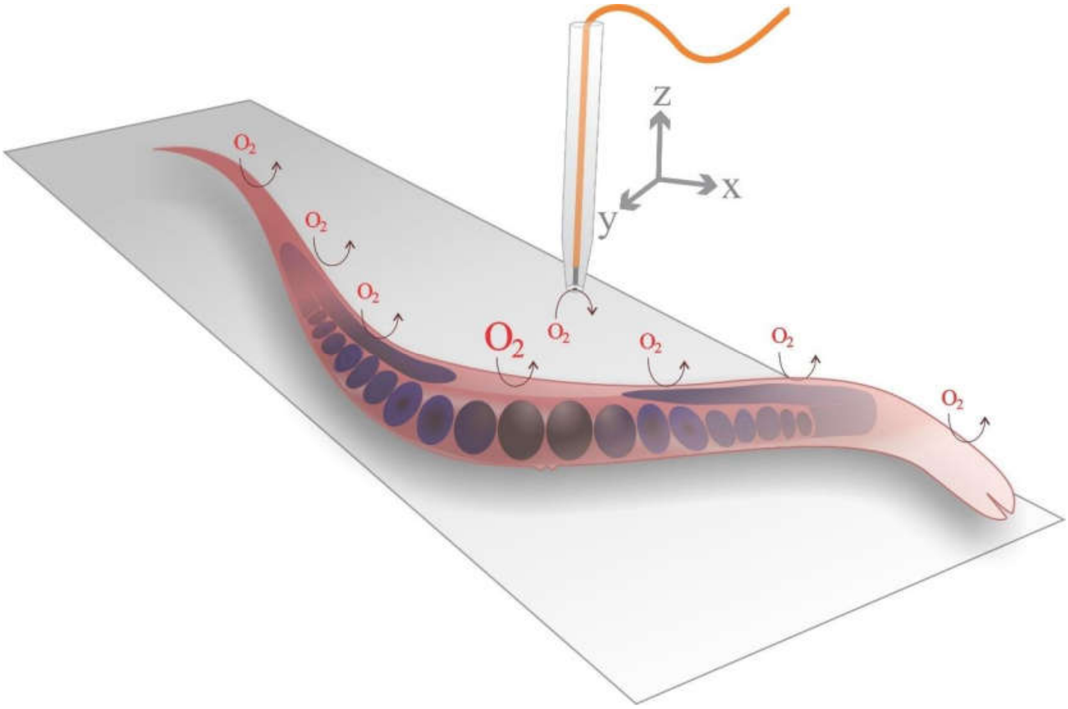

In the previous chapter, the capability of SECM to get localized information on oxygen consumption by the mitochondria in a single-cell was demonstrated and such approach was repeated with a nematode. The nematode *Caenorhabditis elegans* is an animal used as a model for aging and effects of caloric restriction (diets) studies due to its metabolism and physiology, as well as easy handling and short-lifespan. The evaluation of drugs effects on its metabolism is commonly done by checking the respiration activity by means of oxygen concentration measurements of a large amount of worms. Herein, we used the advantages of SECM to evaluate to gain localized information of the role of the reproductive system of the animal in the oxygen consumption. The experiments were performed in collaboration with Dr. Fernanda Marques da Cunha, from the Federal University of São Paulo (UNIFESP), and her PhD student, Felipe M. dos Santos. Dr. Gabriel Negrão Meloni, researcher in Patrick Unwin's group at the University of Warwick (UK) did the simulation studies.

The *C. elegans* culture was grown by Felipe M. dos Santos. Carla Santana Santos performed all the electrochemical measurements and prepared the animals to the electrochemical measurements. G. N. M. and C. S. S. treated the data and G. N. M. modeled the experimental data to get information on local OCR values. C. S. S., F. M. C. and A. J. K planned and designed the experiments with the co-authors.

4.1. Introduction.

The oxidative phosphorylation is the last stage of the majority of metabolic processes and the oxygen concentration measurement is an efficient tool to monitor any variation at the bioenergetics process in different samples e.g.: cells, tissues, organisms. In fact, commercial equipments with high sensitivity to measure oxygen consumption have been developed in studies carried out with isolated mitochondria using Clark electrodes [1–3] and in attached cell cultures with fluorescent sensors [4]. These equipments have been successfully applied to investigate metabolic conditions and to understand mitochondrial diseases, inflammation, diabetes and aging processes [5–8]. Specific inhibitors have been used to modulate the mitochondrial respiration for checking specific contributions on the mitochondrial activity [4,9]. For these studies, model animals are used to allow the understanding of specific processes in more specific systems. The nematode *Caenorhabditis elegans* is a simple and multicellular organism and has been used as a model in aging and effects of caloric restriction studies due to its metabolism and physiology, as well as easy handling and short-lifespan [10,11]. In addition, the life cycle of the *C. elegans* follows a standard cell division which rarely changes [10], hence leading to a fast and easy recognition of the life phase of the animal. Recent studies have shown that changes in the mitochondrial activity (effect of diets during the life cycle of the *C. elegans*) were responsible for reducing the reproduction capacity [12]. Then, the understanding of the role of the reproductive system in the metabolism of the whole animal is needed. However, commercial equipments can only detect the variation on the oxygen concentration in a sample population, offering no information of the respiration rate (oxygen consumption) at individual organisms or even the variation along the same single-organism. We have already shown that a platinised platinum microelectrode in SECM (scanning electrochemical microscopy) redox competition mode[13] (electrode/sensor and a single cell consumed the same species, oxygen) can be used as a tool for mapping the oxygen consumption in the vicinity of single cells. Measurements on the oxygen consumption rate were performed and the results were in agreement with those obtained with a standard equipment [14]. The single cell oxygen maps showed the oxygen consumption is not homogeneous throughout the cell. Thus, the same method can be employed to investigate the contribution of bioenergetic processes in individual organisms. Herein, SECM has been used for mapping the oxygen consumption along a single *C. elegans* and to study the role of the reproductive system in the respiration process.

4.2. Experimental Section.

4.2.1. Chemicals.

All chemicals were used as received: hexaamineruthenium (III) chloride ($[Ru(NH_3)_6Cl_3]$, CAS 14282-91-8, Alfa Aesar), hexachloroplatinic acid hexahydrate ($H_2PtCl_6{\cdot}6H_2O$, CAS 18497-13-7, Sigma Aldrich), potassium ferricyanide(III) ($K_3Fe(CN)_6$, CAS 13746-66-2, Sigma Aldrich), phosphate buffer saline (Sigma Aldrich) and sulfuric acid (H_2SO_4, CAS 7664-93-9, Merck). The solutions were prepared using water purified via a Nanopure Infinity (Barnstead, USA). The solutions were purged with argon and oxygen (Air Products SA, Brazil) for measurements in absence and presence of oxygen.

4.2.2. Microelectrode fabrication and electrochemical characterization (more details in Chapter 2).

Platinum microelectrodes were fabricated by sealing a 50 μm diameter platinum wire (99.99% purity; hard, Goodfellow, UK) inside a quartz glass capillary (L, 150 mm; o.d., 1.0 mm; i.d., 0.3 mm, Sutter Instruments, USA). The capillary was then pulled using a P-2000 Micropipette Puller (Sutter Instrument Company, USA). A Ag/AgCl (saturated KCl solution) electrode was used as reference. The microelectrodes were electrochemically characterized by recording cyclic voltammograms in the bulk solution and by approach curves recorded towards a silicon wafer surface in a 5 mmol L^{-1} $[Ru(NH_3)_6]Cl_3$ and 0.1 mol L^{-1} KCl solution. The electrochemical active radius and the RG values ($RG = rg/ r$, where rg is the radius of the overall tip, including the active platinum disc and the surrounding glass; r is the radius of the platinum microdisc). The platinum microelectrode surface was platinised by recording cyclic voltammograms (from 0.3 V to – 0.5 V, 30 cycles) in a 1 mmol L^{-1} $H_2PtCl_6 \cdot H_2O$ and 0.5 mol L^{-1} H_2SO_4 solution [15].

4.2.3. *C. elegans* culture conditions and sample preparation.

Experiments were performed with *C. elegans* hermaphrodite animals (lineage N2 Bristol) in the adult phase. The animals were grown in NGM (Nematode Growth Medium, 51 mmol L^{-1} NaCl, 0.25 % (m/v) bacto-peptone, 1 mmol L^{-1} $CaCl_2$, 1 mmol L^{-1} $MgSO_4$, 5 µg mL^{-1} cholesterol, 20 mmol L^{-1} KH_2PO_4, 5 mmol L^{-1} K_2HPO_4, 2 % (m/v) bacto-agar, pH 6.0 culture medium in the presence of 100 µg mL^{-1}streptomycin and *E. Coli* OP50-1, which was grown overnight at 37 °C in the culture medium LB. The temperature (20 °C) of the *C. elegans* culture was controlled in an incubator. For the electrochemical experiments, adults were collected using a tweezer and transferred to a Petri dish (TC dish 35, Sarstedt, Germany) with M9 buffer solution (KH_2PO_4 22 mmol L^{-1}, Na_2HPO_4 42 mmol L^{-1}, NaCl 86 mmol L^{-1}, $MgSO_4$ 1 mmol L^{-1}) and in presence of an anesthetic 0.3 mol L^{-1} 2,3- butanedione monoxime (CAS 57-71-6, Sigma , USA). The anesthetic was used to avoid any movement of the animals during the SECM measurements.

4.2.4. SECM map of oxygen concentration over a single *C. elegans* animal.

The electrochemical measurements were performed using an Autolab PGSTAT128 bipotentiostat/galvanostat (Ecochemie, Netherlands) and a scanning electrochemical microscope SECM (Sensolytics, Germany) placed on top of an optical inverted microscope Axio Vert. A1 (Zeiss, Germany). Platinised platinum microelectrodes (bare electrode r = 500 nm, RG between 20 and 25) were used as tips to record the SECM map. The tip height (vertical distance from the substrate) was assessed by recording approach curves towards the Petri dish surface in the vicinity of a single *C. elegans* using the oxygen reduction reaction (ORR). For the SECM maps, the platinised platinum microelectrode was positioned at a constant height of 100 μm (tip-to-surface distance) over the Petri dish. . Compensation of the surface tilt was accomplished by approaching the tip to the membrane at three different x,y positions and calculating the resulting plane. The surface tilt was compensated by scanning the probe in a X-Y plane created by the software using information of approach curves in the Petri dish. In order to avoid any significant local depletion of oxygen caused by amperometric measurements, the SECM map was obtained by recording cyclic voltammograms at each X-Y position [14-16]. An inhibitor of the ATP synthase (FoF1 system) was used to induce ORR current changes due to mitochondria activity and not to topographical effects. Measurements were recorded in M9 solution in the presence of 20 μmol L^{-1} N,N′-diciclohexilcarbodiimide (DCCD, CAS 538- 75-0, Sigma-Aldrich, USA) + 0.5 % (v/v) dimetilsulfoxide (DMSO, CAS 67-68-6, Merck, USA). The role of the eggs development in the reproductive system on the respiration activity was studied by repeating the experiments in the presence of 15 μmol L^{-1} FUdR (5-Fluoro-2’-deoxyuridine, CAS 50-91-9) after the phase L1 in the C. elegans cycle of life. FUdR is an inhibitor of the DNA replication, hence the larvae inside the eggs will not grow.

4.2.5. Determination of oxygen consumption rate using Finite Element Method.

The oxygen consumption rate was determined by recording cyclic voltammograms at a fixed distance along the animal body. Firstly, an approach curve was recorded towards a Petri dish surface in the vicinity of the animal region (head and vulva of a single *C. elegans*). Assuming the nematode body has a cylindrical shape, the microelectrode was moved upwards until the tip-to-sample surface reached 20 and 40 μm (working distance from the Petri dish surface = diameter of the animal + fixed distance of 20 or 40 µm), as shown in Figure 4.1. Afterwards, ORR steady state current values were used to determine the animal oxygen consumption rate by the Finite Element Method (FEM) simulations using the software COMSOL Multiphysics 5.3. The transport of diluted species was simulated considering the Nernst-Plank equation for the diffusion process and the Butler-Volmer equation for the charge transfer. The migration effect was disregarded. The OCR values were calculated for head and vulva regions of wild-type animals (wt *C elegans*) grown in the presence and absence of FUdR.

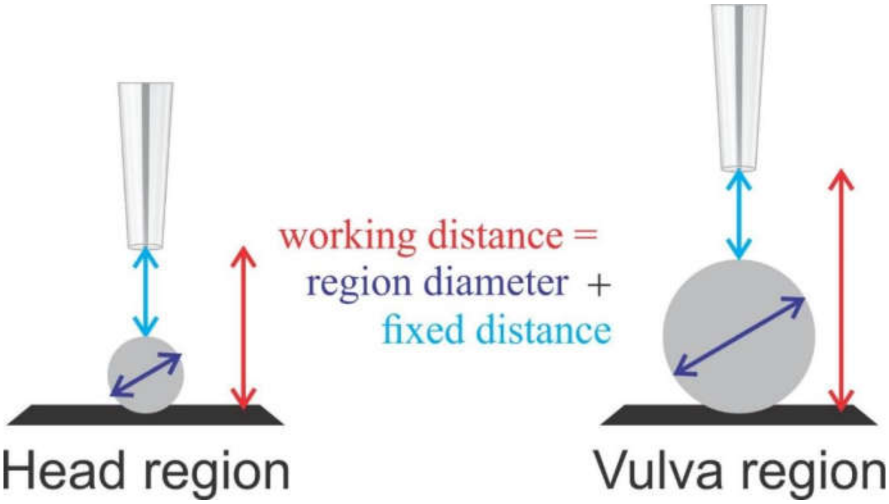

Figure 4.1. Scheme of the microelectrode positioning over the animal. The gray circle is a cross section of the cylindrical animal body. Measurements were performed in a fixed distance of 20 or 40 µm.

4.3. Results and discussion.

4.3.1. Platinised platinum microelectrode.

The platinisation of the platinum microelectrode by formation of black platinum onto the bare platinum surface was a strategy employed for enhancing the reactivity of the surface regarding the oxygen reduction. The oxygen microsensor was first used to record cyclic voltammograms in the M9 solution in the absence and presence of oxygen (Figure 4.2). In solutions containing oxygen, a steady state current at – 0.4 V is clearly noticed.

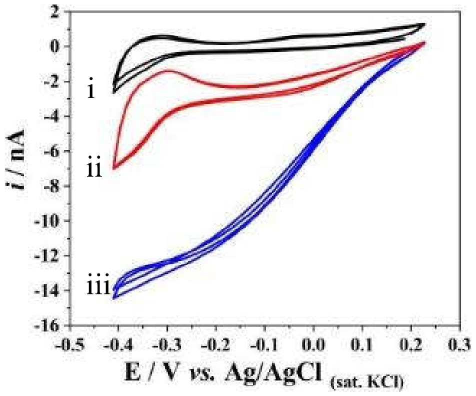

Figure 4.2. Cyclic voltammograms recorded using a platinised platinum microelectrode (r = 0.5 µm, RG = 20) in M9 solution in the absence (argon purged, black curve, i) and presence of oxygen (air saturated: red curve, ii; oxygen saturated: blue curve, iii). Scan rate: 100 mV s $^{-1}$.

4.3.2. SECM map over a single *C. elegans*.

The oxygen consumption in a single *C elegans* was firstly investigated by scanning a platinised platinum microelectrode over an animal at a constant height (100 µm) mode and by recording cyclic voltammograms at each X-Y position. At this working distance, a small effect of the hindered diffusion in the current was noted using data from approach curves recorded in the Petri dish, hence tip current changes are mostly governed by localized oxygen consumption at the animal, which generates an oxygen concentration gradient that reaches the tip.

In order to facilitate the comparison, SECM current maps were normalized by the highest current measured during the scan. Figure 4.3 shows results of two independent experiments performed with 2 animals and a similar behavior was observed: a lower oxygen reduction current was measured in the middle region of the animal, whereas higher ORR current values were obtained in the head. These results suggest a high oxygen consumption activity in the middle region of the *C. elegans*, as the ORR current decreased to around 60 % of the bulk value. This animal region corresponds to the vulva, an aperture linked to the gonad (reproductive system) of the nematode, which is responsible for the eggs development [17]. Thus, the obtained SECM maps indicated the oxygen consumption along the *C. elegans* is heterogenous and the respiratory activity is more pronounced in the reproductive system.

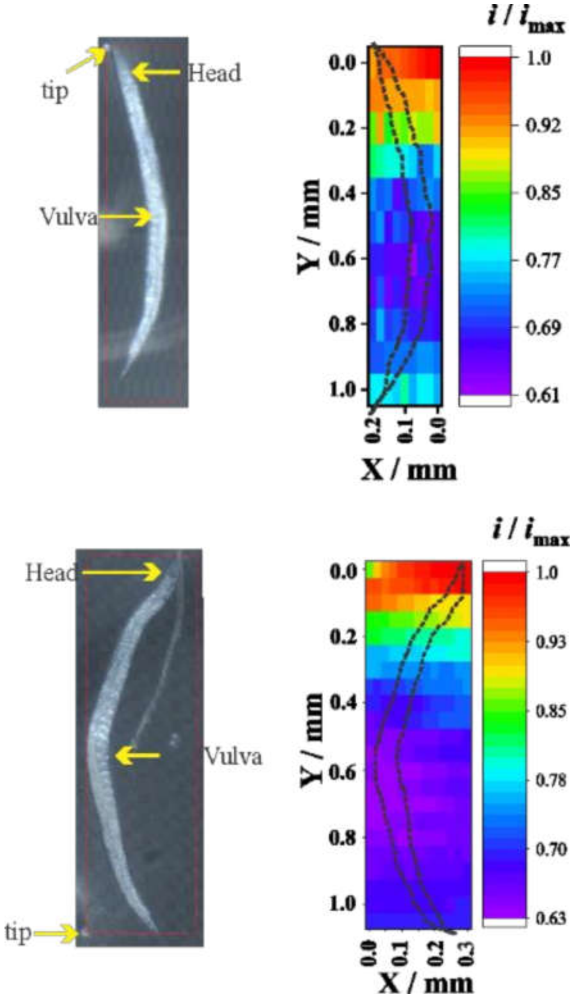

Figure 4.3. Photos and SECM maps of two single wt C elegans animals. Normalized oxygen reduction current maps correspond to values measured at – 0.4 V in the cyclic voltammograms recorded at each X-Y position with a platinised platinum microelectrode (r = 0.5 µm, RG = 20). Current were normalized by the highest current obtained during the scan. Black dot line in the SECM maps correspond to the animal shape. The arrows indicate the head and the vulva regions. Tip-to-Petri dish distance = 100 µm.

The gonad area is located in the centre of the animal, whose diameter is larger, hence the tip-surface distance is lower at this animal region in comparison to the head. Hence, one could assume such lower O_2 concentration values would be related to any possible topographic effect (hindered diffusion or negative feedback) or because of a higher consumption just due to the higher area of the vulva. In order to evaluate the influence of the topographic effect on this system, cyclic voltammograms were recorded locally just above the head and the vulva for 5 animals in the presence and absence of 20 µmol L^{-1} DCCD, an ATP synthase complex inhibitor that blocks mitochondrial activity. It should be mentioned that DCCD is not a specific inhibitor such as oligomycin, but it is used because it can penetrate the animal cuticle. Normalized current values at steady-state condition obtained in the basal and DCCD condition with a platinised platinum microelectrode positioned at 100 µm (tip-to-Petri dish surface distance) are shown in Figure 4.4. The average basal ORR current value in the head region is higher than the one obtained over the vulva, as already shown in the SECM maps (Figure 4.2). In the presence of the inhibitor, current values for both the head and the vulva increase in comparison to the basal condition and the value for the head is similar to the one obtained in the solution bulk. The results of such experiment confirm changes in the respiration activity in the vulva are more pronounced and the contribution of the topography change is not important.

To investigate the role of the gonad system on the respiration of an adult *C. elegans*, similar SECM experiments (same microelectrode, working distance and CV at each X-Y position) were carried out with an animal cultivated in presence of FUdR. The DNA replication is blocked for wild-type *C. Elegans* animals cultivated in the life phase L1 at this condition and, as a consequence, the development of viable eggs in the animal gonad is affected resulting in the FUdR animal. This strategy is commonly used to control the development stage of a large population of animals, ensuring they are all in the same life phase. However, here the strategy was only to reduce any possible contribution of the eggs development in the oxygen consumption. It is worth noting that as we are measuring OCR in single animals by SECM, there is no need for controlling the population life cycle as such information for each animal can be individually assessed by optical microscopy prior to every electrochemical measurement.

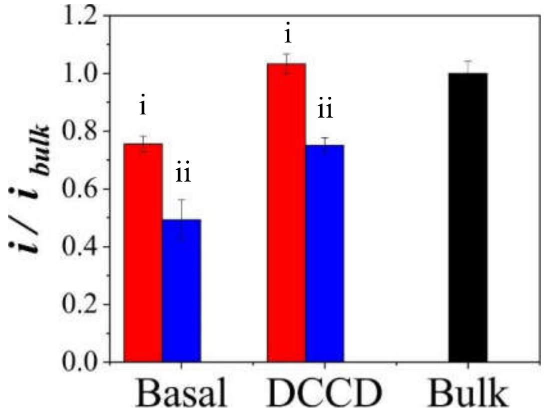

Figure 1.4. Local normalized ORR current values measured at– 0.4 V from cyclic voltammograms recorded over the head (red barrels, i) and vulva (blue barrels, ii) regions of the C. elegans nematode. Experiments were performed in absence (basal) and presence of the inhibitor DCCD and in the bulk solution. CVs were recorded after 90 minutes of the inhibitor addition (n = 5).

The map of oxygen reduction current for an animal treated with FUdR is shown in Figure 4.5 and the result is similar to the map obtained for the basal animal, i.e., the lower oxygen concentration is found in the vulva region. It is important to note the lower normalized current in this experiment (animal treated with FUdR) was around 0.8, whereas a much more significant decrease was observed for the basal condition (around 0.6, Figure 4.2). This result indicates the development of the eggs has a role on the oxygen consumption in the gonad system.

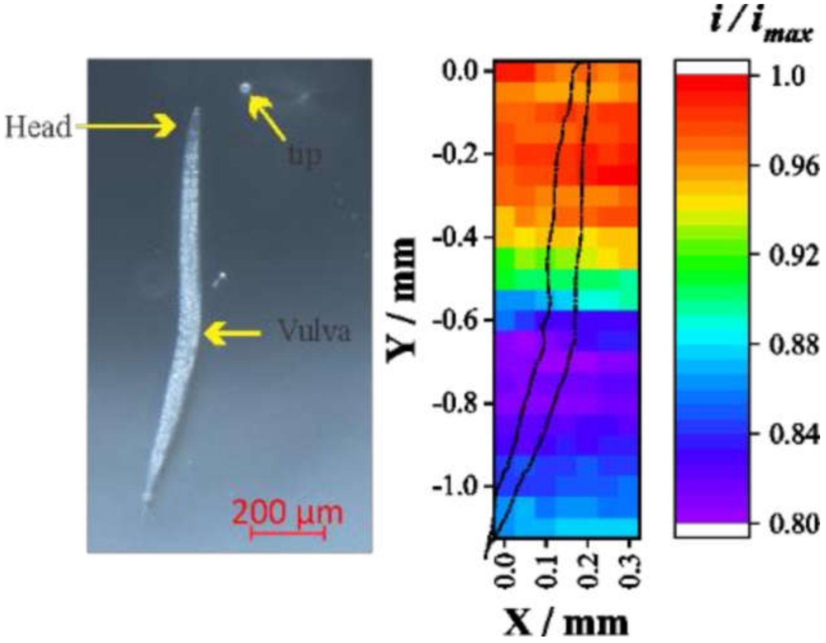

Figure 4.5. Photo and SECM map of a single C elegans animal cultivated in the presence of FUdR. The normalized oxygen reduction current map corresponds to current values measured at – 0.4 V from cyclic voltammograms recorded at each X-Y position with a platinised platinum microelectrode (r = 0.5 µm, RG = 25). The black line in the SECM map corresponds to the animal shape. The arrows indicate the head and the vulva. Tip-to-Petri dish distance = 100 µm.

4.3.3. Determination of the local OCR.

The rate of oxygen consumption rate (OCR) is the main parameter in studies involving the respiration process of cells/tissues or for more complex organisms such as *C. elegans*. OCR values were obtained by recording cyclic voltammograms at a known tip-to-animal surface distance. For such, approach curves were recorded towards the Petri dish surface at a region close to the head and the vulva to establish the working distance. Then, the microelectrode was retracted to a known distance from the animal surface accounting for the local diameter of the cylindrical animal body. Although the experimental data (ORR current) is related to the local OCR, quantitative information cannot be directly extracted due to the well-known entanglement between topography and activity always present in

SECM measurements. In order to access quantitative values for the local OCR, a simulation relying on Finite Element Method (FEM) was performed in a 2D axis-symmetric model and the impact of the inward flux of oxygen from solution towards the animal surface (caused by respiration) on the electrode response was investigated. The proposed model consisted of a sphere with the same diameter as the animal cross-section (head and vulva regions). The electrode was placed at two different fixed distances (20 and 40 μm) from the animal surface, as shown in the scheme in Figure 4.1. The software COMSOL Multiphysics was used to solve for the potential dependent oxygen flux towards the electrode surface at fixed inward oxygen flux values at the investigated nematode region. The flux towards the electrode was simulated assuming a Butler-Volmer model for the 4-electron oxygen reduction at platinum surfaces. The simulation was performed for a range of flux values towards the animal accounting for possible different respiration rates. OCR values were calculated by integrating the flux of oxygen over the investigated region. The experimental currents were obtained using a platinised platinum microelectrode positioned at tip-to-*C. elegans* surface separations of 40 and 20 μm. The only parameter used to fit the model to the experimental data was the electroactive area of the electrode, which can be greatly increased by the platinisation procedure. Such information was obtained by the cyclic voltammograms towards ORR recorded in the bulk of the solution.

The oxygen consumption rate (OCR) values presented in Figure 4.6 were obtained by fitting the experimental currents to the proposed model. OCR values for the head and the vulva are significantly different in the control/basal experiment (no FUdR), confirming again the reliabilility of the information obtained in the SECM map shown in Figure 4.3 (current changes are due to heterogeneous rate of the oxygen consumption and not to the local high area surface). The average OCR value in the head region was 4 ± 1 pmol min^{-}

^{1} in basal conditions and 2.9 ± 0.6 pmol min^{-1} for animals cultivated in the presence of FUdR. According to ANOVA statistic analysis, such values are not significantly different, suggesting the presence of FUdR has no effect in the oxygen consumption in the head region. On the other hand, the influence of FUdR is much more important in the vulva region: OCR in basal condition was 11.1 ± 0.7 pmol min^{-1} and in the presence of the inhibitor the value decreased to 6 ± 1 pmol min^{-1} (ANOVA $p < 0.05$). Such results indicate the development of the eggs has a significant contribution in the respiration activity of the animal and the reduction of the local OCR in the presence of the inhibitor reinforces such conclusion.

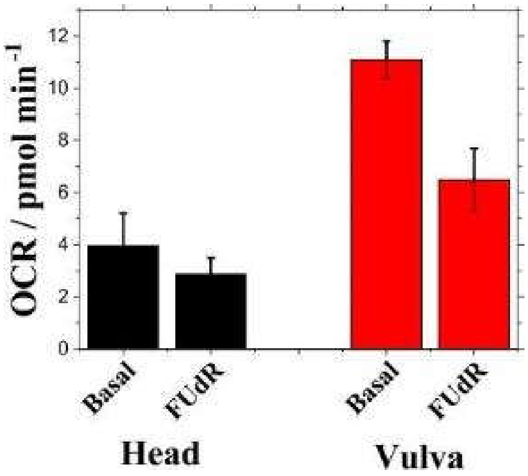

Figure 4.6 Simulated OCRs values for two animal regions: head (black barrels) and vulva (red barrels). OCR values were calculated for C. elegans in basal conditions at the vulva (n = 10) and head (n = 12) and C. elegans cultivated in the presence of FUdR (n= 20). α= 0.05. One-way ANOVA is significantly different for p < 0.05. Dunn's multiple comparison tests: for head basal vs. head FUdR, p = 0.097; for vulva basal vs. vulva FUdR, p = 0.00002; for head basal vs vulva FUdR, p = 0.012.

Further experiments to confirm the role of the whole gonad in the oxygen consumption of the animal will be performed by using a mutant animal with no gonad, hence one will be able to discriminate the contribution of each part of the reproductive system in the oxygen consumption.

4.4. Conclusions.

The usefulness of SECM as a tool for investigating the heterogeneous oxygen consumption in a single adult *C. elegans* was demonstrated here. By using an inhibitor of the mitochondria activity one could confirm the SECM measurements suffered no important influence from topography of the animals and the oxygen consumption is more effective in the gonad region because of the metabolism involved in the reproductive process. We have also reported for the first time that the respiration activity is more effective in the vulva than in the head, hence the contribution of the gonad activity in studies on oxygen consumption monitored in large populations of the animal is more important. To evaluate the contribution of the gonad in the oxygen consumption of a single animal, SECM experiments were performed with *C. elegans* animals cultivated in the presence of an inhibitor of the development of the eggs (FUdR). The results indicated the influence of such compound was only significant in the vulva region, and that OCR values were still higher than those obtained in the head. This induces us to conclude the gonad activity was reduced for animals treated with FUdR, even though the respiration acitivity at this region was more significant in comparison to other regions of the animal. Future experiments will be devised to study the *C. elegans* animals containing no gonad. However, the presented results can already show the respiration activity in a single adult animal is more effective in the reproductive system.

4.5. References.

1. Kahn, J. S. *Anal. Biochem.* **1964**, 9, 389–391.

2. Gnaiger, E.; Steinlechner-Maran, R.; Méndez, G.; Eberl, T.; Margreiter, R. *J. Bioenerg. Biomembr.* **1995**, 27, 583–596.

3. Simonnet, H.; Vigneron, A.; Pouysségur, J. *Methods Enzymol.* **2014**, 542, 151–161.

4. Wu, M.; Neilson, A.; Swift, A. L.; Moran, R.; Tamagnine, J.; Parslow, D.;

Armistead, S.; Lemire, K.; Orrell, J.; Teich, J.; et al. *AJP Cell Physiol*. **2006**, 292, C125–C136.

5. Zharikov, S.; Shiva, S. Platelet Mitochondrial Function: From Regulation of Thrombosis to Biomarker of Disease. *Biochem. Soc. Trans.* **2013**, 41, 118–123.

6. Kramer, P. A.; Ravi, S.; Chacko, B.; Johnson, M. S.; Darley-Usmar, V. M. A. *Redox Biol*. **2014**, 2, 206–210.

7. Perry, C. G.; Kane, D. A.; Lanza, I. R.; Neufer, P. D. *Diabetes* **2013**, 62, 1041–1053.

8. Horan, M. P.; Pichaud, N.; Ballard, J. W. O. *Journals of Gerontology - Series A Biological Sciences and Medical Sciences*. **2012**, 67, 1022–1035.

9. van der Windt, G. J. W.; Chang, C. H.; Pearce, E. L. *Curr. Protoc. Immunol*. **2016**, 113, 1-3.

10. Luyten, W.; Antal, P.; Braeckman, B. P.; Bundy, J.; Cirulli, F.; Fang-Yen, C.; Fuellen, G.; Leroi, A.; Liu, Q.; Martorell, P.; et al. *Biogerontology* **2016**, 17, 771-782.

11. Dancy, B. M. *Front. Biosci*. **2015**, 20, 198-228.

12. Hansen, M.; Flatt, T.; Aguilaniu, H. *Cell Metabolism*. **2013**, 17, 10-19.

13. Eckhard, K.; Chen, X.; Turcu, F.; Schuhmann, W. *Phys. Chem. Chem. Phys*. **2006**, 8, 5359-5365.

14. Santos, C. S.; Kowaltowski, A. J.; Bertotti, M. *Sci. Rep*. **2017**, 7, 11428.

15. Nebel, M.; Grützke, S.; Diab, N.; Schulte, A.; Schuhmann, W. *Faraday Discuss*. **2013**, 164, 19-32.

16. Nebel, M.; Grützke, S.; Diab, N.; Schulte, A.; Schuhmann, W. *Angew. Chemie - Int. Ed*. **2013**, 52, 6335–6338.

17. Kimble, J. E.; White, J. G. *Dev. Biol*. **1981**, 81, 208-219.

Chapter 5.

Scanning Bipolar Electrochemical Microscopy

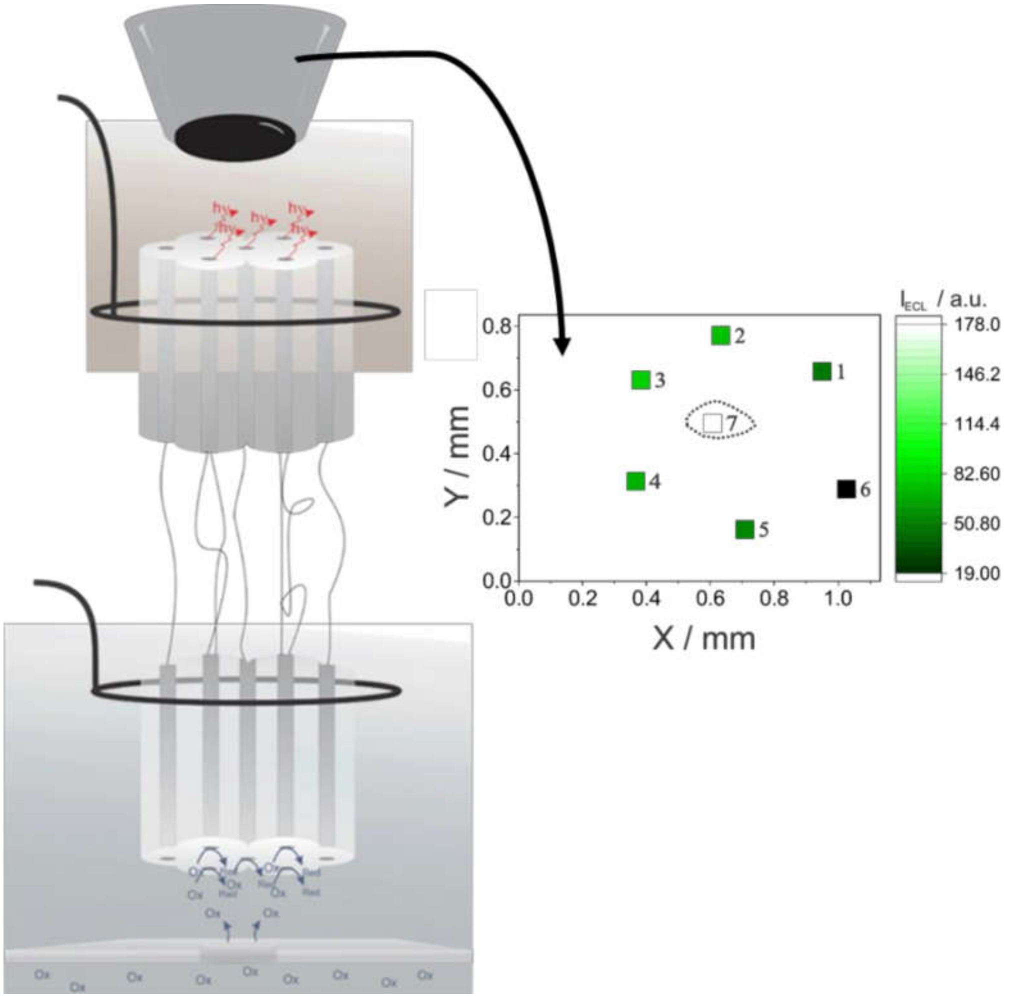

This chapter shows the results of the one-year experience of C. S. S. as visiting student under the supervision of Prof. Wolfgang Schuhmann in the Elektroanalytik und Sensorik's laboratory at the Ruhr-Universität Bochum (Germany). C. S. S. followed and contributed to the development of a novel electroanalytical technique named "scanning bipolar electrochemical microscopy" with Vera Eßmann (at that time, a PhD student). Herein, the challenges associated with the development of a high spatial and temporal resolution technique aimed to be used as a multi respirometer are reported. The SBECM was introduced through description of the experimental setup and demonstration of its working principle using a single bipolar electrode. Moreover, the release of a compound from a model system was imaged with an array of bipolar electrodes. Then, molecules released at two different sites were monitored using the bipolar array. The resulting data were published as follows:

Scanning Bipolar Electrochemical Microscopy. Vera Eßmann, **Carla S. Santos**, Tsvetan Tarnev, Mauro Bertotti, Wolfgang Schuhmann. *Analytical Chemistry,* 2018, 90, 10, 6267-6274.

The permission of use of the text was requested to the publisher American Chemical Society (ACS) and the copy of the right is attached in the Annex. Reprinted (adapted) with permission from Analytical Chemistry, 2018, 90, 10, 6267-6274 Copyright (2018) American Chemical Society.

The setup and conceptual discussions were done by Vera Eßmann and Wolfgang Schuhmann. All measurements were carried out by C. S. S. and V. E. The text was written by V. E. in discussion with C. S. S. and W. S., T. T. contributed to the software development and support. The figures and graphs were done by C. S. S. and V. E. All the authors revised the text.

5.1. Abstract.

Electrochemical techniques offer high temporal resolution for studying the dynamics of electroactive species at samples of interest. To monitor fastest concentration changes, a micro or nanoelectrode is accurately positioned in the vicinity of the sample surface. Using a microelectrode array, it is even possible to investigate several sites - simultaneously and obtain an instantaneous image of local dynamics. However, the spatial resolution is limited by the minimal electrode size required in order to contact the electrodes. To provide a remedy, we introduce the concept of scanning bipolar electrochemical microscopy and the corresponding experimental system. This technique allows precise positioning of a wireless scanning bipolar electrode to convert spatially heterogeneous concentrations of the analyte of interest into an electrochemiluminescence map of the sample reactivity. After elucidating the working principle by recording bipolar line and array scans, a multi bipolar electrode array is positioned at the site of interest to record an electrochemical image of the localized release of analyte molecules.

5.2. Introduction.

Active biological cells dynamically modulate the local concentration of a variety of different molecules in their surroundings as, for instance, due to the consumption of O_2, the release and uptake of neurotransmitters for intercellular communication, or the acidification of the extracellular environment. The transfer of such species can be correlated with the cell’s metabolism and biophysical properties and can thus help to understand a disease, the effect of metabolically active pharmaceuticals or other external influences. In this regard, the release or consumption of electrochemically active analyte species have been assessed with micro- or nanoelectrodes accurately positioned close to a single adherently growing cell [1–4]. The current response due to electrochemical conversion of analyte molecules at the electrode surface allows to quantify temporarily changing analyte concentrations. Here, the response time of electrochemical conversion is a clear asset. However, for investigations at the sub-cellular scale, the probability that a single electrode tip is accidentally positioned close to the site of interest is rather low. In addition, scanning the probe to resolve analyte release from the entire cell surface is far too time-consuming as these processes occur on a millisecond timescale. Instead, electrode arrays working like a camera have been employed.[5] Each electrode with sub-cellular dimensions monitors the release at a specific site leading to an instantaneous picture of several sites with the spatial resolution depending on the size and distance of the electrodes. Production of multi-electrode arrays (MEAs) is accomplished by *i.e.* screen-printing, photolithography, and the assembly of electrode materials[6]. The latter two were reported for the fabrication of MEAs of up to 36 electrodes[7–10]. In most reports, exocytosis of catecholamines has been studied by either positioning the MEA above a PC12 cell or by cultivating it on top of the array. While the geometry and success rate do limit the physical assembly of MEAs, more reproducible arrays may be produced with photolithography. However, it is equally difficult to connect many micro- or even nanoscopic electrodes to a (multi)potentiostat.

In this respect, bipolar electrochemistry (BPE) offers a clear advantage. The application of an electric field to an electrolyte solution via two feeder electrodes generates anodic and cathodic interfacial potential differences at the opposite extremities of a conductive object located in between. Consequently, oxidation and reduction reactions occur at the electrically unconnected, bipolar electrode (BE)[11]. In the same way it is possible to control electrochemical reactions at multiple non-wired BEs in parallel[12,13]. The asymmetry intrinsic to BPE has previously been exploited for site-selective electrodeposition[10,13–15], electrochemically generated motion[16,17], mimicking neuronal behavior[18] or material characterisation[19,20] among others. In order to quantify the reactions without wiring the BE, optical reporter reactions can be employed as oxidation or reduction reaction [21,22]. Since anodic and cathodic currents at the BE have to be equal ($i_a = i_c$), the optical signal serves to derive the bipolar current i_{BE}. This principle has already been applied to detect biologically relevant analytes such as H_2O_2, glucose or dopamine[23] from the change in the optical signal at the reporting pole[23,24]. The first approach using BPE for the spatial resolution of heterogeneous analyte concentrations employed an array of thousands of carbon fiber BEs (Ø = 6 µm). Heterogenic catalytic activity[20] or the diffusion profile of $[Fe(CN)_6]^{3-}$ at an UME[25] were imaged via the accordingly changing intensity of reductive fluorescence at the other pole. For this, a so-called closed bipolar system was used, in which the two BE poles are physically separated in two different compartments, thereby enabling the use of two different solutions at the sensing and reporting poles[23,26]. However, this system is not flexible to allow precise positioning of the array and can therefore not be used to study the spatially heterogeneous electrochemical activity at surfaces. Moreover, the use of fluorescence as reporter reaction requiring an excitation light source and hence background subtraction overcomplicates the experimental setup.

In this work, we address the challenges associated with the highly spatial and temporal resolution of multiple release events step by step. First, a novel electroanalytical method named “scanning bipolar electrochemical microscopy” (SBECM) is introduced through description of the experimental setup and demonstration of its working principle using a single BE. In the next step, the release of analyte species from a model system is imaged with a BE bundle. Finally, molecules released at two sites are monitored using the BE array.

5.3. Experimental Section.

5.3.1. Chemicals.

All chemicals were used as received. $[Ru(NH_3)_6]Cl_3$ (Sigma-Aldrich, Germany), tripropylamine (TPrA, *Caution! TPrA is highly flammable, toxic, and irritant and must be handled with extreme care*, Sigma-Aldrich, D), $[Ru(bpy)_3]Cl_2$ (Sigma-Aldrich, Germany), $[Fc(MeOH)_2]$ (Acros Organics, Belgium), KH_2PO_4 (VWR BDH Prolabo, Belgium), K_2HPO_4 (Roth, D). All solutions were prepared with ultrapure water (SG water, Germany).

5.3.2. Set-up for scanning bipolar electrochemical microscopy.

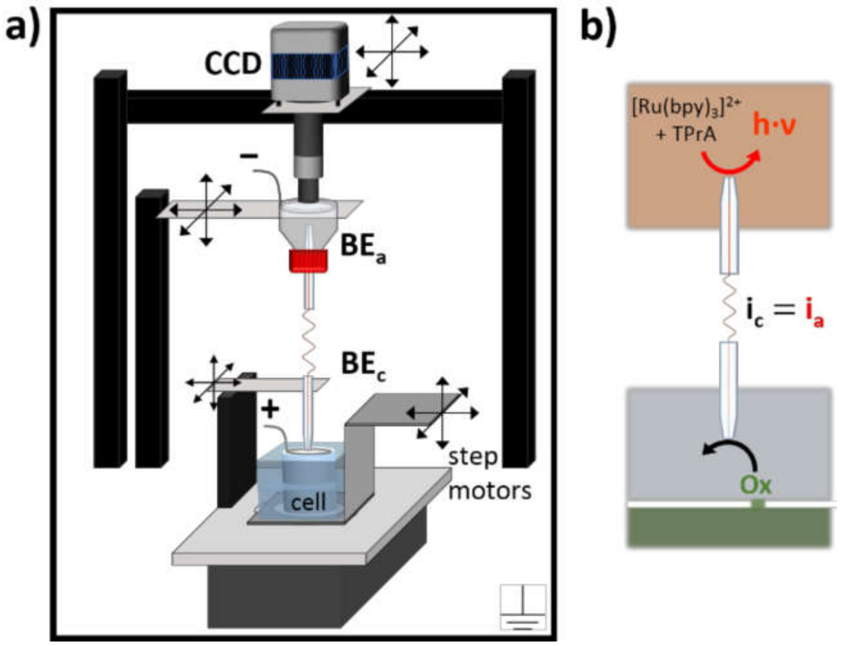

Scheme 5.1. a) Schematic of the SBECM setup located inside a light-tight Faraday cage. The voltage between the feeder electrodes is applied with a potentiostat. Anodic and cathodic BE poles can be positioned manually, while the cathodic BE compartment is placed on a stage that is moved in x-, y-, and z-directions by step motors. ECL emitted at BE_a *is recorded with a highly sensitive EMCCD camera equipped with an immersible microscope objective via a tube lens and two adapters. b) Fundamental reactions for SBECM: The locally available analyte molecules are reduced at the* BE_c *and converted into a proportional ECL signal at* BE_a*.*

The measuring cell consists of two compartments (Scheme 5.1). The glass cell containing the reporting BE pole, in this case the BE_a, is opened to the top towards an EMCCD camera (Photometrics, USA), controlled via MicroManager 1.4 (Open Imaging, USA) which is fixed in a way that it records images of objects placed beneath it. The disc-shaped Pt-microelectrode or microelectrode bundle working as ECL-emitting pole(s) point upwards and are inserted into the cell through a rubber platelet in a screw cap. A ring-shaped Pt-wire (Ø = 1 mm) serving as cathodic feeder electrode is located along the inner wall of the vessel. This assembly can be manually positioned in all three directions to bring the electrode surface into the focus of the immersible objective (10× magnification, UMPlan FLN, Olympus, Germany) that is connected to the EMCCD camera via a spacer, a tube lens (no magnification, Olympus, Germany), and an adapter (Olympus, Germany). Four screw holes are exploited for holding the camera on the four rubber spacers of a specifically developed holder to damp vibrations from the fan. Since the holder and the profile, to which the camera is attached to, are flexible, the camera can be coarse positioned in all three directions.

The BE_a is connected to another microelectrode, which is employed as sensing pole, BE_c, and fixed in an electrode holder that can be manually positioned in all three directions as well. A PMMA cell with a cylindrical volume is used as cathodic BE compartment. A Pt-wire ring (Ø = 1 mm) located around the opening serves as anodic feeder electrode. For the experimental design, the cell volume is separated from another identical vessel by a PTFE membrane (20 nm pore width, 75 µm thick, 50 % porosity) featuring one or two holes. The two vessels are placed onto a holder, which can be moved in x-, y-, and z-directions by step motors (SPI, Germany). They are connected to the computer via position control cards (PS30, Owis, Germany). V_{app} is applied with a potentiostat (Jaissle, IPS, Germany), which is controlled via a specifically programmed

Visual Basic software. The entire setup is located in a light-tight Faraday cage on a vibration-cushioned table (CVI Melles Griot, Netherlands). All cables are inserted through a cable entry plate with rubber grommets.

5.3.3. Evaluation of the system behavior.

Three-electrode LSVs were recorded in the respective bipolar compartment using the feeder electrode as counter electrode (CE) and a Ag/AgCl (3 M KCl) electrode as reference. All potentials are referred to this reference electrode if not otherwise stated. For the cathodic LSV, the potential of the Pt-microelectrode (Ø = 50 μm) was scanned from 0.1 V to –0.8 V with a scan rate of 10 mV s^{-1} in 0.1 M KCl in the absence and presence of 1 mM $[Ru(NH_3)_6]Cl_3$. The potential of the Pt-microelectrode later used as BE_a (Ø = 25 μm) was increased from 0 V to 2.0 V with a scan rate of 10 mV s^{-1} in 0.1 M phosphate buffer solution (PBS) (pH 7.4) with 1 mM $[Ru(bpy)_3]Cl_2$ and 50 mM TPrA. Bipolar LSVs were recorded by sweeping the applied feeder voltage V_{app} from 0 V to 3 V with a scan rate of 10 mVs^{-1} in presence and absence of 1 mM $[Ru(NH_3)_6]Cl_3$ in the BE_c compartment.

Interfacial potential differences were assessed by connecting a multimeter (CEM instruments, Germany) via a high input impedance module (IPS, Germany) to the BE and a Ag/AgCl (3 M KCl) electrode. The latter was positioned manually close to the BE pole of interest.

5.3.4. Bipolar line and array scans.

Prior to a bipolar experiment, the microelectrode used as BE_a is brought into the focus of the optical detection unit before filling the compartment with solution.

For detection of local $[Ru(NH_3)_6]Cl_3$ release, one hole (approx. 145 μm×245 μm) was made into the PTFE membrane. The lower PMMA cell was filled with 5 mM

$[Ru(NH_3)_6]Cl_3$ in 0.1 M KCl before tightly fixing the top cell on it. For adjusting a $d_{tip\text{-}membrane}$ of 50 µm by approach curves, the microelectrode, later working as SBECM tip, was polarized to 0.4 V in 0.1 M KCl with 1 mM $[Fc(MeOH)_2]$ using the ring-shaped Pt-wire as CE. Compensation of the surface tilt was accomplished by approaching the tip to the membrane at three different x,y-positions and calculating the resulting plane.

A 2 mm long SECM line scan in x-direction at –0.4 V with increments of 50 µm, a delay time of 100 ms, and a speed of 50 µm s^{-1}, was recorded in this three-electrode configuration. Afterwards, the RE was removed and the microelectrodes for the anodic and cathodic BE poles were connected. The anodic BE compartment was filled with 1 mM $[Ru(bpy)_3]Cl_2$ and 50 mM TPrA in 0.1 M PBS (pH 7.4), before refocusing the BE_a. While V_{app} = 1.6 V was applied between the feeder electrodes, the line scan was repeated in the bipolar configuration with the same parameters. To record single CCD images in parallel to single i_{sys} values at each point of the line scan, the exposition of the camera is triggered by the measuring software (EM gain = 250). Finally, the $[Ru(NH_3)_6]Cl_3$ diffusion profile was mapped by the SBECM tip in an array scan, meaning I_{ECL} and i_{sys} at V_{app} = 1.6 V were recorded as a function of the x- and y-position. An area of 2×2 mm was investigated with increments of 50 µm and at $d_{tip\text{-}membrane}$ = 50 µm.

5.3.5. A bipolar multi-electrode array as an electrochemical camera.

Sevenfold Pt-microelectrode arrays are fabricated from sevenfold borosilicate glass capillaries (Hilgenberg, Germany). After pulling them to a tip, a piece of Pt-wire (Ø = 10 µm) is inserted into each capillary and melted with the glass. Each Pt-wire is contacted with a Cu-wire using silver glue (Polytech, Germany) and cured at 150°C for 15 min. To obtain a BE array, the Cu-wires of two microelectrode arrays are connected. The array is approached to the membrane using the SECM feedback mode by oxidation of

[Fc(MeOH)$_2$] at the central BE 7 including tilt correction. The cathodic part of the BE array was positioned next to the hole (approx. 118 µm×140 µm) at $d_{\text{tip-membrane}} = 50$ µm. It has to be ensured that all BE$_a$s are in focus of the optical detection unit. The 1.5 mm long SBECM line scans were recorded at 1.6 V with increments of 50 µm, a speed of 100 µm s^{-1} and an EM gain of 250. To map the analyte diffusion through one or two (approx. 150 µm×190 µm and 120 µm×110 µm) holes with the sevenfold BE array, array scans were recorded over an area of 0.9×0.8 mm or 1.5×2.15 mm, respectively.

5.4. Results and Discussion.

5.4.1. Introduction to scanning bipolar electrochemical microscopy.

If instantaneous information on localized concentration changes of electroactive molecules at multiple sites is to be obtained, the spatial resolution achievable with MEAs has to be increased significantly. To overcome the necessity of a minimal electrode dimension required for connecting each electrode to the (multi)potentiostat, which clearly limits the spatial resolution and the number of electrodes in the MEA, BPE is the method of choice as no electrical contact is required. However, for signal read-out the current flowing through the BE, i_{BE}, has to be converted into an optical signal. The use of a closed BPE system avoids interferences between the anodic and cathodic reactions and leads to a higher sensitivity due to the elimination of ionic current between the feeder electrodes [23]. Moreover, a lower applied feeder voltage (V_{app}) is required to generate the inverse interfacial potential differences at the two poles, at the cathodic pole (BE$_c$) $dE_{BE_c\text{-Sol}}$ and at the anodic pole (BE$_a$) $dE_{BE_a\text{-Sol}}$. Although a BE is not connected with a cable, the potentials driving oxidation and reduction can be adjusted not only via V_{app}, but also via the size ratio of the electrochemically accessible surface area of BE$_a$ and BE$_c$[27,28]. The conceptual device designed to meet these prerequisites is shown in Scheme 5.1a.

To demonstrate the general feasibility of mapping spatially heterogeneous analyte concentrations by converting the molecules in dependency of the exact BE position into an accordingly changing optical signal, a single BE is employed in the first measurements. Because the BE_c, serving as detecting pole, can be positioned in x-, y-, and z-directions and is thus able to scan above the surface in a defined distance, the technique is denoted as scanning bipolar electrochemical microscopy (SBECM). For this, the BE_c, *i.e.* a disc-shaped Pt-microelectrode, is held vertically by a conventional SECM tip holder. The cylindrical PMMA measuring cell used as cathodic BE compartment contains the respective electrolyte solution as well as a Pt-wire ring at the outer rim as anodic feeder electrode. The volume is separated from another identical vessel by a PTFE membrane. It can be provided with one or several holes to model the release of molecules. This assembly is fixed onto a stage movable in x-, y-, and z-direction by step motors allowing the positioning of the detecting BE pole with respect to the sample of interest.

The BE_c is connected to another Pt-microelectrode employed as anodic pole of the BE. Here, oxidative $[Ru(bpy)_3Cl_2]$-based electrochemiluminescence (ECL) is utilized to derive information on i_{BE} as a function of the magnitude of reduction reactions occurring at BE_c (Scheme 5.1b). In accordance with the concept of closed BPE, BE_a is located in another isolated cell. This anodic BE compartment contains a ring-shaped Pt-wire as cathodic feeder electrode and the corresponding electrolyte. Since a single BE is employed in this configuration, the system current flowing through the feeder electrodes, i_{sys}, equals i_{BE} and consequently serves to verify the obtained ECL signal. BE_a is oriented upside down to be directly interfaced with an immersible objective (10× magnification, NA = 0.3) connected to a highly-sensitive EMCCD (electron-multiplying charge-coupled device) camera. A tube lens in between, focusing the light onto the sensor, is connected to the camera via an adapter and to the objective via a precisely manufactured spacer element. The spacer ensures the compulsory minimal distance of 50 mm between the two components. The possibility to manually move the holder of the BE_a compartment in all three directions allows to position the microelectrode surface in the focal plane of the optical detection unit. Also, the camera can be roughly positioned in x-, y-, and z-direction. The entire experimental setup is located on a vibration-cushioned table inside a light-tight Faraday cage.

A SBECM setup requires four main components: the BE compartments, a potentiostat, an optical detection unit and a positioning system. Simultaneous control and read out is achieved with a computer. The potentiostat is controlled via a specifically developed Visual Basic-based software, while data collection from the camera is accomplished with the open source software “MicroManager 1.4”. “ImageJ” is used for data treatment. Triggering of camera exposition is enabled via an I/O connector located at the camera’s power supply. A trigger input of ≥ 3.15 V for high and ≤ 0.9 V for low, is realized by a DA card upon controlled by the software.

5.4.2. Evaluation of the system behavior.

For evaluation of the SBECM set-up, the diffusion of $[Ru(NH_3)_6]Cl_3$ through a hole in the PTFE membrane at the bottom of the cathodic BE compartment was imaged using a single BE. In this way, the general functionality of the system was elucidated and all relevant parameters for the performance of the system were evaluated. First of all, linear sweep voltammograms (LSVs) in a conventional three-electrode setup were recorded to assess the possible electrode processes at the later BE_c and BE_a. For cathodic reactions, the electrode potential was scanned from 0.1 V to –0.8 V in 0.1 M KCl solution in absence and presence of 1 mM $[Ru(NH_3)_6]Cl_3$. The additional reduction of $[Ru(NH_3)_6]Cl_3$ starting approximately at –0.1 V causes a significant increase of the cathodic current compared to the current originating from the oxygen reduction reaction only (data not shown). When the potential of the Pt-microelectrode was scanned between 0 V and 2.0 V in 0.1 M PBS (pH 7.4) with 1 mM $[Ru(bpy)_3]Cl_2$ and 50 mM TPrA, the current begins to increase significantly from 0.98 V on when $[Ru(bpy)_3]Cl_2$ is oxidized. Surpassing the threshold current at 1.02 V, ECL is observed showing a maximum at 1.15 V. At more positive potentials, water oxidation acidifies the solution and produces e.g. O_2 as ECL quencher, thus impairing the ECL reaction. The potentials of these reactions were relevant for the next step of adjusting $dE_{BE_a\text{-Sol}}$ and $dE_{BE_c\text{-Sol}}$. For this, the size ratio of the BE poles (A_{BE_a}/A_{BE_c}) and V_{app} were altered while the resulting interfacial potential differences were assessed[29,30] with a reference electrode (RE) connected via a high input resistance potentiometer to the BE[29,30]. At V_{app} of 1.6 V and a size ratio of A_{BE_a}/A_{BE_c} of 0.5, $dE_{BE_c\text{-Sol}}$ was measured to be about –0.4 V in the absence of analyte at the sensing pole. This value ensures a sufficiently high reduction rate of $[Ru(NH_3)_6]Cl_3$, while avoiding significant water reduction. A $dE_{BE_a\text{-Sol}}$ value of approximately 1.27 V results in a small ECL signal in absence of $[Ru(NH_3)_6]Cl_3$ in the cathodic compartment, which is anticipated to allow immediate detection of smallest changes in the ECL reaction upon small changes in the analyte concentration. A size ratio of < 1 causes $dE_{BE\text{-Sol}}$ values to shift to more positive values compared to equally large poles, because the potential of the BE E_{BE} moves to more positive values enabling a higher $dE_{BE_a\text{-Sol}}$ at the smaller reporting pole to balance the current at the larger sensing pole[27]. Moreover, it has been previously demonstrated that a smaller BE_a results in an improved signal-to-noise ratio (SNR)[28]. In a final preliminary experiment, V_{app} was scanned from 0 V to 3 V while measuring i_{sys}, I_{ECL}, and the $dE_{BE\text{-Sol}}$. With the reducible analyte present in the BE_c compartment, i_{sys} and hence I_{ECL} begin to increase at a lower V_{app} value (1.01 V and 1.05 V, respectively) than in absence of the analyte (1.17 V and 1.22 V, respectively). This can be explained with the lower $dE_{BE_c\text{-}Sol}$ required to provide the threshold current for ECL emission.

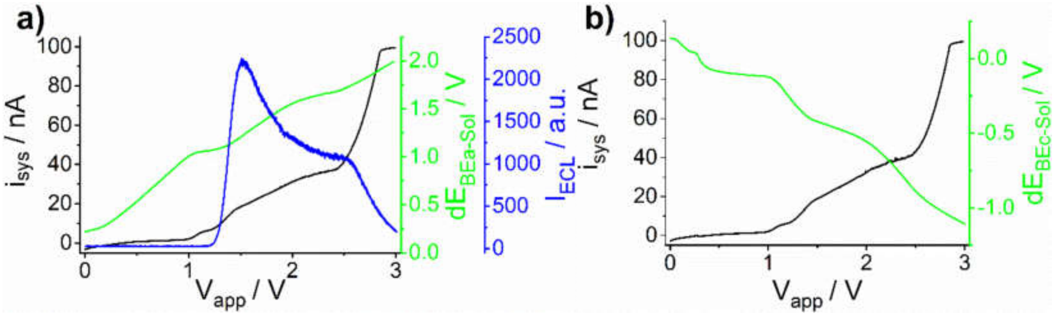

Figure 5.1. Bipolar LSVs showing a) i_{sys}*,* I_{ECL}*, and* $dE_{BE_a\text{-}Sol}$ *versus* V_{app} *and b)* i_{sys} *and* $dE_{BE_c\text{-}Sol}$ *versus* V_{app}*. For all measurements, a solution of 1 mM [Fc(MeOH)*$_2$*] and 1 mM [Ru(NH*$_3$*)*$_6$*]Cl*$_3$ *in 0.1 M KCl was used in the cathodic cell (BE*$_c$*: Ø 50 µm Pt-microelectrode), while a solution of 1 mM [Ru(bpy)*$_3$*]*$^{2+}$ *and 50 mM TPrA in 0.1 M PBS (pH 7.4) was used in the anodic compartment (BE*$_a$*: Ø 25 µm Pt-microelectrode).*

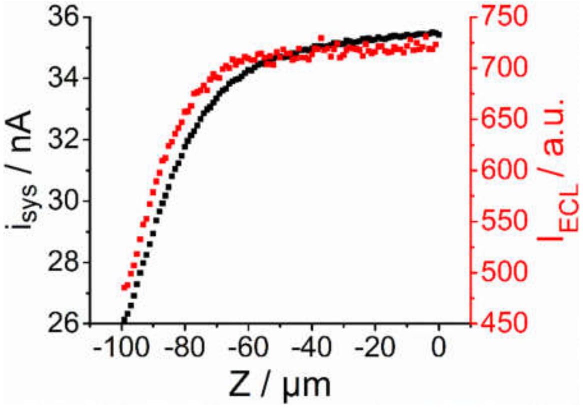

Figure 5.2. Bipolar approach curve using 1 mM [Ru(NH$_3$*)*$_6$*]Cl*$_3$ *in 0.1 M KCl solution in the cathodic compartment and a solution of 1 mM [Ru(bpy)*$_3$*]*$^{2+}$ *and 50 mM TPrA in 0.1 M PBS (pH 7.4) in the anodic compartment. In the bipolar configuration, BE*$_c$ *was approached to non-conducting bottom of the cathodic chamber while* i_{sys} *and* I_{ECL} *were recorded as indicators of the negative feedback upon approach.* V_{app} *= 1.6 V, EM gain = 250.*

Consequently, a higher $dE_{BE_a\text{-}Sol}$ is adjusted so that the threshold current is already reached at lower V_{app}. Both bipolar LSVs recorded in presence of [Ru(NH$_3$)$_6$]Cl$_3$ at BE$_c$ are exemplarily shown in the Figure 5.1, $dE_{BE_a\text{-}Sol}$ and I_{ECL} monitored in one, while

$dE_{BE_c\text{-}Sol}$ was recorded in the other LSV. For the following experiments, the tip-to-sample distance $d_{tip\text{-}membrane}$ was adjusted to 50 µm including correction of a possible surface tilt. This was accomplished by means of SECM z-approach curves in the negative feedback mode using $[Fc(MeOH)_2]$ as free-diffusing redox mediator which is oxidized at the Pt-microelectrode later used as BE_c. In principle, it is also possible to record approach curves in the bipolar configuration based on the ECL signal as a function of the negative feedback at the BE_c (Figure 5.2).

5.4.3. Bipolar line and array scans.

To compare SBECM results with conventional SECM measurements and thereby validate the general functionality of our device, the diffusion of $[Ru(NH_3)_6]Cl_3$ through a hole in the PTFE membrane was first detected in a SECM line scan. The Pt-microelectrode (Ø = 50 µm), which is subsequently used as BE_c, was polarized to –0.4 V (Figure 5.3a, black). The cathodic current clearly increases due to the reduction of $[Ru(NH_3)_6]Cl_3$ as the electrode passes the hole (approx. 145 µm×245 µm).

For repeating the line scan in the bipolar configuration with the same settings, the SECM tip was used as BE_c and connected to the BE_a in the anodic compartment. A V_{app} of 1.6 V was applied to the feeder electrodes. Indeed, i_{sys} and I_{ECL} show a behavior nearly identical to the SECM tip current (Figure 5.3a, red and blue). The results clearly illustrate the dependence of i_{BE} and hence I_{ECL} on the locally changing analyte concentration at the detecting pole, as desired. This suggests that the ECL response contains the same information as the SECM tip current i_{SECM} and is therefore an equally reliable measure.

To elucidate the performance of the SBECM system, $dE_{BE\text{-}Sol}$ was monitored during the SBECM line scan. As illustrated earlier[31], driving forces are continuously adjusted as a function of the reaction rate at both BE poles. Hence, $dE_{BE\text{-}Sol}$ values are modulated in accordance with the concentration of reducible analyte species at the SBECM tip. In fact, $dE_{BE_c\text{-}Sol}$ and $dE_{BE_a\text{-}Sol}$ are significantly shifted to more positive potentials with the extent being proportional to the analyte concentration. In one line scan, for instance, $dE_{BE_a\text{-}Sol}$ increased from 1.27 V to 1.53 V at the maximal i_{sys}, whereas $dE_{BE_c\text{-}Sol}$ has changed from –0.4 V to –0.16 V (data not shown). This means that the higher interfacial potential difference driving the cathodic electrode processes is no longer required, which in turn leads to a higher $dE_{BE_a\text{-}Sol}$ to enable a higher i_{BE}. Hence, E_{BE} presumably becomes more positive to re-adjust $dE_{BE\text{-}Sol}$ for maximized i_{BE}.

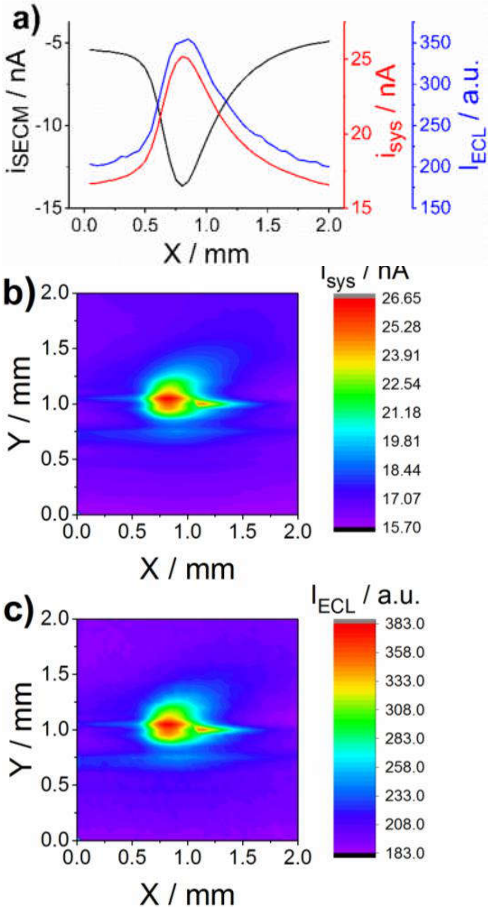

Figure 5.3. a) Comparison between SECM (i_{SECM} at –0.4 V, black) and SBECM (i_{sys}, red, and I_{ECL}, blue, at V_{app} = 1.6 V) line scans across the hole. b) i_{sys} and c) I_{ECL} signal during the array scan at V_{app} = 1.6 V. For all measurements, the cathodic compartment was filled with 1 mM $[Fc(MeOH)_2]$ in 0.1 M KCl, while a solution of 1 mM $[Ru(bpy)_3]Cl_2$ and 50 mM TPrA in 0.1 M PBS (pH 7.4) was filled into the anodic compartment. x- and y-increments: 50 µm, $d_{tip\text{-}membrane}$ = 50 µm.

In the next step, the ability to visualize locally different and temporarily changing analyte concentrations has been exploited by 2D mapping of the diffusion field of $[Ru(NH_3)_6]Cl_3$. Scanning the SBECM tip in x- and y-direction leads to simultaneous local increases in i_{sys} and I_{ECL} in agreement with the shape of the hole (Figure 5.3b,c). Maximal values of i_{sys} = 26.6 nA and I_{ECL} = 382.2 a.u. were recorded at x = 0.8 mm, y = 1.05 mm. The optical signal recorded at the reporting pole of the BE directly correlates with i_{sys} and hence with the analyte concentration at the sensing pole. It demonstrates that the ECL intensity at the reporting BE pole depends on the position of the detecting pole above the sample surface so that a BE can be used to visualize local analyte concentration changes. Moreover, the suggested SBECM system meets the prerequisites defined above for overcoming the previously existing limitations on the way to the simultaneous resolution of locally heterogeneous analyte concentrations

5.4.4. A bipolar multi-electrode array as an electrochemical camera.

Utilization of MEAs is a key to avoid the time-consuming scanning process and record snapshots of the analyte concentrations at multiple locations simultaneously. The reliability of I_{ECL} as a measure for the magnitude of analyte conversion in the SBECM setup allows now to extend the system by a multi-BE array. For this, two bundles of seven disc-shaped Pt-microelectrodes with a diameter of 10 μm each were fabricated (Figure 5.4). The BEs are labelled with numbers from 1-7 with BEs 1-6 oriented counterclockwise around the central BE 7. They are used as BE_as and BE_cs in the SBECM setup. Again, $d_{tip\text{-}membrane}$ was adjusted using the feedback current of $[Fc(MEOH)_2]$, now connecting BE 7 as WE in the three-electrode configuration in the cathodic compartment. Also, a likely surface tilt was considered. Although $dE_{BE\text{-}Sol}$ values were optimized by altering the surface areas of anodic and cathodic BE poles, V_{app} = 1.6 V was sufficient to enable a low ECL signal in the absence of $[Ru(NH_3)_6]Cl_3$. Specifically, $dE_{BE_a\text{-}Sol}$ of BE 7 was determined to be about 1.09 V, while $dE_{BE_c\text{-}Sol}$ of BE 7 was about –0.55 V, which illustrates that a surface area ratio of $A_{BE_a}/A_{BE_c} < 1$ results in a shift of $dE_{BE\text{-}Sol}$ to more positive values as described in the previous section. During a bipolar LSV, i_{sys} and I_{ECL} start again to increase at a lower V_{app} in presence of 1 mM $[Ru(NH_3)_6]Cl_3$ in the cathodic compartment. While i_{sys} increases from 1.28 V and I_{ECL} from 1.37 V in absence of the analyte in the cathodic compartment, the values of i_{sys} and I_{ECL} are shifted to 1.05 V and 1.13 V, respectively, in presence of $[Ru(NH_3)_6]Cl_3$.

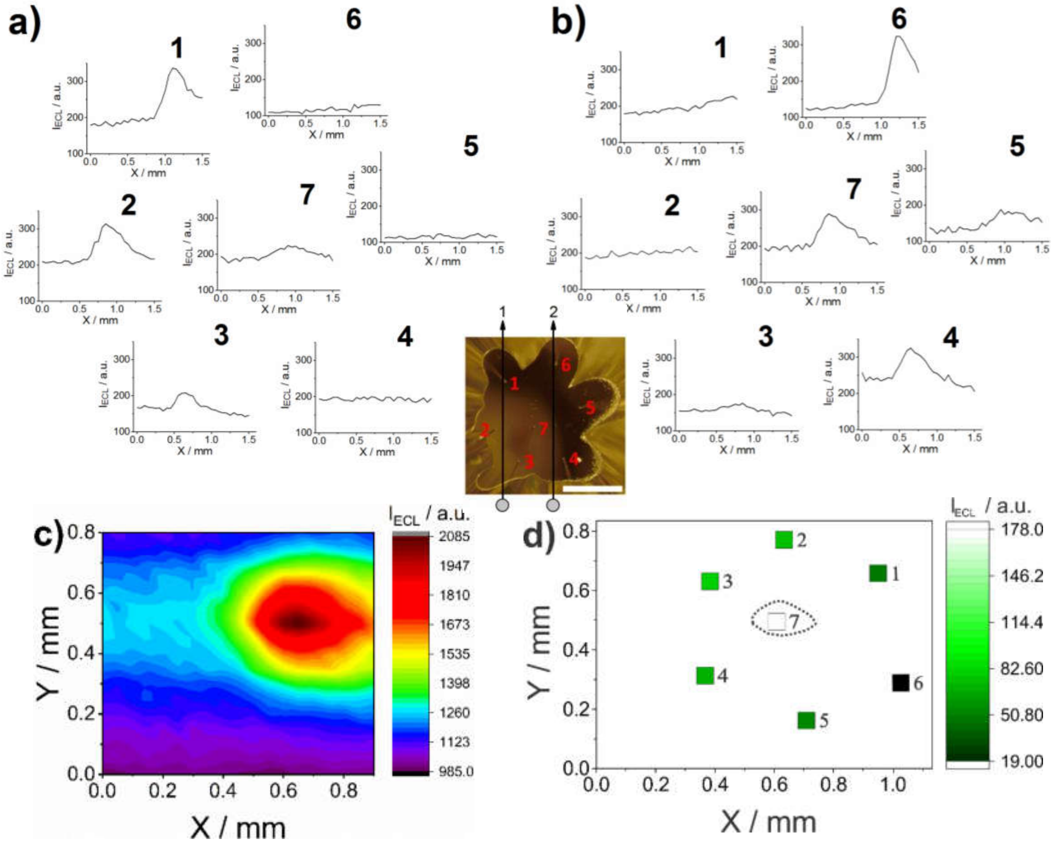

Figure 5.4. a) ECL responses at all seven BEs during line scan 1 in x-direction. b) ECL responses at all seven BEs during line scan 2 in x-direction, at another y-position than line scan 1. The position of the $[Ru(NH_3)_6]Cl_3$-releasing hole versus the BE_c poles during line scans 1 and 2 is shown as the grey circles in the photograph of the microelectrode array. Scale bar: 500 µm. c) Overlaid net ECL signals of all seven BEs during an array scan. d) ECL intensities at all seven BEs when BE 7 is positioned right above the $[Ru(NH_3)_6]Cl_3$-releasing hole. For all measurements, a 1 mM $[Fc(MeOH)_2]$ in 0.1 M KCl solution was used in the cathodic compartment, while a solution containing 1 mM $[Ru(bpy)_3]Cl_2$ and 50 mM TPrA in 0.1 M PBS (pH 7.4) was used in the anodic compartment. x-, y-increments: 50 µm, $d_{tip-membrane}$ = 50 µm.

In a first step, two line scans in x-direction over the hole (118 µm×140 µm) at different y-positions were recorded (Figure 5.4a, b). For one (Figure 5.4a), the side of the cathodic BE bundle with BEs 1 and 2 passes the hole in closest distance. The ECL response of each BE along the line scan is shown in the same order as the denomination of BEs. The side with BEs 3 and 4 approached the hole first, resulting in an ECL increase for BE 3 at about 0.45 mm, but not for BE 4 as this BE is too distant to the hole. Next, I_{ECL} increases for both BEs 2 and 7 at approximately 0.6 mm and with peaks at about 0.85 mm and 0.9 mm, respectively, as these two BEs are located at very similar x-positions. Yet, the ECL response at BE 7 is relatively small. At last, an increase in I_{ECL} was recorded for BE 1 starting at approximately 0.85 mm with a maximum at 1.1 mm. For another line scan, the cathodic BE array was moved 0.3 mm in y-direction. Again, the side with BEs 3 and 4 approaches the analyte diffusion field first, but now the ECL increase is more prominent at BE 4 starting at 0.4 mm and showing a peak at 0.65 mm. The next ECL response was recorded at BE 7 rising at 0.6 mm by about 90 a.u. until 0.85 mm before it declines back to the initial value at approximately 1.4 mm. BE 6, presumably passing the hole in shortest distance, shows the most significant change in I_{ECL} starting at 0.95 mm with a maximum at 1.2 mm.

Measurements of $dE_{BE\text{-}Sol}$ values at different BEs revealed that also in case of multiple BEs, $dE_{BE\text{-}Sol}$ values only change upon analyte conversion at BE_c. This means that $dE_{BE\text{-}Sol}$ remains constant as long as the BE processes remain the same when the individual BE is located in large distance to the hole, but $dE_{BE\text{-}Sol}$ changes for the other BEs of the array with increasing i_{BE} due to analyte reduction.

These results demonstrate that the position and intensity of ECL peaks are in alignment with the position of each BE towards the hole. In particular, the BE position in x-direction during the course of the line scan defines the position of the ECL peak while the BE position in y-direction determines its magnitude. Each ECL peak appears at the point of closest distance between the BE and the hole. As a result, the ECL responses can in principle be used to localize the hole using simple geometric calculations.

By recording an array scan with the multi-BE array and overlaying the resulting ECL maps with respect to the maximal I_{ECL}, an ELC map of the analyte-releasing hole with higher signal-to-noise ratio as compared to the measurement with a single BE is obtained (Figure 5.4c). This strategy may be useful to visualize samples with low and temporarily constant electrochemical activity. However, as outlined above, a scanning process impairs the advantage of a short response time of electrochemical methods. Consequently, we also recorded a static image when BE 7 was positioned directly above the hole (Figure 5.4d). The corresponding ECL intensities at all other BEs clearly scale with the distance to the hole. I_{ECL} decreases almost linearly from the closest BE 3 to the furthest BE 6 with respect to BE 7. Small deviations may arise from a tilt of the BE array with respect to the membrane.

Finally, the BE array is employed to image the diffusion of $[Ru(NH_3)_6]^{3+}$ through two holes in the membrane at a distance of about 0.9 mm. The overlay of ECL maps obtained for each BE in an array scan visualizes the diffusion field of $[Ru(NH_3)_6]^{3+}$ around hole one (left in Figure 5.5a, 150 μm×190 μm) and hole two (right in Figure 5.5a, 120 μm×110 μm). Also here, electrochemical “photographs” were taken by recording I_{ECL} at the seven BEs when the array is positioned above the site of interest (Figure 5.5b). The emission of light clearly scales with the distance from both holes and thus with the analyte concentration. Therefore, the light intensities show an inverse dependence on the distance to BE 7 (Figure 5.5b, 1 and 3). As the diffusion field at the smaller hole is more confined (Figure 5.5b, 3), I_{ECL} values tend to be smaller here. In this case, ECL intensities of BEs 3 and 4 are also slightly influenced by the diffusion of electroactive species from hole one. When BE 7 is positioned between the two holes, the diffusion of $[Ru(NH_3)_6]^{3+}$ through both holes is clearly detected (Figure 5.5b, 2). Highest intensities were detected at BE 3 and BE 1 being closest to the larger and the smaller hole, respectively. BE 5 being furthest away from both holes shows the lowest emission. As a result, BE arrays can be used to map the release of analyte species from a sample surface without a time-consuming scanning process and most importantly, in a wireless manner.

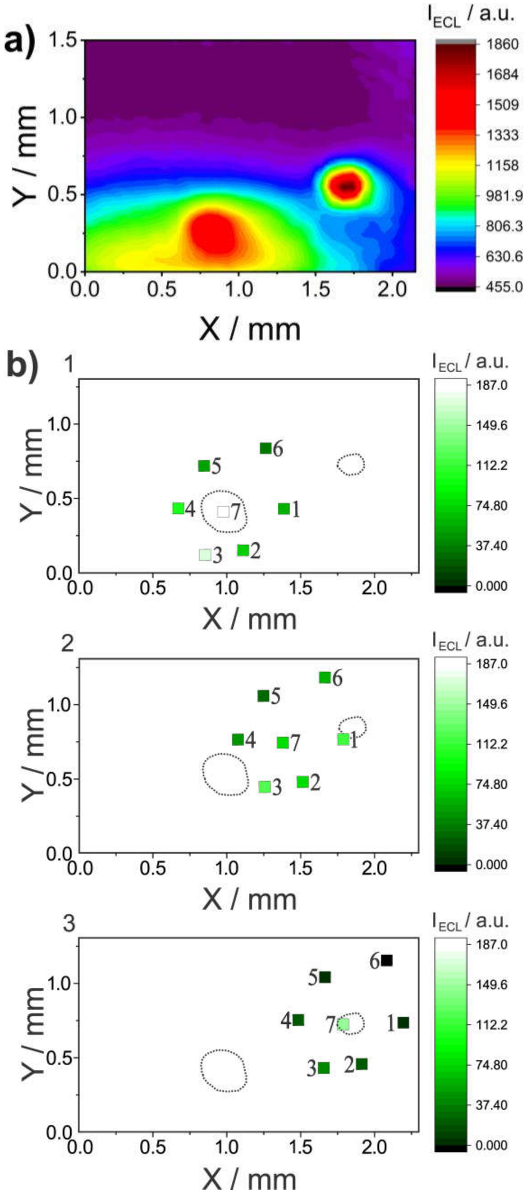

Figure 5.5. a) *Overlaid ECL signals of all seven BEs during an array scan above two holes. b) ECL intensities at all seven BEs at three different static positions of the cathodic BE array: 1) BE 7 is positioned above the larger of the two holes, 2) in between the two holes, and 3) BE 7 is placed above the smaller hole. The holes are indicated by the dotted circles.*

On the way to image electrochemical activity or analyte release at a sample surface with highest temporal and spatial resolution, the BE array and BEs themselves need to be miniaturized while employing a higher number of BEs.

5.5. Conclusions.

We have introduced scanning bipolar electrochemical microscopy (SBECM) and demonstrated its functionality. This enables precise positioning of the BE and hence introduces a spatial dependency to the assessment of electrochemical conversion of analyte molecules by a proportional optical signal at the wirelessly connected electrode. In this way, bipolar line and array scans yielded ECL maps of the localized release of a model analyte. Notably, possible electrode processes and the dynamics of interfacial electrode potentials adjusted in the SBECM system have been studied *operando* to demonstrate the working principle of SBECM. On the way to electrochemical monitoring of the dynamics of analyte concentrations at a sample surface with a high temporal and spatial resolution, a multi-BE array has been employed. When accurately positioned above the site of interest, the ECL response at each BE is a function of the distance to the analyte-releasing surface feature. When the array and BEs are miniaturized in future, this approach will allow to record an immediate image of several sites simultaneously with an improved spatial resolution. Moreover, suitable reductive signaling reactions will be considered to broaden the range of application of SBECM.

5.6. Acknowledgments.

This work was supported by the Deutsche Forschungsgemeinschaft (DFG) in the framework of the Cluster of Excellence Resolv (EXC1069). V.E. and C.S.S. are grateful to the German National Academic Foundation and the FAPESP (Fundação de Amparo à

Pesquisa do Estado de São Paulo, #2014/22396-6 and #2017/12629-1), respectively. The authors acknowledge Prof. Christian Amatore, Paris, and Prof. Alexander Kuhn, Bordeaux, for initial conceptual discussions, and Alexander Botz, Ruhr-Universität Bochum, for support during setting up the instrument.

5.7. References.

1. Leszczyszy, D. L.; Jankowski, J. A.; Viveros, O. H.; Diliberto Jr, E. J.; Near, J. A.; Wightman, R. M. *J. Biol. Chem.,* **1990**, 265, 14736–14737.

2. Fathali, H.; Cans, A.-S. *Eur. J. Physiol.,* **2018**, 470, 125–134.

3. Amatore, C.; Arbault, S.; Guille, M.; Lemaître, F. *Chem. Rev.,* **2008**, 108, 2585–2621.

4. Wang, W.; Zhang, S.-H.; Li, L.-M.; Wang, Z.-L.; Cheng, J.-K.; Huang, W.-H. *Anal. Bioanal. Chem.,* **2009**, 394, 17–32.

5. Amatore, C.; Delacotte, J.; Guille-Collignon, M.; Lemaître, F. *Analyst,* **2015**, 140, 3687–3695.

6. Huang, X.-J.; O'Mahony, A. M.; Compton, R. G. *Small,* **2009**, 5, 776–788.

7. Zhang, B.; Adams, K. L.; Luber, S. J.; Eves, D. J.; Heien, M. L.; Ewing, A. G. *Anal. Chem.,* **2008**, 80, 1394–1400.

8. Lin, Y.; Trouillon, R.; Svensson, M. I.; Keighron, J. D.; Cans, A.-S.; Ewing, A. G. *Anal. Chem.,* **2012**, 84, 2949–2954.

9. Wang, J.; Trouillon, R.; Lin, Y.; Svensson, M. I.; Ewing, A. G. *Anal. Chem.,* **2013**, 85, 5600–5608.

10. Wigström, J.; Dunevall, J.; Najafinobar, N.; Lovric, J.; Wang, J.; Ewing, A. G.; Cans, A.-S. *Anal. Chem.,* **2016**, 88, 4, 2080–2087.

11. Fosdick, S. E.; Knust, K. N.; Scida, K.; Crooks, R. M. *Angew. Chem. Int. Ed.,* **2013**, 52, 10438–10456.

12. Chow, K.-F.; Mavré, F.; Crooks, R. M. *J. Am. Chem. Soc.,* **2008**, 130, 7544–7545.

13. Koefoed, L.; Pedersen, E. B.; Thyssen, L.; Vinther, J.; Kristiansen, T.; Pedersen, S. U.; Daasbjerg, K. *Langmuir,* **2016**, 32, 5289–5296.

14. Braun, T. M.; Schwartz, D. T. *J. Electrochem. Soc.,* **2015**, 162, D180–D185.

15. Loget, G.; Roche, J.; Kuhn, A. *Adv. Mater.,* **2012**, 24, 5111-6, 5144.

16. Bouffier, L.; Ravaine, V.; Sojic, N.; Kuhn, A. *Curr. Opin. Colloid interface Sci.,* **2016**, 21, 57–64.

17. Eßmann, V.; Voci, S.; Loget, G.; Sojic, N.; Schuhmann, W.; Kuhn, A. *J. Phys. Chem. Lett.,* **2017**, 8, 4930–4934.

18. Amatore, C., Brown, A. R., Thouin, L., Warkocz, J.-S. *C. R. Acad. Sci., Ser. IIc: Chim.,* **1998**, 1, 509–515.

19. Kayran, Y. U.; Eßmann, V.; Grützke, S.; Schuhmann, W. *ChemElectroChem.,* **2015**, 3, 399–403.

20. Guerrette, J. P.; Percival, S. J.; Zhang, B. *J. Am. Chem. Soc.,* **2013**, 135, 855–861.

21. Arora, A.; Eijkel, J. C. T.; Morf, W. E.; Manz, A. *Anal. Chem.* **2001**, 73, 3282–3288.

22. Zhang, X.; Zhai, Q.; Xing, H.; Li, J.; Wang, E. *ACS Sens.,* **2017**, 2, 320– 326.

23. Zhang, X.; Chen, C.; Li, J.; Zhang, L.; Wang, E. *Anal. Chem.,* **2013**, 85, 5335–5339.

24. Zhang, X.; Li, J.; Jia, X.; Li, D.; Wang, E. *Anal. Chem.,* **2014**, 86, 5595–5599.

25. Oja, S. M.; Zhang, B. *Anal. Chem.,* **2014**, 86, 12299-12307.

26. Hotta, H.; Akagi, N.; Sugihara, T.; Ichikawa, S.; Osakai, T. *Electrochem. Commun.,* **2002**, 4, 472–477.

27. Mavré, F.; Chow, K.-F.; Sheridan, E.; Chang, B.-Y.; Crooks, J. A.; Crooks, R. M. *Anal. Chem.,* **2009**, 81, 6218–6225.

28. Oja, S. M.; Zhang, B. *ChemElectroChem.,* **2016**, 3, 457–464.

29. Ulrich, C.; Andersson, O.; Nyholm, L.; Björefors, F. *Anal. Chem.,* **2009**, 81, 453–459.

30. Eßmann, V.; Barwe, S.; Masa, J.; Schuhmann, W. *Anal. Chem.,* **2016**, 88, 8835–8840.

31. Eßmann, V.; Zhao, F.; Hartmann, V.; Nowaczyk, M. M.; Schuhmann, W.; Conzuelo, F. *Anal. Chem.* **2017**, 89, 7160–7165.

Chapter 6.

Oxygen detection by Scanning Bipolar Electrochemical Microscopy

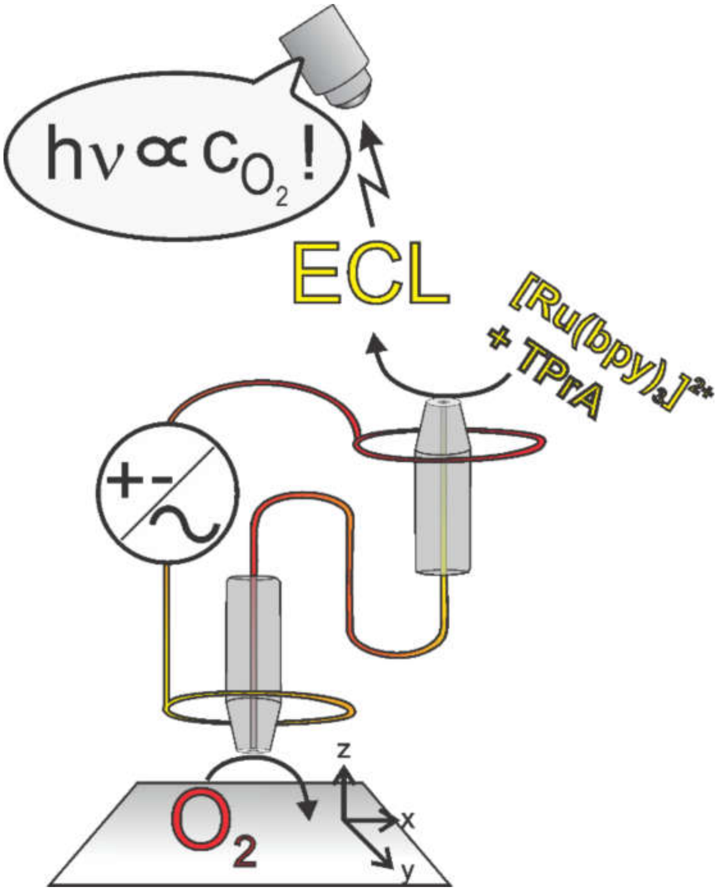

Following the last chapter, the developed scanning bipolar electrochemical microscopy (SBECM) was here applied to the oxygen detection. Since changes of oxygen concentration are small in the vicinity of biological samples, the SBECM setup was optimized to get improved sensitivity. This work focused on the enhancement of the detection performance of the SBECM technique. A bunch of experimental parameters, such as electrode materials, pH solutions and driving potential were optimized and the improved performance was demonstrated by topographical imaging (Cr stripes on Si wafer), where the hindered diffusion was used to adjust the concentration of oxygen. Moreover, the detection of the oxygen evolution was monitored by the SBECM technique using a photocatalyitcal semiconductor material. This work was also developed during the one-year experience in the Prof. Wolfgang Schuhmann's group and the data presented in this chapter were published in Analytica Chimica Acta as:

Enhanced Sensitivity of Scanning Bipolar Electrochemical Microscopy for O_2 Detection
Carla S. Santos, Felipe Conzuelo, Vera Eßmann, Mauro Bertotti, Wolfgang Schuhmann.
Analytica Chimica Acta, 2019, 1087, 36-43.

The permission of use of the text was requested to the publisher Elsevier and the copy of the right is attached in the Annex. However, the authors can use their articles, in full or in part, for a wide range of scholarly, with non-commercial purposes.

C. S. S., F. C. and W. S. idealized, planned and designed the experiments. The measurements were performed by C. S. S. with close support of F. C.. Data were analyzed and discussed by C. S. S., F. C., V. E. and W. S.. C. S. S. and F. C. made the figures. All the authors revised the text.

6.1. Abstract.

The Scanning Bipolar Electrochemical Microscope (SBECM) allows a precise positioning of an electrochemical probe serving as bipolar electrode that can be wirelessly interrogated by coupling the electrochemical detection reaction with an electrochemiluminescent reporting process. As a result, the spatially heterogeneous concentrations of an analyte of interest can be converted in real time into a map of sample reactivity. However, this can only be achieved upon optimization of the analytical technique performance ensuring an adequate sensitivity. Here, we present the evaluation and optimized operation of the SBECM for the detection of small changes in local O_2 concentrations. Parameters for achieving an improved sensitivity as well as possibilities for improving the signal-to-noise ratio in the optical signal readout are evaluated. The capability of the SBECM for O_2 detection is shown in controlled conditions by recording the topography of a patterned sample and monitoring O_2 evolution from a photocatalyst material

6.2. Introduction.

Oxygen concentration measurements are relevant for the evaluation of rates of electrocatalytic water-splitting reactions as well as respiration processes in biological samples of interest. In particular, oxygen detection in the surroundings of a cell can be correlated with cellular metabolism, bioenergetic activity and cellular biophysical properties. In this context, the application of accurately positioned micro-/nanoelectrodes making possible to monitor the release or consumption of O_2 *in situ* has been demonstrated [1]. Most of the measurements are commonly performed by scanning a sensing probe in order to sequentially monitor the area of analyte release. This strategy is time consuming and compromises an efficient monitoring of biological processes that occur often at the millisecond time scale. As an alternative approach, the use of electrode arrays for the simultaneous detection of an analyte at different locations of the sample has been suggested [2]. In this context, we have demonstrated a bipolar electrochemical setup that can be used for the spatially resolved detection of the release of compounds of interest [3]. The basic concept of bipolar electrochemistry consists of an applied electric field in an electrolyte solution that is able to induce the wireless polarization of one or multiple conductive objects immersed in the same electrolyte solution. As a result, the interface between the conducting object and the solution experiences a potential difference with respect to the established electric field leading to the polarization of the object, by this enabling oxidation and reduction reactions at the poles of the bipolar electrode (BE) [4–6]. When each of the individual poles of the bipolar electrode are placed in two physically separated compartments, a closed bipolar electrochemical setup is obtained, where the only current path between the two compartments is the bipolar electrode itself [7–10]. In bipolar electrochemistry, reactions occurring at one of the individual poles can be coupled to an optical reporter reaction taking place at the opposite pole [11]. This concept has been recently combined with probe electrochemistry enabling to perform local measurements [12–15] and was the basis for the recently introduced scanning bipolar electrochemical microscope (SBECM)[3]. In a closed-bipolar configuration, two interconnected microelectrodes or arrays of microelectrodes were employed as BE. The bipolar cathode (BE_c) acting as the sensing pole could be precisely positioned in close proximity to a surface of interest in a similar way as the tip used in scanning electrochemical microscopy (SECM) and was used to record the concentration map of a model analyte above a sample in question. In the other compartment, the bipolar anode (BE_a) operated as the reporting pole, with the oxidative generation of an electrochemiluminescent (ECL) complex enabling the detection of the analyte of interest. Since anodic and cathodic currents at the

BE must be equal ($i_{BEa} = i_{BEc}$), the optical ECL signal allowed to derive the bipolar system current (i_{sys}) that depends on the extent of electrochemical reduction of the analyte. The working principle of the SBECM was demonstrated by monitoring the release of $[Ru(NH_3)_6]Cl_3$ using a single BE and an array of BEs. Towards the application of the developed analytical tool for the detection of analytes of interest, a sufficient detectability must be previously ensured.

Herein, the capability of SBECM for the detection of O_2 is investigated and optimized in order to provide the instrumental basis and required sensitivity allowing future mapping of the cellular activity reflected by changes in local O_2 concentrations. Thus, our focus is to achieve high sensitivity and optimized experimental conditions for an improved O_2 detection. Experimental validation of the optimized SBECM operation is performed while monitoring small variations of O_2 concentrations by scanning the BE_c over a patterned sample with a defined topography. Moreover, SBECM is also successfully applied for the local detection of O_2 evolved at a semiconductor material which is able to catalyze light-induced water oxidation.

6.3. Experimental section.

6.3.1. Chemicals and materials.

All chemicals were of analytical grade and used as received: hexaammineruthenium (III) chloride (CAS 14282-91-8, Sigma-Aldrich, Germany), tri-*n*-propylamine (TPrA, CAS 102-69-2, Sigma-Aldrich, Germany; ***Caution!*** *TPrA is highly flammable, toxic, and irritant and must be handled with personal protective equipment*), tris(2,2'-bipyridyl)ruthenium (II) chloride hexahydrate ($[Ru(bpy)_3]Cl_2$, CAS 50525-27-4, Sigma-Aldrich, Germany), monopotassium phosphate (CAS 7778-77-0, VWR Chemicals, Germany), potassium phosphate dibasic (CAS 7758-11-4, Carl Roth, Germany). All solutions were prepared with ultrapure water (SG water, Germany). Single Pt microelectrodes were fabricated by placing a Pt wire (Ø = 10 μm – Goodfellow, Germany) inside a borosilicate glass capillary and then sealing the glass body surrounding the wire by using a heating coil. The Pt wire was further contacted with a copper wire using soldering tin. The array electrode (7-fold) was fabricated as previously described[3], by pulling and sealing a 7-barrel borosilicate capillary (Hilgenberg, Germany) with a heating coil. At each barrel, a piece of Pt wire (Ø = 10 μm – Goodfellow, Germany) was inserted. The wires were sealed by heating the tip with a torch. The Pt wires were then connected with copper wires by filling the barrels with a conductive epoxy (EC 151 L, Polytec PT, Germany). Finally, the tip was polished to expose the seven disc-shaped Pt microelectrodes.

6.3.2. Scanning bipolar electrochemical microscopy setup.

Bipolar electrochemistry experiments were performed in a setup as described previously[3] and shown in Scheme 6.1. As feeder electrodes, rings of Pt wire were employed and placed along the inner wall of each compartment. The anode pole of the bipolar electrode (BE_a) consisted of a single microelectrode or a microelectrode array that was connected to a corresponding equivalent counterpart that was employed as the cathode pole of the bipolar electrode (BE_c). The cathode compartment was placed in a holder that can be moved in X-, Y-, and Z-directions using computer-controlled stepper motors (PS30, Owis, Germany). The applied voltage between the feeder electrodes (V_{app}) was controlled using a Jaissle PG 100 bipotentiostat (IPS Elektroniklabor, Germany). A Visual Basic-based in-house written software was used for instrumental control and data acquisition. The optical detection system consisted of an electron multiplying charge-coupled device (CCD) camera (Evolve Delta 512, Photometrics, USA) and an immersible objective (10× magnification, UMPlan FLN, Olympus, Japan). The electron multiplying (EM) gain was set to 250 under dark conditions and the CCD camera was cooled down to –70 °C. Data collection from the CCD camera used to read out the ECL signal was accomplished with the open source software "MicroManager 1.4" (Vale Lab, USA). Treatment of the images was done using the software "Image J".

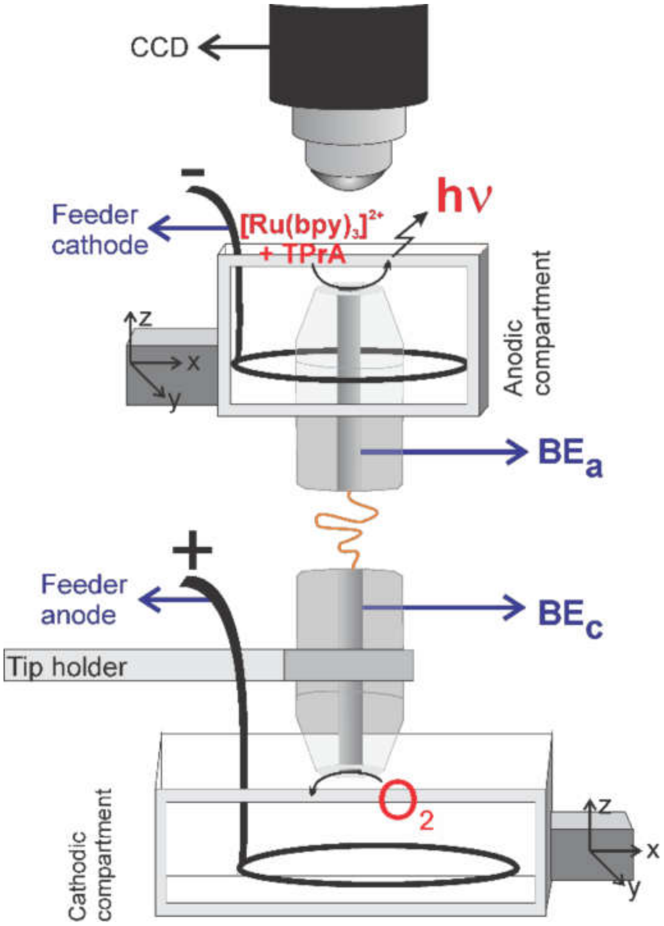

Scheme 6.1. Schematic representation of the SBECM main components. BE_a: bipolar anode; BE_c: bipolar cathode; CCD: charge-coupled device camera. A single electrode or an array of electrodes can be used as bipolar electrode.

The CCD camera parameters were controlled using the software *Micro Manager 1.4*. Sequential images were taken while simultaneously performing the electrochemical measurement. Background subtraction of the collected images was done with the software *Image J* to remove the dark noise. I_{ECL} values were obtained by integrating the light intensity of the pixels comprised within the region of interest (ROI) of the image. The ROI was a circular area with a radius of 5 pixels located on the electrode surface. AC I_{ECL} data were treated using fast Fourier transform (FFT) and a low-pass filter, suppressing the contribution of noise with higher frequency than the applied AC perturbation.

6.3.3. Optimization of experimental parameters for O_2 detection.

The optimal electrode material for the anode bipolar pole was evaluated by recording linear sweep voltammograms from 0 V to 3 V in bipolar configuration using a Pt microelectrode (Ø = 10 μm) as BE_c and a disc-shaped carbon fiber (Ø = 8 μm) or a Pt microelectrode (Ø = 10 μm) as BE_a. The optimum pH value for the electrolyte solution in the anode compartment was optimized by evaluating I_{ECL} in linear sweep voltammograms from 0 V to 1.5 V vs. Ag/AgCl/3 M KCl. The effect of the pH value in the cathode compartment on the ECL signal was evaluated by recording linear sweep voltammograms in bipolar configuration while monitoring the interfacial potential difference between the individual bipolar electrodes and the electrolyte solution (dE_{BE-Sol}). A multimeter (CEM instruments, Germany) was connected through a high impedance module (IPS Elektroniklabor, Germany) to the bipolar electrode and a Ag/AgCl/3 M KCl reference electrode located in the working solution. In addition, an AC signal modulation of the bipolar voltage was evaluated as a means to increase the signal-to-noise ratio. For this, the feeder electrodes were polarized using a PGU 50 mA potentiostat (IPS Elektroniklabor, Germany) incorporating a summing amplifier. The frequency and amplitude of the AC sinusoidal wave (1 Hz and 100 $mV_{peak\text{-}to\text{-}peak}$, respectively) were set using an arbitrary waveform generator (33120A, Agilent, USA). Bipolar approach curves were recorded at a given applied voltage between the feeder electrodes in the direct and alternating current modes (DC and AC, respectively) under optimized conditions.

6.3.4. SBECM with controlled local modulation of O_2 concentrations.

A silicon wafer with patterned chromium structures (Figure 6.1) prepared by sputter deposition using a metallic mask was employed as sample with defined topographic features, and analyzed by SBECM using both single and 7-fold Pt disc microelectrodes. Precise positioning of the tip above the sample surface was performed by recording approach curves in a conventional SECM configuration. Line scans were recorded moving the BE_c over the patterned sample. Surface tilt correction was performed by recording approach curves at three different X,Y locations and calculating the resulting tilt plane that was further considered during the performed scan. The bipolar compartments were filled with the optimized solutions, 200 mM phosphate buffer pH 6.0 in the cathode compartment and 1 mM $[Ru(bpy)_3]Cl_2$ + 50 mM TPrA in 200 mM phosphate buffer pH 8.0 in the anode compartment. The Pt microelectrode was polarized at −0.6 V vs. Ag/AgCl/3 M KCl for measurements carried out in the conventional SECM configuration. A voltage difference of 1.6 V was established between feeder electrodes for SBECM measurements.

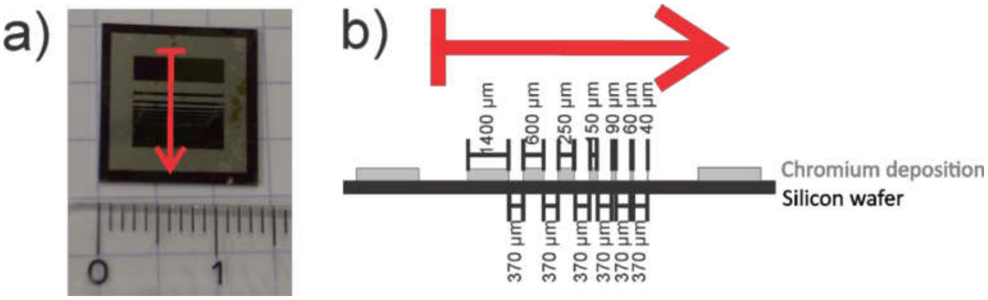

Figure 6.1. a) Photograph of the sample analyzed by SBECM, consisting of a silicon wafer with a patterned deposition of chromium. The direction of the scan is indicated by the red arrow. b) Schematic representation of the sample along the SBECM scan direction (indicated by the arrow) including the dimensions determined by optical microscopy.

6.3.5. Monitoring of O_2 evolution at a photocatalyst material.

Mo-doped $BiVO_4$ (Mo-$BiVO_4$), a photoanode material for water oxidation[10–12], was employed as model sample for controlled light-induced O_2 generation. The sample consists of Mo-$BiVO_4$ deposited on fluorine-doped tin oxide (FTO) and was polarized at 0.25 V vs. Ag/AgCl/3 M KCl using a PG 100 potentiostat (IPS Elektroniklabor, Germany) in floating mode to avoid undesired electrical coupling with the potentiostat used to apply the voltage difference between the feeder electrodes. For irradiation of the sample, a 150 W Hg-Xe lamp (LC8, Hamamatsu Photonics, Japan) was used as light source, focalizing the irradiation to the Mo-$BiVO_4$ spot by means of a light fiber coupled to the setup. Two single Pt microelectrodes (Ø = 10 μm) were used as bipolar electrodes and the feeder electrodes were polarized in DC as well as AC modes. The anode compartment was filled with the electrolyte solution for ECL at pH 8.0 and the cathode compartment was filled with 200 mM phosphate buffer pH 8.5. Approach curves in bipolar configuration (V_{app} = 1.8 V) were recorded while the sample was irradiated (incident power of 5 mW cm^{-2}). The Pt microelectrode constituting the BE_c was positioned 10 μm above the sample surface. A voltage difference of 1.2 V was set between the feeder electrodes in DC as well as AC modes. In AC mode a sinusoidal wave with a frequency of 1 Hz and an oscillation amplitude of 0.1 $V_{peak\text{-}to\text{-}peak}$ was applied.

6.4. Results and discussion.

6.4.1. Selection of the bipolar electrode material.

For highest sensitivity of O_2 detection with the SBECM system, different experimental parameters such as the bipolar electrode material and the pH value of the solutions were initially optimized. First, the electrode material was investigated with the aim of obtaining optimal conditions to promote the reactions of interest: the O_2 reduction reaction (ORR) at the cathode pole (sensing compartment) and ECL at the anode pole (reporting compartment). Since Pt is highly active for the ORR, Pt microelectrodes were selected for an efficient O_2 detection in the sensing compartment. Moreover, since it is known that the formation of surface oxides at metal electrodes such as Pt or Au effectively block direct oxidation of TPrA on the electrode surface[17,18], the use of Pt and carbon microelectrodes exhibiting different kinetics for TPrA oxidation was evaluated in the anode compartment. Linear sweep voltammograms were recorded in bipolar configuration by filling the anode compartment with 1 mM $[Ru(bpy)_3]Cl_2$ and 50 mM TPrA in 200 mM phosphate buffer (pH 7.4). As counter reaction at the cathode compartment, the reduction of $[Ru(NH_3)_6]^{3+}$ was selected, because a defined reduction wave is obtained. The recorded bipolar linear sweep voltammograms revealed the expected different behavior for carbon and Pt (Figure 6.2). When a Pt microelectrode was employed as BE_a, an increase in the bipolar system current (i_{sys}) was observed at similar applied voltages than those required for generating an ECL signal ($V_{app} > 1.2$ V; Figure 6.2a). On the other hand, when a carbon fiber microelectrode was used as BE_a, the initial increase in i_{sys} was observed already at a V_{app} which was 0.4 V lower than that required for ECL (Figure 6.2b). Since TPrA can be oxidized at the carbon surface at less positive potentials than $[Ru(bpy)_3]^{2+}$, an oxidation current which is able to balance the reduction reaction at the cathode bipolar pole can arise before ECL emission can be detected. Even though the oxidation of TPrA produces radicals able to induce ECL, the route implying a direct oxidation process of $[Ru(bpy)_3]^{2+}$ at the electrode surface is more efficient for ECL generation and the associated detection with SBECM. Therefore, Pt microelectrodes were selected as BE_a, enabling an unambiguous direct correlation of the generated i_{sys} and ECL. At higher applied feeder voltages, water oxidation occurs at both Pt and C electrodes, not only competing with ECL generation but also leading to the generation of quenchers of the excited Ru complex ($[Ru(bpy)_3]^{2+*}$) resulting in a significant decay in I_{ECL}[17,18] and were therefore avoided.

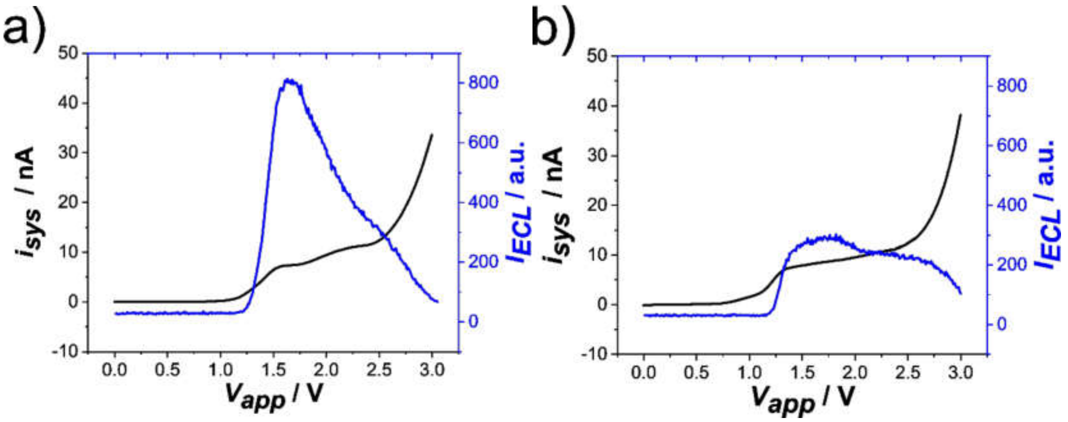

Figure 6.2. Comparison of different electrode materials for the BE_a. Bipolar linear sweep voltammograms recorded using: a) Pt (Ø = 10 µm) and b) carbon fiber (Ø = 8 µm) microelectrodes as BE_a. A Pt microelectrode (Ø = 10 µm) was used as BE_c. Anode compartment: 1 mM $[Ru(bpy)_3]Cl_2$ + 50 mM TPrA in 200 mM PBS (pH 7.4). Cathode compartment: 5 mM $[Ru(NH_3)_6]Cl_3$ in 100 mM KCl. Frame rate for ECL detection: 1 FPS. The system current (i_{sys}) as well as the intensity of recorded ECL signal (I_{ECL}) are presented as a function of the applied voltage between feeder electrodes (V_{app}). Scan rate: 10 mV s^{-1}.

6.4.2. Evaluation of the pH value at the individual bipolar compartments.

The influence of the pH value in the anode compartment on the ECL efficiency was first evaluated. A Pt microelectrode was used to record linear sweep voltammograms in a three-electrode configuration, using solutions containing 1 mM $[Ru(bpy)_3]Cl_2$ and 50 mM TPrA prepared in 200 mM phosphate buffer of different pH values. In accordance with previous reports [19–22], an increase in ECL was observed from pH 7.0 to pH 8.0 (Figure 6.3), with a further decrease at higher pH values until pH 9.0. Additionally, an increase in the ECL response was noticed at pH values higher than 9.0, with a maximum intensity at around pH 10.0. The latter can be attributed to the previously described reaction between OH^- and $[Ru(bpy)_3]^{3+}$ generated at the electrode, causing a significant

ECL background signal[22]. Therefore, a pH value of 8.0 in the anode compartment was chosen for subsequent experiments.

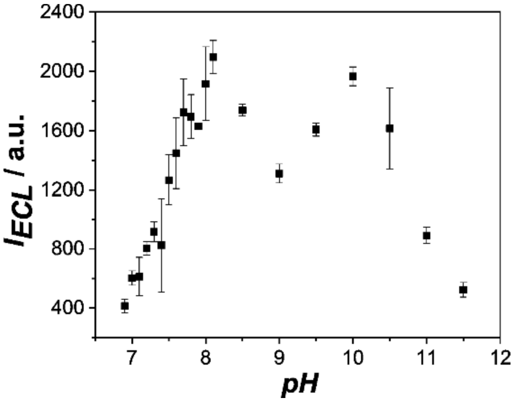

Figure 6.3. Influence of the pH value on ECL intensity. Maximum in I_{ECL} obtained (at E = 1.2 V vs. Ag/AgCl/3 M KCl) for linear sweep voltammograms recorded in 1 mM $[Ru(bpy)_3]Cl_2$ and 50 mM TPrA in 200 mM PBS of different pH values, ranging from 6.9 to 11.5. Three-electrode configuration. A Pt microelectrode (Ø = 10 µm) was used as working electrode. Error bars represent the standard deviation (n = 6 for pH ≤ 8.1; n = 2 for pH > 8.1).

Moreover, although the pH influence on the ORR at Pt electrodes is well known, the influence of the pH value in the cathode compartment for the detection of O_2 in the SBECM configuration was also investigated. Linear sweep voltammograms were recorded in bipolar configuration in order to evaluate the relation of ORR at different pH values with the ECL reaction. In these experiments, Pt microelectrodes were used both as BE_a and BE_c, and the individual interfacial potentials at the two bipolar poles ($dE_{BEc\text{-}Sol}$ and $dE_{BEa\text{-}Sol}$) were monitored (see experimental section). The measured $dE_{BEa\text{-}Sol}$ at V_{app} < 2.0 V were very similar for all evaluated pH values in the cathode compartment (Figure 6.4a). This confirmed that the ECL reaction in the anode compartment was the non-limiting process, which is a prerequisite to detect changes in the O_2 concentration in the cathode compartment. In contrast, $dE_{BEc\text{-}Sol}$ was significantly influenced by the pH value. Since a more negative potential is required for the reduction of O_2 at the Pt surface at higher pH values, a more negative $dE_{BEc\text{-}Sol}$ must be established at any given V_{app} in order to satisfy the reactions under these experimental conditions. The results also revealed the appropriate V_{app} range required for enabling O_2 detection (shaded region in Figure 6.4a). A V_{app} value of at least 1.2 V was necessary to reach an applied potential more negative than – 0.3 V (vs. Ag/AgCl/3 M KCl) at the BE_c, thus enabling a significant ORR. Moreover, at V_{app} values higher than 2.0 V, the potential at the BE_c was sufficiently negative for the reduction of protons, which may interfere with O_2 detection. For V_{app} values between 1.2 V and 2.0 V, the ORR at the BE_c was proportional to the ECL signal at the BE_a. Although maximum I_{ECL} was achieved at different V_{app} in dependence on the pH value in the cathode compartment (data not shown), O_2 detection was possible in the whole investigated pH range.

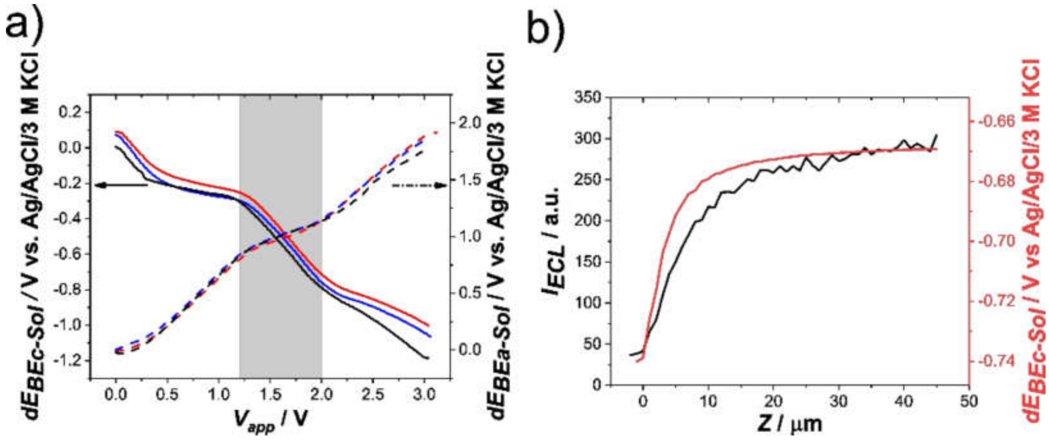

Figure 6.4. a) Cathodic (solid lines) and anodic (dashed lines) interfacial potentials as a function of V_{app}. Anode compartment: 1 mM $[Ru(bpy)_3]Cl_2$ + 50 mM TPrA in 200 mM phosphate buffer (pH 8.0). Cathode compartment: phosphate buffer pH 6.0 (red curves), pH 7.0 (blue curves), and pH 8.0 (black curves). The shaded region indicates the V_{app} range enabling O_2 detection by monitoring ECL. Scan rate: 20 mV s^{-1}. b) Bipolar approach curve recorded with a single Pt microelectrode as BE_c towards an inert insulating surface. V_{app} = 1.9 V, cathode compartment: phosphate buffer pH 7.4. Frame rate for ECL detection: 1 frame per s (FPS) at each Z position. Scan increment: 1 µm. Approach curve speed: 1 µm s^{-1}.

The capability for the detection of varying concentrations of O_2 was investigated by recording an approach curve of a Pt microelectrode as BE_c towards an insulating surface while the ECL response at the BE_a was recorded. The SBECM experiment was performed at constant V_{app} and a close to physiological pH value. During the approach of the Pt microelectrode towards the surface, the diffusion of O_2 was decreased in a typical negative feedback situation of SECM. As a result, the intensity of the ECL signal decreased from its bulk value, as obtained when the BE_c was positioned far away from the sample surface Figure 6.4b). Concomitantly, $dE_{BEc\text{-}Sol}$ revealed a shift towards more negative values for lower O_2 concentrations, as a response of the system to ensure maximum achievable current flow through the bipolar electrode. Hence, selection of V_{app} closer to the upper limit of the optimum detection range (i.e., V_{app} close to 2.0 V) was avoided in further experiments to prevent a shift in $dE_{BEc\text{-}Sol}$ towards values negative enough to enable the reduction of protons interfering with the detection of O_2.

6.4.3. SBECM using topographic features for controlled O_2 availability.

As a means of controlled variable analyte concentration, SBECM was applied for the analysis of a patterned sample surface exhibiting well-defined topographic features. Thus, causing the variation of O_2 availability due to negative feedback when performing a line scan at a constant tip height. The sample consisted of a silicon wafer with deposited chromium stripes (

Figure *6.1*). The Pt microelectrode used as BE_c was positioned at a distance of 5 µm above the sample and scanned across the deposited Cr stripes. Simultaneously, the current flowing through the bipolar system (i_{sys}) and the ECL signal at the BE_a were also monitored (Figure 6.5). As a result of a lower O_2 availability, a decreased current response was expected when the microelectrode was positioned above the Cr modified regions protruding above the Si substrate. Both recorded parameters followed the topographic variations of the sample, i.e., a decreased response was noticed when the BE_c tip was positioned above a Cr stripe. Noticeably, I_{ECL} allowed to detect variations in i_{sys} as low as 20 pA. The scan was repeated in a conventional SECM three-electrode configuration using the same Pt microelectrode as SECM tip. The tip current profile was similar to the one obtained with SBECM (Figure 6.5), confirming the observed changes in i_{sys} and I_{ECL} as a result of variable O_2 availability.

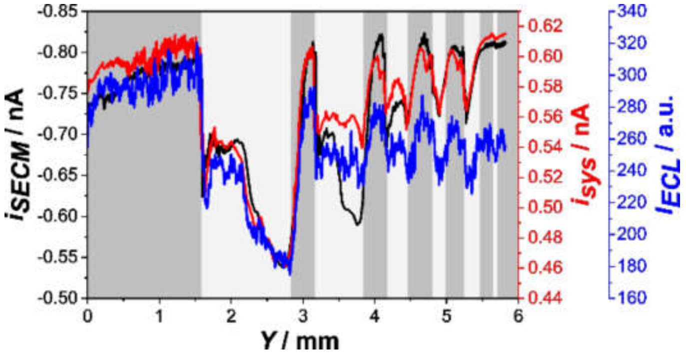

Figure 6.5. Comparison of SECM (black curve, inverted axis for clarity of the plot) and SBECM (red and blue curves) line scans obtained at a fixed tip height (5 µm) above a patterned sample using a single Pt microelectrode as SECM tip or SBECM BE_c. Light gray background: short tip-to-sample distance (Cr-stripes). Dark gray background: large tip-to-sample distance (Si wafer surface), see Fig. S1. Scan increment: 10 µm. Scan speed: 10 µm s^{-1}. Sample immersed in 200 mM phosphate buffer pH 6.0. SECM: E_{tip} = −0.6 V vs. Ag/AgCl/3 M KCl. SBECM: V_{app} = 1.6 V, frame rate for ECL readout: 10 FPS.

The bipolar configuration used in SBECM allows correlation of the current flowing through the BE with the ECL signal. Hence, no electrical contact is required to monitor the response obtained with an array of electrodes. The ECL signal can be easily acquired and analyzed at all reporter electrodes simultaneously without the need of a complex electrochemical setup for isolating the corresponding individual system currents. As a proof of concept, a SBECM line scan was recorded using an array of 7 electrodes. Two 7-fold Pt microdisc electrodes were used both as BE_c and BE_a. The BE_c array was positioned 30 μm above the surface by performing an approach curve for ORR using the central electrode of the array as SECM tip. In comparison to the single Pt microelectrode, the 7-fold electrode was considerably larger in diameter, justifying the working distance in order to avoid tip crash. Each of the Pt microdisc electrodes of the BE_c was connected to a corresponding counterpart of a BE_a array where the ECL response was monitored. The bipolar line scans are shown in Figure 6.6 and the recorded I_{ECL} for each of the seven electrodes is provided as function of the array position along the line scan. Because of the larger distance between tip and sample, ECL profiles were less pronounced. Nevertheless, the ECL response of each individual Pt microdisc during the line scan proved to be dependent on its relative position within the array (see scheme in Figure 6.6). The overall result was consistent with local changes in tip-to-sample distance due to the variation of the sample topography during tip movement.

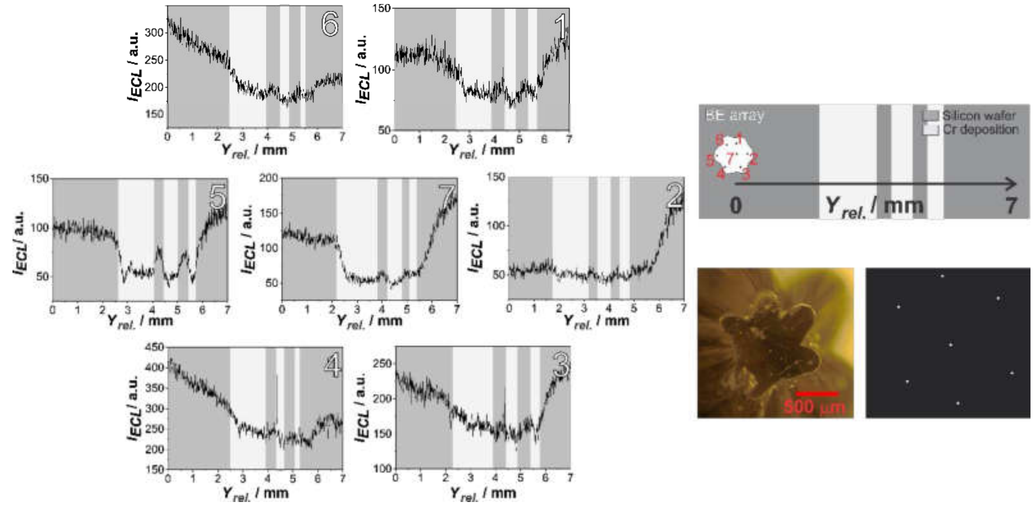

Figure 6.6. SBECM line scans obtained at a fixed tip height (30 µm) above a patterned sample using a 7-fold bipolar array. The array was moved according to the direction shown in the schematic representation (top right panel). Light gray background: short tip-to-sample distance (Cr-stripes). Dark gray background: large tip-to-sample distance (Si wafer surface). $V_{app} = 1.6$ *V. Scan increment: 10 µm. Scan speed: 25 µm* s^{-1}*. Sample immersed in 200 mM phosphate buffer pH 6.0. Frame rate for ECL readout: 10 FPS. A*

photograph of the cathode microelectrode array and a representative ECL image of the anode array are shown in the bottom right panel

6.4.4. AC modulation of the SBECM signal.

The possibility of improving the signal-to-noise ratio of the ECL signal was also investigated. Figure 6.7a shows the comparison of SBECM approach curves recorded at different V_{app} with an approach curve obtained by using conventional SECM, demonstrating that the ECL response exhibits a considerably higher background noise. Experimentally recorded noise in I_{ECL} can be related to background signal variations with the recorded CCD camera relevant to the low intensity of generated ECL. Although the SBECM approach curves followed the same profile as the current signal in the SECM approach curve, the background noise of the ECL signal compromises the limit of detection at low O_2 concentrations. Therefore, in order to minimize the stochastic contribution of the background signal by lowering the signal-to-noise ratio, an AC modulation of the applied DC feeder voltage ($f = 1$ Hz, $A = 0.1$ $V_{\text{peak-to-peak}}$) was applied. The recorded AC signal response was filtered in the frequency domain to remove background noise that appears especially at higher frequencies. Figure 6.7b shows that the AC approach curves follow the SECM current profile, but with an improvement in the signal-to-noise ratio.

Since for lower V_{app} values the ECL background noise was more relevant, the improvement of the signal-to-noise ratio due to AC modulation was also evaluated after decreasing V_{app}. This led to a shift of $dE_{BEc\text{-}Sol}$ towards less negative values (see Figure 6.4a) which decreased the performance of the ORR at the BE_c and provided an overall lower ECL response. This was reflected in the modulation of i_{sys} during approach curves recorded at V_{app} between 1.2 V and 1.4 V (Figure 6.8a). The corresponding I_{ECL} as a function of tip-to-sample distance indicated a considerable increase in ECL background noise with decreasing V_{app}. Noise reduction by AC modulation and FFT filtering was therefore essential to resolve the bipolar signals at $V_{app} \leq 1.3$ V (Figure 6.8b-d).

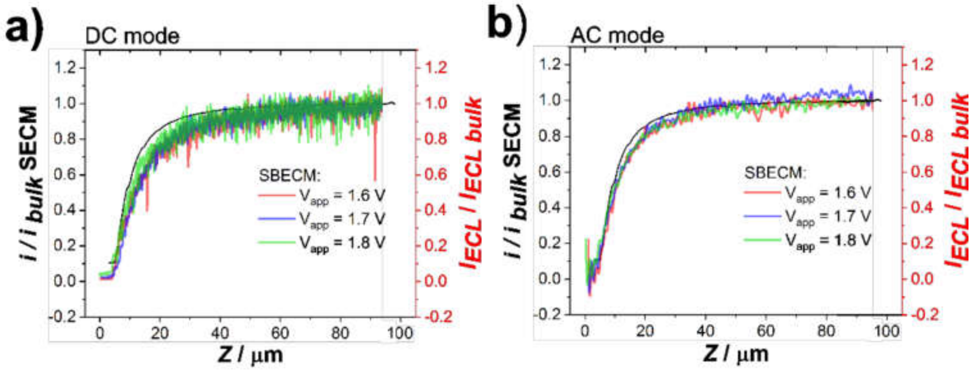

Figure 6.7. Normalized approach curves recorded with a single Pt microelectrode in SECM and SBECM configurations in DC (a) and AC (b) modes. SECM (left ordinate): $E_{tip} = -0.6$ V vs. Ag/AgCl/3 M KCl (black curves). SBECM (right ordinate): $V_{app} = 1.6$ V (red curves), 1.7 V (blue curves), and 1.8 V (green curves). AC mode: oscillation frequency = 1 Hz, amplitude = 0.1 $V_{peak\text{-}to\text{-}peak}$; I_{ECL} signal was treated using low-pass FFT filtering. Frame rate for ECL detection: 10 FPS. Approach curve speed: 1 µm s^{-1}.

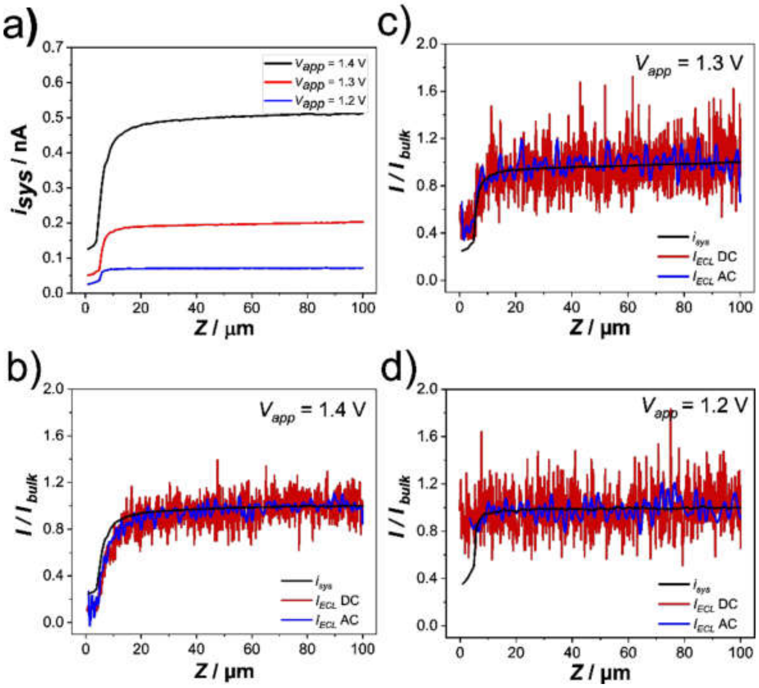

Figure 6.8. Approach curves recorded in the bipolar configuration with a single Pt microelectrode as BE_c. a) Absolute system current at different V_{app}; b-d) normalized responses obtained for V_{app}: b) 1.4 V, c) 1.3 V, and d) 1.2 V. DC mode: i_{sys} (black curves)

and I_{ECL} (red curves). AC mode: I_{ECL} signal after low-pass FFT filtering (blue curves). Frame rate for ECL detection: 10 FPS. Scan increment: 1 µm. Approach curve speed: 1 µm s^{-1}

6.4.5. Monitoring light-induced O_2 evolution at an n-type semiconductor surface.

SBECM was used to study photoelectrocatalytic light-induced O_2 evolution at Mo-$BiVO_4$ deposited on a FTO glass[21,22]. Bipolar approach curves towards a Mo-$BiVO_4$ modified surface were carried out at different conditions (Figure 6.9). The approach curves recorded in the dark showed a similar behavior with a decrease in I_{ECL} upon approaching of the BE_c to the sample surface. Both approach curves (Figure 6.9, black and red) were independent of the sample potential, because the material was unable to catalyze the oxidation of water in the dark. By repeating the experiment during sample irradiation, a completely different profile was obtained, as higher I_{ECL} values were obtained at lower tip-to-sample distances (Z < 40 µm, Figure 6.9, blue and pink) due to the increased availability of O_2 produced by photocatalytic water oxidation. Since the kinetics of the catalytic water splitting reaction depends on the applied potential, larger collection of O_2 leading concomitantly to the highest recorded I_{ECL} was obtained when the sample was polarized at 0.25 V vs. Ag/AgCl/3 M KCl in comparison to 0 V. It is important to mention that the anode compartment was isolated from external light sources and therefore it was not affected by the irradiation of the semiconductor sample.

The ECL signal terminally caused by O_2 evolution at illuminated Mo-$BiVO_4$ was recorded in both DC and AC modes. For this, the BE_c was positioned at a fixed distance of 10 µm above the sample surface and irradiated for periods of 5 s and 10 s (Figure 6.10). Even when V_{app} as low as 1.2 V was used, the large flux of O_2 generated directly in front of the Pt tip upon irradiation of the sample led to a simultaneous increase in I_{ECL}. The recorded I_{ECL} decreased as soon as the irradiation was stopped, confirming the fast response of the SBECM system. As expected, the AC mode provided an improved signal-to-noise ratio. Moreover, the alternating V_{app} enabled a faster stabilization of the recorded signal for O_2 reduction. Hence, the recorded AC I_{ECL} provided a signal almost twice as large as that recorded in the DC mode.

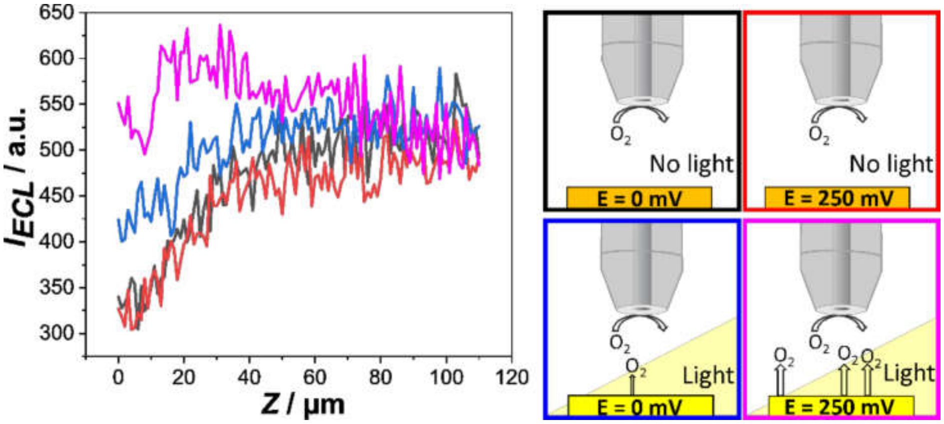

Figure 6.9. Bipolar approach curves towards an FTO glass modified with Mo-doped $BiVO_4$ (200 mM phosphate buffer, pH 8.5). V_{app} = 1.8 V; the Mo-doped $BiVO_4$ sample was polarized at 0 mV (black and blue curves) and 250 mV (red and pink curves) vs. Ag/AgCl/3 M KCl. The sample was kept under dark (black and red curves) or irradiated (blue and pink curves) at an incident power of 5 mW cm^{-2}. Frame rate for ECL detection: 1 FPS (at each Z position). Scan increment: 1 µm. Approach curve speed: 1 µm s^{-1}.

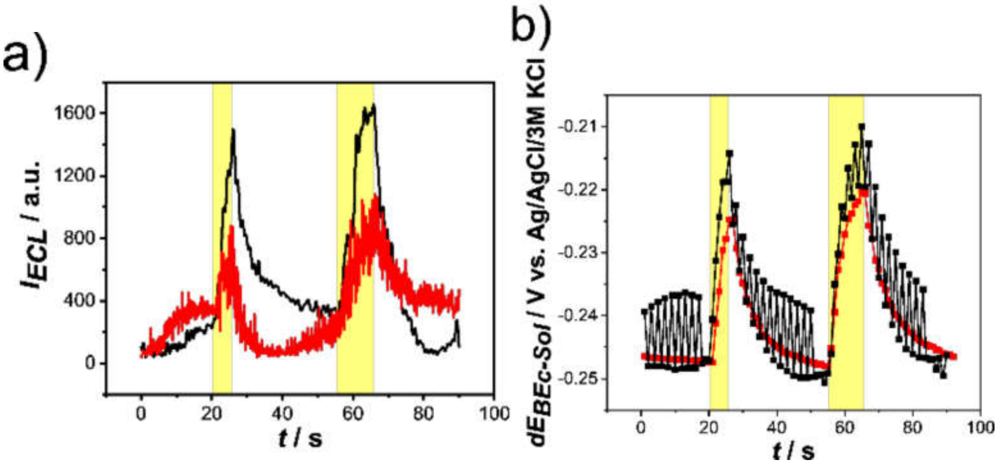

Figure 6.10. a) I_{ECL} and b) interfacial cathodic potential recorded while monitoring O_2 production at the Mo-$BiVO_4$ modified sample. V_{app} = 1.2 V: DC mode (red curves) and AC mode after noise filtering (black curves). Distance between BE_c and sample: 10 µm. The sample was irradiated as indicated by the yellow regions in the graphs at an incident

power of 5 mW cm^{-2}*. Frame rate for ECL readout: 10 FPS.* $dE_{BEc\text{-}Sol}$ *was taken every second.*

6.5. Conclusions.

We have successfully demonstrated the use of a closed bipolar setup in the scanning bipolar electrochemical microscope for local O_2 detection. After improving the sensitivity of SBECM measurements for modulations in the local O_2 concentration at BE_c we have demonstrated an improved signal-to-noise ratio of I_{ECL} by means of an AC modulation of V_{app} at the feeder electrodes. The optimized conditions were applied for investigations on topographic features of a patterned sample for controlling the availability of O_2 by means of a negative feedback. SBECM was then employed to monitor O_2 evolution at Mo-$BiVO_4$ surfaces upon irradiation. SBECM showed a fast response to local O_2 production when Mo-$BiVO_4$ was photoexcited. Bipolar current changes as low as 20 pA can be measured by recording of the corresponding ECL signal. We hypothesize that the system is able to monitor cellular respiratory activity with current changes as reported in literature in the range of 60 pA to 110 pA [23–2]. Future SBECM applications will be performed after miniaturizing of the tip electrodes and increasing the number of bipolar electrodes in the array.

6.6. Acknowledgments.

This work was supported by the Deutsche Forschungsgemeinschaft (DFG) in the framework of the Cluster of Excellence Resolv [EXC-2033 – 390677874]. C.S.S. and V.E. are grateful to the FAPESP (Fundacão de Amparo à Pesquisa do Estado de Sao Paulo [#2014/22396-6] and [#2017/12629-1]) and the German National Academic Foundation, respectively. The authors acknowledge João Ricardo Coelho Junqueira for the preparation of the Mo-$BiVO_4$ sample and setting up the measurement software.

6.7. References.

1. N. Géza, N. Lívia, Application of scanning electrochemical microscopy in bioanalytical chemistry, in: F.-M. Matysik (Ed.), Trends Bioelectroanal., 2017: pp. 281–339.

2. C. Amatore, J. Delacotte, M. Guille-Collignon, F. Lemaître, *Analyst*, **2015**, 140, 3687–3695.

3. V. Eßmann, C. Santana Santos, T. Tarnev, M. Bertotti, W. Schuhmann, *Anal. Chem.,* **2018**, 90, 6267–6274.

4. S.E. Fosdick, K.N. Knust, K. Scida, R.M. Crooks, *Angew. Chem. Int. Ed*., **2013**, 52, 10438–10456.

5. L. Bouffier, S. Arbault, A. Kuhn, N. Sojic, *Anal. Bioanal. Chem*., **2016**, 408, 7003–7011.

6. L. Bouffier, D. Zigah, N. Sojic, A. Kuhn, Recent advances in bipolar electrochemistry, in: Electroanal. Chem. A Ser. Adv. Vol. 27, CRC Press, 2017: pp. 27–117.

7. S. Goodwin, D.A. Walsh, *ACS Appl. Mater. Interfaces*, **2017**, 9, 23654–23661.

8. R. Poorghasem, R.S. Saberi, M. Shayan, M.A. Mehrgardi, A. Kiani, *Electrochim. Acta*, **2016**, 222, 1483–1490.

9. M.S. Wu, Z. Liu, H.W. Shi, H.Y. Chen, J.J. Xu, *Anal. Chem*., **2015**, 87, 530–537.

10. J.P. Guerrette, S.M. Oja, B. Zhang, *Anal. Chem.*, **2012**, 84, 1609–1616.

11. A. Arora, J.C.T. Eijkel, W.E. Morf, A. Manz, *Anal. Chem*., **2001**, 73, 3282–3288.

12. W. Xu, C. Ma, P.W. Bohn, *ChemElectroChem*., **2016**, 3, 422–428.

13. R. Hao, Y. Fan, B. Zhang, *J. Am. Chem. Soc*., **2017**, 139, 12274–12282.

14. C. Han, R. Hao, Y. Fan, M.A. Edwards, H. Gao, B. Zhang, *Langmuir*, **2019**, 35, 7180–7190.

15. T.M. Braun, D.T. Schwartz, *Front. Chem*., **2019**, 7, 340.

16. H.S. Park, K.C. Leonard, A.J. Bard, *J. Phys. Chem. C,* **2013**, 117, 12093–12102.

17. F. Conzuelo, K. Sliozberg, R. Gutkowski, S. Grutzke, M. Nebe, W. Schuhmann, *Anal. Chem*., **2017**, 89, 1222–1228.

18. R. Gutkowski, C. Khare, F. Conzuelo, Y.U. Kayran, A. Ludwig, W. Schuhmann, *Energy Environ. Sci.,* **2017**, 10, 1213–1221.

19. Y. Zu, A.J. Bard, *Anal. Chem.*, **2000**, 72, 3223–3232.

20. F. Kanoufi, Y. Zu, A.J. Bard, *J. Phys. Chem. B*, **2001**, 105, 210–216.

21. W. Miao, J.P. Choi, A.J. Bard, *J. Am. Chem. Soc.,* **2002**, 124, 14478–14485.

22. W. Miao, J.-P. Choi, Electrogenerated chemiluminescence, Marcel Dekker, Inc., New York, 2004.

23. C.S. Santos, A.J. Kowaltowski, M. Bertotti, *Sci. Rep.,* **2017**, 7, 11428.

24. M. Nishizawa, K. Takoh, T. Matsue, *Langmuir*, **2002**, 18, 3645–3649.

25. T. Kaya, Y.S. Torisawa, D. Oyamatsu, M. Nishizawa, T. Matsue, *Biosens. Bioelectron.*, **2003**, 18, 1379–1383.

Appendix

Collaboration works:
Application of microsensors in biological samples.

Appendix 1.

Investigation of the role of Peroxiredoxin Protein Prx 1 of *Aspergillus fumigatus* by monitoring H_2O_2

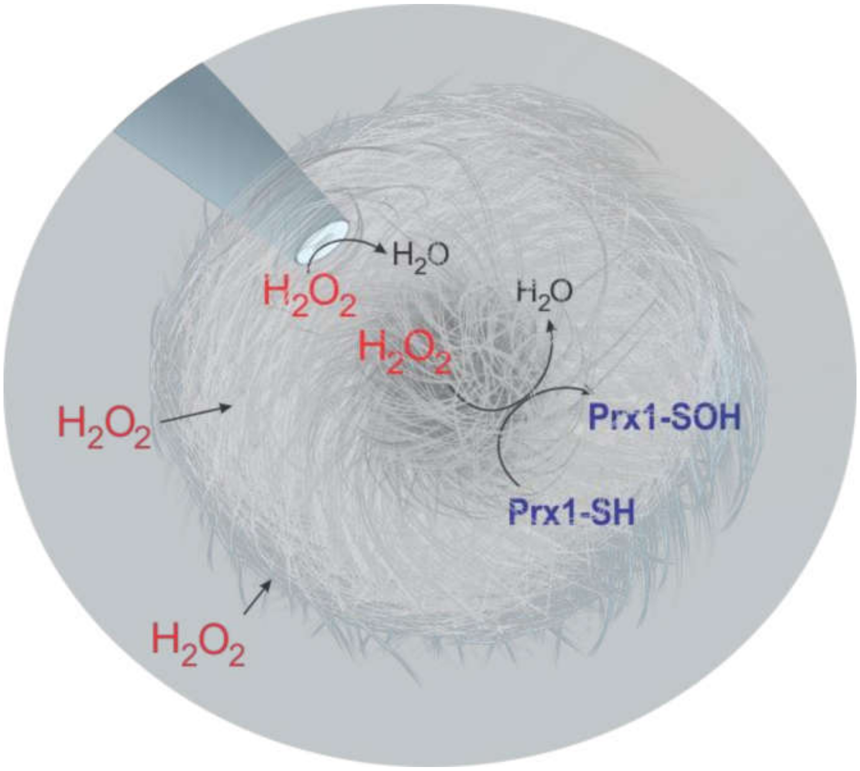

This work corresponds to the collaboration with Renata Bannitz-Fernandes, PhD student of Prof. Luis E. S. Netto (Institute of Biosciences, University of Sao Paulo). The study on defense mechanism of fungi is routinely evaluated by its inoculation in a host (mouse) and checking the animal survival index. As an option to avoid the use of mammals, here is presented a new approach involving local measurements with a microelectrode inserted on a mycelium (fungus) for further simulation of the defense mechanism by adding H_2O_2 to its the external microenvironment. The experiments confirm a specific peroxiredoxin (Prx1) present in the *Aspergillus fumigatus* fungus was responsible for the selective the degradation of H_2O_2 and the results were published in Analytical Chemistry:

Monitoring H_2O_2 inside *Aspergillus fumigatus* with an Integrated Microelectrode: The role of Peroxiredoxin Protein Prx 1. **Carla S. Santos**, Renata Bannitz-Fernandes, Alex S. Lima, Carlos A. Tairum, Iran Malavazi, Luis E. S. Netto, Mauro Bertotti. *Analytical Chemistry*,2018, 90, 4, 2587-2593

The permission of use of the text was requested to the publisher American Chemical Society (ACS) and the copy of the right is attached in the Annex. Reprinted (adapted) with permission from Analytical Chemistry 2018, 90, 4, 2587-2593 Copyright (2018) American Chemical Society.

A. S. L., C. S. S. and R. B-F. planned and designed all the experiments. R. B-F. and C. A. T. prepared the *Aspergillus fumigatus* samples. C. S. S. and A. S. L fabricated the dual-function microelectrodes. C. S. S. performed the electrochemical measurements with A. S. L support. C. S. S. and R. B-F. performed the survival tests. All authors were responsible for writing and correcting the manuscript. All authors approved the text.

A1.1. Abstract.

Peroxiredoxins (Prx) are important proteins involved in hydroperoxide degradation and are related to virulence in several pathogens, including *Aspergillus fumigatus*. In this work, *in vivo* studies on the degradation of hydrogen peroxide (H_2O_2) in the microenvironment of *A. fumigatus* fungus were performed by using an integrated Pt microelectrode. Three *A. fumigatus* strains were used to confirm the role of the cytosolic protein Prx1 in the defense mechanism of this microorganism: a wild-type strain, capable to expressing the protein Prx1; a Δ*prx* strain, whose gene *prx1* was removed; and a genetically complemented Δ*prx1::prx1* $^+$strain generated-from the Δ*prx1* and in which the gene *prx1* was re-introduced. The fabricated microelectrode was shown to be a reliable inert probe tip for *in situ* and real-time measurements of H_2O_2 in such microenvironments, with potential applications in investigations involving the mechanism of oxidative stress.

A1.2. Introduction.

Recent advances in transplant medicine have substantially reduced the overall morbimortality associated with these clinical approaches. However, immunosuppressive regimens required for the transplantation procedures are the main cause of the increased incidence of opportunistic infections in this group of immunosuppressed patients worldwide [1–3]. Among the leading causative agents of these nosocomial infections is the mold *Aspergillus fumigatus*, which causes invasive pulmonary aspergillosis (IA), a life-threatening infection which kills 60-90% of the infected patients with prolonged neutropenia [3,4]. IA is launched by the inhalation of the highly dispersive and abundant conidia of this fungus that subsequently reach the lungs, germinate and colonize the tissue [5,6]. Following *A. fumigatus* conidia inhalation, the respiratory immune system coordinates several responses that cause fungal clearing and precludes infection in the immune competent host. These events include killing by oxidative (peroxides, superoxides and hydroxyl radical) and non-oxidative (hydrolases, lipases, and DNases) mechanisms [7–10]. Specifically, the oxidative response plays a pivotal role in fungal clearance [11]. An evidence for that is the strong positive correlation between deficient reactive oxygen species (ROS) production and the high incidence of IA (26% to 45%) in patients with the genetic disorder called Chronic Granulomatous Disease (CGD), a condition that causes the immune system to malfunction where innate immune cells cannot elicit the oxidative burst [12,13].

To successfully colonize the host, pathogens must nullify the host-driven ROS release [14]. Among the enzymatic detoxifying defenses, peroxiredoxins (Prx) play an important role in hydroperoxide removal [15] and also contribute for the regulation of peroxide levels within cells. Importantly, Prx are involved in virulence in several pathogens [14,16–19], including *A. fumigatus* [20]. These enzymes are often presented at high levels in different cell types and compartments, where they can rapidly and efficiently reduce hydroperoxides [21]. Prx are cysteine-based peroxidases that contain one (1-Cys) or two (2-Cys) conserved Cys residues for their activity [22], presenting elevated catalytic rates ranging from 10^6 to 10^8 M^{-1} s^{-1} [23–25].

There are still several questions in the understanding on how the fungus decomposes peroxide *in vivo* and how these reactions impact the fungal cell physiology. Direct determination of H_2O_2 levels in the fungus extract is technically complex because this molecule can be oxidized. In addition, information regarding the sub-cellular localization of the H_2O_2 molecules is lost in cell-free approaches. Besides the spatial-temporal limitations, the H_2O_2 real-time measurements are also a challenge in filamentous fungi cell biology. Currently, most of the available methods for H_2O_2 determinations are indirect and therefore have limited specificity. Determinations based on genetically encoded H_2O_2 probes have also been developed [26], however, limitations associated with this approach include in some cases artefacts due to pH effects within the cells [27]. Furthermore, not all organisms are amenable for genetic manipulation.

Electrochemical sensors are generally easy to use, compact and portable, relatively low-cost and have low power requirements. Moreover, there is no need for sample collection, preservation and transportation, as well as laborious pretreatment procedures to make the target compound available for further analysis in remote laboratories. Hence, they are an attractive tool to get fast and real-time information on changes in the concentrations of chemical species. If electrochemical sensors are fabricated in micrometric dimensions, additional advantages are expected as chemical information can be extracted with high spatial resolution. Because mass-transport is very fast and the influence of the capacitive response is reduced for microelectrodes, information can be obtained in microscopic domains with high sensitivity. Indeed, such valuable information can have high impact on the study of *A. fumigatus* biology and in host pathogens interaction.

Accordingly, in this paper we show our efforts to monitor the degradation of H_2O_2 in the important human opportunistic pathogen *A. fumigatus* by using a microelectrode inserted in the mycelium clump environment. To our knowledge, this is the first time a microelectrode was applied as an inert tool to measure degradation of H_2O_2 in fungus. We have decided to analyze the Prx1 participation in H_2O_2 detoxification once this cytosolic protein is important to oxidative defense and it is the major 1-Cys Prx involved in virulence of *A. fumigatus* [28]. Therefore, wild-type, Δ*prx* and Δ*prx1::prx1*$^+$ strains were compared according to their capability of detoxifying exogenous H_2O_2 using the proposed methodology.

A1.3. Experimental section.

A1.3.1. Chemicals.

Reagents were of analytical grade (purity > 99%) and used as received. Potassium ferricyanide, potassium chloride, hydrogen peroxide and catalase (C-40) were purchased from Sigma Aldrich. All solutions were prepared using water purified via a Nanopure Infinity system from Barnstead (Dubuque, IA - USA). Measurements in absence of oxygen were performed in solutions purged with argon (Air Products SA - Brasil).

A1.3.2. Strains, culture and preparation of *Aspergillus fumigatus*.

The *A. fumigatus* strains used in this study were: wild-type (Δ*akuB*^{KU80})[2]; Δ*prx1*; and the respective complemented strain (Δ*prx1::prx1*$^{+}$)[43]. All the strains were maintained in complete medium [YG; glucose 2% (w/v), 0.5% yeast extract (w/v) and trace elements)] or minimal medium [MM; glucose 1% (w/v), a high nitrate salt solution and trace elements, pH 6.5]. The composition of the trace elements and nitrate salt solution were described previously[4]. For solid media, 2% agar (w/v) was added.

In order to obtain the conidia solution, the fungus was grown in YG plates at 37° C for 72 hours. The conidia were collected scraping the plate with 15 mL water (per plate) using a disposable Pasteur pipette. The solution was filtered using Miracloth (Merck Millipore 475855) and counted using a Neubauer chamber. 1×10^{6} conidia from wild-type, mutant (Δ*prx1*) and complemented mutant (Δ*prx1::prx1*$^{+}$) strains were incubated in 50 mL of liquid MM at 37 °C for exactly 24 hours (200 rpm) to obtain the mycelium that was challenged with H_2O_2. At this submerged liquid culture conditions with orbital agitation, *A. fumigatus* grows as a mycelial mass, which tends to aggregate and form spherical aggregates of anastomosed hyphae (mycelium clumps). These spherical aggregates in general have 3-4 mm (diameter) and were collected and used as the *in vivo* material for the electrochemical measurements and survival assays on the above-mentioned strains.

A1.3.3. Fabrication and characterization of the Pt/AgQRCE integrated microelectrode.

The platinum microelectrode was fabricated by embedding a 25 μm diameter platinum wire (purity, 99.99%; hard, Goodfellow- UK) inside a borosilicate glass capillary tube (L, 150 mm; o.d., 1.0 mm; i.d., 0.58 mm, Sutter Instruments - USA) and sealing both materials commonly using a P-2000 Micropipette Puller (Sutter Instrument Company - USA). In order to perform local measurements and facilitate the insertion of the sensor into the fungus, the external body of the microelectrode was coated with a coaxial silver epoxy layer (EPO-TEK – USA) to get an integrated microelectrode, where the silver coat acted as a quasi reversible counter-reference electrode[29]. Nickel chromium wires were used as electrical connectors. The resulting integrated microelectrode was characterized by cyclic voltammetry in a 15 mM $[Fe(CN)_6]^{-3}$ solution containing 0.1 M KCl and the radius of the microelectrode was found to be 5 μm by using the equation that gives the limiting current, i_L, at steady state condition ($i_L = 4nFDCr$, where D is the diffusion coefficient ($cm^2.s^{-1}$), C the bulk concentration of the electroactive species ($mol.cm^{-3}$), r the radius of the microdisc electrode (cm), n the number of electrons involved in the electrodic reaction and F the Faraday constant ($s.A.mol^{-1}$)[30]). A calibration curve for H_2O_2 was obtained by measuring steady-state current values (at -0.8 V) from cyclic voltammograms recorded in culture medium. Before and after all measurements, voltammograms were recorded in a solution containing $[Fe(CN)_6]^{3-}$ and no significance difference in the electrochemical profile was noticed, attesting the stability of the quasi reversible counter-reference electrode.

A1.3.4. *In vivo* electrochemical measurements.

All electrochemical experiments were carried out using an Autolab PGSTAT 128N potentiostat (Ecochemie – Netherlands) in a conventional electrochemical cell using the fabricated integrated microelectrode. The experiments were carried out by inserting the integrated microelectrode in the microenvironment inside the fungus (mycelium clump), which was immersed in 10 mL minimal medium (MM; glucose 1% (w/v), high nitrate salt solution, pH 6.5, trace elements) solution in a 6 cm Petri dish at room temperature. Figure A1.1 shows a scheme of the arrangement for *in vivo* measurements of H_2O_2 with the integrated microelectrode.

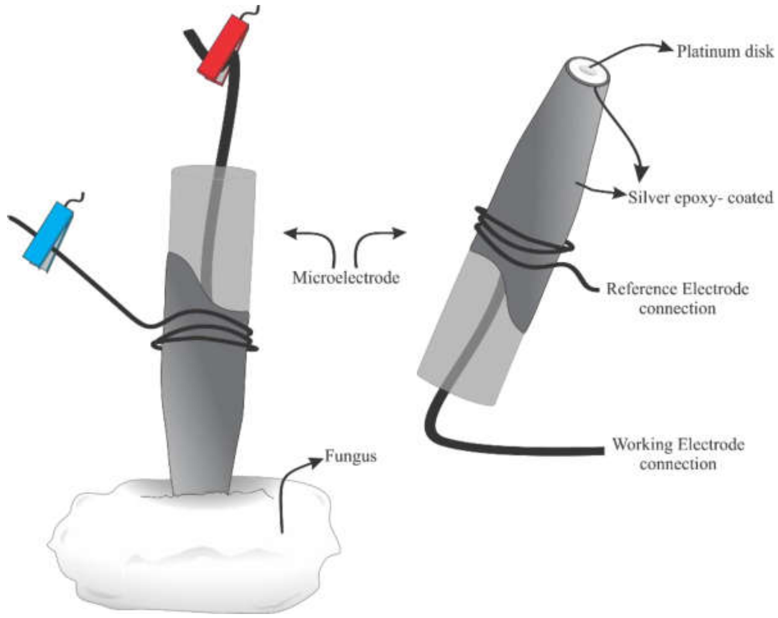

Figure A1.1. Schematic image of the Pt/AgQRCE integrated microelectrode and its insertion into a fungus (mycelium clumps).

Cyclic voltammograms were recorded sequentially every 2 minutes before and after the insertion of the probe into a fungus immersed in culture medium. Once the microelectrode was inserted, cyclic voltammograms were recorded before and after addition of aliquots (100 or 200 μL) of a 0.1 M H_2O_2 solution into the MM solution (10 mL). Solutions were carefully stirred after H_2O_2 additions using a pipette tip. All the experiments were performed in quadruplicate (N = 4) and the representative results are presented.

A1.3.5. Analysis of cell survival after oxidative stress and/or microelectrode insertion.

In order to evaluate whether the mycelium clumps survive after experiments performed according to the protocol described in the previous section (treatment with H_2O_2 and insertion of the microelectrode), studies were carried out using two different protocols. An individual mycelium clump was kept in a plate containing MM solution and it was submitted to the protocol previously described. After the assay, the individual mycelium clump was washed by immersion in MM. Four mycelium clumps per each treatment were gently inoculated in solid YG (2% glucose, 1% yeast extract, trace elements) media plates and kept at 37 °C by 48 hours, then the plates were photographed and the diameter of the colony was measured by using the software CorelDraw Graphics Suite 7 (Corel Corporation - Canada).

An additional approach was also carried out and it was based on the use of the alamarBlue® assay (Thermo Fisher Scientific), which relies on a redox reagent that gives information about the metabolic activity of cells[31–35]. If the organism is viable, the reagent becomes reduced by the mitochondrial activity and gives a response at 570 nm (pink color); if not, the reagent responds at 600 nm (blue color). Each mycelium clump was inserted in a well of 24 well plates containing 1 mL of 10 % alamarBlue® in MM and incubated at 37 °C for 24 and 48 hours. To compare the viability between each strain with the wild-type (wt), the percent difference in reduction was calculated using the Equation A1.1.

$$\frac{(\varepsilon_{OX})\lambda_{600}A\lambda_{570} - (\varepsilon_{OX})\lambda_{570}A\lambda_{600}}{(\varepsilon_{OX})\lambda_{600}A^0\lambda_{570} - (\varepsilon_{OX})\lambda_{570}A^0\lambda_{600}} \quad \text{Equation A1.1}$$

Where: $A\lambda_{570}$ = Observed absorbance reading for test well in λ = 570 nm; $A\lambda_{600}$ = Observed absorbance reading for test well in λ_2; $A^0\lambda_{570}$ = Observed absorbance reading for wt well in 570 nm; $A^0\lambda_{600}$ = Observed absorbance reading for wt well in λ_{600}; $(\varepsilon_{OX})\lambda_{600}$ = 117,216; $(\varepsilon_{OX})\lambda_{570}$ = 80,586).

A1.4. Results and discussion.

A1.4.1. Characterization of the Pt/AgQRCE integrated microelectrode and response to H_2O_2.

The electrochemical behavior of the fabricated integrated microelectrode was first assessed in a well-known system, i.e., a 15 mM $[Fe(CN)_6]^{3-}$ + 0.1 M KCl solution. The recorded cyclic voltammogram and the observed sigmoidal behavior is typical of the one obtained when mass-transport is fast (Figure A1.2A), hence there is no indication of a time-dependent event and a steady-state situation is rapidly achieved[1]. The H_2O_2 response at the fabricated integrated microelectrode was established by recording cyclic voltammograms in supporting electrolyte solution in absence of O_2 (argon was purged into the solution during 10 minutes to remove dissolved O_2) (Figure A1.2B, black curve *i*) and presence of 1 mM H_2O_2 only (Figure A1.2B, red curve *ii*). From these results, one can anticipate that the Pt/AgQRCE integrated microelectrode is a suitable sensor for measuring H_2O_2 at steady-state condition.

A calibration plot in the range 1 to 12 mM was obtained by recording cyclic voltammograms upon addition of H_2O_2 to the supporting electrolyte solution. Figure A1.3A shows results (current values measured from CVs at -0.8 V) of such experiment, including the response of the sensor after addition of catalase to the solution. Owing to the selective consumption of H_2O_2, a fast current decrease was noticeable upon addition of the enzyme, confirming the sensor responds rapidly to the target analyte. The calibration plot obtained in the experiment is shown in Figure A1.3B (i = – (3.7 nA L $mmol^{-1}$)C ; R^2 = 0.996) and a linear dependence of sensor response and H_2O_2 concentration is noticed at this concentration range.

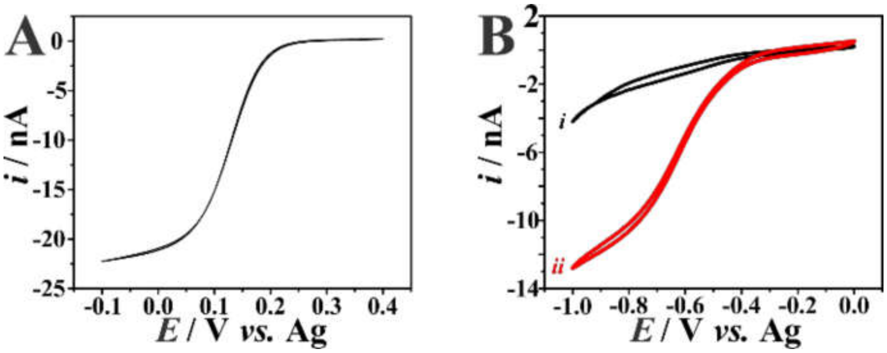

Figure A1.2. Cyclic voltammograms recorded with the Pt/AgQRCE integrated microelectrode in a 0.1 M KCl +15 mM $[Fe(CN)_6]^{3-}$ solution (A) and in a deoxygenated 0.1 M KCl solution before (black curve i) and after addition of H_2O_2 (1 mM, red curve ii) (B). υ: 0.1 V s^{-1}.

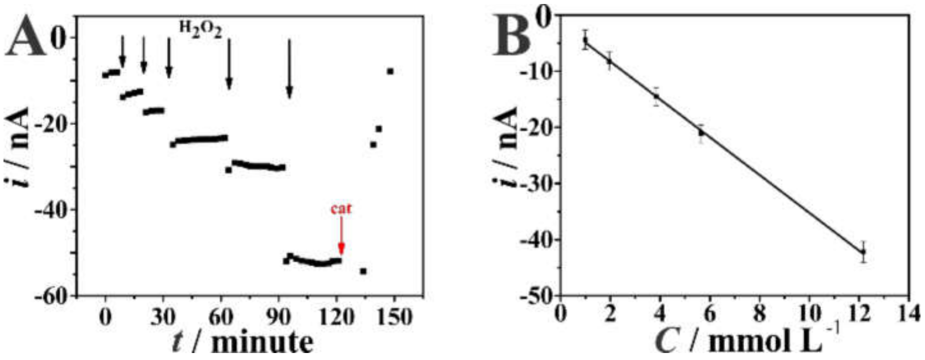

Figure A1.3. Current measured with the Pt/AgQRCE integrated microelectrode at -0.8 V from CVs recorded during consecutive additions of H_2O_2 to supporting electrolyte solution (from 1 to 12 mM, final concentration) and 100 µL of catalase (400 units mL^{-1}) (A) and calibration plot (current values were corrected by subtracting the response of the background (B).

A1.4.2. Study of H_2O_2 degradation by Prx1 in *Aspergillus fumigatus*

The integrated microelectrode was attached to a micromanipulator to provide an accurate and slow penetration in the middle of the *A. fumigatus* mycelium clump placed in culture medium (Figure A1.4A). The recorded cyclic voltammogram in culture medium is shown in Figure A1.4B (black curve) and the response corresponds to the cathodic reduction of dissolved O_2. Then, the sensor was inserted in the fungus and a new voltammogram was recorded (Figure A1.4B, red curve). In this case, a significant decrease in the faradaic response was noticed because of the lower concentration of O_2 in this microenvironment. The O_2 levels are lower in biological tissues than in aqueous solutions due to the action of bioenergetics systems such as active mitochondria[36]. Hence, the absence of faradaic response due to O_2 electrochemical reduction was used in subsequent experiments to assure the sensor was inside the fungus.

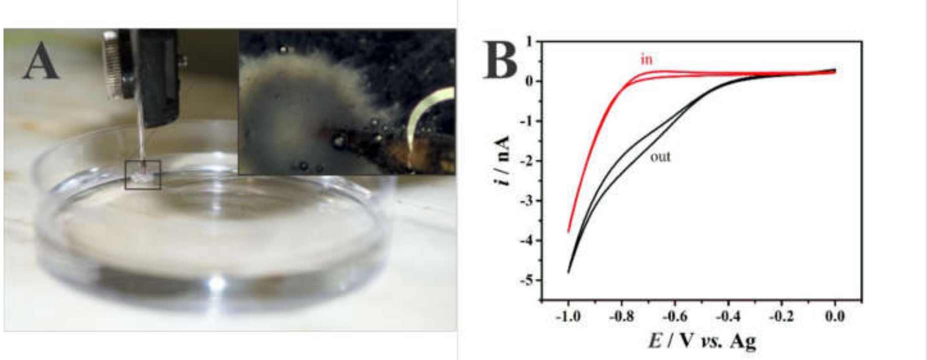

Figure A1.4. Images of the arrangement for in vivo measurements of H_2O_2 in the microenvironment of A. fumigatus (A). Cyclic voltammograms recorded with the Pt/AgQRCE integrated microelectrode in a growth medium solution (black curve) and inside the fungus (red curve) (B). υ: 0.1 V s^{-1}.

The Figure A1.5A shows results on the monitoring of H_2O_2 inside a mycelium clump by measurements of limiting current at -0.8 V from cyclic voltammograms. Before the insertion of the microelectrode in the fungus, the sensor response is due to dissolved O_2 in the MM. With the sensor inside the fungus microenvironment, cyclic voltammograms were recorded before and after repetitive additions of H_2O_2 aliquots to the culture medium. After the first addition, current values remained almost constant (first arrow, 1 mM final concentration), suggesting the H_2O_2 removing enzymes rapidly decomposed this oxidant (Figure A1.5A). A slight increase was noticed after addition of H_2O_2 to give a final concentration of 1.96 mM (second arrow) (Figure A1.5A). Reactions catalyzed by peroxiredoxins do not generate O_2, as catalases. Instead, peroxiredoxins utilize a reactive cysteine to reduce hydroperoxide to its corresponding alcohol or H_2O, in the case of H_2O_2. The overall reaction[37] catalyzed by Prx is

$$H_2O_2 + 2\ RSH \rightarrow 2\ H_2O + RSSR \quad (2)$$

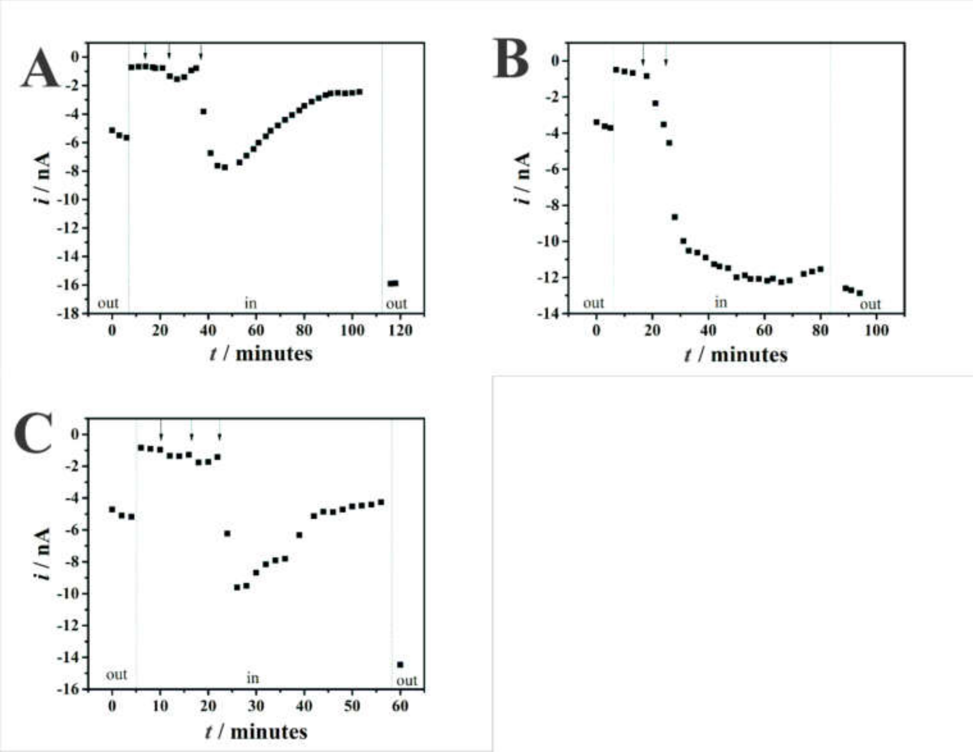

Figure A1.5. Current values measured at -0.8 V from CVs recorded with a Pt/AgQRCE integrated microelectrode in a culture medium containing A. fumigatus wild-type (A), Δprx1 mutant (B) and Δprx1::Δprx1⁺ complemented strains (C) as a function of time. Arrows indicate the addition of samples of a 100 mM H_2O_2 solution to 10 mL of culture medium to give the following final exogenous H_2O_2 concentrations: 1 mM (first arrow), 1.96 mM (second arrow) and 3.85 mM (third arrow).

Hence, one can assure that the current measured with the microelectrode inside the fungus is mainly due to H_2O_2. Thus, the current increase occurred as a consequence of the transport of exogenous H_2O_2 through the microenvironment of the fungus and the microelectrode surface. A subsequent current decrease was observed and it may be related to a response of H_2O_2 enzymatic and non-enzymatic defense mechanism[38]. Then, a new H_2O_2 aliquot was added to the culture medium (third arrow, 3.85 mM final concentration) and a much higher current increase was noticed. In this case, H_2O_2 was provided to the enzymes in a higher level, which was probably not instantly degraded. Moreover, the formation of bubbles at the mycelium was noted, which might be due to H_2O_2 degradation to O_2 by the action of the five catalases present in the genome of *A. fumigatus* (see the bubbles in the inset of Figure A1.4A). Notwithstanding, after 10 minutes a new gradual current decrease was observed probably due to H_2O_2 removing enzymes, such as peroxiredoxin Prx1 and catalase[39]. In most aerobic cells, there are tens of enzymes capable of removing hydrogen peroxide. Indeed, both catalase and peroxiredoxins react with hydrogen peroxide at extremely rapid rates (10^6 - 10^7 M^{-1} s^{-1}) and cooperate in the protection of microorganisms against this oxidant [40]. Nevertheless, factors such as compartmentalization, substrate affinity (K_M) and turn over (k_{cat}) may favor a particular enzyme to be the main hydrogen peroxide removal enzyme in a particular condition. Peroxiredoxins besides reacting extremely rapid with H_2O_2, are also highly abundant enzymes and thereby it has been increasingly appreciated that these Cys-based peroxidases are the major H_2O_2 removal enzymes in cells [41,42]. In the last section of this experiment, the sensor was removed from the fungus microenvironment, remaining in contact with exogenous H_2O_2 present in the culture medium. As expected, current values were higher than those measured inside the fungus microenvironment, where several antioxidant systems for H_2O_2 removal are available. One can also conclude from this experiment that the rate of H_2O_2 decomposition catalyzed by enzymes is quite fast, but the similar natural process (decomposition to water and O_2) is much slower and could not be noticed in the time window of the experiments in this work.

Evidences of the participation of Prx1 in the consumption of H_2O_2 by *A. fumigatus* were confirmed by repeating experiments with a strain in which the *prx1* gene was deleted (Δ*prx1*). Again, lower current values were obtained from experiments employing the Δ*prx1* strain compared to the values recorded in solution. In contrast to the wild-type strain, no decrease in the concentration of H_2O_2 was observed in the Δ*prx1* strain (Figure A1.5B), indicating a major role of Prx1 in the decomposition of this oxidant, at least in the conditions employed herein. From Figure A1.5B one can notice that a steady current value was recorded a few minutes after the final addition of H_2O_2, indicating the equilibrium between H_2O_2 inside and outside the fungus. As a matter of fact, the current value obtained before removing the sensor from the Δ*prx1* strain was just slightly lower than the one recorded outside the mycelium in the end of the experiment. From the calibration plot, maximum H_2O_2 concentration values found in the microenvironments using *prx1* and Δ*prx1* strains were 1.7 mM and 1.6 mM, respectively, and in the end of the experiments such values decreased to 0.44 and 1.5 mM. Roughly one can conclude the wild-type strain decomposed 71 ± 7% (n = 4) of H_2O_2, whereas this value was much lower for the mutant strain, 8 ± 3% (Figure A1.6).

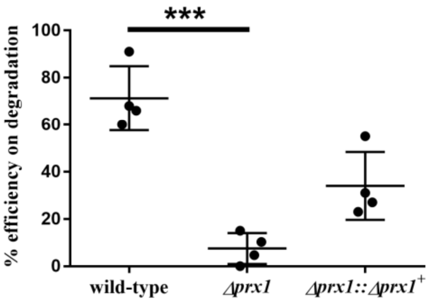

Figure A1.6. Efficiency of the H_2O_2 degradation in percentage for each strain. N = 4. One-way ANOVA significantly different $p < 0.05$. Dunn's multiple comparisons test: wild-type vs. Δprx1 $p = 0.0051$; wild-type vs. Δprx1:: $Δprx1^+$ $p = 0.3502$; Δprx1 vs. Δprx1:: $Δprx1^+$ $p = 0.3502$.

Finally, a control experiment was performed using the Δ*prx1::*Δ*prx1*$^+$ complemented strain, in which the *prx1* gene was re-introduced as an ectopic transgene. This is important because gene replacement procedures can sometimes generate mutations, besides that targeted to the *prx1* locus. As expected, the results obtained with wild-type and Δ*prx1::*Δ*prx1*$^+$ strains were highly similar (Figure A1.5A, C). The complemented strains decomposed 34 ± 7% of H_2O_2, a higher value than the one corresponding to the mutant strain (8%), further suggesting the relevance of Prx1 in the H_2O_2 decomposition by *A. fumigatus*. Altogether, we can overall speculate that all the other antioxidant systems which include the catalases and the other two *A. fumigatus* peroxiredoxins [28] are not sufficient to decompose H_2O_2 to reach wild type levels of this molecule in the genetic background of the Δ*prx1* null mutant strain.

A1.4.3. Evaluation of *Aspergillus fumigatus* survival after oxidative stress and/or microelectrode insertion.

In addition to the oxidative stress effect, the inserted microelectrode might also cause some physical damage to the mycelium clumps, and one can speculate whether such protocol may decrease the viability of the fungi. Hence, additional experiments were performed to examine whether the fungi remained alive after the electrochemical experiments performed according to the proposed protocol.

The mycelium clumps were submitted to the same protocol carried out in the H_2O_2 degradation assay with the microelectrode, followed by inoculation of the individual fungus in plates containing solid medium (YG solution with 2 % agar, w/v) to evaluate the fungus viability. The results showed that the mycelium clumps of the three strains (wild type, Δ*prx1* and *Δprx1::Δprx1*$^+$) developed hyphae and conidia, independently of the contact with H_2O_2 or the microelectrode insertion (Figure A1.7). Indeed, in all cases the recovered colonies presented similar diameter after 48 hours of growing (Table A1.1).

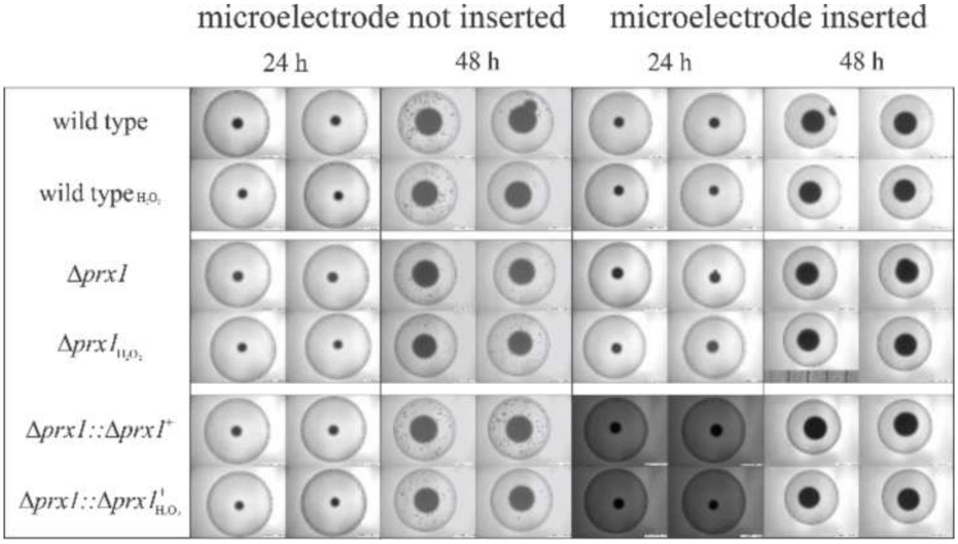

Figure A1.7. Images of plates containing a mycelium after 24 and 48 hours. Each fungus was exposed to H_2O_2 and experiments were carried out in two different conditions: microelectrode inserted and not inserted in the fungus. N=4. Plates were kept at 37 ^oC.

Similar conclusions were achieved by using the alamarBlue® assay, according to which the metabolic activity of the fungus can be evaluated by measuring the relative growth calculated from equation (1) (Figure A1.8). Again, no difference was observed among the three strains in the different experimental conditions, i.e., all tests with fungi stuck with the microelectrode and/or exposed to H_2O_2 presented pink color, indicating mitochondrial activity, whereas blue color (no mitochondrial activity) was noticed for the control (without fungus) (Figure A1.9). Curiously, wild-type and Δprx1:: Δprx1$^+$ strains showed the production of conidia (dark dots) (Figure A1.10) after 48 hours of incubation, and this was not observed for the mutant Δ*prx1* strain. This may indicate a delay in the conidia development for the mutant strain, which is independent of the microelectrode insertion or oxidative stress.

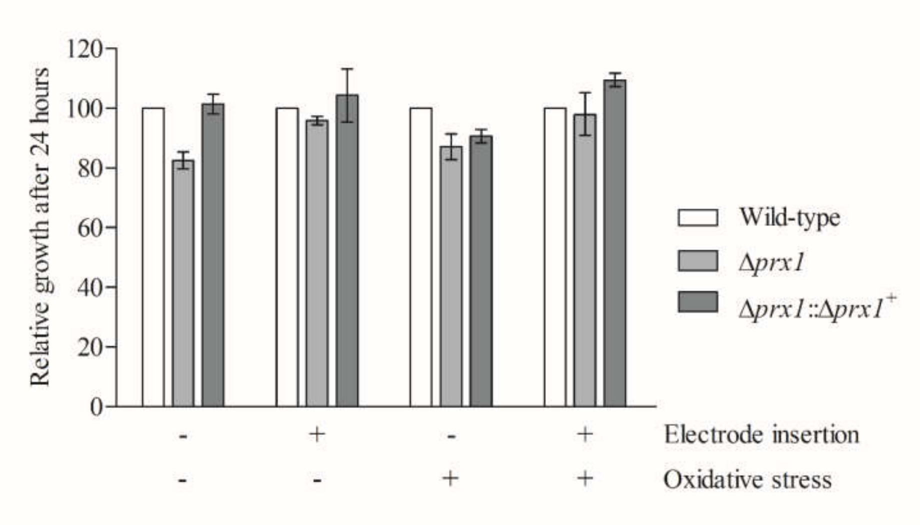

Figure A1.8. Relative growth after 24 hours using the alamarBlue® assay. The absorbance was measured at 600 nm and 570 nm in order to detect metabolic activity. Wild-type strain calculated measurements were considered as 100% growth. No significant differences were found among the groups.

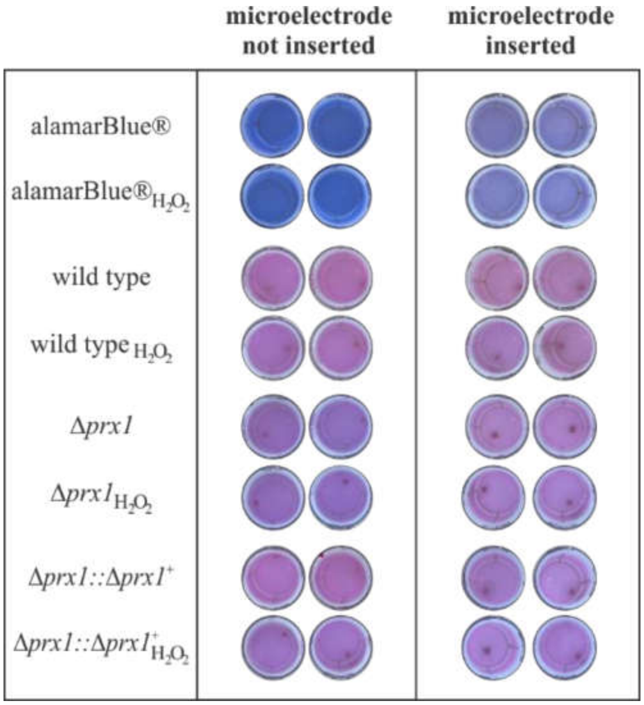

Figure A1.9. Images of wells containing one mycelium (exposed and not exposed to H_2O_2) after 24 hours and in two different conditions: microelectrode inserted and not inserted in the fungus. N=4. Wells were kept at 37 °C.

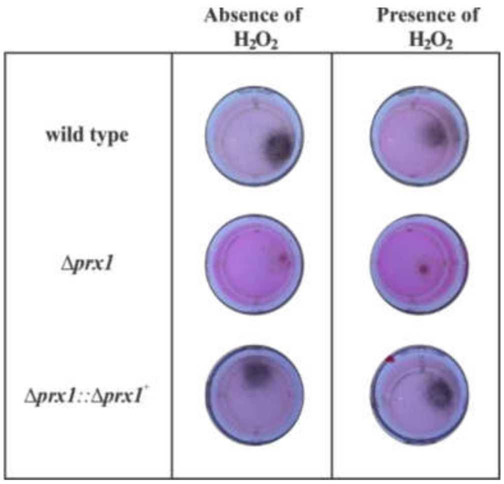

Figure A1.10. Images of wells containing one mycelium (exposed and not exposed to H_2O_2) after 48 hours. N=4. Wells were kept at 37 °C.

Table A1.1. Diameter of the colony (in centimeters) after 48 hours of growing at 37 °C in YG plates after different protocols: insertion of microelectrode and exposition of H_2O_2.

Diameter of the colony / cm				
Strains	Not exposed to H_2O_2		Exposed to H_2O_2	
	Microelectrode		Microelectrode	
	inserted	not inserted	Inserted	not inserted
wild-type	4.2±0.1	4.3±0.3	4.1±0.1	4.1±0.1
Δprx1	4.3±0.1	4.1±0.1	4.1±0.1	3.9±0.1
Δprx1::Δprx1$^+$	4.5±0.2	4.3±0.1	4.1±0.1	4.1±0.1

Even though the Δ*prx1* mutant showed a lower capacity to detoxify H_2O_2 compared to the wild-type and complemented *Δprx1::Δprx1*$^+$ strains (Figure A1.5), the results of experiments described in this section unequivocally demonstrated the fungus was alive and presented similar growth comparing to the wild-type, even when it was submitted to oxidative stress conditions and after the insertion of the microelectrode. Therefore, current changes noticed for experiments with the Δ*prx1* mutant are likely to be a consequence of the absence of the enzyme and not by cell death. Additionally, the inability of the mutant fungus to reduce H_2O_2 highlights the importance of Prx1 in *A. fumigatus* homeostasis. Indeed, the loss-of-function of this peroxiredoxin in *A. fumigatus* leads to attenuated virulence in mice model for invasive pulmonary aspergillosis, further emphasizing the *in vivo* importance of this protein for this opportunistic pathogen [28].

A1.5. Conclusions.

The results shown in this work demonstrate that the fabricated Pt/AgQRCE integrated microelectrode can be used as a sensing system to get fast and *in-situ* reliable information on the concentration of H_2O_2 in small biological environments. Here, we unprecedentedly implemented this approach to monitor the H_2O_2 concentration inside of a filamentous fungus (*A. fumigatus* mycelium clumps) after its transfer from a culture medium. Therefore, it was possible to evaluate the H_2O_2 concentration in the surrounding solution, its diffusion through the fungus and subsequent decomposition by a sort of non-enzymatic and enzymatic molecules. Interestingly, a specific antioxidant protein Prx1 from the peroxiredoxin family seems to be essential for H_2O_2 detoxification in *A. fumigatus,* once the mutant strain Δ*prx1* is incapable of restoring its basal concentration after exogenous addition. This finding reinforces the advantages of the application of this integrated microelectrode as an inert tool for H_2O_2 measurements in different microenvironments and further evaluation of the role of other proteins and enzymes. It also opens up the possibility of large scale analysis of mutant strains in this important human opportunistic pathogen aiming to understand the basis for H2O2 detoxification in filamentous fungus.

A1.6. Acknowledgments.

The authors are grateful to Aline S. Barbosa and Thiago G. P. Alegria for the outstanding technical support and the financial support from CNPq (Conselho Nacional de Desenvolvimento Científico e Tecnológico), CAPES (Coordenação de Aperfeiçoamento de Pessoal de Nível Superior) and FAPESP (Fundação de Amparo à

Pesquisa do Estado de São Paulo). Grants #2015/02095-4, #2014/22396-6, #2015/20776-9 and #2013/14955-2 from FAPESP to A.S.L., C.S.S., M.B., and R.B-F., respectively.

A1.7. References.

1. Vazquez, J. A.; Miceli, M. H.; Alangaden, G. *Ther. Adv. Infect. Dis.* **2013**, 1, 85–105.
2. Silveira, F. P.; Husain, S. *Med. Mycol.* **2007**, 45, 305–320.
3. Brown, G. D.; Denning, D. W.; Gow, N. A. R.; Levitz, S. M.; Netea, M. G.; White, T. C. *Sci. Transl. Med.* **2012**, 4 , 1–9.
4. Brakhage, A. A.; Bruns, S.; Thywissen, A.; Zipfel, P. F.; Behnsen, J. *Curr. Opin. Microbiol.* **2010**, 13, 409–415.
5. Lessing, F.; Kniemeyer, O.; Wozniok, I.; Loeffler, J.; Kurzai, O.; Haertl, A.; Brakhage, A. A. *Eukaryot. Cell* **2007**, 6, 2290–2302.
6. Latgé, J.-P. *Clin. Microbiol. Rev.* **1999**, 12, 310–350.
7. Vinh, D. C. *Lancet Infect. Dis.* **2011**, 11, 780–792.
8. Heinekamp, T.; Schmidt, H.; Lapp, K.; Pähtz, V.; Shopova, I.; Köster-Eiserfunke, N.; Krüger, T.; Kniemeyer, O.; Brakhage, A. A. *Semin. Immunopathol.* **2015**, 37, 141–152.
9. Nauseef, W. M. *Immunol. Rev.* ***2007,*** 219, 88–102.
10. Dambuza, I. M.; Levitz, S. M.; Netea, M. G.; Brown, G. D. *Microbiol. Spectr.* **2017**, 5, 1–16.
11. Chai, L. Y. A.; Netea, M. G.; Vonk, A. G.; Kullberg, B.-J. *Med. Mycol.* **2009**, 47, 227–236.
12. Marciano, B. E.; Spalding, C.; Fitzgerald, A.; Mann, D.; Brown, T.; Osgood, S.; Yockey, L.; Darnell, D. N.; Barnhart, L.; Daub, J.; Boris, L.; Rump, a. P.; Anderson, V. L.; Haney, C.; Kuhns, D. B.; Rosenzweig, S. D.; Kelly, C.; Zelazny, A.; Mason, T.; DeRavin, S. S.; Kang, E.; Gallin, J. I.; Malech, H. L.; Olivier, K. N.; Uzel, G.; Freeman, a. F.; Heller, T.; Zerbe, C. S.; Holland, S. M. *Clin. Infect. Dis.* **2014**, 60, 1176–1183.
13. Segal, B. H.; Romani, L. R. *Med. Mycol.* **2009**, 47, S282-s2890.
14. Mir, A. A.; Park, S.-Y.; Sadat, M. A.; Kim, S.; Choi, J.; Jeon, J.; Lee, Y.-H. *Sci. Rep.* **2015**, 5 , 11831.
15. Perkins, A.; Parsonage, D.; Nelson, K. J.; Ogba, O. M.; Cheong, P. H.-Y.; Poole,

L. B.; Karplus, P. A. *Structure* **2016**, 24, 1668–1678.

16. Rouhier, N.; Gelhaye, E.; Gualberto, J. M.; Jordy, M.; Fay, E. De; Hirasawa, M.; Duplessis, S.; Lemaire, S. D.; Frey, P.; Martin, F.; Manieri, W.; Knaff, D. B.; Jacquot, J.; Poincare, H.; R, V. F. N.; Mole, I. D. B. **2004**, 134 , 1027–1038.

17. Dons, L. E.; Mosa, A.; Rottenberg, M. E.; Rosenkrantz, J. T.; Kristensson, K.; Olsen, J. E. *Pathog. Dis.* **2014**, 70, 70–74.

18. Dayer, R.; Fischer, B. B.; Eggen, R. I. L.; Lemaire, S. D. *Genetics* **2008**, 179, 41–57.

19. Kaihami, G. H.; de Almeida, J. R. F.; dos Santos, S. S.; Netto, L. E. S.; de Almeida, S. R.; Baldini, R. L. *PLoS Pathog*. **2014**, DOI: 10.1371/journal.ppat.1004442.

20. Hillmann, F.; Bagramyan, K.; Straßburger, M.; Heinekamp, T.; Hong, T. B.; Bzymek, K. P.; Williams, J. C.; Brakhage, A. A.; Kalkum, M. *Sci. Rep.* **2016**, 6, 33396.

21. Perkins, A.; Poole, L. B.; Karplus, P. A. *Biochemistry* **2014**, 53, 7693–7705.

22. Chae, H. Z.; Robison, K.; Poole, L. B.; Church, G.; Storz, G.; Rhee, S. G. *Proc. Natl. Acad. Sci. U. S. A.* **1994**, *91,* 7017–7021.

23. Tairum, C. A.; Santos, M. C.; Breyer, C. A.; Geyer, R. R.; Nieves, C. J.; Portillo-Ledesma, S.; Ferrer-Sueta, G.; Toledo, J. C.; Toyama, M. H.; Augusto, O.; Netto, L. E. S.; de Oliveira, M. A. *Sci. Rep.* **2016**, 6, 33133.

24. Netto, L. E. S.; Antunes, F. *Mol. Cells* **2016**, *39,* 65–71.

25. Flohe, L.; Toppo, S.; Cozza, G.; Ursini, F. *Antioxid. Redox Signal.* **2011**, 0, 1–18.

26. Morgan, B.; Sobotta, M. C.; Dick, T. P. *Free Radic. Biol. Med.* **2011**, 51, 1943–1951.

27. Roma, L. P.; Duprez, J.; Takahashi, H. K.; Gilon, P.; Wiederkehr, A.; Jonas, J.-C. *Biochem. J.* **2012**, 441, 971–978.

28. Godoy, K.F., Rocha, M.C., Bannitz-Fernandes, R., Fabri, J.H.T.M, Barbosa, M.M.F., de Castro, P.A., Goldman, G.H., da Cunha, A.F., Netto, L.E.S., de Oliveira, M.A., *Sci. Report.,* **2018**, 8, 12314.

29. Lima, A. S.; Prieto, K. R.; Santos, C. S.; Paula Valerio, H.; Garcia-Ochoa, E. Y.; Huerta-Robles, A.; Beltran-Garcia, M. J.; Di Mascio, P.; Bertotti, M. *Biosens. Bioelectron.* **2018**, 99, 108–114.

30. Bard, A. J.; Faulkner, L. R. *Electrochemical Methods: Fundamentals and applications*, 2nd ed.; John Wiley & Sons, 2001.

31. Rampersad, S. N. *Sensors* **2012**, 12, 12347–12360.

32. Repp, K. K.; Menor, S. A.; Pettit, R. K. *Med. Mycol.* **2007**, 45, 603–607.

33. Fai, P. B.; Grant, A. *Chemosphere* **2009**, 74, 1165–1170.

34. Meletiadis, J.; Mouton, J. W.; Meis, J. F. G. M.; Bouman, B. A.; Verweij, P. E.; Roilides, E.; Maglaveras, N.; Abrahamsen, T.; Gaustad, P.; Denning, D. W.; Rodriguez-Tudela, J. L.; Petrikkos, G. *J. Clin. Microbiol.* **2002**, 40, 2876–2885.

35. Yamaguchi, H.; Uchida, K.; Nagino, K.; Matsunaga, T. *J. Infect. Chemother.* **2002**, 8, 374–377.

36. Solaini, G.; Baracca, A.; Lenaz, G.; Sgarbi, G. *Biochim. Biophys. Acta - Bioenerg.* **2010**, 1797, 1171–1177.

37. Netto, L. E. S.; Chae, H. Z.; Kang, S. W.; Rhee, S. G.; Stadtmant, E. R. *J. Biol. Chem.* **1996**, 271, 15315–15321.

38. Halliwell, B.; Gutteridge, J. M. C. *Free Radicals in Biology and Medicine*, 5th edition; 2015.

39. Fréalle, E.; Aliouat-Denis, C. M.; Delhaes, L.; Hot, D.; Dei-Cas, E. *Curr. Pharm. Des.* **2013**, 19, 3713–3737.

40. Mishra, S.; Imlay, J. *Arch. Biochem. Biophys.* **2012**, 525, 145–160.

41. Winterbourn, C. C.; Hampton, M. B. *Free Radic. Biol. Med.* **2008**, 45, 549–561.

42. Dagnell, M.; Pace, P. E.; Cheng, Q.; Frijhoff, J.; Östman, A.; Arnér, E. S. J.; Hampton, M. B.; Winterbourn, C. C. *J. Biol. Chem.* **2017**, 292, 14371–14380.

43. Rocha, M. C., Godoy, K. F., Bannitz-Fernandes, R., Fabri, J. H. T. M, Barbosa, M. M. F., de Castro, P. A., Almeida, F., Goldman, G. H., da Cunha, A. F., Netto, L. E. S., de Oliveira, M.A., Malavazi, I.. Sci. Report, **2018**, 8, 12314.

Appendix 2.

Monitoring of H_2O_2 production induced by root-inoculated endophytic bacteria in *Agave tequilana* leaves

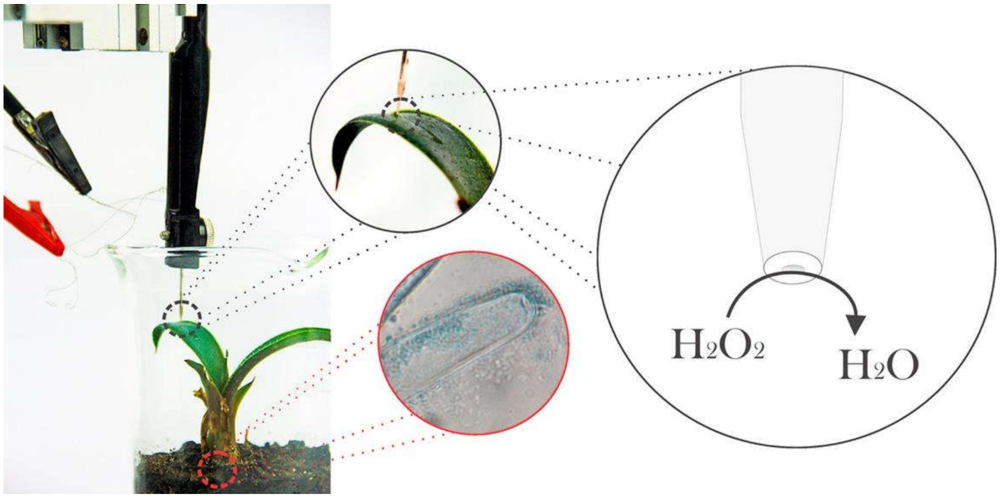

This work corresponds to a collaboration with Katia R. Prieto and Prof. Paolo Di Mascio (Department of Biochemistry, Institute of Chemistry, University of Sao Paulo) and Prof. Miguel J. Beltran-Garcia (Department of Chemistry ICET, Universidad Autonoma de Guadalajara, Mexico).

Agave tequilana is an important plant to the mexican economy because of the Tequila production. The cultivation of *Agave tequilana* is challenging when pathogenic species such as fungi or bacteria are found. However, the plant also has a probiotic environment and these endophytic microorganisms can transfer organic nitrogen, specially under nutrient-limiting conditions. The starving stress can induce the plant to produce large quantities of H_2O_2 to degrade bacterial cells, including the probiotics. Herein, we used microelectrodes to detect the H_2O_2 production and to monitor the local pH in the leaves of *Agave tequilana* in the presence of probiotic bacteria under nutrition stress conditions. Such strategy was considered to be relevant because the electrochemical sensor are innocent probes and the fast response allowed measurement with almost no manipulation of the plant to be performed. Hence, the approach used in this work is likely to correspond to an *in vivo* measurement. The work was published in Biosensor and Bioelectronics:
In-vivo electrochemical monitoring of H_2O_2 production induced by root-inoculated endophytic bacteria in *Agave tequilana* leaves Alex S. Lima, Kátia R. Prieto, **Carla S. Santos**, Hellen Paula Valerio, Evelyn Y. Garcia-Ochoa, Aurora Huerta-Robles, Miguel J. Beltran-Garcia, Paolo Di Mascio, Mauro Bertotti. *Biosensors and Bioelectronics,* 2018, 99, 108-114.

The permission of use of the text was requested to the publisher Elsevier and the copy of the right is attached in the Annex. However, the authors can use their articles, in full or in part, for a wide range of scholarly, non-commercial purposes.

A. S. L. and K. R. P. idealized the experiments. A. S. L. and C. S. S. planned and performed the electrochemical measurements. E. Y. G-O, A. H-R. provided the characterized the agave and bacteria in Mexico. K. R. P and H. P. V cultivated and prepared the biological samples, and performed the visualization of H_2O_2 in *A. tequilana* roots after *E. cloacae* inoculation. A. S. L., C. S. S., K. R. P. and M. J. B-G. discussed the results. A. S. L., K. R. P. and C. S. S. prepared the figures. All authors were responsible for writing and correcting the manuscript. All authors approved the text.

A2.1. Abstract.

A dual-function platinum disc microelectrode sensor was used for *in-situ* monitoring of H_2O_2 produced in *A. tequilana* leaves after inoculation of their endophytic bacteria *(Enterobacter cloacae*). Voltammetric experiments were carried out from 0.0 to -1.0 V, a potential range where H_2O_2 is electrochemically reduced. A needle was used to create a small cavity in the upper epidermis of *A. tequilana* leaves, where the fabricated electrochemical sensor was inserted by using a manual three-dimensional micropositioner. Control experiments were performed with untreated plants and the obtained electrochemical results clearly proved the formation of H_2O_2 in the leaves of plants 3 hours after the *E. cloacae* inoculation, according to a mechanism involving endogenous signaling pathways. In order to compare the sensitivity of the microelectrode sensor, the presence of H_2O_2 was detected in the root hairs by 3,3-diaminobenzidine (DAB) stain 72 hours after bacterial inoculation. *In-situ* pH measurements were also carried out with a gold disc microelectrode modified with a film of iridium oxide and lower pH values were found in *A. tequilana* leaves treated with bacteria, which may indicate the plant produces acidic substances by biosynthesis of secondary metabolites.

This microsensor could be an advantegous tool for further studies on the understanding of the mechanism of H_2O_2 production during the plant-endophyte interaction.

A2.2. Introduction.

Agave tequilana Weber blue variety, usually known as "Agave azul", is one of the most important economically crops for Mexico [1]. The stem (or "piña") is cooked to obtain a juice with higher fructose, sucrose and glucose contents, then it is fermented and distilled to produce Tequila, the principal alcoholic beverage in Mexico consumed worldwide[2,3]. The agave plant is perennial and its metabolic activity as well as its physiological and morphological characteristics support its development in arid and semiarid environments, so it can be adapted to several habitats [4]. However, some of *Agave* species have been domesticated and grown in large extensions of land, harboring millions of plants with commercial purposes. This agro-cultural practice has induced fungal and bacterial diseases in agave plantations, hence reducing the number of plants useful for tequila production.

In plants, the microorganisms belonging to their own "plant microbiome" might be an important alternative for disease control. Some of these microorganisms are considered to be "probiotic" and the decrease of their population can cause the development of diseases or difficulties for the plants to adapt to the environment [5,6]. Among the components of plant microbiomes, the microbial endophytes have attracted the attention [7,8]. These microorganisms act as nitrogen fixers, facilitate the assimilation of nutrients, produce phytohormones, antibiotics, provide resistance to stress through the elimination of ethylene and promote plant growth [9]. There are only a few reports in the literature on the endophytic microorganisms that colonize *A. tequilana.* [10–13].

The striking release of reactive oxygen species (ROS) in plants, including the versatile

H_2O_2, is correlated with a number of plant-pathogen interactions or environmental stresses and may play an important role in disease resistance. A number of possible mechanisms for ROS release have been proposed: direct killing, involvement in structural changes in the cell wall, promotion of programmed cell death under hypersensitive response and induction of the expression of defense genes. The release of H_2O_2 by plants is also triggered by beneficial endophytic microbes, such as endogenous signaling molecules, which control or mediate symbiotic responses [14], or catalysts that can synthesize oxygenous molecules with biological activity [15]. On the other hand, White et al. [16] proposed that endophytic microorganisms can transfer organic nitrogen to plants growing under nutrient-limiting conditions according to a process called "oxidative nitrogen scavenging". During this nutritional stress condition, plants release H_2O_2 in large quantities to degrade bacterial cells and thus get nutrients as nitrogen [13,17]. Accordingly, the detection of H_2O_2 may give crucial information for the understanding of the biological signaling pathways involved in the degradation of bacterial cells or in the bacterial colonization process.

Sensitive and selective techniques have been used for detecting H_2O_2 in leaves, including its cellular localization and *in vivo* concentration measurements. Fluorescent probes are largely used for such goal [18–20] and results on the evaluation of the versatility of different probes for H_2O_2 detection have been reported in the literature [21]. Even though the use of such optical probes is widespread, there are some drawbacks, including the need to separate plant samples, the time-consuming steps, and the stress resulting from the detachment of the leaves. Moreover, non-specific fluorescent probes lack selectivity towards H_2O_2 detection, as other ROS may also respond. Hence, despite the emergence of new fluorescent dyes for detecting intracellular compounds, analytical methods based on the use of electrochemical sensors have received great attention as they can give relevant insights in the study of biochemical processes in plants. As for H_2O_2, significant efforts have been driven towards the design of novel sensing platforms in an attempt to improve the analytical performance of the developed sensors [22–26]

Electrochemical methods are advantageous because of their simplicity, low cost, speed of use and sensitivity, as well as the possibility of performing measurements in microscopic environments due to miniaturization of sensor elements [27–34]. This facilitates the collection of chemical information with high spatial resolution, and measurements can be done in living cells and tissues with minimized perturbation or damage. To do such kind of experiment, microelectrodes are well-suited, as they possess many advantages such as enhanced mass-transport and reduced capacitive response, which allows for increased signal-to-noise ratio. As the response associated to a microelectrode is very rapid and they can be constructed in microscopic dimensions, they are suitable to get *in vivo* and *in situ* real time chemical information.

Microelectrodes have been used to investigate the respiration process of leaves [35] and the release of compounds from plants [36–40], but only a few reports have described the use of microelectrodes for *in-situ* measurements in leaves [41–43]. Some of us have been involved with electroanalysis at micro-scales [44,45], hence in this paper we report on the use of electrochemical tools to monitor the production of hydrogen peroxide in *A. tequilana* leaves few hours after inoculation of their endophytic bacteria *Enterobacter cloacae*. Such *in-situ* approach is much faster and reliable in comparison to the usual protocol for H_2O_2 visualization in plants after bacteria or fungus inoculation, which is based on staining of roots or tissues by histochemistry using diaminobenzidine stain under light microscopy.

Electrochemical information on the production of H_2O_2 in *A. tequilana* leaves after inoculation of *Enterobacter* in roots was compared to the one obtained by the conventional staining method. The use of the proposed electrochemical sensor for H_2O_2 detection is important as a strategy for monitoring the application of bio-microbial inoculants as fertilizers for *A. tequilana* industry and possibly for other purposes as biotic stress. Since the formation of hydrogen peroxide in *A. tequilana* leaves is likely to involve changes in the acidity, additional *in-situ* pH measurements were also performed by using an iridium oxide pH microelectrode probe.

A2.3. Experimental section.

A2.3.1. Plant Materials.

Plantlets (bulbillos) approximately one year old of *A. tequilana* Weber originally collected in Atotonilco el alto Jalisco, Mexico, were used in the experiments. The plantlets were throughout the experiment cultivated on sand previously autoclaved and maintained in an incubation chamber at 27 °C day/night temperature, and 14 hours photoperiod. Every week, 3 hours before the experiment, the bacteria were inoculated into the plantlets and the hydrogen peroxide production was analyzed.

A2.3.2. Plant treatments and inoculation with bacteria.

Firstly, the seed-transmitted endophyte *Enterobacter cloacae* was isolated and identified. After that, the isolated bacteria were cultured in Tryptic Soy Agar (TSA) plates at 37 ºC and maintained in an incubator for 18 hours. After this period, the bacteria colonies were transferred to minimum medium M9 (6g Na_2HPO_4, 3g KH_2PO_4, 5g NaCl, 3g NH_4Cl, 0.2 g $MgSO_4.7H_2O$, 2% glucose in 1L distilled water), the absorbance was adjusted to 0.2 optical density at 600 nm (OD_{600nm}) (equivalent to $5.3x10^4$ CFU mL^{-1}) and the mixture was incubated in a shaker at 37 ºC, 200 rpm, for 18 hours. Then, the bacteria were centrifuged (5000 x gravity, 20 min, 4 ºC) and washed three times with sterile water containing glucose (0.08%). Four mL of *E. cloacae* mixture with optical density adjusted to 1 at O.D.$_{600nm}$ (equivalent to $8.0x10^6$ CFU mL^{-1}) were inoculated near the root of the *A. tequilana* plantlets maintained in a microcosm.

A2.3.3. Fabrication of platinum and gold disc microelectrodes.

The integrated working/reference Pt microelectrode used for hydrogen peroxide detection was fabricated from an adapted procedure reported previously [46]. Briefly, a Pt wire (d = 50 μm) was inserted into a quartz glass capillary and vacuum-sealed with a P-2000 Micropipette Puller (Sutter Instrument Company, USA). The external body of the glass capillary was coated with silver epoxy (EPO-TEK, USA) to get a dual function electrode, i.e., Pt was the working electrode and the silver coat acted as a pseudo reference electrode, hence measurements can be performed by using a single device. Figure A2.1 shows an image of the fabricated dual-function Pt microelectrode. A 25-μm diameter Au disc microelectrode was fabricated following a conventional method, based on the insertion of a cleaned gold fiber into a glass capillary and vacuum-sealing with a P-97 Flaming/Brown Micropipette Puller (Sutter Instrument Company, USA). The surface of both Pt and Au microelectrodes was polished with alumina powder (1, 0.3 and 0.05 μm, Alfa Aesar, Massachusetts, USA) on a microcloth polishing pad. Then, the microelectrodes were rinsed with water and sonicated for 5 minutes in distilled water. Before and after all experiments involving the monitoring of hydrogen peroxide on leaves, the Pt microelectrodes were tested regarding the electrochemical behaviour by performing a series of cyclic voltammetry experiments in a 10 mmol L^{-1} potassium ferricyanide solution containing 0.1 mol L^{-1} KCl (data not shown) until the expected electrochemical behavior was noticed (sigmoidal curve with low hysteresis). The radius of both Pt and Au microelectrodes was evaluated from the steady-state diffusion-controlled limiting current (i_L) by use of the equation $i_L = 4nFc^*Da$, where n is the number of electrons, F is Faraday constant (A.s.mol^{-1}), c^* is the concentration of the electroactive species (mol.cm^{-3}), D is the diffusion coefficient (cm^2.s^{-1}), and a is the radius (cm) of the microelectrode. To evaluate the influence of the pseudo reference electrode on the sensor response, hydrogen peroxide calibration curves were obtained using as reference electrodes the silver epoxy coat and a Ag/AgCl$_{(\mathrm{Sat.\ KCl})}$ electrode. Calibration curves were plotted using limiting currents from CVs recorded in phosphate buffer saline (PBS) solution after addition of aliquots of a 0.1 mol L^{-1} H_2O_2 solution.

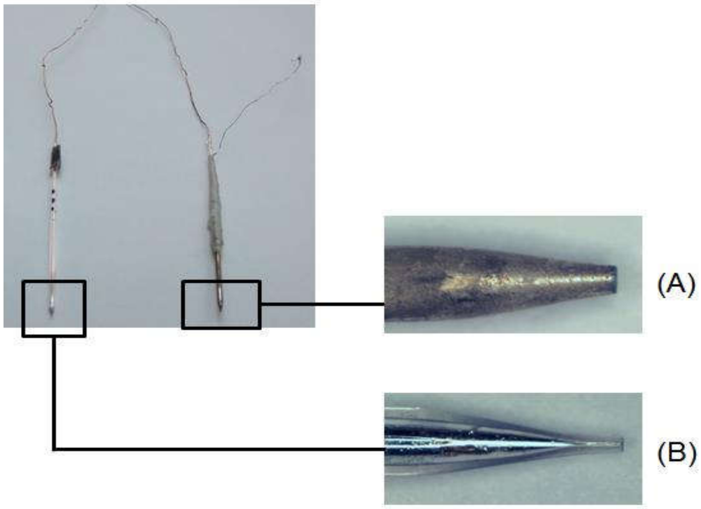

Figure A2.1. Images of the fabricated dual-function Pt microelectrode after (A) and before (B) coating with a silver epoxy layer.

A2.3.4. Potentiometric pH microsensor fabrication.

The pH microsensor was fabricated according to a procedure already reported in the literature [47] and based on the electrodeposition of a film of iridium oxide onto the Au microelectrode surface from an alkaline solution containing the $[\mathrm{Ir(COO)_2(OH)_4}]^{2-}$ complex. The electrodeposition of the iridium oxide film was performed in two steps: first applying 0.8 V (vs Ag/AgCl$_{(\mathrm{Sat.\ KCl})}$) for 600 seconds and then cyclic voltammograms were continuously recorded in the same solution (100 cycles). The gold surface was completely covered with the iridium oxide film, as shown in SEM images (Figure A2.2). Calibration curves were obtained by measuring potential values at open circuit with the IrO_x sensor in buffer solutions of different pH values in the range 2 to 8. A typical calibration plot with super-Nernstian response was obtained during the microsensor characterization, as described previously [47] (Figure A2.3).

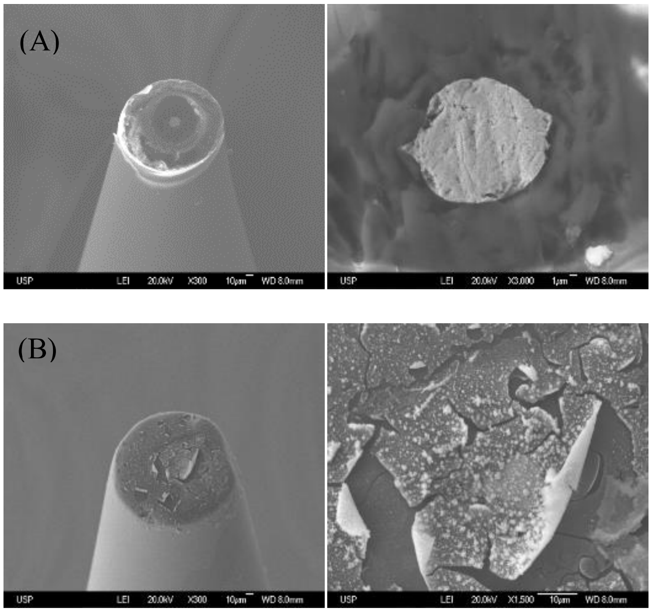

Figure A2.2. SEM images of a bare gold microelectrode before (A) and after immobilization of an iridium oxide layer (B).

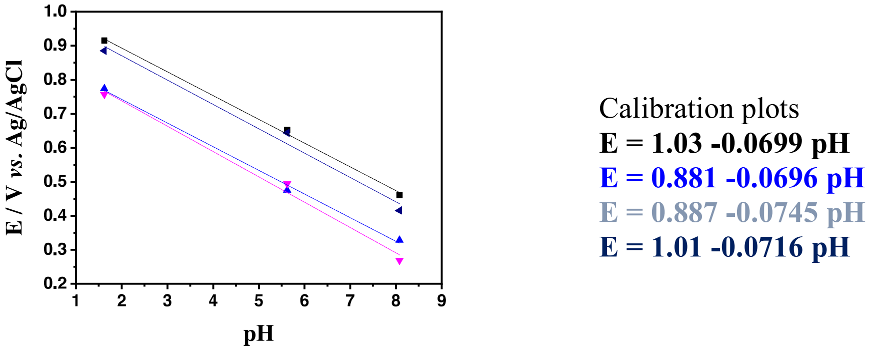

Figure A2.3. Calibration curves using different pH sensors in phosphate buffer saline (PBS) solution. The pH values of the PBS solution were adjusted by addition of H_2SO_4 and NaOH solutions. Plotted measurements correspond to values obtained after 30 seconds of potential monitoring.

A2.3.5. Apparatus and measurements.

All electrochemical experiments (amperometric and potentiometric) were performed using an Autolab PGSTAT 128 potentiostat (Eco Chemie b.V., Utrecht, the Netherlands). *In-vivo* hydrogen peroxide detection and pH measurements were carried out by inserting the microsensors in the upper epidermis of *A. tequilana* leaves using a manual three-dimensional micropositioner (World Precision Instruments, USA) under microscope control. A needle was used to create a small cavity in the upper epidermis of the leaves. Figure A2.4 shows the experimental arrangement used for electrochemical measurements in the *A. tequilana* leaves.

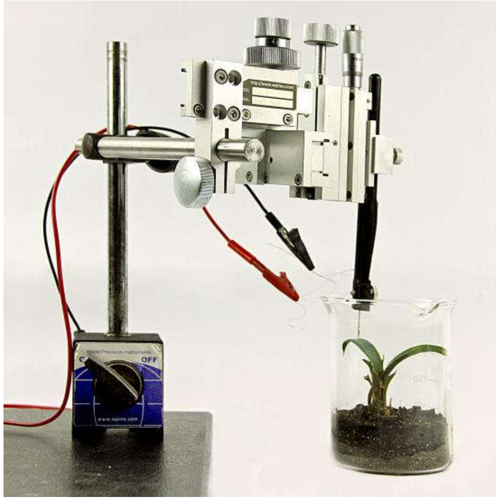

Figure A2.4. Experimental arrangement used for electrochemical measurements in A. tequilana leaves.

A2.3.6. Visualization of H_2O_2 in *A. tequilana* roots after *E. cloacae* inoculation.

Prior to treatment with the *E. cloacae* suspension, plants were always washed with sterile distilled water to remove sand and placed for 24 hours in DAB solution, which covered only the roots. Then, entire roots were collected and aniline blue solution was added for 15 minutes to generate a contrast. The excess was removed with sterile distilled water and the roots were observed under light microscope. This was done in order to find microorganisms inside the roots before starting bacteria inoculation. *E. cloacae* ($8.0x10^6$ CFU mL^{-1}) was inoculated into 4 plants in the microcosm and then incubated by 48, 72, 144 and 168 hours. Two complete roots of each plant (n = 4) were analyzed. To visualize H_2O_2 and the bacterial colonization, roots of *A. tequilana* plantlets were cut, placed in 1 mg mL^{-1} 3,3-diaminobenzidine tetrachloride, pH 6.9 (Sigma MO, USA, D4418), and incubated overnight. Transferring roots into distilled water stopped the reaction. Roots were excised, placed on a slide containing aniline blue/lactophenol stain (aniline blue dye 0.05 g, phenol crystals 20 g, glycerol 40 mL, lactic acid 20 mL, H_2O 20 mL), and examined by using bright field microscopy. The presence of H_2O_2 is visualized as a reddish-brown colouration.

A2.4. Results and discussion.

A2.4.1. Analytical performance of the sensor.

The analytical performance of the dual-function Pt microelectrode as a sensor for H_2O_2 detection was assessed by recording CVs in absence (curves *i*) and presence (curves *ii*) of the target analyte (Figure A2.5A) using pseudo reference (silver coated) and conventional reference ($Ag/AgCl_{(Sat.\ KCl)}$) electrodes. Steady-state responses owing to enhanced mass-transport conditions were obtained by using both reference electrodes. In absence of H_2O_2, a cathodic response is noticed because of the reduction of dissolved O_2, whereas a current increase is observed upon addition of H_2O_2 to the solution from 0.1 to 100 mmol L^{-1}. A small shift in the potential can be observed by comparing voltammograms recorded with both reference electrodes, but such potential difference was expected, as their constitution was not the same. However, the pseudo-reference electrode used in this work was practical, effective and its response was stable, hence experiments can be carried out by using a single miniaturized sensor. The relationship between limiting current and H_2O_2 concentration was established for both reference electrodes after subtraction of the response corresponding to molecular oxygen (Figure A2.5B) and the sensitivity was almost the same. Therefore, one can confirm the usefulness of the fabricated dual-functional sensor towards H_2O_2 detection in a large dynamic concentration range.

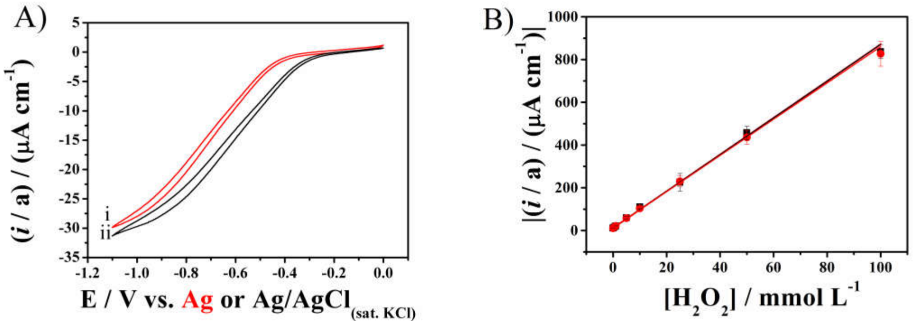

Figure A2.5. Cyclic voltammograms recorded with dual-function microelectrodes in phosphate buffer saline (PBS) solution in absence (curve i) and presence of 5 mmol L^{-1} H_2O_2 (curve ii) using silver coated (red curve) and Ag/AgCl$_{(sat.\ KCl)}$ (black curve) as reference electrodes (A). Calibration curves obtained using limiting currents of CVs in PBS solution, red curve vs. Ag and black curve vs. Ag/AgCl$_{(sat.\ KCl)}$ (B). v: 100 mV s^{-1}. Current values were normalized by the radius (a) of the microelectrodes.

A2.4.2. *In vivo* H_2O_2 monitoring.

As the release of H_2O_2 in plant leaves can be induced by stress [48–50], a control experiment was performed to examine whether the effect of the wounding caused by the insertion of the microsensor in the leaf could result in the formation of such reactive oxidant species. Figure A2.6A shows the cyclic voltammogram obtained with the dual function microsensor placed inside the leaf and one can see a current increase at around -0.7 V (curve i), corresponding to the reduction of some compound present in the fluid. Then, by using a micropipette the cavity originated by the insertion of the microsensor was flooded with 5 μL catalase (400 units mL^{-1}), hence the enzyme would selectively consume any generated H_2O_2. No change in the voltammogram was noticed upon the addition of catalase (curve *ii*). Accordingly, one can conclude that such faradaic response was not due to H_2O_2 and it is likely a response caused by the cathodic reduction of O_2 or other oxygen reactive species dissolved in the leaf fluid. The same experiment was repeated with plantlets inoculated with *Enterobacter cloacae* bacteria after 2 hours post inoculation. Curve *i* in Figure A2.6B corresponds to the cathodic reduction of generated H_2O_2, whereas a complete suppression of the faradaic current was observed after injection of catalase (curve *ii*). Hence, the cathodic process corresponding to curve *i* in Figure A2.6B is likely to involve the reduction of generated H_2O_2. From the limiting current of such recorded voltammogram and by using the equation for the steady-state current at a microelectrode ($I_L = 4nFDCr$), a value of around 2.5 mmol L^{-1} was found. The results of such experiments are important taking into account the selectivity of the sensor response. The main compounds found in *A. tequilana* leaves are ascorbic acid, phenolic acids and peroxidases and it is clear the mentioned substances cannot be considered as interfering species at the potential range employed in this work.

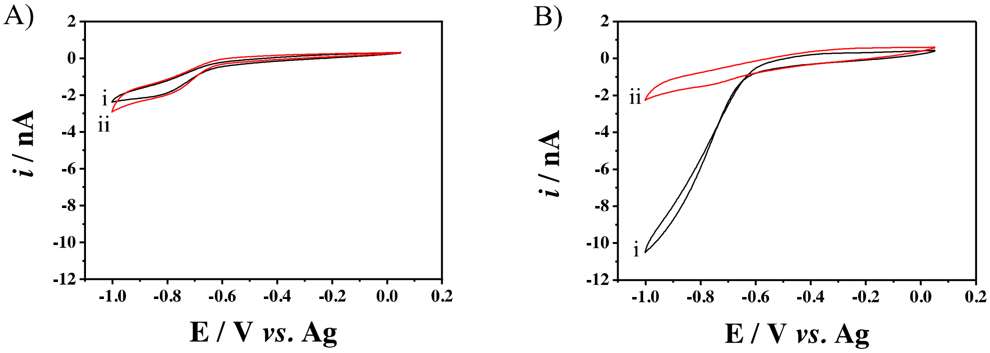

Figure A2.6. Cyclic voltammograms recorded with a dual-function Pt microelectrode (r = 3 µm) inserted in the epidermis of an A. tequilana leaf control (A) and an A. tequilana leaf inoculated with E. cloacae (B). Experiments performed in absence (i) and presence (ii) of catalase. v = 50 mV s^{-1}.

The influence of the location of the dual-probe Pt microsensor in a leaf was also examined. Figure A2.7 shows voltammograms recorded at two different regions of the leaf, at the centre and at the upper end. The higher current value obtained when the microsensor was inserted in the centre of the leaf suggests the concentration of H_2O_2 is not the same inside of all regions of the leaves. All experiments were repeated with 3 different *A. Tequilana* plantlets and similar results were obtained.

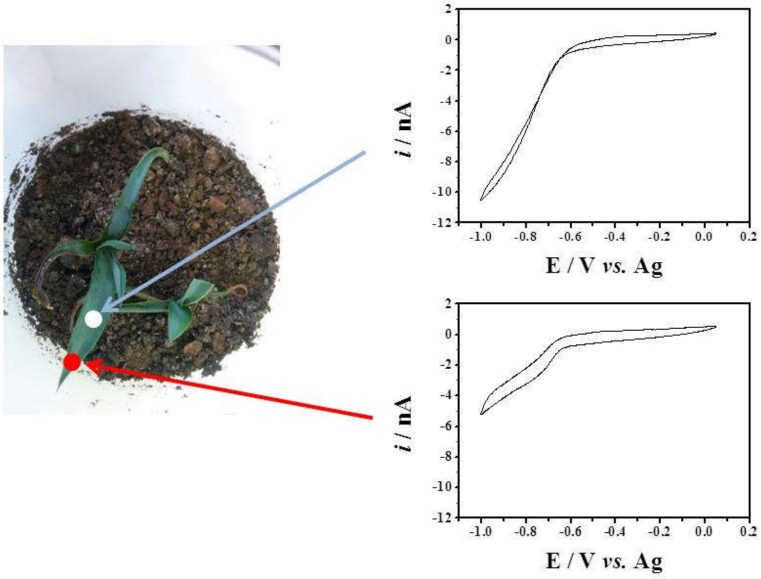

Figure A2.7. Cyclic voltammograms recorded with a Pt microelectrode (r = 3 μm) positioned at two different regions of the epidermis of an A. tequilana leaf inoculated with E. cloacae bacteria. $v = 50\ mV\ s^{-1}$.

A2.4.3. *In vivo* pH measurements.

The plants treated with bacteria were inoculated 6 hours prior to pH measurements, which were performed by positioning the microsensor within a cavity made by using a needle. During the insertion procedure, attention was paid to avoid any touch of the microsensor surface to the leaf tissue, hence the integrity of the film was preserved and, consequently, the pH response. pH values were recorded after equilibrating for about 30 seconds and in the untreated plants such values (8.4 ± 0.5) were higher than those obtained in plants inoculated with bacteria (7.3 ± 1.0), with a confidence interval of 95% (n = 4). The tendency of a lower pH in *A. tequilana* treated with bacteria confirms the existence of a process pathway according to which *A. tequilana* produces acidic substances. Such observation is consistent with the fact that H_2O_2 acts as a signal molecule mediating the biosynthesis of secondary metabolites in plants, hence it is likely that acidic substances such as benzoic acid, salycilic acid and other phenolic acids are synthesized during the oxidative burst process caused by the contact of the roots with endophytes [51–53]. It should be mentioned that such substances are not electroactive in a negative potential range, hence they are not likely to act as interfering species in the detection of H_2O_2, which was carried out from 0 to -1.0 V.

A2.4.4. *In vitro* experiments.

In vitro experiments were carried out to investigate whether H_2O_2 was released by the plant or the inoculated bacteria. This was accomplished by monitoring the formation of H_2O_2 in a liquid culture medium by cyclic voltammetry in the absence and presence of *E. cloacae*. By comparing voltammograms shown in Figure A2.8, one can see a cathodic response corresponding to the reduction of dissolved O_2 (curve *i*) in the experiment performed in the absence of bacteria, whereas such process is completely suppressed when the experiment was repeated in a solution containing *E. cloacae* (curve *ii*) owing to the consumption of O_2 by the bacteria. The experiment was repeated in the absence of bacteria and after removal of O_2 by bubbling argon to the solution the resulting voltammogram was similar to the one corresponding to curve *ii* (i.e., the electrode process in curve *i* involves the electrochemical reduction of dissolved O_2). Hence, as the presence of the bacteria in the culture medium did not induce the formation of H_2O_2 (only the consumption of O_2 by the bacteria was noticed), one can conclude that H_2O_2 electrochemically measured inside the leaves comes from the plant in response to bacterial inoculation.

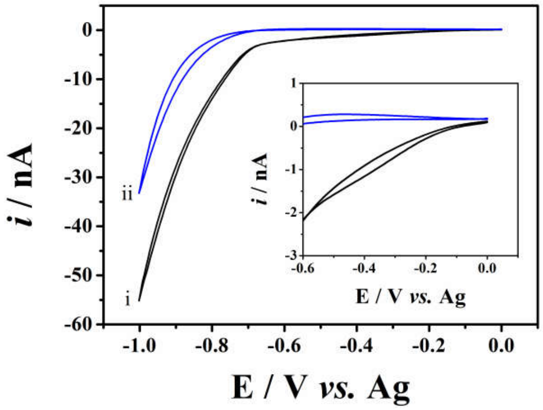

Figure A2.8. Cyclic voltammograms recorded in culture medium in absence (i) and presence (ii) of E. cloacae bacteria. v = 50 mV s^{-1}*. Inset shows the magnification of the voltammogram in a narrow potential range.*

A2.4.5. Visualization of H_2O_2 in *A. tequilana* roots after *E. cloacae* inoculation.

In order to compare and evaluate the ability of the dual Pt microsensor to detect H_2O_2 production after endophyte inoculation in *A. tequilana* roots tissues, DAB staining was employed. Figure A2.9A shows a root hair in absence of bacteria and hydrogen peroxide (control). After 48 hours post-inoculation (Figure A2.9B), a microbial biofilm around the root hair can be observed, without H_2O_2 production. At 72 hours after inoculation, zones with H_2O_2 can be visualized throughout the root hair, with internalized and degraded bacterial cells (Figure A2.9C). This confirms that under conditions of nutrient limitation, the bacterial cells are degraded by the plant as it has been previously shown [15]. Finally, Figure A2.9D shows a root hair at 7 days post-inoculation and in this case no bacterial cells and only a few spots corresponding to the presence of H_2O_2 can be noticed.

The plant perception of pathogenic microorganisms triggers a plethora of cellular responses. One of the responses is a rapid and transient burst of reactive oxygen species, including H_2O_2. In laboratory conditions, the ROS burst can be detected a few hours after the treatment using chemical probes. In biological systems, H_2O_2 has been usually detected using several analytical techniques such as spectrophotometry [54] and chemiluminiscence [55]. Furthermore, dyes are also widely used to determine H_2O_2 [49], but these methods are time-consuming and highly prone to interferences.

The use of the microsensor constructed here is advantageous with respect to the use of stains or other methods to evaluate the presence of H_2O_2 in plant tissues after bacteria inoculation, because it possesses excellent temporal resolution and allows information of both production and consumption of H_2O_2 to be obtained in real time without interferences. We have found only one report on electrochemical detection of H_2O_2 by using Pt microsensors in plant cell suspensions of *Arabidopsis thaliana* [39]. To our knowledge, this is the first report on the detection of hydrogen peroxide in leaves of plants which were inoculated with beneficial bacteria.

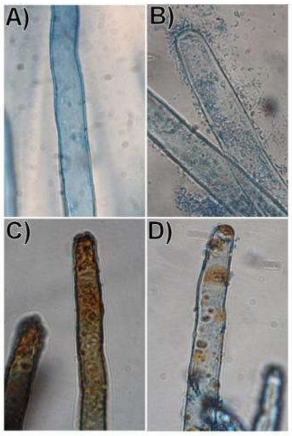

Figure A2.9. Agave tequilana root hair staining with DAB for H_2O_2 detection. Control root hair (not inoculated) with no evidence of E. cloacae or another bacteria (A). Root hair of plantlets inoculated with E. cloacae at 48 hrs post-inoculation (PI) with a biofilm on the surface of root-hair and no evidence of H_2O_2 (B). Root hair inoculated at 72 hrs PI with bacterial cells inside and high amount of H_2O_2 (C). Root hair at 144 hrs PI with swollen lysing bacteria and some areas of brown staining (DAB- H_2O_2)(D).

A2.5. Conclusions.

A dual-function platinum microelectrode was fabricated and used for *in-situ* detection of H_2O_2 in *A. tequilana* leaves by cyclic voltammetry. The results confirmed the relationship between inoculated bacteria and the formation of H_2O_2, but we have no defined mechanism to explain the appearance of such ROS in the leaves. Also, this microelectrode could detect ROS in leaves 3 hours after inoculation, whereas in root hairs the DAB staining showed H_2O_2 only after 72 hours. By small manipulation of the leave, a minimum disruption is produced in the plant and the information obtained from such electrochemical experiments most probably represents those corresponding to the *in vivo* situation. As an additional advantage of the electrochemical sensor in comparison to conventional techniques such as fluorescence microscopy, one can cite the portability and short response, allowing field measurements to be performed. By using an iridium oxide gold modified microelectrode, *in situ* pH measurements were also carried out in leaves from plants with inoculated endophytic bacteria and the obtained results support the idea that the formation of H_2O_2 induces the production of acidic substances by the plant. Further studies are needed to understand the biochemistry of the plant-endophyte interaction involving ROS production, but this is beyond the purpose intended in this work. Our electrochemical method will be used as emerging tool to detect H_2O_2 quickly in *Agave* plants during their interaction with microorganisms (beneficial or pathogenic), from the early stage before the biofilm formation or root tissue penetration without destroying or altering the physiology of the plant.

A2.6. Acknowledments.

The authors are grateful to CNPq, FAPESP and CONACYT for the financial support. Grants #2015/02095-4, #2014/22396-6, and #2015-20776-9, São Paulo Research Foundation (FAPESP) to A.S.L., C.S.S. and M.B., respectively. Grant 500342/2014-8, National Counsel of Technological and Scientific Development (CNPq) to K.R.P. Miguel

J. Beltran-Garcia gratefully acknowledges the financial support from CONACYT: Proyectos de Desarrollo Cientifico para atender Problemas Nacionales (CONACYT 212875), CONACYT 269607 Apoyo al Fortalecimiento y Desarrollo de la Infraestructura Científica y Tecnologica 2016 and Project 207400 of Bilateral Cooperation Mexico-Brazil funded by CONACYT and CNPq (Brazil, No. 490440/2013-4). A H-R thanks CONACYT for PhD fellowship #414739. Paolo Di Mascio thanks FAPESP (Fundação de Amparo à Pesquisa do Estado de São Paulo, # 2012/12663-1, CEPID Redoxoma # 2013/07937-8), CNPq (Conselho Nacional para o Desenvolvimento Científico e Tecnológico, # 301307/2013-0, # 59068/2014-2) and PRPUSP (Pro-Reitoria de Pesquisa da Universidade de São Paulo, NAP Redoxoma # 2011.1.9352.1.8) for financial support. Project of Bilateral Cooperation Mexico-Brazil funded by CONACYT and CNPq (Brazil, # 490440/2013-4).

A2.7. References.

1. Nava-Cruz, N. Y.; Medina-Morales, M. A.; Martinez, J. L.; Rodriguez, R.; Aguilar, C. N. *Crit. Rev. Biotechnol.* **2015**, 35, 4, 546–559.

2. Cedeño, M. *Crit. Rev. Biotechnol.* **1995**, 15, 1, 1–11.

3. Corbin, K. R.; Byrt, C. S.; Bauer, S.; DeBolt, S.; Chambers, D.; Holtum, J. A. M.; Karem, G.; Henderson, M.; Lahnstein, J.; Beahan, C. T.; Bacic, A.; Fincher, G. B.; Betts, N. S.; Burton, R. A. *PLoS One* **2015**, 10, 8.

4. Gross, S. M.; Martin, J. A.; Simpson, J.; Jazmin Abraham-Juarez, M.; Wang, Z.; Visel, A. *BMC Genomics* **2013**, 14.

5. Muller, C. A.; Obermeier, M. M.; Berg, G. *J. Biotechnol.* **2016**, 235, 171–180.

6. van der Heijden, M. G. A.; Hartmann, M. *PLOS Biol.* **2016**, 14, 2.

7. Hardoim, P. R.; van Overbeek, L. S.; Berg, G.; Pirttila, A. M.; Compant, S.; Campisano, A.; Doering, M.; Sessitsch, A. *Microbiol. Mol. Biol. Rev.* **2015**, 79, 3, 293–320.

8. Barret, M.; Briand, M.; Bonneau, S.; Preveaux, A.; Valiere, S.; Bouchez, O.; Hunault, G.; Simoneau, P.; Jacques, M.-A. *Appl. Environ. Microbiol.* **2015**, 81, 4, 1257–1266.

9. Gaiero, J. R.; McCall, C. A.; Thompson, K. A.; Day, N. J.; Best, A. S.; Dunfield, K. E. *Am. J. Bot.* **2013**, 100, 9, 1738–1750.

10. Desgarennes, D.; Garrido, E.; Torres-Gomez, M. J.; Pena-Cabriales, J. J.; Partida-Martinez, L. P. *FEMS Microbiol. Ecol.* **2014**, 90, 3, 844–857.

11. Coleman-Derr, D.; Desgarennes, D.; Fonseca-Garcia, C.; Gross, S.; Clingenpeel, S.; Woyke, T.; North, G.; Visel, A.; Partida-Martinez, L. P.; Tringe, S. G. *NEW Phytol.* **2016**, 209, 2, 798–811.

12. Martinez-Rodriguez, J. del C.; la Mora-Amutio, M.; Plascencia-Correa, L. A.; Audelo-Regalado, E.; Guardado, F. R.; Hernandez-Sanchez, E.; Pena-Ramirez, Y. J.; Escalante, A.; Beltran-Garcia, M. J.; Ogura, T. *BRAZILIAN J. Microbiol.* **2014**, 45, 4, 1333–1339.

13. Beltran-Garcia, M. J.; White Jr., J. F.; Prado, F. M.; Prieto, K. R.; Yamaguchi, L. F.; Torres, M. S.; Kato, M. J.; Medeiros, M. H. G.; Di Mascio, P. *Sci. Rep.* **2014**, 4.

14. Zhou, J.-Y.; Yuan, J.; Li, X.; Ning, Y.-F.; Dai, C.-C. *Appl. Environ. Microbiol.* **2016**, 82, 5, 1577–1585.

15. Zhou, J.-Y.; Li, X.; Zhao, D.; Deng-Wang, M.-Y.; Dai, C.-C. *Planta* **2016**, 244, 3, 699–712.

16. White Jr., J. F.; Crawford, H.; Torres, M. S.; Mattera, R.; Irizarry, I.; Bergen, M. *SYMBIOSIS* **2012**, 57, 3, 161–171.

17. White Jr., J. F.; Torres, M. S.; Somu, M. P.; Johnson, H.; Irizarry, I.; Chen, Q.; Zhang, N.; Walsh, E.; Tadych, M.; Bergen, M. *Microsc. Res. Tech.* **2014**, 77, 8, 566–573.

18. Soh, N.; Sakawaki, O.; Makihara, K.; Odo, Y.; Fukaminato, T.; Kawai, T.; Irie, M.; Imato, T. *Bioorg. Med. Chem.* **2005**, 13, 4, 1131–1139.

19. Ledoux, Q.; Veys, P.; Van Cutsem, P.; Mauro, S.; Lucaccioni, F.; Marko, I. *Plant Signal. Behav.* **2013**, 8, 11.

20. Ledoux, Q.; Van Cutsem, P.; Markó, I. E.; Veys, P. *Plant Signal. Behav.* **2014**, 9.

21. Šnyrychová, I.; Ayaydin, F.; Hideg, E. *Physiol. Plant.* **2009**, 135, 1, 1–18.

22. Zhang, L.; Li, S.; Dong, M.; Jiang, Y.; Li, R.; Zhang, S.; Lv, X.; Chen, L.; Wang, H. *Biosens. Bioelectron.* **2017**, 87, 1036–1043.

23. Paixao, T. R. L. C.; Bertotti, M. *Electroanalysis* **2008**, 20, 15, 1671–1677.

24. Sukeri, A.; Lima, A. S.; Bertotti, M. *Microchem. J.* **2017**, 133, 149–154.

25. O'Riordan, S. L.; Lowry, J. P. *Anal. METHODS* **2017**, 9, 8, 1253–1264.

26. Chakraborty, S.; Raj, C. R. *Biosens. Bioelectron.* **2009**, 24, 11, 3264–3268.

27. Phillips, P. E. M.; Wightman, R. M. *TrAC - Trends Anal. Chem.* **2003**, 22, 9, 509–514.

28. Nagy, G.; Nagy, L. *Anal. Lett.* **2007**, 40, 1, 3–38.

29. Wilson, G. S.; Johnson, M. A. *Chem. Rev.* **2008**, 108, 7, 2462–2481.

30. Robinson, D. L.; Hermans, A.; Seipel, A. T.; Wightman, R. M. *Chem. Rev.* **2008**, 108, 7, 2554–2584.

31. Amatore, C.; Arbault, S.; Guille, M.; Lemaître, F. *Chem. Rev.* **2008**, 108, 7, 2585–2621.

32. Li, C. M.; Hu, W. *J. Electroanal. Chem.* **2013**, 688, 20–31.

33. Oja, S. M.; Wood, M.; Zhang, B. *Anal. Chem.* **2013**, 85, 2, 473–486.

34. Clausmeyer, J.; Schuhmann, W. *TrAC - Trends Anal. Chem.* **2016**, 79, 46–59.

35. Mancuso, S.; Papeschi, G.; Marras, A. M. *Planta* **2000**, 211, 3, 384–389.

36. Lauver, T. L.; McCune, D. C.; Shaff, J. E.; Kochian, L. V. *NEW Phytol.* **1992**, 121, 0, 2, 179–185.

37. Sun, L.; Liu, X.; Gao, L.; Lu, Y.; Li, Y.; Pan, Z.; Bao, N.; Gu, H. *Anal. Lett.* **2015**, 48, 10, 1578–1592.

38. Subraya, K. K.; Diggs, A.; Porterfield, D. M. *Commun. Soil Sci. Plant Anal.* **2013**, 44, 11, 1749–1763.

39. González-Sánchez, M. I.; González-Macia, L.; Pérez-Prior, M. T.; Valero, E.; Hancock, J.; Killard, A. J. *Plant, Cell Environ.* **2013**, 36, 4, 869–878.

40. Ai, F.; Chen, H.; Zhang, S.-H.; Liu, S.-Y.; Wei, F.; Dong, X.-Y.; Cheng, J.-K.; Huang, W.-H. *Anal. Chem.* **2009**, 81, 20, 8453–8458.

41. Hanstein, S.; Martinez-Bonastre, A.; Nestler, U.; Bartlett, P. N. *Sensors Actuators, B Chem.* **2007**, 125, 1, 284–300.

42. Ren, Q.-Q.; Yuan, X.-J.; Huang, X.-R.; Wen, W.; Zhao, Y.-D.; Chen, W. *Biosens. Bioelectron.* **2013**, 50, 318–324.

43. Ren, Q.-Q.; Huang, X.-R.; Liu, G.-C.; Jun, O.-Y.; Li, M.-T.; Chen, H.; Zhao, Y.-D.; Chen, W. *Sensors Actuators, B Chem.* **2015**, 220, 743–748.

44. Paixão, T. R. L. C.; Lowinsohn, D.; Bertotti, M. *J. Agric. Food Chem.* **2006**, 54, 8, 3072–3077.

45. Paixão, T. R. L. C.; Barbosa, L. F.; Carrì, M. T.; Medeiros, M. H. G.; Bertotti, M. *Analyst,* **2008**, 133, 11, 1605–1610.

46. Turcu, F.; Schulte, A.; Schuhmann, W. *Anal. Bioanal. Chem.* **2004**, 380, 5–6, 736–741.

47. Santos, C. S.; Lima, A. S.; Battistel, D.; Daniele, S.; Bertotti, M. *Electroanalysis* **2016**, 28, 7, 1441–1447.

48. Sharma, P.; Jha, A. B.; Dubey, R. S.; Pessarakli, M. *J. Bot.* **2012**, 2012, 1–26.

49. Orozco-Cardenas, M.; Ryan, C. A. *Proc. Natl. Acad. Sci. U. S. A.* **1999**, 96, 11, 6553–6557.

50. Kristiansen, K. A.; Jensen, P. E.; Møller, I. M.; Schulz, A. *Physiol. Plant.* **2009**, 136, 4, 369–383.

51. Leon, J.; Lawton, M. A.; Raskin, I. *PLANT Physiol.* **1995**, 108, 4, 1673–1678.

52. Ben Rejeb, K.; Lefebvre-De Vos, D.; Le Disquet, I.; Leprince, A.-S.; Bordenave, M.; Maldiney, R.; Jdey, A.; Abdelly, C.; Savoure, A. *NEW Phytol.* **2015**, 208, 4, 1138–1148.

53. Strand, D. D.; Livingston, A. K.; Satoh-Cruz, M.; Froehlich, J. E.; Maurino, V. G.; Kramer, D. M. *Proc. Natl. Acad. Sci. U. S. A.* **2015**, 112, 17, 5539–5544.

54. Cheeseman, J. M. *J. Exp. Bot.* **2006**, 57, 10, 2435–2444.

55. Alpeeva, I. S.; Sakharov, I. Y. *Luminescence* **2007**, 22, 2, 92–96.

Appendix 3.

Use of microsensor to determine the pH along the larval midgut of *Musca domestica*

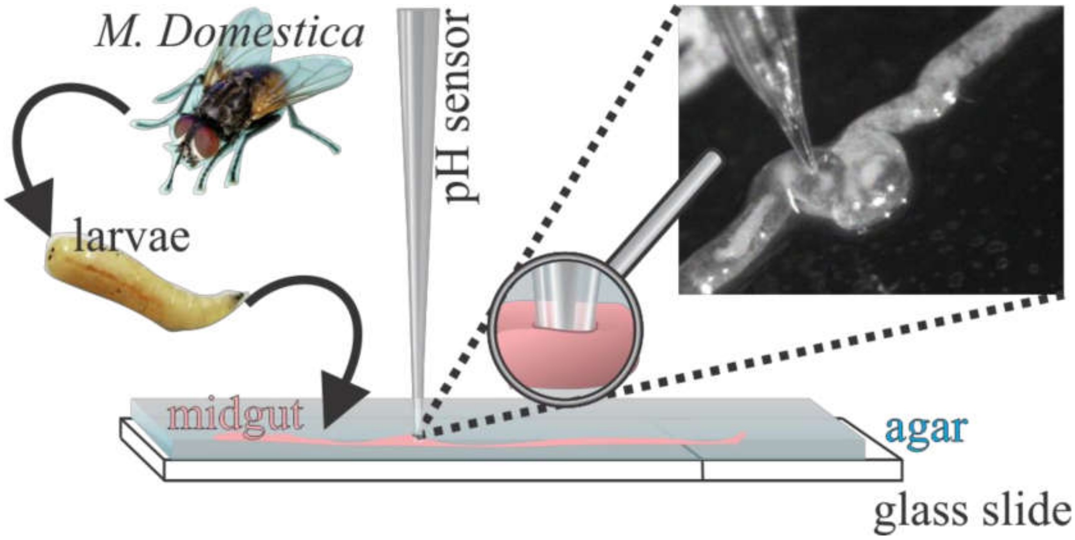

In this chapter, the results of a collaboration with Ignacio Granja and Prof. Walter Terra (Department of Biochemistry of Institute of Chemistry, University of Sao Paulo) are presented. The pH of the midgut is an important property to describe the enzyme efficiency in the digestive system and here a pH microsensor was employed to determine the pH along the *Musca domestica* larvae midgut. The pH microsensors were fabricated by modification of platinum microelectrode surfaces with an iridium oxide film. The modified microelectrode was developed during C. C. S. undergraduation work, as described in Carla. S. Santos, Alex S. Lima, Dario Battistel, Salvatore Daniele, Mauro Bertotti, *Electroanalysis,* 2016, 28, 7, 1441-1447. The several local pH measurements with the potentiometric microsensor helped in the study of the mechanism of acidification and alkalization in different sections of the animal midgut. The larvaes were fed with diets to provide specific amino acids used by the enzymes. The presented data in this chapter were published in Comparative Biochemistry and Physiology - Part A: Molecular & Integrative Physiology as:

Molecular mechanisms associated with acidification and alkalization along the larval midgut of Musca domestica. Ignacio Granja Barroso, **Carla S. Santos**, Mauro Bertotti, C Ferreira, Walter R. Terra. *Comp Biochem Physiol A Mol Integr Physiol.*, 2019, 237, 110535.

The permission of use of the text was requested to the publisher Elsevier and the copy of the right is attached in the Annex. However, the authors can use their articles, in full or in part, for a wide range of scholarly, non-commercial purposes.

I. G. B., W. R. T. and C. F. idealized the experiments. I. G. B. performed the RNA analysis, the proteomic analysis and pH determination with the indicator. C. S. S. prepared the pH microsensors and performed the local pH measurements. All authors were responsible for writing and correcting the manuscript. All authors approved the text.

A.3.1. Abstract.

To disclose the molecular mechanisms involved in luminal midgut buffering of *M. domestica*, we used RNA-seq analyses from triplicate samples of seven sections along the midgut to evaluate the expression levels of genes coding for selected manually curated protein sequences. Channels, pumps and transporters were confirmed as being apical by proteomics of purified microvillar membranes. Midgut pH determinations with a microsensor and a pH indicator were carried out in larvae in different diets with or without added compounds to evaluate the role of proteins in buffering. The data suggested that acidification occurs at middle midgut by the action of H^+ V-ATPase with protons produced by carbonic anhydrase, followed by chloride ions transported by a K^+Cl^- symporter. K^+ ions are recovered by an apical K^+ channel and K^+ homeostasis maintained by a basolateral Na^+/K^+-ATPase. Acidification is also affected by a Na^+/H^+ exchanger and a multidrug resistance protein. Posterior midgut alkalization results from the action of a NH_3 transporter and H^+-coupled peptide transporter, mainly in a diet rich in free peptides. A working model was proposed for the midgut luminal acidification and alkalization, as well as for mucosal protection against acid by a neutralized mucus layer.

Abbreviations:

AE, Anion Exchanger (Cl^-/HCO_3^- exchanger); **CA**, Carbonic Anhydrase; **HVA**, H^+ V-ATPase; **KCC**, Potassium Chloride Cotransporter (K^+Cl^- symporter); **Mfm**, Mucus-forming mucins; **MRP1**, Multidrug Resistance Protein 1 (metal-GSH); **NDAE**, Sodium-Driven Anion Exchanger ($Na^+:HCO_3^-/H^+:Cl^-$); **NHA**, Sodium/Proton Antiporter (Na^+/H^+ antiporter); **NHE**, Sodium/Proton Exchanger (Na^+/H^+ exchanger); **NKA**, Na^+/K^+-ATPase; **Ork**, Open Rectifier Potassium channel; **PAT**, Proton-coupled Amino Acid Transporter (H^+:AA); **PepT1**, Proton-coupled Peptide Transporter 1 (H^+:Peptide or

H^+:AA$_2$;AA$_3$)); **pHCl-2**, pH-sensitive Chloride channel 2; **Rh**, Ammonium transporter Rhesus-type.

A.3.2. Introduction.

An acid midgut region probably appeared in detritus feeding vertebrates as an adaptation to lyse bacteria to be used as food (a condition still found in some fishes as tilapia [1]). Cyclorrhaphous Diptera like vertebrates display a very acid region in their midguts [2], which is related to the fact they usually live in highly infected food. The larvae of *M. domestica* develop in dung [3] and some authors have shown that bacteria may be the sole food of *M. domestica* larvae and that in these conditions the larvae undergo metamorphosis to fertile adults [4]. Moreover, impairment of acidification results in increase of midgut bacteria population [5].

The pH values change remarkably along the major morphological regions of the midgut of *M. domestica*. The anterior midgut contents display a pH of 6.1, the middle midgut contents a pH of 3.1 and the posterior midgut ones, a pH of 6.8 [6]. The existence of a very acid region is associated with the capacity of digesting bacteria in the middle midgut with the aid of a special lysozyme and cathepsin D, which seems to be an ancestral trait of Diptera Cyclorrhapha [7].

The first mechanism for pH buffering along the midgut of *M. domestica* was proposed by [8]. They found a strong carbonic anhydrase activity along the whole midgut and a bicarbonate-activated ATPase in the anterior and posterior midgut. Based on these results they proposed the following mechanism. Carbonic anhydrase produces carbonic acid that dissociates into bicarbonate and proton. In the anterior and posterior midguts, bicarbonate is secreted through the action of a putative ATP-driven pump, neutralizing the contents. In middle midgut, protons are actively transported into midgut lumen, in a manner reminiscent of that of mammals, by cells whose ultrastructure resembles that of mammalian parietal (oxyntic) cells [8].

Further work on *M. domestica* midgut buffering mechanisms were based on the evaluation of the effect of inhibitors added to the diet on the pH of the midgut contents and in the determination of selected compounds at different points along the lumen of the midgut [9]. This work confirmed the role of carbonic anhydrase, with the use of acetazolamide (inhibitor of the enzyme) and discounted the role of a bicarbonate-driven ATPase pump, because of the negligible amounts of bicarbonate found in the midgut contents. Furthermore, the high levels of chloride ions in middle midguts and of ammonia in the posterior midgut contents led to the proposal that chloride ions follow protons pumped by the oxyntic cells and ammonia neutralizes the posterior midgut contents. Finally, the importance of the Na^+/K^+-ATPase in the process was recognized by *in vivo* experiments with oubain [9]. Nevertheless, the authors did not describe the sequences and associated properties of the proteins underlying the physiological phenomena described, nor clearly recognized the proton ATPase responsible for pumping protons and the alkalizing processes occurring in the posterior midgut.

The present paper combines *in vivo* electrochemical pH determinations at different conditions with data on selected transporter expression (by RNA-seq) and proteomic analyses of purified midgut microvillar membranes from different regions along the midgut of *M. domestica* larvae. The results support a detailed model of the molecular processes responsible for pH buffering along the midgut and of mucosal cell protection against acid.

A.3.3. Experimental section.

A3.3.1. Animals.

M. domestica larvae (Diptera, Cyclorrhapha, Muscidae) were reared in a fermented mixture of commercial pig food and rice hull (1:2) [10], in controlled conditions (24-26°C). Third instar larvae were used in this study.

A3.3.2. RNA extraction.

Total RNA was extracted from three biological replicates of six *M. domestica* larvae from seven sections throughout the midgut: anterior (A1, A2), middle (M1, M2) and posterior (P1, P2, P3) (Figure A3.1A), and the carcass (larva less midgut). For this, RNeasy Kit (Qiagen, Valencia, CA, USA) was used following manufacturer's instructions.

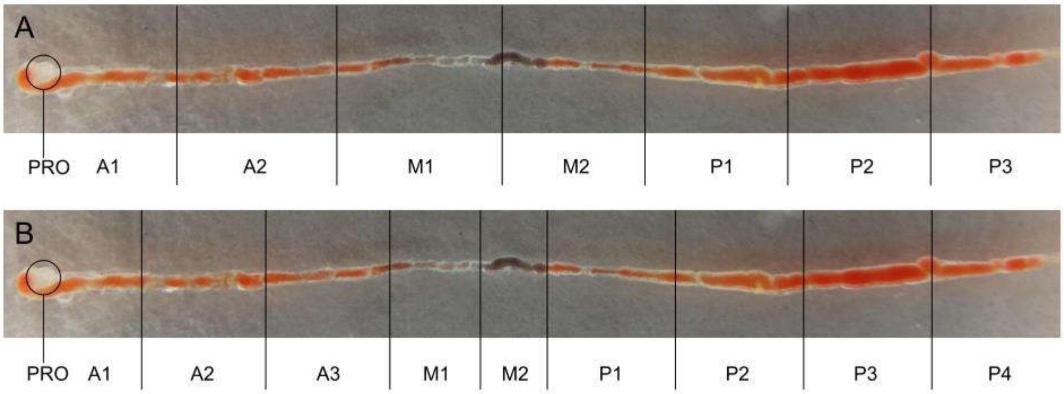

Figure A3.1. Division of the M. domestica midgut in sections used in this work. Pro, proventriculus; A, anterior midgut; M, middle midgut; P, posterior midgut. To favor visualization the larvae were fed with 1% agarose gel containing 0.025% Congo Red (blue 3.0-5.2 red). A) Midgut division for RNAseq analysis; B) Midgut division for microvillar membrane proteomics and pH determinations with microsensors. A pH gradient is suggested between A3 and M2 sections with an abrupt alkalization in P1 section. pH determinations with dimethyl ammonium (DMA) and imidazole were carried out inserting the microsensor in the M2-P1 border. Proventriculus is not a midgut section. Seven sections were used for RNAseq, but according to preliminary data, to better characterize physiological events, the midgut was divided into 9 sections for pH measurements and proteomics.

A3.3.3. RNA-seq analysis.

RNA-seq analyses were performed by genome guided transcriptome assembly method with Illumina reads as detailed in Dias *et al*. (2018)[11]. Expression values for each gene were normalized as transcripts per million of transcripts (TPM).

A3.3.4. Annotation and computational analysis of selected sequences.

Sequences of proteins putatively involved in luminal pH buffering and associated phenomena were chosen from literature searches regarding vertebrates and insects (mainly from Diptera). They were: a) Pumps: Na^+/K^+-ATPase, H^+ V-ATPase; b) Antiporters: Cl^-/HCO_3^-, Na^+/H^+, Na^+/Ca^{2+}, $Na^+:HCO_3^-/H^+:Cl^-$; c) Symporters: $K^+:Cl^-$, H^+:amino acid, H^+:peptide; d) Channels: Cl^-, K^+, Na^+; e) Uniporters: NH_3, metal-GSH; f) Enzymes: carbonic anhydrase. They were identified in the *M. domestica* genome by Blast [12], using as query annotated protein sequences of UniProtKB/Swiss-Prot, with preference for Diptera sequences. The retrieved sequences were used to perform another Blast against the *M. domestica* genome, in order to ensure that all related sequences were identified. The retrieved sequences were discounted when the midgut expression levels were less than 5% of the expression of the most expressed gene of the same type in at least one midgut section or if they were ten-fold more expressed in carcass than in the midgut. The remaining sequences were then filtered according to the InterPro accession numbers (InterProScan software [13]) and manually curated. For curation, *M. domestica* amino acid sequences were submitted to multiple sequence alignments, using MAFFT [14] through Jalview 2 [15], with annotated sequences from UniProtKB/Swiss-Prot.

Computational analyses were carried out to predict the presence or absence of signal peptide (SignalP 4.1 Server [16]), the number of transmembrane domains (TMHHM Server v2 [17,18]), the conserved sequences and signatures (ScanPROSITE [19]), the potential Nglycosylation (NetNGly 1.0 Server [20]), O-glycosylation (NetOGly 4.0 Server [21]) and phosphorylation sites (NetPhos, Blom *et al.*, 2004), the presence of GPI anchor (PredGPI [23]) and the potential disulfide bonds (DiANNA [24]).

Orthologs of *M. domestica* proteins in other Diptera were predicted using InParanoid 8 [25] setting the orthologous score ≥0.95.

A3.3.5. Purification of midgut microvillar membranes.

Larvae were rinsed with distilled water and fed with 10% corn starch gel for 100-120 min. Thereafter, they were immobilized on ice and dissected in cold 150 mM NaCl. *M. domestica* midgut was divided into three sections for the anterior (A1, A2, A3), two for the middle (M1, M2) and four for the posterior (P1, P2, P3, P4) midgut (Figure A3.1B). Purification of the *M. domestica* microvillar membranes was performed according to Jordão *et al.* (1995)[26] for 3 samples of 100 larvae each, as detailed elsewhere (Barroso *et al.*, submitted to publication). The quality of the preparations was evaluated with aminopeptidase assays, the enzyme marker of the midgut microvillar membranes.

A3.3.6. Microvillar membrane proteomics.

The microvillar membrane preparations of different midgut sections, obtained as described above, were submitted to in-gel and in-solution digestion for proteomics, as detailed elsewhere (Barroso *et al.*, submitted to publication).

A3.3.7. Production and calibration of the pH microssensor.

The pH microsensor was made as previously reported [27], wherein the microelectrode surface was modified with the electrodeposition of a film of iridium oxide. Calibration curves were obtained by measuring potential values at open circuit with the IrO_x sensor in Ringer's solution (128 mM NaCl, 1.3 mM KCl, 18 mM $CaCl_2$, 2.3 mM $Na^+HCO_3^-$) at different pH values, in a range from 2 to 10, before and after the experiments to evaluate any change on the sensor response. A typical calibration plot with super-Nernstian response was obtained during the microsensor characterization, as described previously [27].

A3.3.8. *Ex vivo* pH determinations with a pH microssensor.

Groups of 30 larvae were rinsed with distilled water and placed on layers of 10% corn starch gels. The gels contained one of these compounds: 1% of partial milk protein hydrolysate, 1% ovalbumin, 1 mM amiloride, 1 mM glibenclamide, 10 (or 100) mM dimethyl ammonia (DMA), 10 (or 100) mM imidazole. Two control groups include larvae fed on 10% corn starch gel in water and larvae fed on rearing ration. Larvae were maintained between 120-180 min at 25°C in darkness. pH measurements were performed in recent dissected midguts. For this, larvae were quickly immobilized, by placing them on ice and then dissected in cold 150 mM NaCl. The midguts were stretched using tweezers and placed onto a glass slide with 2 mm height layer of 0.5% agarose in Ringer Solution (128 mM NaCl, 1.3 mM KCl, 18 mM $CaCl_2$, 2.3 mM $Na^+HCO_3^-$) and adjusted to the *M. domestica* hemolymph pH 6.5 [28]. The agarose gel maintained the tissue moisture and was used to place the reference electrode.

Electrochemical experiments were performed using an Autolab PGSTAT128 bipotentiostat/galvanostat (Ecochemie, Netherlands) and a Sensolytics (Sensolytics, Germany) SECM (high accurancy micromanipulator) coupled to an inverted microscope (Zeiss, Germany). The microsensor was attached to the micromanipulator of SECM equipment and a CCD camera and an inverted microscope were used to assist the insertion of the microsensor in the desire local for pH determination (Figure A3.2). Where the midgut was too thin, a hole was done with a needle before the insertion of the electrode.

The pH measurements were performed inserting the microsensor into the lumen at different positions along the midgut, usually at the middle of each section (Figure A3.1B). Measurement controls were carried out by inserting the pH microsensor into the agarose gel. A stabilization time of around 2-5 min was required before the pH measurement. A total of 5 determinations were done per section for each condition.

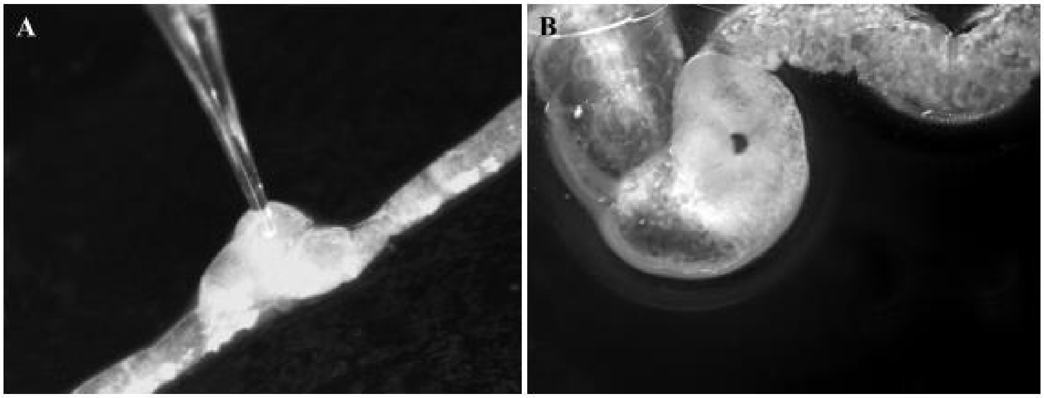

Figure A3.2. Insertion of the pH microsensor in the lumen of the midgut captured with a CCD camera (A) and a inverted microscope (B).

A3.3.9. *Ex vivo* pH determinations with a pH indicator.

The pH indicator Congo Red (blue 3.0-5.2 red) was used to localize the acid region of the midgut and to check the effect of MdH$^+$ V-ATPase, MdNa$^+$/K$^+$-ATPase and MdKCC inhibitors. Since the activity of KCC is affected by the medium osmolarity, experiments were performed at different osmolarities. For this, groups of 10 larvae were rinsed in distilled water and placed on layers of 1% agarose with 0.025% Congo Red in hypotonic (150 mOsm), isotonic (350 mOsm) or hypertonic (1500 mOsm) NaCl-KCl saline plus one of the following inhibitors: 400 nM bafilomycin A1 from *Streptomyces griseus* previously solubilized in methanol; 1 µM, 10 µM, 50 µM, 100 µM, or 1 mM ouabain previously solubilized in hot Milli-Q water and 10 µM, 25 µM, 50 µM, 100 µM, or 1 mM furosemide previously solubilized in methanol. The results were classified in four degrees of inhibition depending on blue-red change of Congo Red in the middle midgut. 0: blue; 1: decreasing blue intensity; 2: bluish red; 3: Red. From each diet, a group of 10 larvae was dissected and the color of the midgut evaluated by eye (0 to 3) and displayed as averages.

A3.3.10. Statistical analysis.

All data are presented as the mean ± SEM. Two-Way ANOVA with Sidak's post-hoc test for multiple comparisons were used to know which results are significantly different with $p<0.05$.

A.3.4. Results.

A3.4.1. Luminal pH along the midgut of *M. domestica* larvae.

A detailed picture of pH variation along the midgut is necessary to define the major sites of acidification and alkalization. With this aim, determinations were carried out *in vivo* with microsensors at nine different midgut sections (Figure A3.1B).

pH values of the midgut contents of larvae actively feeding on ration were around 6.5 units at the anterior midgut (Table A3.1), whereas that of the ration itself is 5.5. This means that there is a significant ($p<0.05$) increase of pH once ration is ingested. A gradient of acidification was observed from A3 to M2 ($p<0.05$), followed by an abrupt alkalization at P1 of more than 2 units of pH ($p<0.05$). A smaller but significant increase of pH was detected in P2, followed by a final decrease in P4 ($p<0.05$). A similar pH profile was observed in larvae actively feeding on starch gel, but with pH values along the midgut significantly lower ($p<0.05$). No increase of pH was observed in the anterior midgut region of larvae feeding on starch, which remained at pH 5.5, the same pH value of starch gel. Moreover, it was not found a significant increase of pH in P2 of larvae feeding on starch, thus differing from those in ration. The reason why ration change the midgut pH is the presence of free amino acids or amino acids liberated by protein digestion. This will become clearer bellow.

Table A3.1. Table1 Luminal pH values at anterior (A), middle (M) and posterior (P) midgut sections of M. domestica larvae maintained in different diets.

	Midgut Sections								
Diet	A1	A2	A3	M1	M2	P1	P2	P3	P4
Ration (pH 5-5.5)	6.59 ± 0.05	6.77 ± 0.21	6.17 ± 0.06*	5.68 ± 0.14*	4.45 ± 0.15*	6.68 ± 0.03*	7.53 ± 0.09*	7.47 ± 0.10	5.37 ± 0.02*
Starch (pH 5.5)	5.34 ± 0.09	5.62 ± 0.07	5.23 ± 0.04*	4.29 ± 0.08*	2.49 ± 0.13*	5.53 ± 0.26*	6.18 ± 0.21	6.44 ± 0.09	5.56 ± 0.32*
PHL	n.d.	n.d.	n.d.	n.d.	2.54 ± 0.24	7.24 ± 0.25*	7.87 ± 0.35	8.02 ± 0.27	7.73 ± 0.33
Ovalbumin	n.d.	n.d.	n.d.	n.d.	2.82 ± 0.14	5.33 ± 0.09*	5.89 ± 0.10*	6.17 ± 0.24	5.3 ± 0.17*

*Values are averages and SEM corresponding to determinations carried out in 8 larvae. * Values significantly different from those of the previous section ($p<0.05$). PHL: Protein hydrolysate; n.d.: not determined.*

A3.4.2. Proteins putatively involved in midgut luminal buffering.

Table A3.1 shows that the main event of acidification occurs at the middle midgut and of alkalization at the beginning of posterior midgut. Thus, genes coding for proteins involved in acidification and alkalization are expected to be most expressed in these regions.

Twenty two proteins among enzymes, transporters, channels and pumps were chosen as candidates to be involved in luminal buffering (Table A3.2 and Table *A3.3*). The majority of the selected proteins have characterized orthologs in other Diptera. Bioinformatics confirmed that all the proteins have the putative family features necessary for its activity. Some of these molecules deserve additional comments.

Carbonic Anhydrase (CA). MdCAs were predicted as αCAs. MdCA1 has a predicted GPI-anchor (N261, 99.1%) agreeing with the homolog in *Aedes aegypti* AaCA10, which actually have one [29]. MdCA2 lacks a signal peptide and a transmembrane helix, whereas MdCA3 has a predicted signal peptide. Thus, based on bioinformatics, MdCAs are expected to be GPI-anchored (MdCA1), cytosolic (MdCA2) and secreted (MdCA3) which agrees with orthologs from other Diptera. Up to now, there is no characterization of secreted CA from insects. Thus, the role of MdCA3 requires further research.

Table A3.2. Table 2 Midgut expression of genes putatively associated with middle midgut acidification, protection against acid and metal homeostasis.

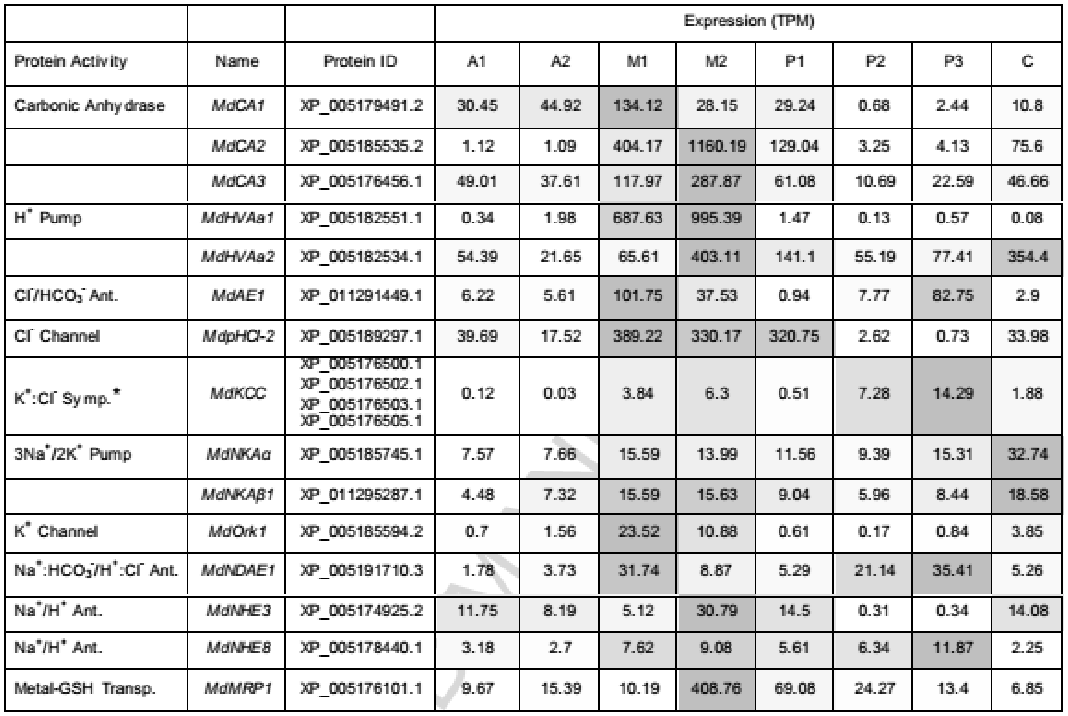

			Expression (TPM)							
Protein Activity	Name	Protein ID	A1	A2	M1	M2	P1	P2	P3	C
Carbonic Anhydrase	*MdCA1*	XP_005179491.2	30.45	44.92	134.12	28.15	29.24	0.68	2.44	10.8
	MdCA2	XP_005185535.2	1.12	1.09	404.17	1160.19	129.04	3.25	4.13	75.6
	MdCA3	XP_005176456.1	49.01	37.61	117.97	287.87	61.08	10.69	22.59	46.66
H^+ Pump	*MdHVAa1*	XP_005182551.1	0.34	1.98	687.63	995.39	1.47	0.13	0.57	0.08
	MdHVAa2	XP_005182534.1	54.39	21.65	65.61	403.11	141.1	55.19	77.41	354.4
Cl^-/HCO_3^- Ant.	*MdAE1*	XP_011291449.1	6.22	5.61	101.75	37.53	0.94	7.77	82.75	2.9
Cl^- Channel	*MdpHCl-2*	XP_005189297.1	39.69	17.52	389.22	330.17	320.75	2.62	0.73	33.98
K^+:Cl^- Symp.*	*MdKCC*	XP_005176500.1 XP_005176502.1 XP_005176503.1 XP_005176505.1	0.12	0.03	3.84	6.3	0.51	7.28	14.29	1.88
$3Na^+/2K^+$ Pump	*MdNKAα*	XP_005185745.1	7.57	7.66	15.59	13.99	11.56	9.39	15.31	32.74
	MdNKAβ1	XP_011295287.1	4.48	7.32	15.59	15.63	9.04	5.96	8.44	18.58
K^+ Channel	*MdOrk1*	XP_005185594.2	0.7	1.56	23.52	10.88	0.61	0.17	0.84	3.85
Na^+:HCO_3^-/H^+:Cl^- Ant.	*MdNDAE1*	XP_005191710.3	1.78	3.73	31.74	8.87	5.29	21.14	35.41	5.26
Na^+/H^+ Ant.	*MdNHE3*	XP_005174925.2	11.75	8.19	5.12	30.79	14.5	0.31	0.34	14.08
Na^+/H^+ Ant.	*MdNHE8*	XP_005178440.1	3.18	2.7	7.62	9.08	5.61	6.34	11.87	2.25
Metal-GSH Transp.	*MdMRP1*	XP_005176101.1	9.67	15.39	10.19	408.76	69.08	24.27	13.4	6.85

Expression data from RNA-seq (average transcripts per million (TPM) values from three biological replicates) where A, M and P corresponds to midgut sections as in Fig. 1a, and carcass (C) is larva less midgut. TPM values of each gene are highlighted different shades of gray so that one can, at a glance, know in which midgut section or carcass it is most expressed. Ant: Antiporter; GSH: glutathione; Symp: Symporter; Transp: transporter. Variation (SEM) among the biological replicates was found to be between 5-20% of the TPM averages for each gene at the sections under study. Taken from Barroso et al., submitted to publication.*

Potassium Chloride Cotransporter (KCC). The gene codes for four isoforms expected to have different location and regulation.

Ammonium transporter Rhesus (Rh). A comparison of the sequence of MdRh with that of AalRh50 from *Aedes albopictus* suggested that MdRh has lower affinity for NH_4^+ than for NH_3 [30]. This is also suggested by highly identity with AgRh50a isoform from *Anopheles gambiae* that is a functional ammonium transporter probably involved in ammonia clearance in head and body of adult female mosquito which mechanism transport may not be electrogenic [31]. Moreover, AeRh50-1 from *Aedes aegypti* involved in ammonia excretion in anal papillae in cooperation with HVA involved in ammonia trapping. Furthermore, until now there is no evidence of NH_4^+ transport by animals ammonium transporters [32,33]. Other proteins involved in ammonia/ammonium transport could be NKA, NHE3 (amiloride insensitive) and HVA.

Table A3.3. Midgut expression of genes putatively associated with posterior midgut alkalization.

Protein Activity	Name	Protein ID	Expression (TPM)							
			A1	A2	M1	M2	P1	P2	P3	C
NH_3 transporter	*MdRh*	XP_005182297.1	0.57	0.75	12.29	67.75	74.48	4.35	0.88	75.43
H^+:AA Symp.	*MdPAT4*	XP_011295206.1	14.82	4.67	18.98	89.22	137.71	30.74	0.05	0.45
	MdPAT5	XP_005184711.2	0.05	0.08	0.03	0	66.79	62.35	30.8	8.61
H^+:Peptide Symp.	*MdPept1*	XP_005182725.1	64.4	149.41	47.58	64.23	372.88	556.38	447.85	8.55
H^+:Cl^- Symp.	*MdNHA1*	XP_005187728.1	7.89	16.55	1.99	0.09	63.04	52.25	3.76	19.14
H^+ Pump	*MdHVAa3*	XP_005178444.1	72.23	207.05	347.36	17.06	186.63	269.9	610.33	36.7
H^+ Pump	*MdHVAa4*	XP_005182101.1	1.18	1.58	3.36	4.65	3.91	7.25	7.33	1.82

Abbreviations and other details as in Table 2.

H^+-Coupled Amino Acid Transporter (PAT). There are 8 MdPATs in *M. domestica* genome and all of them were found expressed in the midgut (data not shown). However, only MdPAT4 and MdPAT5 were selected based on the expression criteria. MdPAT4 has a kinase-binding motif (RFxV/I) and a potential phosphorylation site by protein kinase C (S251), which is absent in the other MdPATs. Thus, MdPAT4 may be regulated by kinases.

Na^+/H^+ Exchanger (NHE). MdNHE3 and MdNHE8 have an amiloride-binding site, but only MdNHE8 has the conserved Leu necessary for amiloride sensitivity [34]. There are proteins other than NHEs that can be inhibited by amiloride, such as Na^+/Ca^{2+} exchangers and Epithelial Na^+ channels (ENaC) [35]. However, the Na^+/Ca^{2+} exchangers expressed in midgut lack the amiloride-binding motif and MdENaC was only expressed in A1 (Table A3.4). Thus, amiloride is a good inhibitor to test the role of MdNHE8 in midgut buffering.

Table A3.4. Midgut expression of genes coding for sodium and potassium channels.

Protein Activity	Name	Protein ID	Expression (TPM)							
			A1	A2	M1	M2	P1	P2	P3	C
Na^+ Channel	*MdENaC*	XP_011290422.1	12.04	0.58	1.8	1.79	0.81	1.61	2.21	38.41
K^+ Channel	*MdSlowpoke*	XP_011291912.1	0	0	0	0.19	0.07	0	0	0.03

Expression data from RNA-seq (average transcripts per million (TPM) values from three biological replicates) where A, M and P corresponds to midgut sections as in Fig. 1a, and carcass (C) is larva less midgut. TPM values of each gene are highlighted different shades of gray so that one can, at a glance, know in which midgut section or carcass it is most expressed. Variation (SEM) among the biological replicates was found to be between 5-20% of the TPM averages for each gene at the sections under study.

A3.4.3. Genes coding for proteins putatively involved in acidification and associated phenomena.

Table A3.2 presents the genes coding for proteins that could have a role in acidification, based on the fact they are more expressed at the middle acidic midgut, except otherwise specified. One CA (*MdCA1*) and the Open Rectifier K^+ channel (*MdOrk1*) were more expressed in M1. Two bicarbonate transporters (*MdAE1* and *MdNDAE1*) were more expressed in M1 and P3. Another two CA (*MdCA2* and *MdCA3)*, two *MdH⁺ V-ATPase subunit a* (*a1* and *a2)*, one NHE (*MdNHE3*), and a multidrug resistance protein (*MdMRP1)* were more expressed in M2. A pH-sensitive chloride channel (*MdpHCl-2*) was highly and almost equally expressed in M1, M2 and P1.

Moreover, three genes with higher expression out of middle midgut were included here because there is experimental evidence that they are involved in acidification. *MdNHE8* was inhibited by amiloride; a K^+Cl^- cotransporter (*MdKCC*) by furosemide and the *MdNa⁺/K⁺-ATPase* (*MdNKA*) *subunits α and β1* inhibited by oubain.

A3.4.4. Genes coding for proteins putatively involved in alkalization and amino acid absorption.

The major event of alkalization occurs at M2-P1 boundary. However, in larvae actively feeding with ration and ovalbumin an increase of alkalization also occurs in P2 (Table A3.1). Therefore, genes coding for proteins putatively responsible for alkalization must be more expressed at the M2-P1 boundary and at P2 (Table A3.3). An ammonium transporter (*MdRh*) and a H^+-coupled amino acid transporter (*MdPAT4*) were predominantly expressed in the M2-P1 boundary, although *MdRh* was also highly expressed in carcass. *MdPAT5* and a Na^+/H^+ antiporter (*MdNHA1*) were highly expressed at P1 and P2. A H^+-coupled Peptide Transporter (*MdPepT1*) was expressed mainly at posterior midgut and *MdHVAa3* at P3 and M1. Finally, *MdHVAa4 has a* higher expression at P2 and P3, although it is a low one.

It is important to emphasize that the four isoforms of *MdHVAa* are the unique pump subunits which differ in expression along the midgut, suggesting different roles [5].

A3.4.5. Identification of selected proteins at the midgut microvillar membranes.

Twelve proteins of the twenty-two protein sequences analyzed were detected in microvillar membranes by proteomics, suggesting they have an apical location (Table A3.5). Eight proteins were detected in specific regions: MdHVAa1 and MdCA1 in M1+M2; MdRh in P1+P2; MdKCC in P3+P4; MdNHE3 in A1 and A2+A3; MdNDAE1 in M1+M2 and P3+P4; MdNHA1 in A2+A3 and P1+P2; and MdNKAβ1 in A1 and M1+M2. The rest of the detected proteins were found along the midgut as MdHVAa2, MdHVAa3, MdPepT1, and MdNKAα. Thus, proteomic analysis correlated well with transcriptomics for nearly all the proteins detected (Compare Table A3.5 with Table A3.2 and Table *A3.3*). The lack of correlation of transcriptomics and proteomics is expected in the case the protein is basolateral. As an example, the absence of NHE3 in microvillar membranes of middle midgut, but highest transcript expression in the same region, means NHE3 may be basolateral.

Table A3.5. Proteins putatively associated with midgut buffering found at purified microvillar cell membranes by proteomics.

Name	Protein ID	A1	A2 + A3	M1 + M2	P1 + P2	P3 + P4
MdCA1	XP_005179491.2	0	0	0.072	0	0
MdHVAa1	XP_005182551.1	0	0	0.735	0	0
MdHVAa2	XP_005182534.1	0.380	0.028	0.282	0.053	0.049
MdHVAa3	XP_005178444.1	0.324	0.199	0.131	0.054	0.229
MdKCC*	XP_005176500.1	0	0	0	0	0.012
MdNHE3	XP_005174925.2	0.049	0.015	0	0	0
MdNDAE1	XP_005191710.3	0	0	0.016	0	0.012
MdRh	XP_005182297.1	0	0	0	0.064	0
MdNHA1	XP_005187728.1	0	0.033	0	0.021	0
MdPepT1	XP_005182725.1	0.321	1.112	0.285	1.050	0.694
MdNKAα	XP_005185745.1	0.539	0.135	0.087	0.028	0.039
MdNKAβ1	XP_005190319.1	0.078	0	0.058	0	0

*Values are expressed in percentage of normalized spectral abundance. Factor values at anterior (A), middle (M) and posterior (P) midgut sections of M. domestica larvae. * Taken from Barroso et al., submitted to publication.*

A3.4.6. Testing the role of proteins with inhibitors and different diets.

The role of transporters and pumps in acidification and alkalization was tested with different inhibitors and diets. For those whose inhibition effect is remarkable at the middle midgut, we used the pH indicator Congo Red (blue 3.0-5.2 red). Thus, the putative role of MdKCC, MdHVA and MdNKA in acidification was tested using their inhibitors: furosemide, bafilomycin A1, and ouabain, respectively. Figure A3.3 shows that these inhibitors impaired acidification by the blue-red change of Congo Red in middle midgut, whereas Table A3.6 shows that the inhibition depends on the inhibitor concentration and on the diet osmolarity. For MdHVA and MdKCC the inhibition was higher in hyperosmotic conditions, whereas for MdNKA it was in hypotonic conditions.

When the inhibition effect was not detected by Congo Red, the role of transporters was tested by measuring luminal pH with microsensors at different conditions.

Table A3.6. Inhibition of middle midgut acidification at different osmolarities expressed in relative numbers.

Osmolarity	Bafilomycin A1	Oubain					Furosemide				
	400 nM	1 µM	10 µM	50 µM	100 µM	1 mM	10 µM	25 µM	50 µM	100 µM	1 mM
Hypotonic (150 mOsm)	1.0	0.8	0.7	2.1	2.1	2.1	0.1	0.2	0.3	0.4	0.9
Isotonic (350 mOsm)	0.9	0.2	0.3	0.6	0.6	1.1	0.1	0.0	0.1	0.5	0.6
Hypertonic (1500 mOsm)	2.0	0.0	0.2	0.3	1.0	0.8	0.2	0.2	0.4	1.0	2.2

M. domestica larvae were fed with 1% agarose gel containing 0.025% Congo Red and one inhibitor (bafilomycin A1: H+ V-ATPase; ouabain: Na+/K+-ATPAse; furosemide: KCC), in media with three different osmolarities. Results were classified in four increasing degrees of inhibition, corresponding to a change of blue to red, as follows: 0, blue; 1, decreasing blue intensity; 2, bluish red; 3, red. Figure 2 shows examples of the inhibition degrees and how the numbers were related to colors. Data are averages of 10 larvae

As Terra and Regel (1995)[9] hypothesized alkalization of posterior midgut by ammonia and we found expression of MdRh at the M2-P1 boundary, we used inhibitors of this transporter to test the proposal. Two different inhibitors, dimethyl ammonium (DMA) and imidazole [36], were used. Table A3.5 shows that in the presence of 10 mM DMA the pH increase at P1 was lesser than in control (starch gel) and that with 100 mM DMA the pH increase was abolished. In comparison, 10 mM imidazole was ineffective, whereas 100 mM also abolished the pH increase. The data indicate that DMA and imidazole affect alkalization and that DMA is a stronger inhibitor of MdRh than imidazole, as proposed by [36] for another ammonium transporter.

The posterior midgut was characterized by high expression of genes coding for MdPATs and MdPepT1. Diet feeding data support the hypothesis that the H^+-coupled transport of amino acids and peptides by MdPATs and MdPepT1, respectively, could be involved in the alkalization of posterior midgut. Thus, larvae fed with 1% of partially hydrolyzed proteins in starch gel had, in comparison with those feeding on starch devoid of amino acids, a higher increase of pH from M2 to P1 that extends to P4 (Table A3.1 and

Table A3.7). Furthermore, the release of peptides and amino acids from ovalbumin and ration under the action of endopeptidases, highly active at posterior midgut [37], is probably the cause of the increase of pH in P2 due to the action of MdPATs and MdPepT.

		Midgut sections		
Transporter affected	Addition	M2	P1	ΔpH P1-M2
None	None	2.49 ± 0.13	5.53 ± 0.26	3.03 ± 0.45
NH3 Transp. (MdRh)	DMA (10mM)	2.72 ± 0.24	4.55 ± 0.11	1.83 ± 0.26*
	DMA (100mM)	3.42 ± 0.09	3.12 ± 0.07	- 0.30 ± 0.06*
	Imidazole (10 mM)	2.61 ± 0.29	5.11 ± 0.42	2.51 ± 0.23*
	Imidazole (100 mM)	3.55 ± 0.14	3.49 ± 0.09	- 0.05 ± 0.12*
H+:Peptide Symp. (MdPepT1)	PHL	2.54 ± 0.24	7.24 ± 0.25	4.47 ± 0.41*
Na+/H+ Ant. (MdNHE8)	Amiloride	1.86 ± 0.11*	n.d.	n.d.
Metal-GSH Transp. (MdMRP1)	Glibenclamide	3.51 ± 0.06*	n.d.	n.d.

Values are averages and SEM corresponding to determinations carried out in 5 larvae. DMA: dimethyl ammonium; PHL: protein hydrolysate; n.d.: not determined.
** Values significantly different from None (p<0.05).*

Figure A3.3. Effect of inhibitors on the midgut pH from M. domestica larvae fed on 1% agarose gel with 0.025% Congo Red (blue 3.0-5.2 red). Inhibitors added: (A), 400 nM *bafilomycin A1; (B), 100 μM oubain; (C), 1 mM ouabain; (D), 100 μM furosemide; (E), 1 mM furosemide. At each condition, controls are at the top and experimental at the bottom of the figures. Results show clearly the impairment of acidification (blue in control) in the presence of inhibitors (red with inhibitor).*

		Midgut sections		
Transporter affected	Addition	M2	P1	ΔpH P1-M2
None	None	2.49 ± 0.13	5.53 ± 0.26	3.03 ± 0.45
NH3 Transp. (MdRh)	DMA (10mM)	2.72 ± 0.24	4.55 ± 0.11	1.83 ± 0.26*
	DMA (100mM)	3.42 ± 0.09	3.12 ± 0.07	- 0.30 ± 0.06*
	Imidazole (10 mM)	2.61 ± 0.29	5.11 ± 0.42	2.51 ± 0.23*
	Imidazole (100 mM)	3.55 ± 0.14	3.49 ± 0.09	- 0.05 ± 0.12*
H+:Peptide Symp. (MdPepT1)	PHL	2.54 ± 0.24	7.24 ± 0.25	4.47 ± 0.41*
Na+/H+ Ant. (MdNHE8)	Amiloride	1.86 ± 0.11*	n.d.	n.d.
Metal-GSH Transp. (MdMRP1)	Glibenclamide	3.51 ± 0.06*	n.d.	n.d.

Values are averages and SEM corresponding to determinations carried out in 5 larvae. DMA: dimethyl ammonium; PHL: protein hydrolysate; n.d.: not determined.
** Values significantly different from None (p<0.05).*

Table A3.7 shows that glibenclamide, a general MRP inhibitor [38], increased one pH unit in M2, suggesting that MdMRP1 could be indirectly involved in acidification [39].

Finally, the decrease in middle midgut pH with amiloride suggests that the amiloride-sensitive MdNHE8 could be involved in regulating acidification of the middle midgut. However, no pH change was detected in P4, where MdNHE8 is also well expressed, which suggests that the transporter may fulfill different roles depending on the midgut section.

Table A3.7. Effect of selected compounds on the luminal pH between middle and posterior midgut of larvae in a starch diet.

A3.5. Discussion.

A3.5.1. Acidification of middle midgut and mucosal protection against acid.

A hypothetic working model was developed taking into account transcriptomics, proteomics, *in vivo* pH determinations at different conditions and literature data on orthologs, in order to explain midgut buffering and mucosal protection against acid.

		Midgut sections		
Transporter affected	Addition	M2	P1	ΔpH P1-M2
None	None	2.49 ± 0.13	5.53 ± 0.26	3.03 ± 0.45
NH_3 Transp. (MdRh)	DMA (10mM)	2.72 ± 0.24	4.55 ± 0.11	1.83 ± 0.26*
	DMA (100mM)	3.42 ± 0.09	3.12 ± 0.07	- 0.30 ± 0.06*
	Imidazole (10 mM)	2.61 ± 0.29	5.11 ± 0.42	2.51 ± 0.23*
	Imidazole (100 mM)	3.55 ± 0.14	3.49 ± 0.09	- 0.05 ± 0.12*
H^+:Peptide Symp. (MdPepT1)	PHL	2.54 ± 0.24	7.24 ± 0.25	4.47 ± 0.41*
Na^+/H^+ Ant. (MdNHE8)	Amiloride	1.86 ± 0.11*	n.d.	n.d.
Metal-GSH Transp. (MdMRP1)	Glibenclamide	3.51 ± 0.06*	n.d.	n.d.

*Values are averages and SEM corresponding to determinations carried out in 5 larvae. DMA: dimethyl ammonium; PHL: protein hydrolysate; n.d.: not determined. * Values significantly different from None (p<0.05).*

Middle midgut acidification by oxyntic cells needs a source of H^+ that is supplied by cytosolic MdCA2, as supported by acetazolamide (CA inhibitor) inhibition (Terra and Regel, 1995)[9] and knockout of ortholog from *D. melanogaster* that impairs acidification [5]. Moreover, MdCA2 is predicted to be highly active, based on activity data of a protein coded by an orthologous gene from *D. melanogaster* [40], agreeing with the high H^+ demand needed for acidification.

H^+ ions are pumped into the oxyntic cell canaliculi by MdHVA. Regarding this, three MdHVAa were found in microvillar membranes, MdHVAa1, MdHVAa2 and MdHVAa3. Based on knockout of the corresponding orthologs from *D. melanogaster* [5], only MdHVAa1 and MdHVAa2 are related to acidification. MdHVAa1 is probably responsible for H^+ pumping in oxyntic cells, since it is specific of the middle midgut, whereas HVAa2 may contribute to buffering in cells other than oxyntic cells, as suggested by its expression along the midgut and carcass.

The HCO_3^- produced by MdCA2 in oxyntic cells must be excreted from the cell to maintain intracellular pH. This is supposed to be done by the Cl^-/HCO_3^- exchanger (MdAE1), absent from microvillar membranes, and expected to be located at the basal membrane infoldings of the interstitial cells [41]. This suggests that HCO_3^- is transferred through gap junctions from oxyntic cells to interstitial cells from where it is eliminated. This is similar to what is supposed to occur between principal and stellate cells of Malpighian tubules [42].

The pH-sensitive chloride channel (MdpHCl-2) expressed in middle midgut and absent in microvillar membranes is supposed to be responsible for the basolateral transport of Cl^- into oxyntic cells [43]. The channel would be open by the surrounding alkaline microenvironment [44] of the hemolymph, caused by HCO_3^- secreted by basal MdAE1 from interstitial cells. Thus, the impairment of MdpHCl-2 or MdAE1 activity would result in abolition of acidification due to lack of Cl^- to follow H^+ ions, as shown as consequences of knockouts of orthologs in *D. melanogaster*.

The apical Cl^- efflux that follow the pumped H^+ may result from the cooperative action of a microvillar K^+Cl^- cotransporter (MdKCC) and MdHVAa1 both present at the apical membrane of oxyntic cells, in analogy with KCC4 and HVA in mammal parietal cells [45]. This is supported by the impairment of acidification with furosemide described here and knockout of the ortholog from *D. melanogaster* [5]. Associated with HCl transport into oxyntic cell canaliculli, water is driven together with K^+ and Cl^- by MdKCC [46] and a hydrostatic pressure is supposed to develop there, propelling HCl through the mucus layer into middle midgut lumen [47]. The lack of MdKCC in microvillar membranes of middle midgut could be a failure of proteomics due to its lower expression compared to posterior midgut, where it was found.

K^+ secreted by MdKCC must be recovered. In human parietal cells, K^+ secreted by KCC4 is transported into the cell by H^+/K^+-ATPase [45]. Differently, in *M. domestica* there is no H^+/K^+-ATPase, implying that K^+ recycling occurs by another mechanism. *MdOrk1* was specifically expressed in middle midgut and absent in microvillar membranes. This pattern of expression agrees with that of another K^+ channel (Slowpoke) from *D. melanogaster,* which was related to acidification [5]. However, *MdSlowpoke* was virtually unexpressed in middle midgut. Due to the impossibility of checking the annotation of the *D. melanogaster* Slowpoke, as no accession number was published [5], and based on the expression pattern of both K^+ channels (Slowpoke and MdOrk1), they seem to be the same channel. Thus, in *M. domestica* the K^+ extruded by MdKCC is supposed to be recovered by apical MdOrk1 in hyperpolarized conditions. Hyperpolarization would result by the large extracellular K^+ concentration relative to intracellular, allowing inwardly K^+ current. A similar model was suggested for another K^+ channel (Kir4.1) in the apical membrane of parietal cells [48].

The impairment of middle midgut acidification by ouabain supports a role of MdNKA in maintaining the Na^+ and K^+ homeostasis needed for secondary active transport. Unexpectedly, MdNKA is apical based on microvillar proteomics. Despite this and the fact that apical NKA was also described in other Diptera [49–51], we will consider MdNKA basal, until further research confirm its unusual apical localization.

Larvae fed with amiloride containing starch showed a significant drop in middle midgut pH. Although MdNHE8 was not found at cell microvillar membranes, the results suggest that amiloride-sensitive MdNHE8 regulates acidification by transporting luminal H^+ into the cell, while extruding Na^+ in the middle midgut. Thus, MdNHE8 seems to be localized in the apical membrane as assigned by Kang' ethe *et al.* (2007)[52] to *A. aegypti* NHE8 in Malpighian tubules rather than in an intracellular subapical location as described by Piermarini *et al.* (2009)[53].

Finally, MdMRP1 was the only MRP with high expression specific of the middle midgut (M2) that is involved in Cu^{2+} and Zn^{2+} absorption [54]. It was absent from microvillar membranes, suggesting a basolateral localization. This expression pattern agrees with transcriptomic analysis in response to heavy metals of the ortholog in *D. melanogaster* (CG10505; Yepiskoposyan *et al.*, 2006)[39]. CG10505 is transcriptionally modulated by Cu^{2+} and Zn^{2+}, supporting the proposal that the coded protein may export metal-GSH (Glutathione). The general inhibitor of MRPs, glibenclamide, results in an increase of pH in middle midgut suggesting that acidification of middle midgut may be indirectly modulated by Cu^{2+} and/or Zn^{2+} homeostasis. Regarding this, Cl^--dependent Cu^{2+} uptake is enhanced by an acidic environment [55] as well as a diet rich in Cu^{2+} impairs acidification [56]. Thus, inhibition of MdMRP1 presumably involved in metal homeostasis could result in a decrease of acidification to avoiding metal toxicity.

The luminal surface of the gastrointestinal tract of vertebrates is lubricated and protected against acid by a mucus formed by different type of mucins, depending on the section (mouth, stomach, small and large intestine) [57].

In insects, a mucus formed by mucus-forming mucins (Mfm) was found in the midgut lumen of *D. melanogaster* [54,58] and it was proposed for other species (including *M. domestica*) based on the expression of Mfms [11].

Mfms from *M. domestica* are generally more expressed in middle midgut and in lesser extent in P3, regions characterized by being more acidic. Among mucins, MdMfm1 was the most expressed with higher expression in the middle midgut (about 100-1000 times more than the other Mfms) [11]. This high expression may be necessary to recover the mucus layer lost with the food bolus in order to protect the middle midgut epithelium from acid.

In vertebrates, the mucus of the stomach is neutralized by HCO_3^- secreted by epithelial cells [57]. Because midgut interstitial cells cover most of the oxyntic cells, except for a small aperture [8,59], Mfms are probably secreted by the interstitial cells, which also secrete HCO_3^- to neutralize the mucus layer. In accordance with this, a GPI-anchored MdCA1 and a putative Na^+:HCO_3^-/H^+:Cl^- exchanger (MdNDAE1) were found in the microvillar membrane of the middle midgut cells. In interstitial cells the concentration of HCO_3^- is expected to be high due to local production and the transference from oxyntic cells, which lacks a HCO_3^- transporter [41]. The mucus layer covering the apical surface of these cells is expected to be permeated by luminal H^+ and Cl^-, favoring the luminal secretion of HCO_3^- and Na^+ in exchange by H^+ and Cl^- by MdNDAE1. Extruded HCO_3^- would react with H^+ forming H_2CO_3 and then CO_2 and H_2O catalyzed by the GPI-anchored MdCA1 in the outer face of the microvillar membrane [60,61]. MdCA1 is expected to be as active as MdCA2 based on activity data from proteins coded by orthologous genes from *D. melanogaster* [40]. The removal of HCO_3^- enhances the exit of more HCO_3^- and the neutralization of the mucus layer. As a result a pH gradient is established from acidic lumen to neutral pH at the surface of interstitial cells. This hypothetical system of buffering agrees with the low concentration of HCO_3^- found along the midgut by Terra and Regel (1995)[9], since HCO_3^- would be only transient.

The incoming H^+ in the interstitial cells caused by MdNDAE1 could be eliminated by basolateral MdNHE3 coupled to the Na^+ gradient established by the basolateral MdNKA, thus extruding acid as was described for the *A. aegypti* NHE3 in Malpighian tubules (Pullikuth *et al.*, 2006) [62].

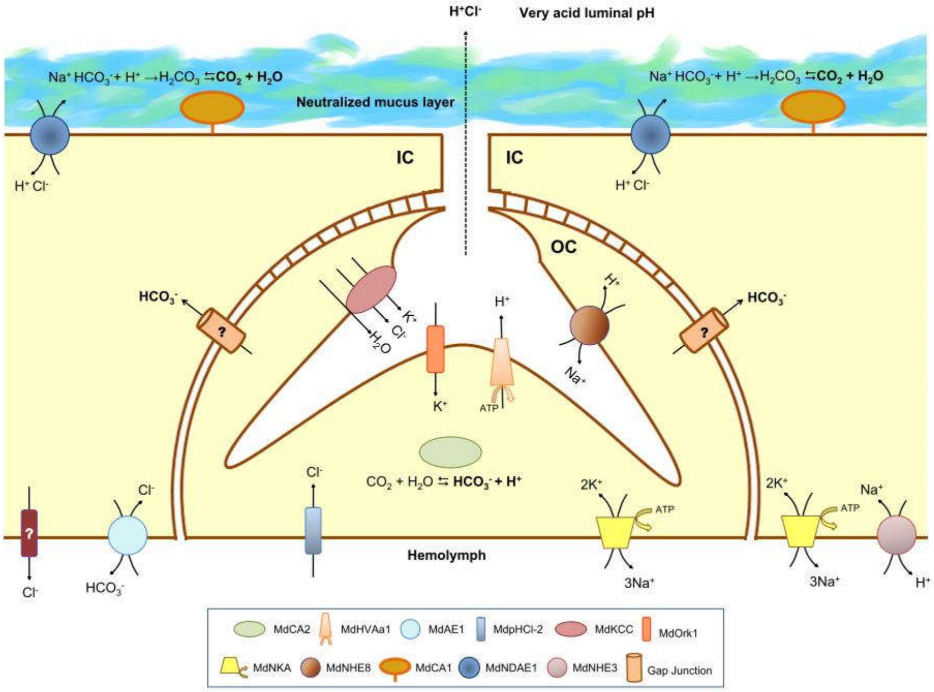

Figure A3.4. Working model of midgut luminal acidification by oxyntic cells (OC) and mucosal acid protection by interstitial cells (IC). Under the action of the MdHVAa1, H^+ is pumped into the canaliculli, accompanied by Cl^- secreted by MdKCC and water. As consequence of increased hydrostatic pressure in the canaliculli, H^+ and Cl^- ions are propelled through the mucus layer into midgut lumen. H^+ resulted from the action of MdCA2 on CO_2, K^+ homeostasis is assured by basolateral MdNKA, and Cl^- is recovered by basolateral MdpHCl-2. HCO_3^- remaining in OC is transferred from OC to IC through gap junctions, thus avoiding OC alkalization. K^+ secreted by MdKCC is recovered by an apical K^+ channel, MdOrk1, in hyperpolarized conditions, enhancing the MdKCC activity. The amiloride-sensitive MdNHE8 controls the H^+ concentration by transporting part of the H^+ extruded by the H^+ pump from the canaliculli to the cell. Interstitial middle midgut cells secrete into the mucus layer HCO_3^- and Na^+ that neutralizes it in exchange for H^+ and Cl^- under the action of MdNDAE1. The HCO_3^- reacts with H^+ permeated from the lumen into the mucus layer, forming H_2CO_3, which is dehydrated by a GPI-anchored MdCA1, resulting in H_2O and CO_2. Excess acid is eliminated from IC by basolateral amiloride-insensitive MdNHE3 and Cl^- by a putative channel.

Figure A3.4 summarizes the putative molecular events associated with acidification and mucosal cell protection in the *M. domestica* middle midgut. Despite the fact that the proposed model explains all described phenomenon, it should be considered a working model demanding further study to be confirmed and extended.

A3.5.2. Alkalization of posterior midgut.

NH_3 was supposed to be involved in the alkalization of the posterior midgut of *M. domestica* larvae based on chemical determinations [9]. The NH_3 may traps the H^+ coming from middle midgut forming NH_4^+ [33], thus alkalinizing the lumen at the beginning of posterior midgut. This hypothesis is supported by the presence of the ammonium transporter MdRh in the microvillar cell membranes at P1+P2 and the decrease in P1 alkalization in the presence of the inhibitors of ammonium transporters, DMA and imidazole. The probable origin of the NH_3 is the hemolymph, which is characteristically rich in this compound among dipterans [63-65]. The NH_3 is proposed to enter in the midgut cells by simple diffusion and to be transported into the lumen by MdRh. Thus, ammonia is thought to be both a buffer and nitrogen excreta.

The increase of P1 alkalization caused by a protein hydrolysate-containing diet points to a role of the H^+-coupled amino acid and peptide transport in posterior midgut alkalization. Regarding this, the H^+:peptide symporter MdPepT1[66] was found in microvillar membranes of posterior midgut cells (Table A3.5), whereas MdPAT4 and MdPAT5 (also highly expressed there) were not. Thus, this contribution to alkalization may be attributed only to MdPepT1. The absence of the typically apical membrane symporters MdPATs from microvillar proteomics data may have resulted from their maintenance in intracellular compartments [67]. This maintenance would be expected mainly in larvae fed with diets devoid of amino acids, as those used for sampling for proteomics. However, it is expected that in larvae fed with protein hydrolysate they are expressed in the apical membrane. Thus, we cannot deny that MdPATs may be also involved in alkalization, although it requires further research.

Larvae fed with ovalbumin or ration showed an increase of pH in P2 section which is characterized by high trypsin activity [37]. As a result of the endopeptidase activity, the resulting peptides would be cotransported with H^+ by MdPepT1, causing the increase of pH at P2.

The transport activity of PepTs as PATs benefits from an acidic extracellular microenvironment (pH5-6) [66,68]. In human intestine the superficial acid microenvironment is maintained by NHE3 [69,70]. In larvae fed on ration or protein hydrolysate, a pH around 7.5 is observed in posterior midgut potentially inhibiting MdPepT1 and MdPATs activities. Nevertheless, MdNHA1 is coexpressed with MdPepT1 in microvillar membranes (Table A3.5). MdNHA1 may provide the acid microenvironment at the cell surface that enhances MdPepT1 (and presumably MdPATs) by recovering H^+ cotransported with peptides by MdPepT1. This recovery may occur if MdNHA1 function as a Na^+/H^+ antiporter or $H^+:Cl^-$ symporter based on orthologs from *An. gambiae* and *D. melanogaster*, respectively [71,72].

Finally, the H^+-coupled amino acid and peptide transport would lead to a pronounced cell acidification [73], which may be avoided by the basal extrusion of H^+ by MdHVA a4 absent from microvillar membranes as described for HVA from *Ae. aegypti* and *A. gambiae* [49,50,74]. Furthermore, MdCA2 also expressed in P1 where alkalization occurs, suggests that intracellular acidification may also be avoided by reaction of intracellular HCO_3^- with H^+ cotransported by MdPepT1 (and presumably MdPATs) generating CO_2 and H_2O.

Figure A3.5 summarizes the molecular events proposed to be associated with posterior midgut alkalization and amino acid absorption. As before, this proposal should be considered a working model to be confirmed and extended by further investigations.

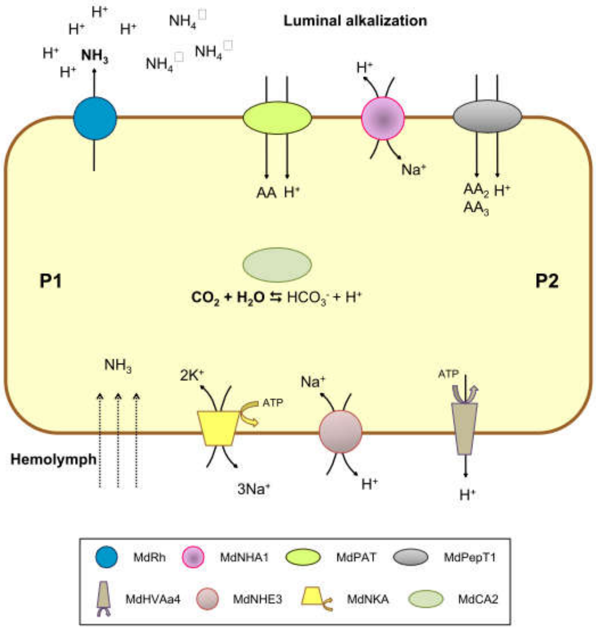

Figure A3.5. Working model of luminal alkalization at posterior midgut. Midgut alkalization occurs mainly at the beginning of the posterior region caused by the transport of NH_3 by MdRh. NH_3 reacts with H^+ coming from the middle midgut contents, forming NH_4^+. Cell NH_3 comes from hemolymph by simple diffusion. Alkalization is further increased in a diet containing protein, as a consequence of the symport of H^+ and peptides carried out by MdPept1 and presumably also by H^+ and amino acids by MdPATs. The MdNHA1 maintains mildly acid the neighborhood of MdPATs and MdPepT 1, thus enhancing their activity. Intracellular acidification is circumvented by basolateral MdNHE3, coupled to the Na^+ gradient established by basolateral MdNKA and H^+ pumping by basolateral MdHVAa4.

A3.6. Conclusions.

Several transporters are involved in midgut buffering, thus affecting digestive enzyme activities and absorptive mechanisms. Middle midgut acidification occurs through the action of H^+ V-ATPase and a K^+Cl^- symporter. The Na^+/K^+-ATPase influence acidification through the maintenance of the Na^+ and K^+ homeostasis, favoring secondary active transport. Acidification is also modulated directly by a Na^+/H^+ exchanger and indirectly by a metal homeostasis protein. The finding of a GPI-anchored carbonic anhydrase and a bicarbonate antiporter at middle midgut microvillar membranes led to the hypothesis of mucus layer neutralization to protect mucosa against acid. Alkalization of posterior midgut depends on ammonia transport, which sequesters H^+ coming from middle midgut, thus forming ammonium. The symport of peptides and perhaps also of amino acids with H^+ increases alkalization. Finally, two models combining all the results and hypotheses are included and are supposed to helping further advances.

A3.7. Acknowledgments.

This work was supported by the Brazilian research agencies Fundação de Amparo à Pesquisa do Estado de São Paulo, FAPESP (Grant “Tematico” no.2017/08103-4 and a Regular Grant no. 2015/20776-9) and Conselho Nacional de Pesquisa, CNPq. Ignacio G. Barroso is a graduate fellow of CNPq. Carla S. Santos is a graduate fellow of FAPESP. Mauro Bertotti, C. Ferreira and W.R. Terra are staff members of their respective departments and research fellows of the CNPq. C. Ferreira and W.R. Terra are also members of the Instituto Nacional de Ciência e Tecnologia em Entomologia Molecular (INCT-EM).

A3.8. References.

1. Bowen, S. H. *Nature* **1976**, 260, 137–138.
2. Vonk, H. J.; Western, J. R. H. *Comparative Biochemistry and Physiology of Enzymatic Digestion*; Academic Press: New York, 1984.
3. Brues, C. T. *Insect dietary*; Harvard University Press: Cambridge, 1946.
4. Levinson, Z. H. *Nature* **1960**, 188, 4748, 427–428.
5. Overend, G.; Luo, Y.; Henderson, L.; Douglas, A. E.; Davies, S. A.; Dow, J. A. T. *Sci. Rep.* **2016**, 6, 1–11.
6. Espinoza-Fuentes, F. P.; Terra, W. R. *Insect Biochem.* **1987**, 17, 6, 809–817.
7. Lemos, F. J. A.; Ribeiro, A. F.; Terra, W. R. *Insect Biochem. Mol. Biol.* **1993**, 23,

4, 533–541.

8. Terra, W. R.; Espinoza-Fuentes, F. P.; Ribeiro, A. F.; Ferreira, C. *J. Insect Physiol.* **1988**, 34, 6, 463–472.

9. Terra, W. R.; Regel, R. *Comp. Biochem. Physiol.* **1995**, 112, 3–4, 559–564.

10. Targa, H. J.; Peres, C. A. *Mutat. Res. Fundam. Mol. Mech. Mutagen. Fundam. Mol. Mech. Mutagen.* **1979**, 63, 1, 153–160.

11. Dias, R. O.; Cardoso, C.; Pimentel, A. C.; Damasceno, T. F.; Ferreira, C.; Terra, W. R. *Insect Mol. Biol.* **2018**, 27, 1, 46–60.

12. Altschul, S. F.; Gish, W.; Miller, W.; Myers, E. W.; Lipman, D. J. *J. Mol. Biol.* **1990**, 215, 3, 403–410.

13. Jones, P.; Binns, D.; Chang, H. Y.; Fraser, M.; Li, W.; McAnulla, C.; McWilliam, H.; Maslen, J.; Mitchell, A.; Nuka, G.; Pesseat, S.; Quinn, A. F.; Sangrador-Vegas, A.; Scheremetjew, M.; Yong, S. Y.; Lopez, R.; Hunter, S. *Bioinformatics* **2014**, 30, 9, 1236–1240.

14. Katoh, K.; Rozewicki, J.; Yamada, K. D. *Brief. Bioinform.* **2017**, bbx108, 1–7.

15. Waterhouse, A. M.; Procter, J. B.; Martin, D. M. A.; Clamp, M.; Barton, G. J. *Bioinformatics* **2009**, 25, 9, 1189–1191.

16. Petersen, T. N.; Brunak, S.; Von Heijne, G.; Nielsen, H. *Nat. Methods* **2011**, 8, 10, 785–786.

17. Krogh, A.; Larsson, B.; Von Heijne, G.; Sonnhammer, E. L. L. *J. Mol. Biol.* **2001**, 305, 3, 567–580.

18. Käll, L.; Krogh, A.; Sonnhammer, E. L. L. *Nucleic Acids Res.* **2007**, 35 (SUPPL.2), 429–432.

19. de Castro, E.; Sigrist, C. J. A.; Gattiker, A.; Bulliard, V.; Langendijk-Genevaux, P. S.; Gasteiger, E.; Bairoch, A.; Hulo, N. *Nucleic Acids Res.* **2006**, 34 (WEB. SERV. ISS.), 362–365.

20. Gupta, R.; Jung, E.; Brunak, S. *Pacific Symp. Biocomput.* **2004**, 7, 310–322.

21. Steentoft, C.; Vakhrushev, S. Y.; Joshi, H. J.; Kong, Y.; Vester-Christensen, M. B.; Schjoldager, K. T. B. G.; Lavrsen, K.; Dabelsteen, S.; Pedersen, N. B.; Marcos-Silva, L.; Gupta, R.; Paul Bennett, E.; Mandel, U.; Brunak, S.; Wandall, H. H.; Levery, S. B.; Clausen, H. *EMBO J.* **2013**, 32, 10, 1478–1488.

22. Blom, N.; Sicheritz-Pontén, T.; Gupta, R.; Gammeltoft, S.; Brunak, S. *Proteomics* **2004**, 4, 6, 1633–1649.

23. Pierleoni, A.; Martelli, P.; Casadio, R. *BMC Bioinformatics* **2008**, 9, 1–11.

24. Ferrè, F.; Clote, P. *Nucleic Acids Res.* **2005**, 33 (SUPPL. 2), 230–232.

25. Sonnhammer, E. L. L.; Östlund, G. *Nucleic Acids Res.* **2015**, 43 (D1), D234–D239.

26. Jordão, B. P.; Terra, W. R.; Ferreira, C. *Insect Biochem. Mol. Biol.* **1995**, 25, 4, 417–426.

27. Santos, C. S.; Lima, A. S.; Battistel, D.; Daniele, S.; Bertotti, M. *Electroanalysis* **2016**, 28, 7, 1441–1447.

28. Buck, J. B. *Physical properties and chemical composition of insect blood*; Ed. Insect Physiology, John Wiley: New York, NY, 1953.

29. Seron, T. J.; Hill, J.; Linser, P. J. *J. Exp. Biol.* **2004**, 207, 26, 4559–4572.

30. Wu, Y.; Zheng, X.; Zhang, M.; He, A.; Li, Z.; Zhan, X. *J. Insect Physiol.* **2010**, 56, 11, 1599–1610.

31. Pitts, R. J.; Derryberry, S. L.; Pulous, F. E.; Zwiebel, L. J. *PLoS One* **2014**, 9, 10, e111858.

32. Weihrauch, D.; Donini, A.; O'Donnell, M. J. *J. Insect Physiol.* **2012**, 58, 4, 473–487.

33. Chasiotis, H.; Ionescu, A.; Misyura, L.; Bui, P.; Fazio, K.; Wang, J.; Patrick, M.;

Weihrauch, D.; Donini, A. *J. Exp. Biol.* **2016**, 219, 1346–1355.

34. Slepkov, E. R.; Rainey, J. K.; Sykes, B. D.; Fliegel, L. *Biochem. J.* **2007**, 401, 3, 623–633.

35. Giannakou, M. E.; Dow, J. A. T. *J. Exp. Biol.* **2001**, 204, 21, 3703–3716.

36. Wacker, T.; Garcia-Celma, J. J.; Lewe, P.; Andrade, S. L. A. *Proc. Natl. Acad. Sci.* **2014**, 111, 27, 9995–10000.

37. Espinoza-Fuentes, F. P.; Ribeiro, A. F.; Terra, W. R. *Insect Biochem.* **1987**, 17, 6, 819–827.

38. Payen, L.; Delugin, L.; Courtois, A.; Trinquart, Y.; Guillouzo, A.; Fardel, O. *Br. J. Pharmacol.* **2001**, 132, 3, 778–784.

39. Yepiskoposyan, H.; Egli, D.; Fergestad, T.; Selvaraj, A.; Treiber, C.; Multhaup, G.; Georgiev, O.; Schaffner, W. *Nucleic Acids Res.* **2006**, 34, 17, 4866–4877.

40. Syrjänen, L.; Tolvanen, M. E. E.; Hilvo, M.; Vullo, D.; Carta, F.; Supuran, C. T.; Parkkila, S. *Bioorganic Med. Chem.* **2013**, 21, 6, 1516–1521.

41. Dubreuil, R. R.; Das, A.; Base, C.; Mazock, G. H. **2010**, 9, 1–9.

42. Piermarini, P. M.; Grogan, L. F.; Lau, K.; Wang, L.; Beyenbach, K. W. *Am. J. Physiol. Regul. Integr. Comp. Physiol.* **2010**, 298, 3, R642-60.

43. Remnant, E. J.; Williams, A.; Lumb, C.; Yang, Y. T.; Chan, J.; Duchêne, S.; Batterham, P.; Perry, T. **2016**, 6, 2003–2012.

44. Feingold, D.; Starc, T.; O'Donnell, M. J.; Nilson, L.; Dent, J. A. **2016**, 2629–2638.

45. Fujii, T.; Fujita, K.; Takeguchi, N.; Sakai, H. *Biol. Pharm. Bull.* **2011**, 34, 6, 810–812.

46. Zeuthen, T. *J. Membr. Biol.* **2010**, 234, 2, 57–73.

47. Boron, W. F.; Boulpaed, E. L. *Medical Physiology*, 3rd Edn.; Elsevier: Philadelphia, 2017.

48. Fujita, A.; Horio, Y.; Higashi, K.; Mouri, T.; Hata, F.; Takeguchi, N.; Kurachi, Y. *J. Physiol.* **2002**, 540, 1, 85–92.

49. Patrick, M. L.; Aimanova, K.; Sanders, H. R.; Gill, S. S. *J. Exp. Biol.* **2006**, 209, 23, 4638–4651.

50. Okech, B. A.; Boudko, D. Y.; Linser, P. J.; Harvey, W. R. *J. Exp. Biol.* **2008**, 211, 6, 957–968.

51. Onken, H.; Patel, M.; Javoroncov, M.; Izeirovski, S.; Moffett, S. B.; Moffett, D. F. *J Exp Zool A Ecol Genet Physiol.* **2009**, 311, 3, 155–161.

52. Kang' ethe, W.; Aimanova, K. G.; Pullikuth, A. K.; Gill, S. S. *Am J Physiol Ren. Physiol* **2007**, 70112, 00487.2005.

53. Piermarini, P. M.; Weihrauch, D.; Meyer, H.; Huss, M.; Beyenbach, K. W. *AJP Ren. Physiol.* **2009**, 296, 4, F730–F750.

54. Buchon, N.; Osman, D.; David, F. P. A.; Fang, H. Y.; Boquete, J.; Deplancke, B.; Lemaitre, B. *CellReports Resour.* **2013**, 3, 5, 1725–1738.

55. Zimnicka, A. M.; Ivy, K.; Kaplan, J. H. *Am. J. Physiol. Cell Physiol.* **2011**, 300, 3, C588–C599.

56. McNulty, M.; Puljung, M.; Jefford, G.; Dubreuil, R. R. *Cell Tissue Res.* **2001**, 304 3, 383–389.

57. Johansson, M. E. V; Sjövall, H.; Hansson, G. C. *Nat Rev Gastroenterol Hepatol* **2013**, 10, 6, 352–361.

58. Syed, Z. A.; Härd, T.; Uv, A.; van Dijk-Härd, I. F. *PLoS One* **2008**, 3, 8, e3041.

59. Dubreuil, R. R. *Int. J. Biochem. Cell Biol.* **2004**, 36, 5, 742–752.

60. Romero, M. F.; Henry, D.; Nelson, S.; Harte, P. J.; Dillon, A. K.; Sciortino, C. M. *J. Biol. Chem.* **2000**, 275, 32, 24552–24559.

61. Ferguson, M. A. J.; Hart, G. M.; Kinoshita, T. In *Essentials of Glycobiology*; Varki,

A., Cummings, R. D., Esko, J. D., Al., E., Eds.; Cold Spring Harbor Laboratory Press: New York, NY, 2017.

62. Pullikuth, A. K.; Aimanova, K.; Kang'ethe, W.; Sanders, H. R.; Gill, S. S. *J. Exp. Biol.* **2006**, 209, 18, 3529–3544.

63. Terra, W. R.; De Bianchi, A. G.; Gambarini, A. G.; Lara, F. J. S. *J. Insect Physiol.* **1973**, 19, 11, 2097–2106.

64. Borash, D. J.; Gibbs, A. G.; Joshi, A.; Mueller, L. D. *Am. Nat.* **1998**, 151, 2, 148–156.

65. Marshall, A. T.; Wood, R. W. *J. Insect Physiol.* **1990**, 36, 9, 635–639.

66. Roman, G.; Meller, V.; Wu, K. H.; Davis, R. L. *Am. Physiol. Soc.* **1998**, 857–869.

67. Thwaites, D. T.; Anderson, C. M. H. *Br. J. Pharmacol.* **2011**, 164, 7, 1802–1816.

68. Goberdhan, D. C. I.; Meredith, D. C. .; Boyd, R.; Wilson, C. *Development* **2005**, 132, 10, 2365–2375.

69. Kennedy, D. J.; Leibach, F. H.; Ganapathy, V.; Thwaites, D. T. **2002**, 445, 139–146.

70. Watanabe, C.; Kato, Y.; Ito, S.; Kubo, Y.; Sai, Y.; Tsuji, A. **2005**, 20, 6, 443–451.

71. Xiang, M. A.; Linser, P. J.; Price, D. A.; Harvey, W. R. *J. Insect Physiol.* **2012**, 58, 4, 570–579.

72. Chintapalli, V. R.; Kato, A.; Henderson, L.; Hirata, T.; Woods, D. J.; Overend, G.; Davies, S. A.; Romero, M. F.; Dow, J. A. T. *Proc. Natl. Acad. Sci.* **2015**, 112, 37, 11720–11725.

73. Chen, Z.; Fei, Y.-J.; Anderson, C. M. H.; Wake, K. A.; Miyauchi, S.; Huang, W.; Thwaites, D. T.; Ganapathy, V. *J. Physiol.* **2003**, 546, 2, 349–361.

74. Onken, H.; Moffett, D. F. *J. Exp. Biol.* **2009**, 212, 3, 373–377.

General Conclusions and Perspectives

The implementation of scanning electrochemical microscopy as an analytical tool to investigate local processes, especially in the field of bioenergetics, is the main contribution of this PhD thesis. The challenge of fabricating very small sensors was faced and the knowledges developed during this work have been completely incorporated by all students in the research group. The micro/nanoelectrodes can now allow the investigation of a broad kind of samples at micro and nanoscales in a wide range fields, comprising nanomaterials research, corrosion investigation and energy studies.

The first Brazilian bio-SECM technique is a powerful tool capable to investigate changes in localized oxygen consumption with high spatial resolution in biological samples. The experimental parameters were adopted to minimize topographical effects and to monitor changes in the oxygen reduction current over an investigated sample. The topographical effect was reduced by choosing suitable working distances and by using small probes. The depletion in the concentration of the electroactive species was minimized by recording cyclic voltammograms, instead of using the conventional amperometry technique.

The redox competition SECM mode was successfully employed to perform single-cell analysis and determine local oxygen consumption rates, OCR, an important bioenergetics parameter in metabolism studies. Thus, information on the extent of respiration in cells of a same population, as well as in a single cell, was reliably obtained allowing the preparation of SECM oxygen maps to be constructed. These new findings opened up the possibility of employing SECM to investigate local bioenergetics and the role of different compartments of a single *C. elegans animals to be* studied, leading to novel information of the contribution of the reproductive system on the animal metabolism. Further applications for investigating local processes in biological samples can be improved with the minituarization of the sensor because it is not completely innocent, i.e., even though in a very small amount, the microelectrode always consumes the electroactive species and can disturb the environment. Then, the understading of the consumption of the electroactive species by the electrode in a biological sample is complex and not really well-known. Nevertheless, one possibility to reduce such effect is by reducing the size of the microelectrode.

More quantitative information of an investigated system can be obtained with the use of softwares (e.g., Comsol) to model the experimental data for further calculation of rate constants or understanding of reactions mechanism. This approach is essential to make SECM as a routine analytical method leading to reproducible and realible results, once many SECM parameters can influence the results and the choice of the setup depends exclusively on the expertise of the users.

The instrumentation for bipolar electrochemistry experiments involving multi-bipolar electrodes as probes in a derivated-SECM configuration is in continuous progress. At this point, the research towards the use of such technique for in situ monitoring of relevant biochemical species in cellular environments is relevant and under development. The scanning bipolar electrochemistry microscopy workstation is capable of measuring changes in oxygen concentration and the miniaturization of the multi-microelectrodes array is the next step for continuous use of the system.

All these results shown in this PhD thesis reveal the progress on microelectrodes fabrication and SECM applications, especially those concerning biological systems.

Curriculum Vitae

Carla Santana Santos
Wasserstraße, 102
44803 Bochum – Germany
santana.santos.carla@gmail.com
+5511 975981030

Education.

2014 – 2019 - University of São Paulo, São Paulo, Brazil.
PhD student in Chemistry.
Supervisor: Mauro Bertotti.
Co-supervisor: Alicia J. Kowaltowski.

2010 – 2014 - University of São Paulo, São Paulo, Brazil.
Bachelor's degree in Chemistry.

Research Experience.

2017 – 2018 - Ruhr-Universität Bochum, Bochum, Germany.
Visiting graduate student (1 year)
Supervisor: Wolfgang Schuhmann.
Scholarship: FAPESP Grant #2017/12629-1.

- Developed a scanning probe microscopy using a bipolar electrochemistry concept.
- Fabricated multi bipolar electrodes to perform high spatial and temporal resolution measurements. Enhanced the sensitivity of the technique to measure oxygen.
- The work in the 1-year period resulted in 2 publication in high impact journals (Analytical Chemistry and Analytica Chimica Acta)

2016 – Ruhr-Universität Bochum, Bochum, Germany.
Visiting graduate student (3 months).
Supervisor: Wolfgang Schuhmann.
Scholarship: FAPESP Grant #2014/22396 -6

- Fabricated carbon fiber microelectrodes with low RG values and platinum nanoelectrodes for SECM application.
- Used the Shear Force mode to monitor the heterogeneous activity of a surface by SECM without topographical effects.
- Implemented and transferred the know-how of Shear force mode and nanoelectrodes fabrication to colleagues in Brazil.

2014 – 2019 – University of São Paulo, São Paulo, Brazil.
PhD student (4.5 years)
Supervisor: Mauro Bertotti.
Co-supervisor: Alicia J. Kowaltowski.

Scholarship: FAPESP Grant #2014/22396 -6

- Fabricated platinum micro/nanoelectrodes for local measurements in SECM.
- Developed a procedure to enhance the reactivity and sensitivity towards ORR.
- First in Brazil to work with bio-SECM.
- Developed a methodology using SECM to map the oxygen consumption in a single-cell and to determine the oxygen consumption rate (OCR).
- Worked in bio-analysis in collaboration with biochemistry research groups.
- The work in the period resulted in publications in high impact journals (Scientific Reports, Biosensors and Bioelectronics, Analytical Chemistry, Comparative Biochemistry and Physiology Part A: Molecular & Integrative Physiology).

2013 – Università Ca' Foscari di Venezia, Venice, Italy.
Visiting bachelor student (3 months).
Supervisor: Salvatore Daniele.
Scholarship: Scholarship to academic merit of University of São Paulo.

- Fabricated a pH microsensor using a chemically modified electrode (iridium oxide film) for SECM application.
- The work resulted in a publication (Electroanalysis).

2011 – 2014 – University of São Paulo, São Paulo, Brazil.
Undergraduate student (3 years).
Supervisor: Mauro Bertotti.
Scholarship: FAPESP Grant #2012/16136-6.

- Worked in the development of an electrochemical sensor for pH monitoring and application in Scanning Electrochemical Microscopy.

Language skills.

Portuguese:	native speaker.
English:	B2.
German:	B1.

Basic knowledge in Italian and Spanish.

Teaching Experience.

Feb. 2015 – jun. 2015 - Instrumental analytical chemistry course.
Teaching assistant.
Worked in preparing, coordinating and teaching lab classes, as well in supporting the preparation and correction of homeworks of students enrolled in the 3rd semester of the oceanography bachelor's degree course.

Jul. 2014 – dec. 2014 - Analytical chemistry course.
Teaching assistant.
Reviewed and prepared protocols of lab classes. Coordinated lab classes and helped

with exams and homeworks for students enrolled in the 3rd semester of the chemistry bachelor's degree course.

Dec. 2012 – 2016 and 2018 – School of Electrochemistry.
Demonstrator.
Coordinated the activity of the participants in the LSEME lab and demonstrated procedures for the fabrication of microelectrodes and the basic concepts of SECM.

Aug. 2012 – dec. 2012 - Analytical chemistry course.
Teaching assistant.
Prepared and coordinated lab classes and helped with exams and homeworks for students enrolled in the 2nd semester Oceanography students.

Complementary experience.

Feb. 2015 – aug. 2016. – Coordination of the Graduate Programm committee.
Member.
Voted to represent the graduate students in the committee of the Institute of Chemistry – University of São Paulo.

Feb. 2015 – aug. 2016. – Research Commission.
Member.
Voted to represent the graduate students in the committee of the Institute of Chemistry – University of São Paulo.

Oct. 2011 – oct. 2013. – Undergraduate Commission.
Member.
Voted to represent the undergraduate students in the committee of the Institute of Chemistry – University of São Paulo.

Oct. 2011 – oct. 2012. – Fundamental Chemistry Department Council.
Member.
Voted to represent the undergraduate students in the committee of the Institute of Chemistry – University of São Paulo.

Technical skills.

Electron microscopy.
Experience in the operation of the JEOL JSM- 7401F, sample preparation and to analyse the results.

Electrochemical methods.
Worked with voltammetry, amperometry, potentiometry, pulse techniques and general electrochemical detection.

Electrode fabrication.
Fabrication and preparation of platinum, gold, copper and carbon fiber microelectrodes. Fabrication of platinum nanoelectrodes (the first time in Brazil). Experience in the preparation of electrodes by etching and heat transfer masks.

Cell culture.
Experience in cell culture, handling and maintenance. Experience in extract primary cells of adipose tissues (mice lab). Worked with 4 mammalian cell lineages. Experience with cytometry, Bradford test and respirometry (SeaHorse and Oroboros equipment).

Events organization.

2017 – Electrochemistry and Electroanalytical Meeting of the Institute of Chemistry at the University of Sao Paulo.
Meeting with the electrochemistry and electroanalytical groups of Intstitute of Chemistry. Lima, A. S. ; Meloni, G. N. ; Dourado, A. H. B. ; Santos, C. S. ; Araujo, W. R. ; Antonio, J. L. S. ; Lopes, F. S. ; Prata, R. B.
Planned and organized the schedule. Participated in the scientific committee and for searching sponsors.

2012 – Chemistry week in the Institute of Chemistry.
Traditional lectures week in the Institute of Chemistry.
Worked in the schedule planning with researchers and sponsors invitation. Contributed in the dissemination of information about the event. Chair in the event opening and in the honor ceremony. Chair in some lectures. Helped in reception of participants and speakers.

Honors and Awards.

2019 - Publication Awards 2018 by the Institute of Chemistry at University of Sao Paulo.

2019 - Publication Awards 2017 by the Institute of Chemistry at University of Sao Paulo.

2018 - Metrohm Young Chemist Award - 2nd Place, Metrohm Brasil.

2014 - Best bachelor student of the Chemistry course in the Institute of Chemistry in the period of 2010 - 2014, Conselho Regional de Quimica - IV Região.

2013 – Best poster in the section "Fundamental Electrochemistry" by the International Society of Electrochemistry Awards at the XIX SIBEE (Simpósio Brasileiro de Eletroquímica e Eletroanalítica).

Publication.

Articles in journals.

Santos, C. S.; Conzuelo, F.; Eßmann, V.; Bertotti, M.; Schuhmann, W.; Enhanced sensitivity of scanning bipolar electrochemical microscopy for O_2 detection. *Analytica Chimica Acta*, **2019**, 1087, (9), 36-43.

Barroso, I. G.; **Santos, C. S.**; Bertotti, M.; Ferreira, C.; Terra, W. R.; Molecular mechanisms associated with acidification and alkalization along the larval midgut of *Musca domestica*. *Comparative Biochemistry and Physiology A-Molecular & Integrative Physiology,* **2019**, 237, 110535.

Lima, A. S.; Prieto, K. R.; **Santos, C. S.**; Paula Valerio, H.; Garcia-Ochoa, E. Y.; Huerta-Robles, A.; Beltran-Garcia, M. J.; Di Mascio, P.; Bertotti, M. In-vivo electrochemical monitoring of H_2O_2 production induced by root-inoculated endophytic bacteria in *Agave tequilana* leaves. *Biosensors & Bioelectronics,* **2018**, 99, 08-114.

Santos, C. S.; Bannitz-Fernandes, R.; Lima, A. S.; Tairum, C. A.; Malavazi, I.; Netto, L. E. S.; Bertotti, M.; Monitoring H_2O_2 inside *Aspergillus fumigatus* with an Integrated Microelectrode: The Role of Peroxiredoxin Protein Prx1, *Analytical Chemistry,* **2018**, 90, 2587-2593.

Eßmann, V.; **Santos, C. S.**; Tarnev, T.; Bertotti, M.; Schuhmann, W.; Scanning Bipolar Electrochemical Microscopy, *Analytical Chemistry,* **2018**, 90, 6267-6274.

Santos, C. S., Kowaltowski, A. J.; Bertotti, M. Single Cell Oxygen Mapping (SCOM) by Scanning Electrochemical Microscopy Uncovers Heterogeneous Intracellular Oxygen Consumption, *Scientific Reports*, **2017**, 7, 11428.

Santos, C. S.; Lima, A. S.; Battistel, D.; Daniele, S.; Bertotti, M.; Fabrication and Use of Dual-function Iridium Oxide Coated Gold SECM Tips. An Application to pH Monitoring above a Copper Electrode Surface during Nitrate Reduction, *Electroanalysis,* **2016**, 28, (7), 1441-1447.

Articles in Newspapers/Magazines.

Bertotti, M.; **Santos, C. S.**; Kowaltowski, A. J.; Is Energy Metabolism Homogeneous Within A Cell?, *Science Trends,* **2018**.

Conferences

Oral presentations.

Schuhmann, W.; Eßmann, V.; Santos, C. S.; *A Bipolar Electrochemical Camera for Spatially and Temporally Resolved Visualization of Substance Release*. **2018**. Bioelectrochemistry and Bioelectronics of Macromolecules in Brno, Czech Republic.

Santos, C. S.; Lima, A. S.; Bertotti, M.; *Use of platinized microelectrodes for* O_2 *monitoring in the cellular respiration process by Scanning Electrochemical Microscopy*. **2015**. XX Simpósio Brasileiro de Eletroquímica e Eletroanalítica in Uberlândia, Brazil.

Santos. C. S.; Lima, A. S.; Bertotti, M.; *Development of a potentiometric and amperometric sensor for use in Scanning Electrochemical Microscopy (SECM)*. **2014.** XXI Congresso de la Sociedad Iberoamericana de Eletroquimica in La Serena, Chile.

Poster presentation.

Santos, C. S.; Conzuelo, F.; Eßmann, V.; Bertotti, M.; Schuhmann, W.; *Enhanced sensitivity of the scanning bipolar electrochemical microscopy for* O_2 *detection*. **2019.** 10th SECM workshop in Paris, France.

Lima, A. S.; Santos, C. S.; Cruz, L. C.; Meotti, F. C.; Bertotti, M.; *An Electrochemical Study of Urate Hydroperoxide Using Carbon Microelectrodes*. **2019.** XXV International Symposium on Bioelectrochemistry and Bioenergetics in Limerick, Irland.

Santos, C. S.; Kowaltowski, A. J.; Bertotti, M.; *Scanning Electrochemical Microscopy as a tool for mitochondrial respiration monitoring*. **2017**. I Encontro de Eletroquímica e Eletronalítica IQ-USP in São Paulo, Brazil.

Lima, A. S.; **Santos, C. S**.; Bannitz-Fernandes, R.; Netto, L. E. S.; Bertotti, M.; *In vivo hydrogen peroxide degradation monitoring in Aspergillus fumigatus Fungus*. **2017.** Pittsburgh Conference & Exposition on Analytical Chemistry and Applied Spectroscopy in Chicago, USA.

Santos, C. S.; Lima, A. S.; Oliveira, K. R. P.; Beltran-Garcia, M. J.; Di Mascio, P.; Bertotti,; *Fabricação de microssensor eletroquímico de pH e aplicação em amostras biológicas*. **2016.** 18° Encontro Nacional de Química Analítica in Florianópolis, Brazil.

Lima, A. S.; Santos, C. S.; Oliveira, K. R. P.; Beltran-Garcia, M. J.; Di Mascio, P.; Bertotti,; *Detecção de* H_2O_2 *em folhas de Agave Tequilana durante a degradação de bactérias endofíticas*. **2016.** 18° Encontro Nacional de Química Analítica in Florianópolis, Brazil.

Santos, C. S.; Bertotti, M.; *Investigation of mitochondrial respiration by Scanning Electrochemical Microscopy*. **2016.** 67th Annual Meeting of the International Society of Electrochemistry in The Hague, Netherlands.

Lima, A. S.; Santos, C. S.; Amemiya, S.; Bertotti, M.; *Transferência de íons entre duas fases imiscíveis: uma alternativa para obtenção de sondas para microscopia eletroquímica*. **2015.** XX Simpósio Brasileiro de Eletroquímica e Eletroanalítica, in Uberlândia, Brazil.

Santos, C. S.; Lima, A. S.; Silva, V. F. G.; Bertotti, M.; *Construção de microeletrodo sensor de pH para aplicação em Microscopía Eletroquímica de Varredura*. **2013**. XIX Simpósio Brasileiro de Eletroquímica e Eletroanalítica in Campos do Jordão, Brazil.

Santos, C. S.; Lima, A. S.; Bertotti, M.; *Desenvolvimento de sensor para o monitoramento de pH em microambientes*. **2012**. 35ª Reunião Anual da Sociedade Brasileira de Química in Águas de Lindóia, Brazil.

List of Annexes